Developing luminescence-based inventories to decipher particle histories in hyperarid alluvial landforms (Atacama Desert, Chile)

Inaugural-Dissertation

zur

Erlangung des Doktorgrades

der Mathematisch-Naturwissenschaftlichen Fakultät

der Universität zu Köln

vorgelegt von

Linda Andrea Elisabeth Maßon

aus Aachen

angenommen im Jahr 2025

Abstract

Deciphering particle histories in hyperarid alluvial landforms is crucial to reconstruct depositional and post-depositional dynamics. This is essential to understand landscape evolution and climatic variability in the Late Quaternary. In the Atacama Desert, the driest non-polar desert on Earth, such reconstructions are scarce since suitable chronological tools are lacking. Organic material for ^{14}C dating is usually absent and cosmogenic nuclide dating methods cannot resolve subsurface processes related to post-depositional mixing. Single-grain feldspar luminescence dating can overcome those challenges, as feldspar grains are abundant and can record both deposition and post-depositional processes. However, this method also has limitations: Atacama Desert feldspars **i)** display unfavourable luminescence properties, **ii)** have heterogeneous geochemical compositions, and **iii)** experience heterogeneous bleaching, which is common in alluvial deposits.

This thesis presents methodological refinements of single-grain feldspar luminescence dating techniques. These techniques are tested by applying them to decipher particle histories along a climatic and elevational transect in the Coastal Cordillera of the Atacama Desert. The overall aim is to establish a chronological toolset for complex alluvial settings in hyperarid regions and to apply it to improve the understanding of palaeoclimatic variability and landscape evolution in the Coastal Cordillera.

The challenging luminescence properties of Atacama Desert feldspars result in time-consuming measurements, as many grains have to be analysed to obtain a sufficient number of suitable luminescence signals. In a first study the application of a standardised growth curve (SGC) was successfully tested on Atacama Desert samples. Measurement times were reduced by at least 60 %. It was further shown that the geochemical composition of feldspar grains is not correlated with their luminescence characteristics. This finding motivated a second study of the internal potassium (K) concentration of feldspar and its effects on dose rate calculations. A comparison of the three most cited literature-based values with measurement-based K-concentrations revealed that literature values overestimate the K-concentration in nine out of ten analysed samples. This results in systematic one-directional errors in the dose rate determination and consequently in the age calculation. To address this, a time- and cost-efficient approach was developed to routinely measure the K-concentration in feldspar for luminescence dating. In the third study of this thesis, this approach was successfully applied to samples from alluvial deposits along the climatic and elevational transect in the Atacama Desert. However, the SGC approach

yielded unreliable results when applied to these samples. Therefore, in the third study a conventional single-aliquot regenerative-dose (SAR) approach was used for equivalent dose (D_e) estimations. The luminescence analyses were integrated into a multi-method framework that included granulometric and geochemical analyses as well as field surveys. Five soil and surface profiles along the climatic and elevational transect were examined. Depositional phases as well as post-depositional processes, including bioturbation and desert pavement formation, were identified. The results indicate wetter phases around 50 ka and since 5 ka, as well as prolonged geomorphic stability under presumably extremely arid conditions around 6 ka. These reconstructions are consistent with other palaeoenvironmental archives from the region and suggest a strong influence of regional climate variability, likely linked to (ENSO-related) weather anomalies.

Overall, this thesis demonstrates that in complex alluvial landforms, which are prone to heterogeneous bleaching and contain feldspars with heterogeneous chemical compositions, special precautions are required. Dose rates must be determined accurately, accounting for variable internal K-concentrations. Furthermore, luminescence results must be interpreted holistically. This involves considering the shape of D_e distributions, age estimates, luminescence-related proxies, and geomorphological evidence, rather than focussing on a single age per sample. Applied in this way, single-grain feldspar luminescence dating provides a robust tool to decipher particle histories and thereby reconstruct the paleoenvironment, thus contribution to an improved understanding of Late Quaternary climatic fluctuations and landscape evolution in the hyperarid Atacama Desert.

Kurzzusammenfassung

Den Weg einzelner Körner in hyperariden alluvialen Ablagerungen nachzuvollziehen ist entscheidend für die Rekonstruktion der Dynamiken von Depositions- und Postdepositionsprozesse. Dieses Wissen ist wesentlich für das Verständnis der Landschaftsentwicklung und der Klimavariabilität im Spätquartär. In der Atacama-Wüste, der trockensten nicht-polaren Wüste der Erde, sind solche Rekonstruktionen selten, da geeignete chronologische Werkzeuge fehlen. In der Regel ist kein organisches Material für die ^{14}C-Datierung vorhanden und mit kosmogener Nukliddatierung können Postdepositionsprozesse im Untergrund nicht aufgelöst werden. Da Feldspatkörner häufig vorkommen und sowohl Depositions- als auch Postdepositionsprozesse aufzeichnen können, ist die Einzelkorn-Lumineszenzdatierung von Feldspat eine vielversprechende chronologische Methode in der Atacama-Wüste. Diese Methode weist jedoch ebenfalls Limitationen auf: Feldspäte in der Atacama-Wüste **i)** besitzen ungünstige Lumineszenzeigenschaften, **ii)** haben heterogene geochemische Zusammensetzungen und **iii)** erfahren heterogenes Bleichen, das bei der alluvialen Ablagerung typisch ist.

In dieser Dissertation wird die Einzelkorn-Feldspat-Lumineszenzdatierung methodisch an die Gegebenheiten in der Atacama-Wüste angepasst. Diese angepassten Techniken werden entlang eines Klima- und Höhentransekts in der Küstenkordillere der Atacama-Wüste angewendet und somit getestet. Das übergeordnete Ziel ist es, einen chronologischen Werkzeugkasten für komplexe alluviale Systeme in hyperariden Regionen zu entwickeln und diesen einzusetzen, um das Verständnis vergangener Klimaschwankungen und der Landschaftsgenese in der Küstenkordillere zu verbessern.

Die herausfordernden Lumineszenzeigenschaften der Feldspäte aus der Atacama-Wüste führen zu zeitaufwändigen Messungen, da viele Körner analysiert werden müssen, um eine ausreichende Zahl geeigneter Lumineszenzsignale zu erhalten. In einer ersten Studie wurde daher die Anwendung einer *standardised growth curve* (SGC) erfolgreich an Proben aus der Atacama-Wüste getestet. Die Messzeiten konnten dadurch um mindestens 60 % reduziert werden. Darüber hinaus wurde in dieser Studie gezeigt, dass die geochemische Zusammensetzung von Feldspatkörnern nicht mit ihren Lumineszenzeigenschaften korreliert. Dieses Ergebnis motivierte eine zweite Studie zur internen Kaliumkonzentration (K-Konzentration) von Feldspat und deren Einfluss auf die Dosisratenberechnungen. Der Vergleich der drei am häufigsten zitierten literaturbasierten K-Konzentration mit gemessenen K-Konzentrationen ergab, dass Literaturwerte die K-Konzentration in neun von zehn analysierten Proben

überschätzen. Dies führt zu einem systematischen Fehler in der Bestimmung der Dosisrate und folglich in der Altersberechnung. Daher wurde innerhalb dieser Studie ein zeit- und kosteneffizientes Verfahren entwickelt, mit dem die K-Konzentration in Feldspat für Lumineszenzdatierungen routinemäßig bestimmt werden kann. In der dritten Studie dieser Dissertation wurde dieser Ansatz erfolgreich auf Proben aus alluvialen Ablagerungen entlang des Klima- und Höhentransekts in der Atacama-Wüste angewandt. Der SGC-Ansatz lieferte für diese Proben jedoch unzuverlässige Ergebnisse. Daher wurde in der dritten Studie ein konventioneller *single-aliquot regenerative-dose* (SAR)-Ansatz zur Bestimmung der Äquivalentdosis (D_e) verwendet. Die Lumineszenzanalysen wurden in ein multimethodisches Konzept integriert, das granulometrische und geochemische Analysen sowie Geländeaufnahmen umfasste. Fünf Boden- und Oberflächenprofile entlang eines Klima- und Höhentransekts wurden untersucht. Dabei konnten sowohl Depositionsphasen als auch postdepositionale Prozesse, einschließlich Bioturbation und Desert-Pavement-Bildung, identifiziert werden. Die Daten deuten auf feuchtere Phasen um etwa 50 ka und seit 5 ka hin sowie auf eine anhaltende geomorphologische Stabilität unter vermutlich extrem ariden Bedingungen um 6 ka. Diese Rekonstruktionen stimmen mit anderen Paläoumweltarchiven aus der Region überein und deuten auf einen starken Einfluss regionaler Klimavariabilität hin, der wahrscheinlich mit (ENSO-bedingten) Wetteranomalien verknüpft ist.

Zusammenfassend wird in dieser Dissertation gezeigt, dass die Rekonstruktionen von komplexen alluvialen Landschaftsformen, die sowohl heterogenes Bleichen von Feldspatkörnern als auch chemische Variabilität in den Feldspäten aufweisen, spezifische qualitätssichernde Vorgehensweisen erfordern. Dosisraten müssen präzise bestimmt werden, wobei ein besonderes Augenmerk auf variable interne K-Konzentrationen zu legen ist. Darüber hinaus müssen Lumineszenzergebnisse holistisch interpretiert werden. Dies erfordert die Berücksichtigung der Form von D_e-Verteilungen, modellierter Alter, lumineszenzbasierter Proxies sowie geomorphologischer Befunde, anstatt sich auf ein einzelnes Alter pro Probe zu konzentrieren. Auf diese Weise angewandt stellt die Einzelkorn-Feldspat-Lumineszenzdatierung ein robustes Werkzeug zur Rekonstruktion der Wege einzelner Körner und somit der Paläoumwelt dar und trägt dadurch wesentlich zum Verständnis der quartären Klimaveränderungen und Landschaftsgenese in der hyperariden Atacama-Wüste bei.

Acknowledgment

The last years have been unforgettable. I was able to meet so many wonderful people along the way and see the most beautiful landscape I can imagine (outside of Iceland). This acknowledgement might seem a bit long but I was born on “world gratitude day” and on top I’m sure it should be even longer because I certainly missed friends and colleagues because I’m stressed out.

First of all, I want to thank my supervisor Prof. Dr. **Tony Reimann**, for giving me the opportunity to work at one of the most fascinating and (literally) breath-taking places on this earth. I am also deeply grateful for the flexibility I was given in adapting my working hours and locations to my health needs. I doubt that many people receive work instructions such as: “Go home, binge-watch the new season of Bridgerton, rest, and get well.”

I would also like to thank Jun.-Prof. Dr. **Svenja Riedesel**, who not only explained the world of luminescence dating to me with a great deal of patience, but also taught me to sweat out every pore of my body under a plastic tarpaulin at extremely high temperatures. I’ve learned so much more than “just” luminescence from your supervision. Your scientific life is truly inspiring!

Further I would like to thank Prof. Dr. **Sumiko Tsukamoto**, for taking the time and patience to examine my thesis. Also thank you for your motivation and support at various conferences throughout the last years.

This work would also not have been possible without the help of numerous other colleagues, who have always supported me not only professionally but also morally. Without **Anja Zander**, I would probably still be sitting in front of a non-functioning reader. Thank you so much for your help, no matter how ‘stupid’ my problem was. Without **Matze May**, I wouldn't have taken a single meaningful sample and probably wouldn't understand my results. Thank you for your help with the fieldwork and for all your support in geomorphology. Without the support of my office crew (**Katharina Seeger**, **Arindam Biswas**, **Xuimin Pan**, and many more), I would have lost my motivation in bad stressful phases. Thank you very much for your friendship and understanding. Without **Andreas Peffeköver**, my fieldwork phases would have been unthinkable. Many thanks for your driving skills, hole-digging skills, tarp-laying skills, photographer skills (cf. pages 16 and XCII), and much more. Without **Mariana Sontag-Gonzales**, I would certainly never have been able to establish a SGC. Thank you for your help with thousands of lines of code, valuable feedback and moral support. Without **Laura Kögler** I wouldn’t know that the young geomorphologists exist. Thank you for teaching me a lot in and outside of the lab and for being my friend.

Without **Sarah Spengel**, **Johanna Steiner**, and **Johanna Schreiber**, I would certainly still be stuck in the sample preparation room. Thank you very much for every sample you had to beat through the preparation process. Without **Stephan Opitz**, I would probably still be shouting at the μ-XRF software. Thank you for your support since my bachelor thesis. Without **Marijn van der Meij**, the quarantine in Chile would have been much worse and my age estimates were non-existing. Thank you very much for your help on a human and professional level. And for always reminding me to take breaks. Without **Lucas Ageby**, the reader of this thesis would be a lot more confused. Thank you for proof reading my drafts and for your moral support along the way! Without **Dorina Kley**, **Susanne Weber**, and **Andreas Bolten**, my daily university-life would have been much harder and I'm not sure if my laptop would still be alive.

Many thanks also to **Martin Kehl** and **Tim Reichenau**, who challenged and supported me during my bachelor's and master's, to **Christine Heim** for her support in Pica-quarantine and onwards and to **Martin Autzen**, who organised a wonderful side quest. Without my CRC 1211-related friends, **Lina**, **Bárbara**, **Cami**, **José**, **Tiago**, **Sniggi**, **Käte**, **Aline**, and many more, I would have missed a lot of fun, beer, Pisco, parties, deep conversation, cultural exchange, love, and drama. I'm so grateful to have you in my life now!

I would also like to thank important people, that haven't been part of my work environment: Starting with **Tobias Gerhardt**, without whom I would probably still have no idea about grammar and spelling. I would also like to thank **Thomas Langkau**, the best therapist ever, without whom I would never have been able to get through a doctorate. My physical therapists **Anna Heim** and **Jenny Stolzenberger**, who helped me endure the pain. My entire **family** and **friends** as well as our lovely neighbours **Uwe** and **Cäcilia**, you all helped me along the way and believed in me and encouraged me to follow my dreams.

In addition to everyone already mentioned (including the ones I forgot!), I would like to thank the five most important people in my life, even if my words are not enough to express my gratitude.

Thank you, **Meme**, for supporting me in everything I do and always being there for me no matter how good or bad I feel (or how annoying I am).

Thank you, **Pepe**, for being my biggest role model (perhaps unintentionally) and for giving me answers to all my questions. And of course, for still loving me even though I choose the "wrong kind of physics".

Thank you, **Julia**, for being there for me from an early age and for not changing that, even during times when I got on your nerves. You're my biggest sports-role

model and you inspired me to keep on trying. I'm so proud of you and what you've archived! Even though you're tiny, I will always look up to you.

Thank you, **Johannes,** for your patience and your help with my scientific language, your Netflix account, and my Pokémon skills even though I punched out one of your teeth. If 25 years ago someone would have told me how grateful I would be to call you my brother and how proud I am at what you archived in your "shitty" job I would have not believed a word of it!

And thank you all four for the time you sacrificed for me in the past 33 years.

Thank you, **Simon,** for understanding me and my dissertation. Thank you for always being there for me, no matter how you felt yourself. Your patience with me is immeasurable. I do not think I would have been strong enough to do this without you.

Table of contents

Abstract III
Kurzzusammenfassung V
Acknowledgements VII
Contents X
List of figures XIV
List of tables XXII
List of equations XXIII
Abbreviations XXIV
1 Introduction 1
1.1 Rationale of the thesis 2
1.2 The Collaborative Research Centre 1211 – Earth - Evolution at the dry limit 3
1.3 Research questions and objectives of this thesis 6
1.4 Research design and methods 12
1.4.1 Luminescence dating methodological framework 14
1.4.2 K-concentration analysis 14
1.4.3 Fieldwork 15
1.4.4 Granulometry and geochemistry 15
2 Luminescence-based inventories and alluvial landforms 16
2.1 Luminescence dating – theoretical background 17
2.1.1 Luminescence dating – brief overview 17
2.1.2 Feldspar luminescence dating 23
2.1.3 Dose rate determination 29
2.2 Alluvial deposits – implications for luminescence dating 33
2.2.1 Alluvial deposits in the Atacama Desert 33
2.2.2 Luminescence dating of alluvial deposits in the Atacama Desert 38
3 Testing the applicability of standardised growth curves (SGC) for chemically heterogeneous single-grain feldspars from the Atacama Desert, Chile 42
Abstract 44
3.1 Introduction 45
3.2 Samples and instrumentation 47
3.2.1 Samples 47
3.2.2 Luminescence 49
3.2.3 Geochemistry (SEM-EDX) 50

3.2.4 Statistic 51
3.3 Standardised growth curve (SGC) application and modification 51
3.3.1 SAR and SGC 51
3.3.1.1 Procedure 51
3.3.1.2 Results & discussion 52
3.3.2 External SGC (xSGC) 55
3.3.2.1 Procedure 55
3.3.2.2 Results & discussion 55
3.3.3 Synthetic R (sR) 56
3.3.3.1 Procedure 56
3.3.3.2 Results & discussion 58
3.3.4 Reduction of SAR cycles (rc) 59
3.3.4.1 Procedure 59
3.3.4.2 Results & discussion 59
3.3.5 Dose recovery ratio (DRR) 61
3.4 Single-grain geochemistry 62
3.4.1 Procedure 62
3.4.2 Results 63
3.5 Correlation of luminescence characteristics and geochemistry 65
3.6 Conclusion 67
3.7 Acknowledgements 69
3.8 CRediT authorship contribution statement 69
3.9 Declaration of competing interest 69
4 How much K is OK? – Evaluating different methods for K-concentration determination and the effect of the internal K-concentration on feldspar luminescence dating 70
Abstract 72
4.1 Introduction 73
4.2 Feldspar luminescence dating 75
4.2.1 Feldspar characteristics 75
4.2.2 Literature review 76
4.3 Sample details, instrumentation, and methods 79
4.3.1 Samples and sample preparation 79
4.3.2 Luminescence measurements 82
4.3.3 Determination of the K-concentration 82

4.3.3.1 β-counter measurements of bulk material 82
4.3.3.2 WDXRF of bulk material 83
4.3.3.3 Single-grain SEM-EDX measurements 84
4.3.3.4 Single-grain μ-XRF measurements 85
4.3.4 Calculations of the luminescence-weighted K estimates 85
4.3.5 Dose rate calculations 86
4.4 Limitations and practicability 86
4.5 Results and discussion 89
4.5.1 Bulk sample measurements and sample average concentrations 89
4.5.2 Distributions of single-grain K-concentrations 91
4.5.3 Practical implications 96
4.6 Effect of the K-concentration on the dose rate 97
4.7 Conclusion 100
4.8 Data availability 102
4.9 Author contributions 102
4.10 Competing interests 102
4.11 Acknowledgements 102
5 Challenges in the application of SGCs to natural Atacama Desert samples 103
6 Geomorphological activity and stability of surfaces and soils formed in hyperarid alluvial deposits (Atacama Desert, Chile) 111
Abstract 113
6.1 Introduction 113
6.2 Physical setting 115
6.2.1 Climate 115
6.2.2 Geology and geomorphology 116
6.3 Methods 117
6.3.1 Field work 117
6.3.2 Geochemistry and granulometry 120
6.3.3 Feldspar luminescence dating 120
6.4 Results and interpretation 122
6.4.1 Geochemistry and granulometry 122
6.4.2 Feldspar luminescence dating 125
6.4.3 Interpretation of profile genesis 128
6.5 Discussion 132
6.5.1 Profile chronology and formation 132

6.5.2 Paleoclimatic significance 135
6.6 Conclusion 141
6.7 Author contributions 142
6.8 Competing interests 142
6.9 Acknowledgements 142
7 Discussion of the research questions 143
7.1 Method refinement and geochemical properties of feldspar 144
7.2 Method application 154
7.3 Concluding remarks 161
8 Conclusion and Outlook 162
8.1 Conclusion 163
8.2 Outlook 165
Appendix XXVII
Appendix A (Chapter 3) XXVIII
Appendix B (Chapter 4) XXXVIII
Appendix C (Chapter 6) XLV
Appendix C-I – Geochemistry and granulometry XLVII
Appendix C-II – Luminescence dating LI
Appendix C-III – Detailed description of the sampling sites LVII
Bibliography LXIV
List of resources XCII

List of figures

Fig. 1.1: Colour-shaded digital elevation model of northern Chile derived from SRTM-data (NASA Shuttle Radar Topography Mission (SRTM), 2013), created using ArcGIS Pro 3.3.0 by Dr. S.M. May. The three CRC 1211 focus areas are outlined in white. Dashed lines indicate elevation transects within the northern (**T1** – Aroma transect) and southern (**T2** – Paposo transect) focus areas. Sampling locations used in Chapters 3 and 4 are shown as white circles (ARO-18-08-LP, CSA-1-2-2, LAGU-1-1, PAG-4-4b, and PAG-4-6b). Samples presented in Chapters 5 and 6 (P1-P5) are marked by coloured circles corresponding to their climatic classification: abiotic (hyperarid), transition, and biotic (more humid, yet still hyperarid). **Inset:** location of the study area in South America (map base: Canuckguy, 2006, Wikimedia Commons public domain). 5

Fig. 1.2: Workflow diagram illustrating the research design of this thesis. Each coloured box represents a distinct methodological or analytical step, with the colour indicating the chapter in which the step is described and implemented in detail. The abbreviations **Q1**, **Q2**, and **Q3** correspond to Research Questions 1 to 3, respectively. All subsequent boxes linked to a given Q-number denote the activities contributing to the resolution of that specific research question. 13

Fig. 2.1: Simplified band gap energy model of optically stimulated luminescence (OSL), adapted from Rhodes (2011), with each defect shown as a single energy state. Electron traps are marked in black; hole traps are marked in green. Electrons are represented by grey circles with black outlines, and holes (including vacancies in luminescence centres) by white circles with green outlines. **a)** Initial state without active ionising radiation or any stimulation. While thermally stable traps may still contain electrons from earlier exposure to ionising radiation, thermally unstable traps near the conduction band are typically empty due to ambient thermal evictions. **b)** During burial, ionising radiation excites electrons from the valence band into the conduction band, leaving behind holes. These holes are filled by electrons from luminescence centres whereby the centres become available again. Excited electrons migrate through the conduction band and become trapped in available electron traps within the band gap. **c)** State after irradiation (b), with one or more traps now occupied by electrons, the hole in the valence band filled, and the luminescence centre reset and available. **d)** Exposure to light causes the eviction of electrons from light-sensitive traps. The excited electron may either recombine with a hole at a luminescence centre, emitting a photon, recombine with a hole at a non-radiative hole trap, emitting heat, or be re-trapped elsewhere. **e)** Laboratory stimulation with controlled light within a luminescence reader induces the same processes as in (d), but emitted photons are passed through optical filters and recorded by a photomultiplier tube. **Note**: In this schematic, potential photon emission resulting from recombination after re-trapping is not shown for reasons of clarity. Furthermore, the path of the electron from trap to luminescence centre is illustrated in a simplified manner. For a more detailed discussion of potential recombination pathways (ground state tunnelling, excited state tunnelling, hopping in band-tail states) and associated energy levels for de-trapping, traps, band-tail states and the band gap, see Baril and Huntley, 2003; Clark and Sanderson, 1994; Kars et al., 2013; Malins et al., 2004; Poolton et al., 2009; Prasad and Jain, 2018; Visocekas, 1985. 18

Fig. 2.2: Simplified conceptual model illustrating the basic principle of charge accumulation and resetting (bleaching) in luminescence dating, modified from Durcan (2021). During burial, minerals are exposed to ionising radiation, causing electrons to become trapped in defects of the crystal lattice (electron traps) and gradually accumulate (Fig. 2.1b). Upon exposure to light (e.g. during transport or surface exposure) these trapped electrons can be released (Fig. 2.1d), effectively resetting the luminescence signal. If the light exposure is sufficient, the sample becomes fully bleached, meaning that the trapped charge is reduced to near zero. Upon reburial, the cycle of radiation-induced charge accumulation begins anew. If the light exposure prior to burial is insufficient to empty all electron traps, the sample is only partially bleached (Chapter 2.2.2). In this case, the residual trapped charge from earlier exposure adds to the newly accumulated signal, 19

potentially leading to an overestimation of burial age if not corrected. Following complete bleaching, burial, and careful sample collection and storage in light-tight conditions, the accumulated trapped charge represents the time elapsed since the last bleaching event. In the laboratory, the sample is stimulated using controlled light, and the resulting luminescence, in form of emitted photons from recombination processes in luminescence centres, is measured to estimate the burial dose, from which the age can be calculated (Fig. 2.1e).

Fig. 2.3: Luminescence measurement results for the feldspar sample P2-3 (Chapter 6). **a)** Single-grain post-infrared infrared stimulated luminescence at 225 °C ($pIRIR_{225}$, cf. Chapter 2.1.2) decay curve (dark purple). Light pink curves in front of a light pink background before and after the measurement represent the so-called dead channels measured 0.1 s prior and post of the stimulation period. The signal integration interval (first 0.2 s of stimulation) and the background integration interval (last 0.4 s of stimulation) are shaded in grey. **b)** Multi-grain $pIRIR_{225}$ decay-curve (dark turquoise). Light blue curves in front of a light blue background before and after the measurement represent the dead channels (5 s each). The signal integration interval (first 10 s of stimulation) and the background integration interval (last 40 s of stimulation) are shaded in grey. **c)** Dose-response curve (black) of the same disc shown in b) of a $pIRIR_{225}$ dose recovery test. The L_n/T_n is shown as a purple dot, and L_x/T_x are shown as turquoise dots. The L_x/T_x of repeated measurements at specific dose (0 s, 700 s, 2097 s) are indicated by light blue dots. **Note:** as only feldspars were measured within this thesis, quartz decay curves are not shown. The main difference between both are: (i) quartz OSL signals typically decay much more rapidly than feldspar infrared stimulated luminescence (IRSL) signals; and (ii) signal intensity is sample-dependent, but feldspar IRSL signals generally exhibit higher intensity than quartz OSL signals. 20

Fig. 2.4: Emission spectra of K- and Na-feldspar grains, transmittance curves of the Corning 7-59 and the Schott BG39 filters, and emission spectra from an IR laser and IR LEDs. The emission spectra of the feldspars are redrawn from Huntley et al. (1991). The main peak emission (~475 – 600 nm) of the Na-feldspar is drawn at x 0.05 of its original height. The transmission spectra for the Corning 7-59 was taken from Lo and Turk, (1982), the transmission spectra for the Schott BG39 and the IR LED emission spectra were taken from DTU Physics (2021), and the emission spectra for the IR laser was taken from Bøtter-Jensen et al. (2000). The grey bar highlights the transmission window of the blue filter combination between ~310 nm and ~490 nm. 25

Fig. 2.5: pIRIR fading test results conducted on sample P5-4 (see Chapter 6), comparing **a)** pIRIR with a measurement temperature of 160° ($pIRIR_{160}$) and **b)** pIRIR with a measurement temperature of 225° ($pIRIR_{225}$) protocols. **a)** A preheat temperature of 190 °C was applied, the sample showed considerable fading with a g-value of 5.87 ± 1.29 %. **b)** A preheat temperature of 250 °C was applied, and the sample experienced negligible fading with a g-value of 0.03 ± 1.45 %. 28

Fig. 2.6: Schematic structure of an alluvial fan system in the Atacama Desert (modified from Walk, 2020, after Blair and McPherson, 2009). The sampling location of alluvial fans and ephemeral channels (Chapter 6) are indicated by coloured boxes and profile names (P1–P5). The abandoned left segment of the terminal alluvial fan is dominated by sheet floods, whereas the right abandoned segment and the active depositional lobe are dominated by debris flows. 37

Fig. 2.7: Single-grain D_e distribution of a hypothetical heterogeneous bleached sample: **a)** at time of burial, and **b)** after a period of burial. **a)** **Fully bleached** grains, exposed to sufficient sunlight prior to deposition, have a D_e around 0 Gy (green section). **Partially bleached** grains, which experienced limited sunlight exposure, have intermediate D_e values (blue section). **Unbleached** grains, completely shielded from sunlight, retain their original D_e of 150 Gy (purple section). **a, b)** The red line indicates the **MAM D_e** calculated based on single-grains. The orange line shows a theoretical D_e of a **multi-grain measurement** of the sample. **Note:** The peak of the distribution is slightly above 0 Gy 39

because grains often retain a small residual dose even after adequate light exposure (e.g. Buylaert et al., 2009; Reimann et al., 2011). During the D_e calculations, each signal is background-corrected (signal – background). In cases where the net luminescence signal approaches zero, background noise can exceed the measured signal, resulting in small negative D_e values (e.g. Arnold et al., 2009; Galbraith and Roberts, 2012). After burial, microdosimetric effects cause a broadening of the D_e distribution (e.g. Murray and Roberts, 1997; Nathan et al., 2003; Olley et al., 1997).

Fig. 2.8: Hypothetical single-grain D_e distributions of samples in alluvial deposits within the Atacama Desert, illustrating different depositional and post-depositional scenarios. **a)** Unimodal broad distribution, potentially resulting from either prolonged burial, intensive mixing or a combination of both processes. **b)** Bimodal distribution with one dominant and one minor peak, typical of mixing between two distinct D_e populations. **c)** Bimodal distribution with broad, less pronounced peaks, characteristic of mixing between two less distinct D_e populations. Modified after Bateman et al. (2003). 40

Fig. 3.1: Evaluation of SGC performance. **A)** comparison of D_e from samples of subset A (Table 3.1) obtained by the standard SAR procedure with D_e obtained using an SGC established with the same measurements, fitted with their L_{r1}/T_{r1} from the eighth regenerative SAR cycle with a D_{r1} of 50 Gy (Table 3.2); **B)** comparison of D_e from samples of subset A obtained by an SGC, established using the same samples, and obtained by a xSGC, constructed with data from subset X (Table 3.1); **C)** comparison of D_e from samples of subset A obtained by the standard SAR procedure with D_e obtained using the xSGC from B) and fitting the individual grains with L_{sR}/T_{sR} from an synthetic cycle with a D_{r1} of 150 Gy (sR_{150}xSGC); **D)** comparison of D_e from samples of subset A obtained by the standard SAR procedure with D_e obtained using the sR_{150}xSGC from C) and reducing the SAR-cycles for individual growth curve fitting to the "natural" 150, 0, 50, 500, 50 Gy cycles (rc_5sR_{150}xSGC). 54

Fig. 3.2: Influence of odd L_x/T_x values and the mitigation strategy of implementing (sR) **A)** Process of L_{sR}/T_{sR} determination with an sR of 200 Gy on an example exponential SG growth curve of the sample CSA-1-2-2 with an odd L_x/T_x value in the third regenerative SAR cycle (D_i = 150 Gy). The vertical line from the X-axes towards the growth curve illustrate the process of calculating the interception. The horizontal line from the growth curve towards the Y-axes illustrate the subsequent determination of L_{sR}/T_{sR}. **B)** Comparison of D_e values of the same grain estimated using different techniques with: SAR using the standard SAR approach, SGC using the SGC constructed with data from subset A and regenerative cycle R8 (50 Gy) used for projection onto the SGC, xSGC using the xSGC constructed with data from subset X and regenerative cycle R8 used for projection onto the xSGC, N + R2 xSGC using only the natural and regenerative cycle R2 (50 Gy) for the rejection process and using the xSGC constructed with data from subset X and regenerative cycle R2 used for projection onto the xSGC, N + R3 using the same procedure as N + R2 but using R3 (150 Gy) instead of R2, sR_{150}xSGC using the same procedure as xSGC but instead of using R8 for projection onto the SGC the sR method with a sR of 150 Gy was used, rc_5sR_{150}xSGC (introduced in Chapter 3.3.4) is using only regenerative cycles N, R1, R2, R4 and R8 (cf. Table 3.3) for the rejection process and the sR method with a sR of 150 Gy for projection onto the xSGC. 57

Fig. 3.3: D_e values from grains of subset A, calculated with the standard SAR procedure (x-axes) and the rc_5sR_{150}xSGC method (y-axes). Colours of the horizontal and vertical 1σ error bars represent if the DRR calculated with SAR or rc_5sR_{150}xSGC are within unity ± 10 % (green), within 1 ± 10 % if the 1σ error is considered (blue) or if they are not within 1 ± 10 %. Shape of the datapoints indicates the sample allocation (cf. legend Fig. 3.2). 62

Fig. 3.4: Statistical distribution of all measured element concentrations for **A)** the grains from subset A and **B)** the grains from subset X grouped into luminescent (purple) and non-luminescent grains (grey). The lower and upper hinges correspond to the first and third quartiles (the 25th and 75th percentiles). The upper whisker extends from the hinge to the largest value no further than 1.5 * IQR from the hinge (where IQR is the inter-quartile range, or distance between the first and third quartiles). The lower whisker extends from the hinge to the smallest value at most 1.5 * IQR of the hinge. Data beyond the end of the 64

whiskers are called "outlying" points and are plotted individually. The horizontal bar represents the median.

Fig. 3.5: Correlation matrix of the complete dataset (subset A + X). Numbers in the squares represent Spearman's rank correlation coefficient values and their colour the strength of the correlation. For not significant correlations with a p-value above 0.05 % the squares are crossed out. The **turquoise square** surrounds the correlation between the geochemical data and the luminescence characteristics. 65

Fig. 4.1: Summary of the literature review. **a)** Amount of published literature, covering the topic of dose rate determination for feldspar luminescence dating, per year from 2009 until 2023. Green bars represent years after a LED in which a LED special issue was published. The purple dashed line shows the trend of publication numbers per year over time. **b)** References given for used K-concentrations in the analysed 432 studies. The white numbers within the diagram show the total citation numbers. Note that the total sum exceeds the sum of 432 studies analysed since some studies cited several references. The "unclear" segment is the sum of studies who did not cite or mention a K-concentration, studies mentioning a value for the K-concentration without a reference, and studies vaguely giving information. 77

Fig. 4.2: K-concentrations for each sample determined with different methods, respectively calculated from measured K-concentrations. For the single-grain measurements (μ-XRF and SEM-EDX), the averages are presented. The error bars represent the standard errors. Horizontal bars represent the most frequently used literature values for the K-concentration and their corresponding errors of 10 ± 2 %, 12.5 ± 0.5 % and 13 ± 1 %. 90

Fig. 4.3: Single-grain K-concentrations for the overall most homogeneous sample MBT-I-2430 (**a**) and the most heterogeneous sample ISM-7 (**b**). The dark blue dashed density curves and dots are based on the SEM-EDX measurements and the light blue ones on the μ-XRF measurements. The red circles around the dark blue dots and the light green density curve represent the luminescent grains. The vertical lines represent the K-concentrations presented in Chapter 4.5.1, boxes above the graph representing their errors. 94

Fig. 4.4: Ḋ results, with $\dot{D}_{int}$ and total Ḋ calculated with DRAC (Durcan et al., 2015) based on the different K-concentrations of the three most cited literature values (open symbols), the measured K-concentrations (filled symbols), and luminescence-weighted K estimates (filled symbols). All other input variables are described in Chapter 4.3.5. **a**) The proportion of the $\dot{D}_{int}$ in the corresponding total Ḋ. **b**) The total Ḋ. **c**) A comparison between the total Ḋ based on the K-concentration of 12.5 ± 0.5 % (Huntley & Baril, 1997) and the total Ḋ based on the measured K-concentrations and luminescence-weighted K estimates. The dashed line indicates a perfect agreement with the total Ḋ based on the K-concentration of 12.5 ± 0.5 % (Huntley & Baril, 1997). 98

Fig. 5.1: Evaluation of the SGC performance. **A)** comparison of D_e obtained by the standard SAR procedure with D_e obtained using the established SGC, fitted with their L_{r1}/T_{r1} from the fourth regenerative SAR cycle with a D_{r1} of 150 Gy. **B)** L_X/T_X values before LS-normalisation. **C)** LS-normalised L_X/T_X values. 105

Fig. 5.2: Evaluation of the rc_5sR_{150}SGC performance. Comparison of D_e results from a set of ten samples calculated using the SAR method (x-axis) and the rc_5sR_{150}SGC method (y-axis). The SGC was build using the same ten samples but using the full available set of SAR cycles for grain rejection and not the reduced set. Dark red symbols besides the x- and y-axis represent unique SAR and unique rc_5sR_{150} SGC D_e values, i.e., grains for which a D_e could only be determined by either the SAR or the rc_5sR_{150}SGC method. 106

Fig. 5.3: Kernel density plot of D_e calculated using the **SAR** approach and the **rc_5sR_{150}SGC** approach for sample P3-4. Dashed lines are the corresponding MAM D_e (calculated with the "Luminescence" R package, log = TRUE, sigma b = 0.3). Dotted lines are the corresponding CAM D_e (calculated with the "Luminescence" R package, log = FALSE) 108

Fig. 5.4: Evaluation of the $rc_5sR_{15\text{-}100}SGC$ performance with differing sR values of 15 Gy in **A**, 25 Gy in **B**, 50 Gy in **C**, 100 Gy in **D**. **A-D**) Comparison of D_e results from a set of ten samples calculated using the SAR method (all x-axis) and the $rc_5sR_{15\text{-}100}SGC$ method (y-axis). The SGC was build using the same ten samples but using the full available set of SAR cycles for grain rejection and not the reduced set. Dark red symbols besides the x- and y-axis represent unique Sar and unique $rc_5sR_{15\text{-}100}SGC$ D_e values, i.e., grains for which a D_e could only be determined by either the SAR or the $rc_5sR_{150}SGC$ method. 109

Fig. 6.1: a) Topography along the Paposo transect, including sampling and weather station locations. **b)** overview map. **c)** Entire catchment of the Paposo Transect. Locations of the sampling sites (P1 – P5) are indicated by coloured (a) and yellow boxes (c). Fog occurrence (approx.) based on Cereceda et al. (2008a). Biotic sampling sites P1 and P2 (fog occurrence & loma vegetation) are located below, transitional sampling sites P3 and P4 and hyperarid sampling site P5 above the marine boundary layer. 116

Fig. 6.2: Satellite (a-e) and UAV (d) images of the study areas. **a)** Profile P1, located in the oldest alluvial fan generation (Q1) according to Walk et al. (2023) in direct adjacency to the erosional edge of the central alluvial channel, where subrecent to recent depositional activity occurs. **b)** Profile P2, located at the bottom edge in the centre of a small and steep alluvial fan at a natural outcrop exposed by lateral fluvial erosion; red area is assumed to represent the older fan section, whereas modern activity takes place in the yellow part. **c)** Profile P3, located within an alluvial channel (red) ~20 m upstream of the confluence of two further channels (yellow) and ~200 m upstream of a truncated alluvial fan. **d)** Profile P4, located in the older section of an alluvial fan (red) already described by Moradi et al. (2020) and Sun et al. (2023), using the profile pit from profile P9 of Sun et al. (2023); modern depositional activity is restricted to the yellow fan section. **e)** Profile P5, located in an alluvial channel deposit. The position of the sampled profiles within alluvial deposits are indicated by yellow boxes, flow directions are indicated by blue arrows. 118

Fig. 6.3: Photographs of the five investigated sampled profiles. **a)** Profile P1 (103 m a.s.l.), **b)** profile P2 (577 m a.s.l.), **c)** profile P3 (1310 m a.s.l.), **d)** profile P4 (1480 m a.s.l.), and **e)** profile P5 (1930 m a.s.l.). White circles indicate the depth of samples used for all analysis and coloured circle the depth of samples only analysed for their geochemistry and granulometry. The individual lithological units within each profile are marked by dashed lines and labelled using Roman numerals and are described in Appendix C-III. Profile units apply only to the respective profile and are not intended for correlations between profiles. 119

Fig. 6.4: a) Soil texture triangle of all sediment samples and the four dust samples, and **b)** grain size distributions of exemplary samples including the mean values for the four dust samples (red dotted line). 123

Fig. 6.5: a) Mobile to immobile ratio ($\sum E_m/\sum E_{im}$) against depth. Smaller ratios indicate the leaching of mobile elements and therefore weathering. **b)** Biplot of the PCA of all sediment samples based on grain size parameters and elemental concentrations. 124

Fig. 6.6: D_e distributions and corresponding MAM (circle) or CAM (square) D_e in Gy (left) and ages in ka (right) of all five sampled profiles, excluding the surface samples. Ages from earlier studies referenced in the main text, are shown as dotted red lines. Their conversion into D_e was based on an average dose rate of the corresponding profile. The x-axis for the D_e distributions is truncated at 500 Gy to facilitate visualisation. 127

Fig. 6.7: Theoretical D_e distributions adapted from Bateman et al. (2003): **a)** complete bleaching with a narrow normal distributed D_e distribution around a dose of 0 Gy, **b)** heterogeneously bleached grains with a distinct peak in a low dose region and a tail towards higher doses, **c)** heterogeneously bleached grains after burial, broadening the low dose peak and shifting it to the right, **d)** prolonged burial or intensive mixing of heterogeneous grain populations represented by a unimodal normal distributed D_e distribution, **e)** mixing of two distinct grain populations resulting in a bi-modal 133

distribution with the older grain population being broader than the recently buried one, **f)** mixing of two less pronounced grain populations.

Fig. 6.8: Regional proxies for humid phases: **a)** Aridity Index ~27 °S (Stuut and Lamy, 2004), **b)** humid phases based on colluvial sediments ~21 °S (Medialdea et al., 2020), colluvial aeolianite cementation ~28 °S (Nash et al., 2018), fluvial terraces ~21 °S (Gayo et al., 2023; Nester et al., 2007), **c)** humid phases based on groundwater recharge ~22-25 °S (Rech et al., 2002; Sáez et al., 2016), **d)** humid phases based on rodent middens ~24-26 °S (Díaz et al., 2012; Maldonado et al., 2005), **e)** pre-CAPE and CAPE events ~20-24 °S (de Porras et al., 2017; Gayo et al., 2012; Pfeiffer et al., 2018; Quade et al., 2008), **f)** alluvial fan active phases from other studies ~20-25 °S (Bartz et al., 2020a, 2020b; Vargas et al., 2006; Vásquez et al., 2018; Walk et al., 2023), **g)** MAM ages (circles) and CAM ages (squares) within alluvial deposits this study ~25 °S; different colours represent the five different profiles (cf. Fig. 6.3-6.6), for sample P4-1 the mode is shown, MAM-4 and CAM ages of P5-6 are slightly transparent since their associated process is ambiguous. 136

Fig. 6.9: Comparison of the luminescence ages (top) of all five profiles during the last 15 ka to independent proxies (bottom). MAM and CAM ages of recently geomorphic active surfaces are depicted as circles and squares respectively. Ages of recently geomorphic stable surfaces are depicted as triangles, with the MAM-4 age for P1-2 and the mode for P4-2. The lithic flux rate, as an indicator for El Niño activity (Rein et al., 2005, 2004), and wet and dry phases, based on the A. cinerea pellet diameters from palaeo-middens in the Atacama Desert (González-Pinilla et al., 2021), are provided as well. 137

Fig. 7.1: Total $\dot{D}$ and age comparison. **a)** Total $\dot{D}$ results per sample, with $\dot{D}_{int}$ and total $\dot{D}$ calculated with DRAC (Durcan et al., 2015) based on measured K-concentrations (filled symbols) and on the three most cited literature values (open symbols) (Huntley and Baril, 1997; Smedley et al., 2012; Zhao and Li, 2005). All other input variables are described in Chapter 6 and Appendix C-II and Appendix C Table C5. **b)** A comparison of the percentage deviation between the total $\dot{D}$ based on the measured K-concentration and the total $\dot{D}$ based on the three most cited literature values. **c)** A comparison of the percentage deviation between the ages calculated with total $\dot{D}$ based on the measured K-concentration and the ages calculated with total $\dot{D}$ based on the three most cited literature values. 153

Fig. 7.2: Abanico plots of **a)** single-grain residual test D_e values from surface samples after 24 h of laboratory bleaching; **b)** single-grain D_e values of the surface samples without laboratory bleaching; and **c)** comparison of the residual test D_e values (turquois) and the surface sample D_e values (purple). Colours in a) and b) correspond to the different profiles: **P1**, **P2**, **P3**, **P4**, and **P5.** Dotted lines in all Abanico plots indicate the weighted mean. In b), D_e values outside the z-axis range (-10 – 20 Gy) are shown semi-transparent. **Note:** the x-axes for standard error, precision, and density are scaled differently in a), b), and c). 155

Fig. A1: comparison of L_X/T_X values before and after LS-normalisation for subset A (**top**) and subset X (**bottom**). XXVIII

Fig. A2: Abanico plots of D_e distributions resulting from dose recovery experiments, with a given dose of 150 Gy. Filled circles are within 2σ of the given dose, empty circles differ more than 2σ from the given dose. The overdispersion was calculated using CAM. **A-D** show D_e distributions of subset A and E from subset X. The **SAR** D_e values were calculated using the standard SAR approach. The **SGC** D_e values were calculated following Li et al. 2015a and using the natural cycle (N) and the eighth regenerative cycle (R8) for projection onto a SGC, constructed with data from subset A, while applying the rejection criteria to the full SAR dataset. The **N + R8 xSGC** D_e values were calculated following Li et al. 2015a and using N and R8 for projection onto the xSGC, constructed with data from subset X, while applying the rejection criteria to a dataset only consisting of the N and R8. The **rc_5sR_{150}xSGC** D_e values were calculated with the new method developed in this paper. XXIX

Fig. A3: evaluation of SGC performance. **Left** comparison of D_e from subset A obtained with the standard SAR procedure with D_e obtained using the xSGC, established with data from subset X, and rejection criteria applied for a reduced dataset from subset A including only the "natural" SAR cycle plus the eighth SAR cycle (R8 = 50 Gy), where R8 used as L_{r1}/T_{r1} to scale and interpolate L_n/T_n onto the xSGC. **Right** comparison of D_e from samples of subset A obtained by the standard SAR procedure with D_e obtained using the sR_{150}xSGC and reducing the SAR-cycles for individual growth curve fitting to the "natural" 150, 0, 50, 500, 50 Gy cycles (rc_5sR_{150}xSGC). Both show the D_e values of the used SGC approaches on a separate axis that yielded no corresponding D_e value when estimating the D_e with the standard SAR procedure. For Abanico plots including both, the D_e with corresponding SAR D_e and those without, see Fig. A2 B, C and D. XXX

Fig. A4: correlation matrices of the complete dataset (subset A + X) in the **first row**, subset A in the **second row** and subset X in the **third row**, for all grains in the first column, luminescent grains in the second column and non-luminescent grains in the third column. Numbers in the squares represent Spearman's rank correlation coefficient values and their colour the strength of the correlation. For not significant correlations with a p-value above 0.05 % the squares are x-ed out. XXXI

Fig. B1: Detailed summary of the literature review. **Inner circle**: allocation of the 432 articles into four groups, where group 1 used one or more literature values for the K-concentration, group 2 measured the K-concentration of their samples but used a literature value instead, group 3 measured the K-concentration of their samples and used it, group 4 did not clearly state what K-concentration they used or where the used K-concentration came from. **Middle circle**: numbers of citations per source for the five most cited literature sources, number of citations of all other sources, number of articles that performed measurements and number of articles that provided only inaccurate information on K concentration. **Outer circle**: detailed information on the categories from the middle circle. XXXVIII

Fig. B2: Preparation of feldspar samples for measurements in the β-counter. **a)** A plastic β-counter cup in its normal position. **b)** A plastic ring with a slightly larger diameter than the β-counter cup. **c)** A plastic β-counter cup in the upside-down position. **d)** 100 mg of feldspar sprinkled onto the upside-down β-counter cup**.** e) A piece of cling film labelled with the sample name is placed on top of the sample material on the upside-down β-counter cup and secured by the plastic ring**.** f) The same as shown in e) but with the excess cling film cut **off**. XXXIX

Fig. B3: Sample preparation for the single grain SEM-EDX and μ-XRF measurements. **a)** A single grain (SG) sample disc after luminescence measurements filled with all 100 grain holes filled. **b)** SG disc facing downward onto double sided sticky tape. The tape is attached to a glass microscope slide on the other side. The directions of the three positioning holes are marked on the tape. **c)** Grains on the sticky tape after disc removal. Red circles show locations where no grain was transferred and yellow circles show locations where only parts of a grain where transferred while still parts stuck in the SG disc. **d)** SG disc after removal from sticky tape. Red circles show position of grains still within grain holes, corresponding to the red circles in c), and yellow circles show part of grains still within grain holes, corresponding to the yellow circles in c). **e)** Grains fixated in resin with a polished surface. XXXIX

Fig. B4: Exemplary spectra including peak fits for selected elements (Na, Mg, Al, Si, K, Ca, Ti, and Fe). **a)** SEM-EDX spectrum of a grain with ~8 wt% K**.** b) SEM-EDX spectrum of a grain with ~2 wt**% K**. c) μ-XRF spectrum of the same grain depicted in a) with ~**8 wt**% K. d) μ-XRF spectrum of the same grain depicted in b) with ~2 wt% K. The peak observed between ~2.5–3 keV in c) and d) originates from the Rh anode of the μ-XRF instrument. Note that oxygen concentrations are not measured directly in either method but are inferred from the stoichiometry of the detected elements **assuming** their oxide forms. XL

Fig. B5: Single-grain K-concentrations for the eight samples not depicted in Fig. 3 of the main text. The dark blue dotted density curves and dots are based on the SEM-EDX measurements and the light blue ones on the μ-XRF measurements. The red circles around the dark blue dots and the light green density curve represent the luminescent grains. The XLI

vertical lines represent the K-concentrations presented in Chapter 4.4.1, boxes above the graph representing their errors.

Fig. B6: Ḋ results. **a)** A comparison between the total Ḋ based on the K-concentration of 13 ± 1 % (Zhao & Li, 2005) and the total Ḋ based on the measured K-concentrations and luminescence-weighted K estimates. **b)** A comparison between the total Ḋ based on the K-concentration of 10 ± 2 % (Smedley et al., 2012) and the total Ḋ based on the measured K-concentrations and luminescence-weighted K estimates. The dashed lines indicate a perfect agreement with the total Ḋ based on the K-concentration of 13 ± 1 % (Zhao & Li, 2005) in a) and of 10 ± 2 % (Smedley et al., 2012) in b). XLII

Fig. C1: Weather station data from 1. May 2021 to 19. August 2023 of the three weather stations **S31**, **S32**, and **S33** situated a few km south of the studied Paposo transect (Hoffmeister, 2018a, 2018c, 2018b). Values represent weekly running averages derived from 10-minute data. **a)** Air temperature at 2 m above ground. **b)** Relative humidity (%) of the air at 2 m above ground. **c)** Fog yield (litres) at 2 m above ground. XLV

Fig. C2: Profile-wise grain size distributions of **a)** P1, **b)** P2, **c)** P3, **d)** P4, **e)** P5, all including the mean distribution of the four dust samples as a reference (black line). **f)** grain size distribution of the four dust samples. XLIX

Fig. C3: Protocol testing. Results of the multi-grain preheat plateau test on sample P3-2 (a-c) and further test on multi-grain level on seven additional samples using a preheat temperature of 250 °C and a pIRIR temperature of 225 °C. **a)** Dose recovery ratios, **b)** residuals, and **c)** g-values of the fading measurements. **d)** Dose recovery ratios, **e)** residuals, and **f)** g-values of the fading measurements. LII

Fig. C4: Abanico plots of the single-grain residual measurements (a-g) and the single-grain dose recovery test (DRT) (h). **a-d)** Abanico plots of the individual samples; **e)** zoomed Abanico plot of all samples, with different colours representing different samples according to (a)-(d); **g)** all single-grain residuals combined. As a result of the dose uniformity of the used luminescence reader, each grain received a different dose for its DRT. The given dose ranged between 106 to 177 Gy. Dotted lines in all Abanico plots represent the weighted mean. LIII

Fig. C5: Stratigraphic, granulometric, geochemical, and luminescence characteristics of profile **P1.** From left to right: schematic lithology; grain size distribution; mobile to immobile elemental ratio ($\sum E_m/\sum E_{im}$); ages (black), saturated grains (red), zero dose grains (blue); D_e distributions. LVII

Fig. C6: Stratigraphic, granulometric, geochemical, and luminescence characteristics of profile **P2.** From left to right: schematic lithology; grain size distribution; mobile to immobile elemental ratio ($\sum E_m/\sum E_{im}$); ages (black), saturated grains (red), zero dose grains (blue); D_e distributions. For legend see Fig. C5. LIX

Fig. C7: Stratigraphic, granulometric, geochemical, and luminescence characteristics of profile **P3.** From left to right: schematic lithology; grain size distribution; mobile to immobile elemental ratio ($\sum E_m/\sum E_{im}$); ages (black), saturated grains (red), zero dose grains (blue); D_e distributions. For legend see Fig. C5. LX

Fig. C8: Stratigraphic, granulometric, geochemical, and luminescence characteristics of profile **P4.** From left to right: schematic lithology; grain size distribution; mobile to immobile elemental ratio ($\sum E_m/\sum E_{im}$); ages (black), saturated grains (red), zero dose grains (blue); D_e distributions. For legend see Fig. C5. LXII

Fig. C9: Stratigraphic, granulometric, geochemical, and luminescence characteristics of profile **P5.** From left to right: schematic lithology; grain size distribution; mobile to immobile elemental ratio ($\sum E_m/\sum E_{im}$); ages (black), saturated grains (red), zero dose grains (blue); D_e distributions. For legend see Fig. C5. LXIII

List of tables

Table 2.1: Example of a standard SAR pIRIR protocol. 27

Table 3.1: Sample description. Sample KTB-383-C was prepared in the laboratory of the University of Lausanne. Sample MBT-I-2430 was prepared at DTU-Risø. All other samples were prepared at the Cologne Luminescence Laboratory. 48

Table 3.2: Single-grain dose recovery test SAR measurement protocol. Heating rate for steps 2-4 and 6-8 2 °C/s. 49

Table 3.3: Reduced cycle scenarios tested for subset A. The full SAR protocol used is given in Table 3.2. 59

Table 4.1: Sample description. Sample MBT-I-2430 was prepared in the laboratory of the University of Lausanne. Sample KTB-383-C was prepared at Risø. All other samples were prepared at the Cologne Luminescence Laboratory. 81

Table 4.2: Summary of the single-grain K-concentration measurements, with CV being the coefficient of variation. 93

Table 6.1: Weather station data (Hoffmeister, 2018a, 2018b, 2018c). For location see Fig. 6.1a and b. Min and mean air temperature as well as mean rel. humidity were recorded between 01. May 2021 and 01. September 2023. 115

Table 6.2: Luminescence results, including the dose model used for calculation of the De, the De, the total dose rate ($\dot{D}$), the age, the fraction of zero-dose grains and the fraction of saturated grains per sample. 126

Table 7.1: Age underestimation of samples from Chapter 6 based on three most cited literature values, compared to the combined multi-grain/single-grain approach from Chapter 4. Results are given in absolute values (ka, left) and relative values (%, right). 152

Table 7.2: Overview of rejection criteria applied to the single-grain dataset, with the corresponding number of grains rejected for each criterion. 156

Table A1: Summary of grain rejection for all ten samples for the SAR procedure, the SGC method (samples 1-5) and the xSGC method (samples 6-10) for the full data sets using all SAR cycles. XXXII

Table A2: Summary of grain rejection for all samples from dataset A for the SGC approach using only the “natural” SAR cycle and SAR cycle R8 (50 Gy). XXXIII

Table A3: Summary of the results for dataset A using the sRxSGC approach, in relation to the D_e calculated with the SAR approach and to a dose recovery ratio (DRR) of 1. The DRR is calculated for all grains yielding a D_e with the sRxSGC approach and for “common grains”, which yield a D_e with the SAR and the sRxSGC approaches. XXXIV

Table A4: Summary of grain rejection for all ten samples for the SAR procedure, the SGC method (samples 1-5) and the xSGC method (samples 6-10) for reduced dataset using the cycles of rc_5. XXXV

Table A5: Summary of the results for dataset A using the $rcsR_{150}$xSGC approach, in relation to the D_e calculated with the SAR approach and to a dose recovery ratio (DRR) of 1. The DRR is calculated for all grains yielding a D_e with the $rcsR_{150}$xSGC approach and for “common grains”, which yield a D_e with the SAR and the $rcsR_{150}$xSGC approaches. Headers indicating the size of the dose (D_i) of the used cycles, with the first 150 being the “natural” cycle. The abbreviations refer to Table 3.3. XXXVI

Table A6: Summary of the SEM-EDX measurement results for the nine elements measured. For each element the results are given for subset A, subset X and the complete XXXVII

dataset. The table is further divided in all grains (upper third), luminescent grains (middle third) and the non-luminescent grains (bottom third).

Table B1: *digital Appendix* digital Appendix

Table B2: Overview of the K-concentrations with which the five most frequently cited sources were quoted. XLIII

Table B3: Single-grain dose recovery test SAR measurement protocol. Heating rate for steps 2–4 and 6–8 2 °C/s. XLIV

Table B4: Example of stoichiometric calculations of elemental concentrations for SEM-EDX and μ-XRF measurements. First the spectral peaks of each target element get fitted to the acquired spectrum (see Fig. B4). Next, the net peak areas (= net counts) under each fitted peak are summed per element and converted to mass concentrations (wt%). Oxygen concentrations are then derived from these oxide formulations rather than measured directly. Finally, these mass concentrations are normalised to 100%. XLIV

Table B5: *digital Appendix* digital Appendix

Table C1: D_e measurements, internal and external dose rate determination, geochemistry analysis and granulometric analysis. XLVI

Table C2: Element specific conversion constants according to Samsonov (2013). XLVII

Table C3: Geochemistry and grain size results. Geochemical results are expressed as the ratio of mobile to immobile elements ($\sum E_m/\sum E_{im}$) and for the grain sizes the fraction of the grain size classes sand, silt, and clay are shown. L

Table C4: Single-grain SAR $pIRIR_{225}$ measurement protocol. Heating rate for steps 2–4 and 6–8 2 °C/s. LII

Table C5: Applied model for sample-wise D_e calculation, sample-wise De, elemental concentrations used for dose rate ($\dot{D}$) determination, corresponding $\dot{D}$s and ages. LVI

List of equations

Eq. 2.1: Luminescence age equation 20

Eq. 2.2: Rb-concentration inferred from the K-concentration 31

Eq. 3.1: L_{sR}/T_{sR} determination 57

List of abbreviations

A	Apex
$\sum E_m/\sum E_{im}$	Ratio of mobile (Na, Mg, K, Ca) to immobile (Al, Ti) element concentrations
µ-XRF	Micro X-ray fluorescence spectrometry
a.s.l.	Above sea level
a.u.	Arbitrary unit
a-value	Alpha efficiency
b.s.	Below surface
B05	CRC 1211 project - Soils of the Atacama Desert
C02	CRC 1211 project - Transport and deposition
C04	CRC 1211 project - Gypsum desert & atmospheric deposition
C08	CRC 1211 project - Hyper-arid landscapes in transition
$CaAl_2Si_2O_8$	Ca-feldspar (anorthite)
CAM	Central age model
CAPE	Central Andean Pluvial Event
CLL	Cologne Luminescence Laboratory
CRC	Collaborative Research Centre
CW-OSL	Continuous-wave stimulation
$\dot{D}$	Dose rate
D0	Characteristic saturation dose
dataset A	Dataset built with five samples from the Atacama Desert (Tab. 3.1)
dataset X	Dataset built with five samples from outside the Atacama Desert (Tab. 3.1)
$\dot{D}_c$	Cosmic dose rate
D_e	Equivalent dose
$\dot{D}_{ext}$	External dose rate
DFG	Deutsche Forschungsgemeinschaft
D_i	Given dose
$\dot{D}_{int}$	Internal dose rate
D_{r1}	Regenerative dose from which the L_x/T_x value is used for fitting onto the SGC
DRAC	Dose Rate and Age Calculator
DRR	Dose recovery ratio
DRT	Dose recovery test
D_t	Given test dose
ECZ	Earth's Critical Zone

EDX	Energy-dispersive X-ray spectroscopy
EDXRF	Energy-dispersive X-ray fluorescence spectrometry
ENSO	El Niño Southern Oscillation
FC	Feeding channel
FFM	Finite mixture model
FOM	Figure of merits
g-value	Fading rate (percentage of signal loss per decade)
H_2O_2	Hydrogen peroxide
HCl	Hydrochloric acid
HF	Hydrofluoric acid
IC	Incised channel
IP	Intersection point
IQR	Interquartile range
IR	Infrared
IRPL	Infrared photoluminescence
IRSL	Infrared stimulated luminescence
$KAlSi_3O_8$	K-feldspar (orthoclase or microcline)
LED	International Luminescence and Electron Spin Resonance Dating Conference
LM-OSL	Linearly modulated optically stimulated luminescence
L_n	Natural luminescence signal
L_{r1} & T_{r1}	Signal and test dose signal used for fitting onto the SGC
LS	Least-squares
L_{sR} & T_{sR}	Synthetic L_{r1} and T_{r1} signal used for fitting onto the SGC
L_x	Luminescence signal of a regenerative dose measurement
MAM	Minimum age model
MAM-3	Three parameter MAM
MAM-4	Four parameter MAM
MAP	Mean annual precipitation
MET	Multiple Elevated Temperature
MIS	Marine isotope stage
MN	Moist northerlies
N	SAR measurement cycle of the natural signal
$Na_2C_2O_4$	Disodium oxalate
$NaAlSi_3O_8$	Na-feldspar (albite)
OSL	Optically stimulated luminescence
p0	Parameter of the MAM: proportion of grains at gamma
PC	Principle component

PCA	Principle component analysis
PDO	Pacific Decadal Oscillation
PHP	Preheat plateau
$pIRIR_{xxx}$	Post-infrared infrared stimulated luminescence, with xxx denoting the measurement temperature of the post IRSL signal
QEM-EDS	Quantitative evaluation of minerals using energy dispersive spectroscopy
R8	Regenerative cycle no. 8
rc	Reduced measurement cycles
$rc_5sR_{150}xSGC$	SGC built with dataset X applied to data from A with reduced cycles version 5 (Table 3.3) and synthetic regenerative dose of 150 Gy
rcsRxSGC	SGC built with dataset X applied to data from A with reduced cycles and synthetic regenerative dose used for fitting
rs	Spearman's rank correlation coefficient
RSE	Relative standard error
SAR	Single-aliquot regenerative-dose
SASM	South American Summer Monsoon
SEM	Scanning electron microscopy
SFB	Sonderforschungsbereich
SGC	Standardised growth curve
SG	Single grain
SiO_2	Quartz
sR	Synthetic regenerative dose
SST	Sea Surface Temperature
TL	Thermoluminescence
T_n	Natural luminescence test dose signal
TR-OSL	Time-resolved optically stimulated luminescence
T_x	Luminescence test dose signal of a regenerative dose measurement
VSL	Violet-stimulated luminescence
WDXRF	Wavelength-dispersive X-ray fluorescence spectrometry
xSGC	SGC built with dataset X
Y-OSL	Yellow-stimulated optically stimulated luminescence
Z03	CRC 1211 project - Ground based observations and experiments
α	Alpha
β	Beta
γ	Gamma
σ_b	Overdispersion
χ^2	Reduced Chi-square

Chapter 1

Introduction

Geography is just physics slowed down, with a couple of trees stuck in it.
(Terry Pratchett)

1.1 Rationale of the thesis

"Study the past if you would define the future." (Confucius)

Understanding how the present Earth's surface evolved is the key to predicting how it might change in the future. Earth's surface evolution is primarily governed by the interaction of parent material, climatic factors (e.g. temperature, wind, and water availability), and biological influences (flora, fauna, funga) (Dietrich and Perron, 2006). However, within this complex interplay it is often impossible to trace the contribution of individual processes in isolation (e.g. Bierman and Nichols, 2004; Dietrich and Perron, 2006; Jenny, 1994). In this context, the Atacama Desert in Chile provides an ideal natural laboratory (Dietrich and Perron, 2006). Its hyperarid conditions minimise the influence of vegetation and water, allowing a focused investigation of fundamental soil processes (Ewing et al., 2006). Due to its persistent aridity, the Atacama Desert is not only an ideal site for investigating soil and surface processes, as studied in this thesis, but also offers unique opportunities for a wide range of other research areas (Dunai et al., 2020). Accordingly, this work was carried out as part of a Collaborative Research Centre, the CRC 1211 (see Chapter 1.2).

This thesis aims to decipher particle histories within soils and surfaces along a climatic transect (Paposo transect, Fig. 1.1) by employing single-grain feldspar luminescence dating to reconstruct the palaeoenvironment of the Coastal Cordillera in the Atacama Desert. Quartz, a commonly used mineral for luminescence dating, has been shown to exhibit extremely low sensitivity and unstable signal components in the Atacama Desert (Bartz et al., 2020a, 2020b; Del Río et al., 2019; May et al., 2015; Veit et al., 2015; Zinelabedin et al., 2022). In contrast, coarse-grained feldspars have demonstrated greater potential, yet their application remains challenging. A previous study conducted within the CRC 1211 revealed substantial heterogeneity in potassium (K) concentrations across individual feldspar grains from the Atacama Desert, and only approximately 1 % of these grains produced post-infrared infrared stimulated luminescence (pIRIR) signals suitable for dating (Zinelabedin et al., 2022). In response to these limitations and to achieve the aim of this study, luminescence-based inventories were tailored to suit the geochemical complexity of feldspar samples from the Atacama Desert. By adapting the single-grain luminescence inventories to the specific needs of Atacama Desert feldspar samples, their measurement shall become both faster and more accurate. First, the standardised growth curve (SGC) method (Li et al., 2018, 2015b) was refined to reduce the measurement time for single-grain feldspar luminescence equivalent dose (D_e) estimations (Chapter 3). Second, the determination of the internal K-concentration for the internal dose rate ($\dot{D}_{int}$) assessment was enhanced (Chapter 4). Finally, the developed methods were applied

to feldspar separates from soil and surface profiles in alluvial deposits along the climatic and elevation Paposo transect in the Atacama Desert (Chapter 5 and 6).

Overall, the results of this thesis provide a valuable contribution for the luminescence community by evaluating the SGC method, investigating the relationship between feldspar geochemistry and luminescence characteristics, and improving internal K-concentration determination for $\dot{D}_{int}$ calculations. Furthermore, they help to close existing knowledge gaps concerning soil and surface processes in the Paposo transect and enhance the regional understanding of Late Pleistocene to Holocene landscape formation and climate variability in the Coastal Cordillera and coastal plain of the Atacama Desert in Chile.

1.2 The Collaborative Research Centre 1211 – Earth - Evolution at the dry limit

The Collaborative Research Centre (CRC) 1211 – *Earth - Evolution at the dry limit* (https://sfb1211.uni-koeln.de/) is funded by the German Research Foundation (Deutsche Forschungsgemeinschaft; DFG SFB 1211). The CRC 1211 is composed of geoscientists, biologists, and physicists from the University of Cologne, University of Bonn, RWTH Aachen University, University of Frankfurt, Heidelberg University, Universidad Católica del Norte, LMU Munich, University of Vienna, Alfred Wegener Institute, GFZ Helmholtz Centre for Geosciences, Leibniz Institute of Plant Genetics and Crop Plant Research, and from cooperation partners in Chile and Namibia. The overarching goal of the CRC 1211 is to investigate the interplay between Earth's surface processes and biota in arid to hyperarid environments where water scarcity constrains both. The strength of the CRC 1211 lies in its multidisciplinary collaboration, bringing together researchers from diverse fields to address questions that no single discipline could answer on its own. During the second phase of the CRC 1211, all projects were organised into five research clusters: **A** *Climate/Palaeoclimate*, **B** *Biological Evolution*, **C** *Earth Surface Evolution*, **D** *Method Development*, and **Z** *Coordination and Support*.

More specifically, the CRC 1211 aims to identify the signatures of biological activity at the edge of habitability and characterise surface processes operating in the near absence of liquid water. This includes determining thresholds for biological colonisation and concurrent fluvial landscape transformation, as well as establishing long-term climatic records for the oldest and driest non-polar regions on Earth. By integrating chronometric and spatial data on biotic colonisation with landscape evolution driven by climate, the CRC 1211 aims to enhance our understanding of the emerging concepts in evolutionary lag time (e.g. Guerrero et al., 2013), how

geographical barriers influence species migration in response to climate change (e.g. Burrows et al., 2014), the geological- and climate-mediated species migration and diversification (e.g. Gillespie and Roderick, 2014), the bio-geomorphology (e.g. Corenblit et al., 2011), and the development of improved methods for dating and quantifying Earth surface processes and biological evolution.

The main target area of the CRC 1211 is the section of the Atacama Desert which is located in Chile (Fig. 1.1). This part of the Atacama Desert can be divided in three geomorphic zones running from north to south, extending from west to east and from sea level upwards: **i)** the Coastal Cordillera, **ii)** the Central Depression, and **iii)** the western Andean flank rising to the Precordillera. Contemporary climatic conditions (e.g. fog availability) together with variations in sediment provenance align with these geomorphic zones, which makes each zone particularly suited for investigating distinct conditions during the past (Dunai et al., 2020). While the Central Depression and the western Andean flank are more appropriate for examining precipitation fluctuations over time in the Precordillera, the Coastal Cordillera is considered being an archive recording climatic variations – especially the degrees of hyperaridity – within the Coastal Cordillera itself.

In the Atacama Desert, most of the research is conducted within three focus areas (Fig. 1.1, white boxes). Each focus area extends from the coast in the west up to the margins of the Andean Cordillera in the east. The focus areas were established to foster interdisciplinary collaboration, as working within the same spatial boundaries simplifies the exchange of ideas and knowledge (Dunai et al., 2020). In addition to collaborations within individual focus areas, cross-focus-area projects are also carried out.

This thesis is part of project **C08** – *Hyper-arid landscapes in transition* – of the **C** cluster – *Earth Surface Evolution* – of the CRC 1211 during the second funding phase. Project **C08** aims to develop and apply innovative luminescence-based dating techniques and Earth surface process-tracing methods that bridge short-term, on-site observations with large-scale geochronological reconstructions. Earlier studies demonstrated that quartz grains from the Atacama Desert generally exhibit low optically stimulated luminescence sensitivity and are characterised by unstable signal components (Bartz et al., 2020a, 2020b; Del Río et al., 2019; May et al., 2015; Veit et al., 2015). Results from project **C04** during the second phase of the CRC 1211 further revealed that feldspar grains also tend to produce weak luminescence signals and that a substantial proportion does not belong to the preferred group of K-rich feldspars (cf. Chapter 2.1.2) (Zinelabedin et al., 2022). Consequently, standard procedures for sample preparation, D_e determination, and dose rate calculation must be critically

assessed and, where necessary, adapted to the specific properties of feldspars from the Atacama Desert.

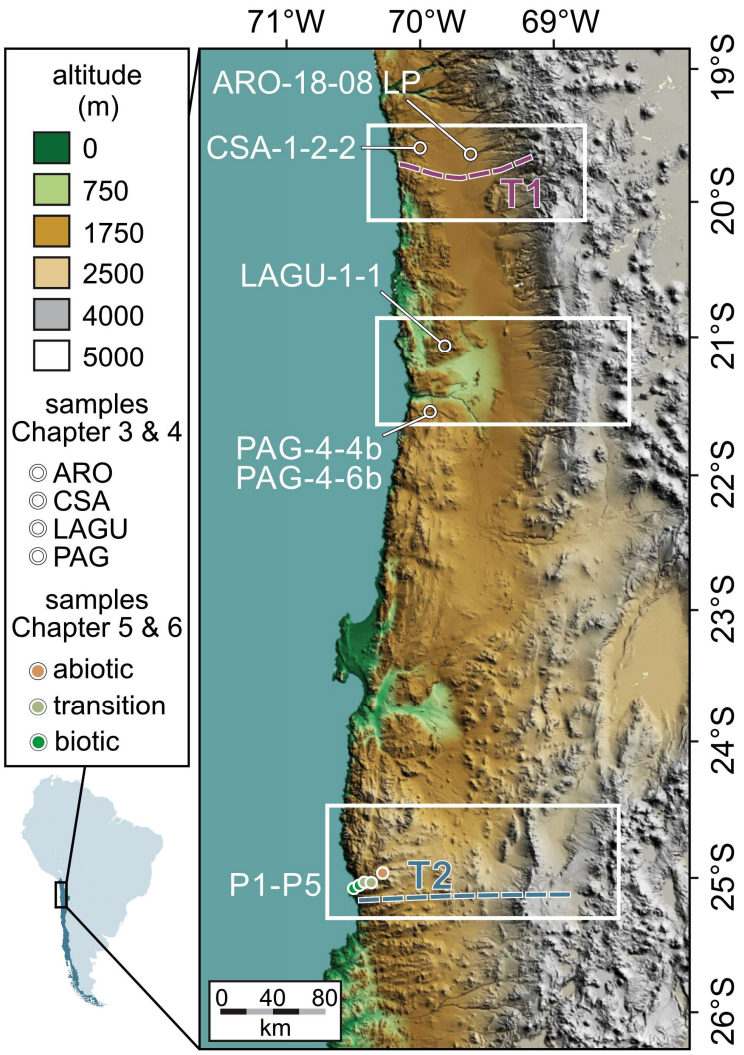

Fig. 1.1: *Colour-shaded digital elevation model of northern Chile derived from SRTM-data (NASA Shuttle Radar Topography Mission (SRTM), 2013), created using ArcGIS Pro 3.3.0 by Dr. S.M. May. The three CRC 1211 focus areas are outlined in white. Dashed lines indicate elevation transects within the northern (**T1** – Aroma transect) and southern (**T2** – Paposo transect) focus areas. Sampling locations used in Chapters 3 and 4 are shown as white circles (ARO-18-08-LP, CSA-1-2-2, LAGU-1-1, PAG-4-4b, and PAG-4-6b). Samples presented in Chapters 5 and 6 (P1-P5) are marked by coloured circles corresponding to their climatic classification: abiotic (hyperarid), transition, and biotic (more humid, yet still hyperarid).* ***Inset:*** *location of the study area in South America (map base: Canuckguy, 2006, Wikimedia Commons public domain).*

The project **C08** focusses on a climatic and altitude transect within the southern focus area of the CRC 1211 (Fig. 1.1, **T2** dotted line). This led to spatial overlaps with subprojects **C02**, **B05**, and **Z03** from the **C**, **B**, and **Z** clusters respectively. Detailed information on the objectives of this thesis can be found in Chapter 1.1 and 1.3. A detailed description of the sampling sites and their local settings can be found in Chapter 6 and the corresponding Appendix C-III.

1.3 Research questions and objectives of this thesis

Luminescence-based dating in the Atacama Desert in Chile has proven to be challenging due to the luminescence insensitivity of quartz, the generally poor luminescence sensitivity of feldspar, and the geochemical complexity of feldspar separates (Bartz et al., 2020a; Del Río et al., 2019; May et al., 2015; Veit et al., 2015; Zinelabedin et al., 2022). However, the investigation of the timing of processes is key for the investigation of the recent past. Due to the focus of subproject **C08** of the CRC 1211, to develop and apply innovative luminescence-based dating techniques in the Atacama Desert, this thesis aims to refine existing methods to adapt them to the conditions in the Atacama Desert and subsequently apply them to decipher surface evolution along a climatic elevation transect. Thus, it contributes to the improvement of feldspar luminescence-based dating methods, applicable beyond this study, and enhances our understanding of soil and surface dynamics since the Late Pleistocene within the hyperarid environment of the Atacama Desert.

Q1: Can standardised growth curves (SGC) be applied to determine single-grain Atacama Desert feldspar equivalent doses and how does intra-sample geochemical variability relate to observed luminescence characteristics, such as equivalent dose, dose recovery ratio, and signal brightness? (Chapters 3 and 5)
Objective 1a: *Construct a standardised growth curve (SGC) with Atacama Desert feldspar separates.*

The overarching goal of this thesis is to identify soil and surface processes in the Atacama Desert, using single-grain feldspar luminescence dating as a process tracer tool. Performing single-grain measurements on feldspar can be very time-intensive, especially when only a limited fraction of grains exhibits suitable luminescence signals (e.g. Brill et al., 2018; Sontag-González et al., 2021; Zinelabedin et al., 2022). Under such conditions, multiple single-grain discs per sample must be analysed to acquire a sufficient number of grains giving suitable signals for reliable D_e determination. The use of a SGC in single-grain feldspar pIRIR protocols offers a significant reduction in measurement time per disc, since the measurement protocol requires fewer cycles than a traditional single-aliquot regenerative-dose (SAR) pIRIR protocol (Li et al., 2018). Furthermore, Sontag-González et al. (2021) demonstrated that SGCs are applicable even to feldspar samples characterised by poor luminescence performance and complex mineralogical compositions, similar to those of Atacama Desert feldspars. Nevertheless, so far, the application of SGCs on Atacama Desert single-grain feldspar pIRIR measurements has not been tested. Within Chapter 3 of this thesis a SGC based on a single-grain dose recovery test (DRT) dataset of five Atacama Desert samples shall be constructed. The D_e estimates obtained applying this

SGC on the same Atacama Desert dataset should then be compared to D_e estimates obtained using a conventional single-grain SAR approach. Within Chapter 5 this approach shall be tested on measurements of the natural luminescence signal from samples of the Paposo transect.

Objective 1b: *Construct an additional SGC with feldspar separates from outside of the Atacama Desert and applying both curves to Atacama Desert samples.*

The development of a SGC requires several initial measurements using a complete measurement protocol (Li et al., 2015b). It is therefore likely that future research in the Atacama Desert will perform these initial measurements on samples with more favourable luminescence properties than Atacama Desert feldspars. Therefore, it needs to be tested if the application of a SGC constructed with samples not originating in the Atacama Desert on Atacama Desert samples yields reliable results. In this study, a second SGC shall be constructed based on five samples not originating in the Atacama Desert. The application of this second SGC for D_e estimation of five Atacama Desert samples should then be evaluated and compared to the D_e estimates obtained using the Atacama Desert SGC and the standard SAR approach (cf. Objective 1a; Chapter 3). If successful, this would enable future measurements to make use of an already existing SGC without the need for constructing a new one.

Objective 1c: *Identifying statistical correlations between elemental composition and luminescence properties, including equivalent dose, dose recovery ratio, and signal brightness.*

For feldspar luminescence dating the internal K-concentration is a crucial input variable for the calculation of the $\dot{D}_{int}$ (Mejdahl, 1987). A previous study on coarse grain luminescence feldspar dating of a calcium sulphate wedge in the Atacama Desert found heterogeneous geochemical compositions of the feldspar grains analysed (Zinelabedin et al., 2022). They also discovered that the K-concentrations are generally low, with an average value of 3.9 ± 1 % K for the luminescent grains. Merely one grain giving a suitable luminescent signal had a K-concentration >7 %, whereas several grains not giving a suitable luminescent signal had greater K-concentrations. This opposes the commonly held assumption that feldspar grains with high internal K-concentrations produce brighter luminescence signals than grains with lower K-concentrations (Reimann et al., 2012; Smedley et al., 2012). Yet, Zinelabedin et al. (2022) did not correlate the signal brightness to the geochemistry. Therefore, within this thesis, it shall be tested whether signal intensity or other luminescence characteristics, such as the D_e or the dose recovery ratio, depend on the geochemical

composition of the grain. For this purpose, correlations will be established between single-grain geochemical data and single-grain luminescence properties of five Atacama Desert samples. In order to identify Atacama Desert specific patterns, the same correlations will be performed on five samples from various geographical and geological origins outside of the Atacama Desert. If a correlation can be identified, this may affect the calculation of the $\dot{D}_{int}$ or indicate that feldspars from the Atacama Desert are not suitable for luminescence dating due to their heterogeneous geochemical composition.

Q2: Is the measurement of the internal K-concentration in feldspar grains essential for accurate internal dose rate calculations? In particular: what level of detail is necessary in those measurements and what effect do different K-concentration determination approaches have on the calculated total dose rate of a sample. (Chapter 4)

Objective 2a: *Reviewing current literature on how the internal K-concentration is determined and used in internal dose rate calculations.*

As mentioned above, the calculation of the $\dot{D}_{int}$ in feldspar luminescence dating requires knowledge of the internal K-concentration of the feldspar (Mejdahl, 1987). Although this is a fundamental aspect of feldspar luminescence dating, there is no consensus on how to determine the internal K-concentration (Huntley and Baril, 1997; Smedley et al., 2012; Zhao and Li, 2005). Moreover, there is no quantitative data available on how it is currently determined by most researchers. A systematic literature review shall be conducted to identify common practices within the luminescence community and to compile the methods that have been used for K-concentration determination for $\dot{D}_{int}$ calculations.

Objective 2b: *Comparing K-concentration results obtained using four different analytical methods.*

Various techniques are available to determine the K-concentration of feldspars. The level of precision ranges from broad measurements of the bulk K-concentration of a feldspar separate, to average values per grain, and down to intra-grain compositional variations (O'Gorman et al., 2021a). In general, higher measurement precision is associated with increased analytical effort. To evaluate the most practical and yet sufficiently accurate approach for determining K-concentrations in feldspars used for luminescence dating, four different K-concentration measurements will be conducted on ten feldspar separates from various geographical and geological contexts. Since this thesis focusses on the Atacama Desert, five of the samples

originate within the Atacama Desert and five outside of it. Two of the four methods will be applied on the bulk samples: wavelength-dispersive X-ray fluorescence spectrometry (WDXRF) and β-counting. In addition, two methods will be used to determine single-grain K-concentrations: scanning electron microscopy (SEM) equipped with energy-dispersive X-ray spectroscopy (EDX) and micro X-ray fluorescence spectrometry (μ-XRF). Based on the SEM-EDX results and luminescence characteristics, two luminescence-weighted K-concentration estimates will be calculated per sample. To assess whether the methods yield consistent outcomes, all results will be compared sample-wise and evaluated against commonly reported K-concentration values in the literature (cf. Objective 2a). In a further step, the sample-wise results and literature-based K-concentrations will be compared with the single-grain data obtained from the SEM-EDX and μ-XRF measurements, to assess whether single-grain measurements are needed or if one common value per sample is sufficient.

Objective 2c: *Assessing the influence of the different methods for the K-concentration determination on internal and total dose rate estimates.*

The internal K-concentration is only one of several input parameters required for total dose rate (total $\dot{D}$) calculation (Aitken, 1985a; Mejdahl, 1987). While the $\dot{D}_{int}$ primarily depends on the internal K-concentration, its overall contribution to the total $\dot{D}$ strongly depends on the values of the other input variables, and hence also on the size of the external dose rate ($\dot{D}_{ext}$) and the cosmic dose rate ($\dot{D}_c$). Therefore, within this study $\dot{D}_{int}$ and total $\dot{D}$ shall be calculated for each of the ten samples using K-concentrations obtained from direct measurements, luminescence-weighted estimates, and literature values (cf. Objective 2b). All other input parameters used for total $\dot{D}$ calculation will be held constant for each sample, regardless of the K-concentration. The influence of variations in K-concentration on the $\dot{D}_{int}$ and total $\dot{D}$ will be assessed.

Objective 2d: *Evaluating the practicality and reliability of each method for routine application in luminescence dating.*

Dose rates are typically calculated per sample rather than per individual grain. This practice is partly based on the common assumption of a homogeneous internal K-concentration within a sample and the fact that other parameters, such as external uranium (U), thorium (Th), and K-concentrations for $\dot{D}_{ext}$ calculations, can currently not be measured at the single-grain scale. Furthermore, single-grain K-concentration measurements are often time-consuming and potentially costly. Therefore, this

objective aims to evaluate the most cost- and time-effective method for determining K-concentration for feldspar luminescence dating, while maintaining the accuracy of total $\dot{D}$ calculations.

Q3: Can individual grain histories, determined with single-grain luminescence dating techniques, reveal sample-specific, site-specific, and transect-wide patterns of deposition and post-depositional mixing in soils and surfaces along a climatic elevation transect in the Atacama Desert, and how can these findings contribute to the understanding of regional palaeoclimatic fluctuations? (Chapter 6)

The Atacama Desert receives less than 2 mm of rainfall per year in its hyperarid core (Houston, 2006a). While the onset of predominantly hyperarid conditions and their past variability remain highly debated (Ritter et al., 2019), regional evidence suggests that hyperaridity has persisted for at least several million years (e.g. Dunai et al., 2005; Evenstar et al., 2017; Hartley and Chong, 2002; Nishiizumi et al., 2005; Rech et al., 2006). Despite this long-term hyperaridity, episodic more humid phases and heavy rainfall events occurred during the Quaternary. These intervals and events led to the activation or intensification of water-driven processes such as alluvial deposition, alluvial reworking or post-depositional mixing (e.g. Gayo et al., 2012; May et al., 2020; Medialdea et al., 2020; Pfeiffer et al., 2018, 2021). However, knowledge of local-scale climate variability during the Quaternary remains fragmentary. While some studies suggest that alluvial deposits have remained stable since the Pleistocene (e.g. Pfeiffer et al., 2021), others provide evidence for recent and more frequent reactivation (e.g. Haug et al., 2010). To date, no high-resolution study has investigated depositional and post-depositional mixing processes in alluvial deposits of the Atacama Desert. Single-grain feldspar luminescence dating has potentially the ability to record both the timing of deposition and of post-depositional mixing, thus being a promising tool to resolve this question.

Objective 3a: *Evaluate the applicability of feldspar single-grain luminescence dating techniques to reconstruct depositional and post-depositional processes of soils and surfaces in the Atacama Desert.*

Single-grain feldspar luminescence dating has been applied to investigate depositional as well as post-depositional processes, such as bioturbation and soil creep, predominantly in temperate environments (e.g. Heimsath et al., 2002; Reimann et al., 2017; van der Meij et al., 2025). Its potential to resolve such processes in hyperarid settings remains largely unexplored. In the Atacama Desert, application of single-grain luminescence dating has so far been limited to decipher the formation of

a gypsum wedge (Zinelabedin et al., 2022). A key challenge of applying this method in the Atacama Desert lies in the low proportion of feldspar grains exhibiting suitable luminescence properties for reliable D_e determination (e.g. Zinelabedin et al., 2022), making single-grain analyses time-intensive. Furthermore, feldspars from alluvial deposits tend to experience heterogeneous bleaching due to incomplete light exposure during transport and deposition (Duller, 2008b; Ventra and Clarke, 2018; cf. Chapter 2.2).

Therefore, the objective specifically aims to:

i) assess the luminescence characteristics of the feldspar grains, including bleaching behaviour at the surface, bleaching depth within the profiles, and conformity with standard rejection criteria (cf. Chapter 2.1.2);

ii) evaluate whether characteristics of D_e distributions can be used to distinguish depositional from post-depositional processes; and

iii) determine whether these luminescence-derived results can be consistently interpreted alongside independent sample and profile characteristics, including granulometric features, geochemical signatures, profile morphology, and local settings.

Ultimately, this objective seeks to assess whether single-grain feldspar luminescence dating can be used to resolve complex feldspar grain histories within individual soil and surface profiles in one of the most hyperarid environments on Earth.

***Objective 3b**: Analysing patterns inferred from geochemistry, granulometry, and single-grain feldspar luminescence measurements (cf. Objective 3a) in the context of the climatic and elevation transect.*

Soil and surface profiles studied within this thesis are located along a climatic and elevation transect (Fig. 1.1, **T2** – Paposo transect). The analysed section of the Paposo transect extends from the relatively humid coastal plain, through the fog-influenced zone of the Coastal Cordillera, to the hyperarid region of the Coastal Cordillera. This objective aims to analyse whether the varying climatic conditions result in similarities respectively distinct differences in geochemical or granulometric characteristics across the Paposo transect and if identified depositional activities or post-depositional mixing processes (Objective 3a) are related to the climatic condition. It further aims to determine whether synchronous depositional or post-depositional activity can be identified across the entire transect, potentially indicating transect-wide uniform responses to past climatic fluctuations.

Objective 3c: *Integrate the site-specific and transect-wide luminescence-based interpretations (Objectives 3a and 3b) into the broader regional geomorphological and (palaeo-) environmental framework of the Atacama Desert.*

Late Pleistocene and Holocene climatic variability in the Atacama Desert has been reconstructed using a range of different archives and proxies, including the analyses of (deep-)sea sediment cores (Rein et al., 2005, 2004; Stuut and Lamy, 2004), rodent middens (Díaz et al., 2012; González-Pinilla et al., 2021; Maldonado et al., 2005), colluvial sediments (Medialdea et al., 2020), fluvial terraces (Gayo et al., 2023; Nester et al., 2007), groundwater recharge (Rech et al., 2002; Sáez et al., 2016), and alluvial fan deposits (Bartz et al., 2020a, 2020b; Vargas et al., 2006; Vásquez et al., 2018). However, palaeoclimatic trends along a present-day climatic transect in the Coastal Cordillera, as analysed in this thesis (Objective 3a and 3b), remain underrepresented in the regional context. The aim of Objective 3c is to integrate the findings from Objectives 3a and 3b into the existing palaeoenvironmental framework, thereby contributing to a more comprehensive understanding of Late Pleistocene and Holocene climatic variability in the Atacama Desert.

1.4 Research design and methods

To address the questions outlined in Chapter 1.3, the research design depicted in Fig. 1.2 was developed. The research design encompasses all methods required to advance established luminescence dating techniques (Chapter 3), outlines the procedure for examining K-concentrations (Chapter 4), and contains the methodological details on the analysis of particle histories in Atacama Desert soil and surface profiles (Chapters 5 and 6).

Detailed descriptions of the individual work flows and methods used therein can be found in the equivalent chapters. The following Chapters 1.4.1 to 1.4.4 will only briefly explain the specific research designs and methods used.

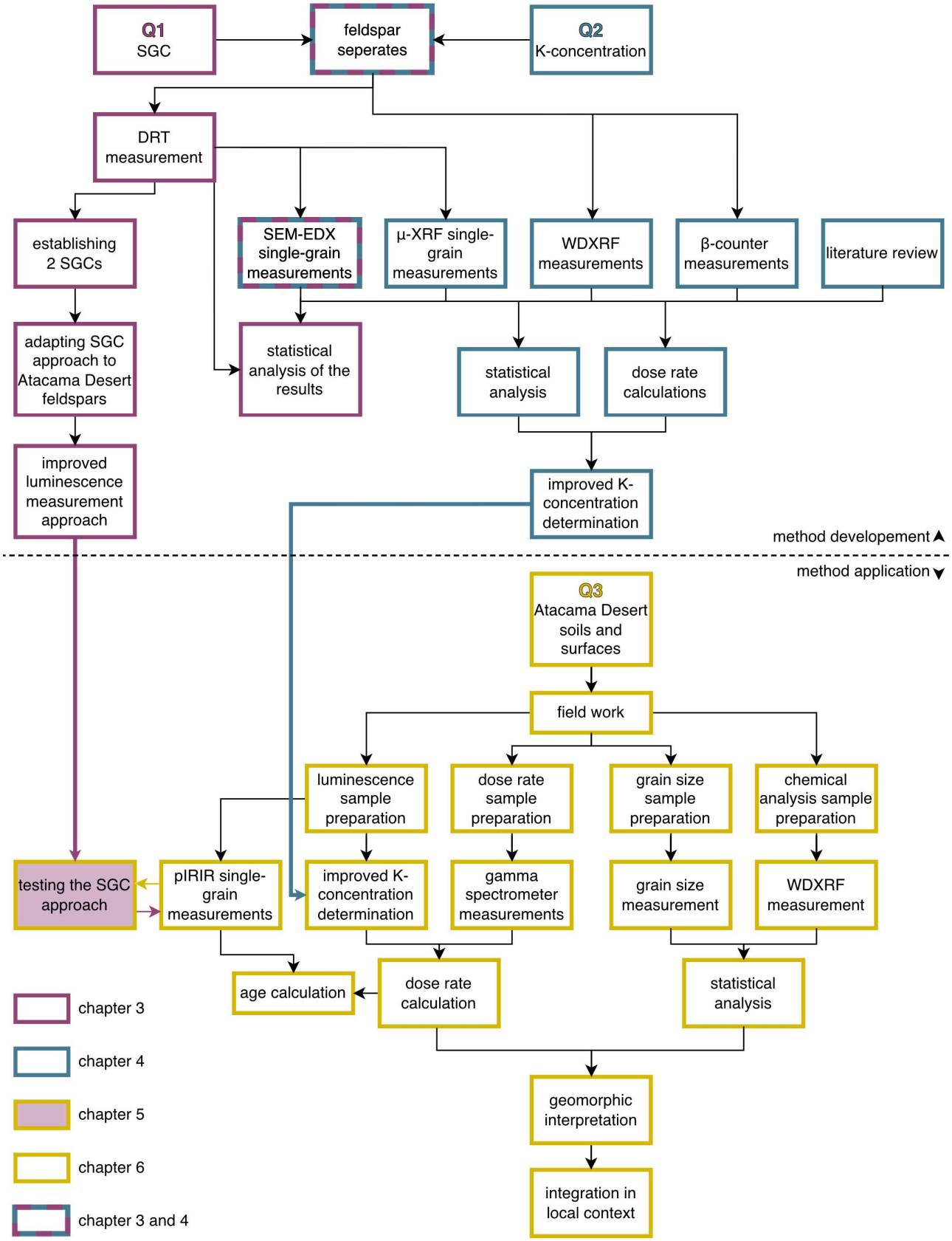

***Fig. 1.2**: Workflow diagram illustrating the research design of this thesis. Each coloured box represents a distinct methodological or analytical step, with the colour indicating the chapter in which the step is described and implemented in detail. The abbreviations **Q1**, **Q2**, and **Q3** correspond to research questions 1 to 3, respectively. All subsequent boxes linked to a given Q-number denote the activities contributing to the resolution of that specific research question.*

1.4.1 Luminescence dating methodological framework

Detailed explanations of the basic principles of feldspar luminescence dating can be found in Chapter 2.1. In the context of this thesis infrared stimulated luminescence techniques have been used to gain detailed understanding of the methods' strength and weaknesses when applied on Atacama Desert feldspars (Chapters 3-5) and to decipher particle histories in Atacama Desert soils and surfaces (Chapter 6). All measurements have been carried out at the Cologne Luminescence Laboratory of the Geography Department of the University of Cologne. In Chapters 3 and 4, single-grain dose recovery tests on ten geochemically different feldspar separates have been performed to test **i)** the applicability of SGCs to Atacama Desert samples, and **ii)** to gain a dataset providing information on single-grain luminescence characteristics, such as signal brightness. In Chapters 5 and 6 single-grain equivalent dose measurements have been performed on 25 Atacama Desert samples. In both cases, pre-heat plateau tests including measurements of the residuals, dose recovery ratios and fading behaviour have been carried out on a subset of samples to determine the measurement protocol. To assess the bleachability of Atacama Desert feldspars, residual tests on a single-grain level have been carried out on five surface samples. Furthermore, $\dot{D}$ have been calculated for all 35 samples. For the $\dot{D}$ calculation of the ten samples from Chapters 3 and 4, different techniques to determine the internal K-concentration have been used (cf. Chapter 1.4.2; Chapter 4). For the $\dot{D}$ calculation of the 25 samples from the Atacama Desert, additional measurements on a gamma spectrometer were carried out.

1.4.2 K-concentration analysis

To identify the most effective procedure to routinely measure the K-concentration in feldspar separates for the determination of the $\dot{D}_{int}$, four different techniques have been employed: WDXRF, β-counting, SEM-EDX, and μ-XRF. The WDXRF, SEM-EDX, and μ-XRF devices also determined a variety of other elements within the samples, while the β-counter only indirectly measured the K-concentration. The WDXRF measurements have been carried out in the MERI X-Ray laboratory at the Sheffield Hallam University. The β-counter measurements have been carried out in the Cologne Luminescence Laboratory and the μ-XRF measurements at the Physical Geography Laboratory of the Geography Department of the University of Cologne. The SEM-EDX measurements have been carried out at the Micropalaeontology and Palaeoecology Laboratory of the Geology and Mineralogy Department of the University of Cologne. Further details on the instruments and operational modes used, sample preparation

for each measurement technique, and theory of operation of each technique can be found in Chapter 4.

1.4.3 Fieldwork

Fieldwork in the Atacama Desert was conducted during September 2022 and March 2023. It included a geomorphological survey of each site, site documentation, and sampling. In total five soil and surface profiles were dug and sampled (cf. Fig. 1.1). All profiles were excavated in alluvial deposits. Luminescence samples were collected under an opaque black plastic tarp under red light conditions. The sample material was carefully carved out of the profiles into opaque black plastic bags. Each profile unit was further sampled under daylight conditions for radionuclide concentration (for $\dot{D}_{ext}$ calculations), as well as granulometric and geochemical analysis. Detailed information on sampling locations, sampling depth, and profile descriptions can be found in Chapter 6 and within its supplementary material in Appendix C.

1.4.4 Granulometry and geochemistry

To elucidate the sediment characteristics and (post-)depositional processes in the alluvial deposits in Chapter 6 of this thesis, sediment and soil properties were analysed at the Physical Geography Laboratory of the Geography Department of the University of Cologne. Grain size distributions (Blott and Pye, 2001; Folk and Ward, 1957) were measured to assess post-depositional processes and the transport dynamics of the sediments. Additionally, energy-dispersive X-ray fluorescence spectrometry (EDXRF) analyses were performed to examine the chemical composition of the samples in order to identify differences among individual samples and across profiles. Besides a principle component analysis (PCA), including grain size fractions and major elements, one elemental ratio has been calculated as a proxy for weathering. The ratio divides the sum of the mobile elements sodium (Na), potassium (K), magnesium (Mg), and calcium (Ca) by the sum of the immobile elements aluminium (Al) and titanium (Ti). During weathering mobile elements are transported downwards whereby the percentage of immobile elements gets enriched, hence the ratio decreases with weathering intensity. Detailed information on the granulometric and geochemical analysis can be found Chapter 6 and within its supplementary material in Appendix C-I.

Chapter 2

Luminescence-based inventories and alluvial landforms

As a young man, my fondest dream was to become a geographer. However, while working in the customs office I thought deeply about the matter and concluded it was too difficult a subject. With some reluctance I then turned to physics as a substitute. (Duane Marble NOT Albert Einstein)

As a young kid, my fondest dream was to become a physicist. However, I ended up here. (Linda Maßon)

2.1 Luminescence dating – theoretical background

2.1.1 Luminescence dating – brief overview

Luminescence dating is a geochronometric method that quantifies the time elapsed since a mineral grain, acting as a natural dosimeter, was last exposed to light or heat (Grögler et al., 1960; Huntley et al., 1985; Kennedy and Knopff, 1960). It is widely applied in geomorphology, palaeoenvironment reconstruction, and archaeology to establish the timing of sediment deposition, soil formation, or anthropogenic activity (e.g. Lian and Roberts, 2006; Liritzis et al., 2013; Mahan et al., 2022; Preusser et al., 2008; Rhodes, 2011; Singhvi and Porat, 2008). Quartz and feldspar are the primary minerals used in luminescence dating, as they are two of the most abundant minerals of the Earth's crust and serve as reliable natural dosimeters (Duller, 2008a).

The fundamental principle underlying the use of quartz and feldspar grains as natural dosimeters is based on the presence of point defects in their crystal lattices, which enables the trapping of electrons and holes (Aitken, 1985a). Their crystal lattices consist of a framework of positively and negatively charged ions. This regular order of charged ions can be disturbed by structural defects, which are caused by factors such as rapid cooling, the incorporation of impurity atoms, or exposure to ionising radiation. Among the various types of defects, two characteristics of point defects are particularly relevant for luminescence dating acting as **electron traps**, which are metastable energy states in the band gap capable of storing electrons over geological timescales, and **hole traps**, which arise when an electron is removed from the valence band and the resulting hole becomes localised at a defect site within the band gap, creating a positive charge (Marfunin, 1979). A subset of hole traps, known as **luminescence centres**, are capable of radiative recombination, leading to the emission of light (Aitken, 1985a).

Ionising radiation from the surrounding, the mineral grains themselves, or cosmic sources progressively frees electrons from the valence band, of which some populate the electron traps (Fig. 2.1b and c) (Aitken, 1985a). Stimulation by either light (optically stimulated luminescence – OSL) or heat (thermoluminescence – TL) releases the trapped electrons (Huntley et al., 1985). This thesis focuses exclusively on OSL; therefore, TL is not addressed further. After the release, the electron can diffuse within the conduction band and subsequently either get re-trapped in an electron trap or recombine with a hole trap (Fig. 2.1d and e). If this recombination occurs at a luminescence centre, a photon is emitted, producing the measurable luminescence signal, if the hole trap is of the non-radiative type, heat will be emitted (Aitken, 1985a, 1998).

It should be noted that charge accumulation occurs over time frames of 10^1 – 10^5 years, while the release of trapped charge can occur within 10^0 – 10^2 seconds (Rhodes, 2011). Since electrons can thermally escape from traps even in the absence of light or heat stimulation, electron traps have finite lifetimes, ranging from hours to millions of years. In luminescence measurements, traps are specifically targeted that exhibit thermal stability, with characteristic lifetimes typically exceeding several tens of thousands of years (Aitken, 1985a).

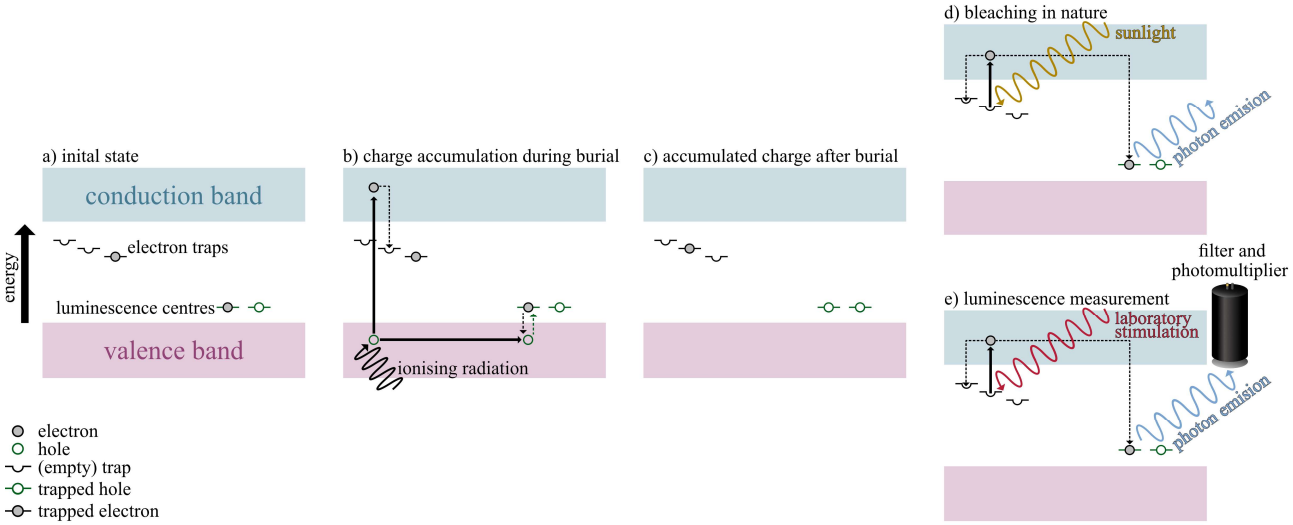

***Fig. 2.1**: Simplified band gap energy model of optically stimulated luminescence (OSL), adapted from Rhodes (2011), with each defect shown as a single energy state. Electron traps are marked in black; hole traps are marked in green. Electrons are represented by grey circles with black outlines, and holes (including vacancies in luminescence centres) by white circles with green outlines. **a)** Initial state without active ionising radiation or any stimulation. While thermally stable traps may still contain electrons from earlier exposure to ionising radiation, thermally unstable traps near the conduction band are typically empty due to ambient thermal evictions. **b)** During burial, ionising radiation excites electrons from the valence band into the conduction band, leaving behind holes. These holes are filled by electrons from luminescence centres whereby the centres become available again. Excited electrons migrate through the conduction band and become trapped in available electron traps within the band gap. **c)** State after irradiation (b), with one or more traps now occupied by electrons, the hole in the valence band filled, and the luminescence centre reset and available. **d)** Exposure to light causes the eviction of electrons from light-sensitive traps. The excited electron may either recombine with a hole at a luminescence centre, emitting a photon, recombine with a hole at a non-radiative hole trap, emitting heat, or be re-trapped elsewhere. **e)** Laboratory stimulation with controlled light within a luminescence reader induces the same processes as in (d), but emitted photons are passed through optical filters and recorded by a photomultiplier tube. **Note**: In this schematic, potential photon emission resulting from recombination after re-trapping is not shown for reasons of clarity. Furthermore, the path of the electron from trap to luminescence centre is illustrated in a simplified manner. For a more detailed discussion of potential recombination pathways (ground state tunnelling, excited state tunnelling, hopping in band-tail states) and associated energy levels for de-trapping, traps, band-tail states and the band gap, see Baril and Huntley, 2003; Clark and Sanderson, 1994; Kars et al., 2013; Malins et al., 2004; Poolton et al., 2009; Prasad and Jain, 2018; Visocekas, 1985.*

Within optically stimulated luminescence, exposure to light empties the corresponding electron traps, which resets the measurable luminescence signal. This process is referred to as bleaching (Aitken, 1985a; Wintle and Huntley, 1980, 1979).

Once shielded from light (e.g. after burial), the cycle of trap filling resumes, allowing the signal to accumulate anew (Fig.2.2). The measured luminescence signal thus reflects the time elapsed since the last exposure to light (Aitken, 1985a). A critical assumption for reliable age estimation is complete bleaching of the signal prior to burial (Duller, 1994). If a grain has not been sufficiently exposed to sunlight, a remnant luminescence signal remains, which may lead to overestimation of the burial age. This so-called incomplete bleaching is particularly relevant in fluvial or colluvial environments where light exposure may be limited (Duller, 2008b, cf. Chapter 2.2.2).

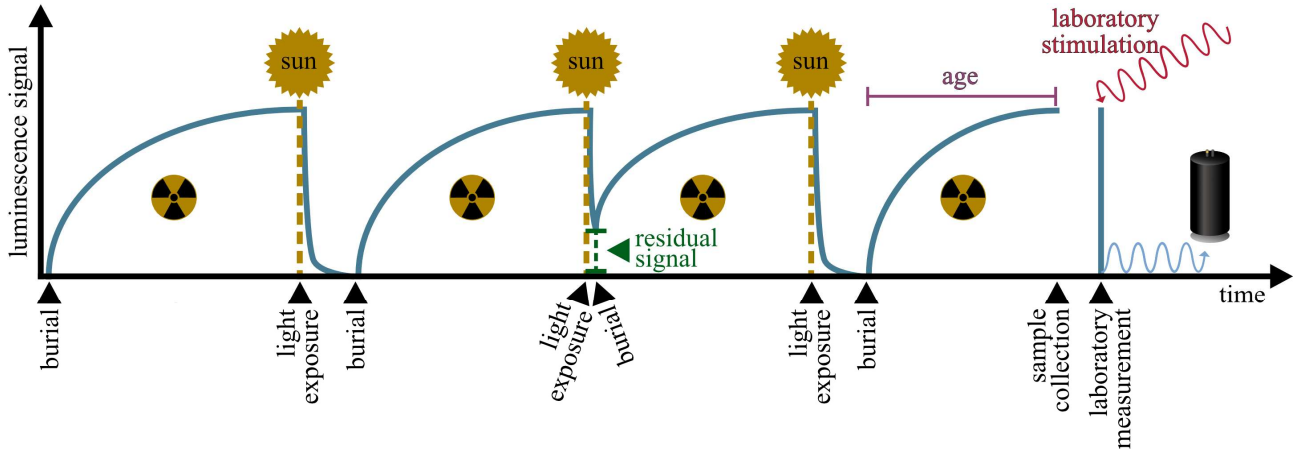

***Fig. 2.2**: Simplified conceptual model illustrating the basic principle of charge accumulation and resetting (bleaching) in luminescence dating, modified from Durcan (2021). During burial, minerals are exposed to ionising radiation, causing electrons to become trapped in defects of the crystal lattice (electron traps) and gradually accumulate (Fig. 2.1b). Upon exposure to light (e.g. during transport or surface exposure) these trapped electrons can be released (Fig. 2.1d), effectively resetting the luminescence signal. If the light exposure is sufficient, the sample becomes fully bleached, meaning that the trapped charge is reduced to near zero. Upon reburial, the cycle of radiation-induced charge accumulation begins anew. If the light exposure prior to burial is insufficient to empty all electron traps, the sample is only partially bleached (Chapter 2.2.2). In this case, the residual trapped charge from earlier exposure adds to the newly accumulated signal, potentially leading to an overestimation of burial age if not corrected. Following complete bleaching, burial, and careful sample collection and storage in light-tight conditions, the accumulated trapped charge represents the time elapsed since the last bleaching event. In the laboratory, the sample is stimulated using controlled light, and the resulting luminescence, in form of emitted photons from recombination processes in luminescence centres, is measured to estimate the burial dose, from which the age can be calculated (Fig. 2.1e).*

Since luminescence dating was first developed in the 1950s for ceramic dating (Daniels et al., 1953), the method and its areas of application have developed considerably. Besides ceramics, heated rocks, sediments, and (recently) rock surfaces are dated using luminescence techniques. Today, the majority of luminescence dating studies, including this thesis, focus on unconsolidated sediments. Accordingly, this thesis exclusively discusses the application of luminescence dating to sedimentary deposits.

Although the measurement techniques have evolved over the years, the fundamental principle underlying age calculation has remained unchanged since the 1950s (Aitken, 1985a; Duller, 2008a; Fleming, 1966; Tite and Waine, 1962). The luminescence **age** results from the division of the total amount of accumulated charge, the equivalent dose ($\mathbf{D_e}$), by the energy delivered each year from radioactive decay and cosmic rays, the total dose rate ($\dot{\mathbf{D}}$) (Eq. 2.1, Aitken, 1985a).

$$luminescence\ age\ (ka) = \frac{equivalent\ dose\ (Gy)}{total\ dose\ rate\ (Gy\ ka^{-1})} = \frac{D_e}{total\ \dot{D}} \qquad (Eq.\ 2.1)$$

With Gray (Gy) being the SI unit of absorbed radiation dose, which is defined as the deposition of one joule of radiation energy per kilogram of matter (Bureau International des Poids et Mesures, 2024). The calculation of the $\dot{D}$ is addressed in Chapter 2.1.3. The D_e is commonly estimated experimentally by using a regenerative-dose protocol, in which the natural luminescence signal is compared to signals generated by known laboratory doses (Aitken, 1985a). Nowadays, the most widely applied approach is the single-aliquot regenerative-dose (SAR) protocol (Murray and Wintle, 2000; see Chapter 2.1.2 and Table 2.1 for more details). This protocol begins by measuring the natural luminescence signal (L_n), followed by a series of regenerative dose measurements (L_x) (Fig. 2.3a, b), each paired with a fixed test dose (T_n, T_x) used to monitor sensitivity changes and to normalise the corresponding L_n and L_x signals. The ratios of L_x/T_x are plotted against their given regenerative dose to construct a dose-response curve (Fig. 2.3c). The natural signal ratio (L_n/T_n) is then interpolated on this curve to estimate D_e.

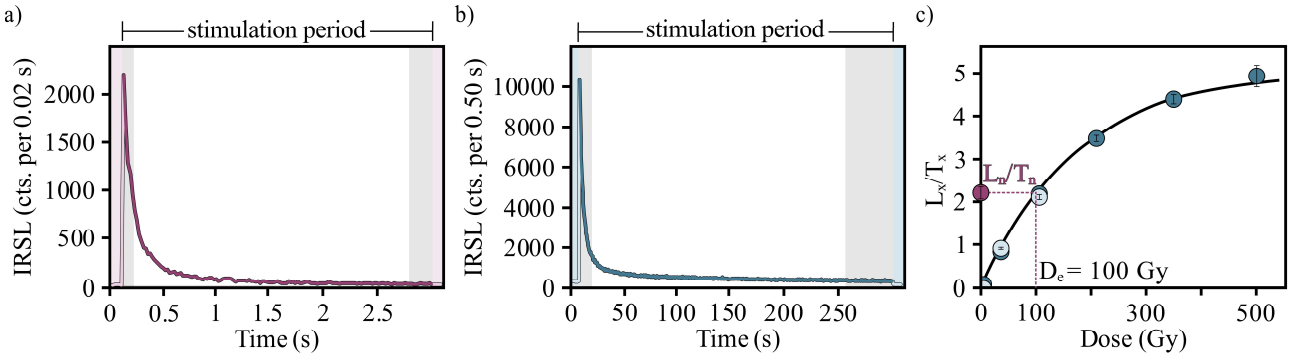

***Fig. 2.3**: Luminescence measurement results for the feldspar sample P2-3 (Chapter 6). **a)** Single-grain post-infrared infrared stimulated luminescence at 225 °C ($pIRIR_{225}$, cf. Chapter 2.1.2) decay curve (dark purple). Light pink curves in front of a light pink background before and after the measurement represent the so-called dead channels measured 0.1 s prior and post of the stimulation period. The signal integration interval (first 0.2 s of stimulation) and the background integration interval (last 0.4 s of stimulation) are shaded in grey. **b)** Multi-grain $pIRIR_{225}$ decay-curve (dark turquoise). Light blue curves in front of a light blue background before and after the measurement represent the dead channels (5 s each). The signal integration interval (first 10 s of stimulation) and the background integration interval (last 40 s of stimulation) are shaded in grey. **c)** Dose-response curve (black) of the same disc shown in b) of a $pIRIR_{225}$ dose recovery test. The L_n/T_n is shown as a purple dot, and L_x/T_x are shown as turquoise dots. The L_x/T_x of repeated measurements at specific dose (0 s, 700 s, 2097 s) are indicated by light blue dots. **Note:** as only feldspars were measured within this thesis,*

quartz decay curves are not shown. The main difference between both are: i) quartz OSL signals typically decay much more rapidly than feldspar infrared stimulated luminescence (IRSL) signals; and ii) signal intensity is sample-dependent, but feldspar IRSL signals generally exhibit higher intensity than quartz OSL signals.

Luminescence measurements on sediments can be performed either on a multi-grain or a single-grain level (Duller, 2008a) (Fig. 2.3a and b). In the case of multi-grain measurements, aliquots consisting of a few to several hundred grains are prepared and measured simultaneously. The measured luminescence signal is therefore the sum of all luminescence signals emitted by the individual grains on the disc (Fig.2.3b). While increasing the overall signal intensity and thus enhancing the measurement precision, grain-to-grain variabilities cannot be determined (Duller, 2008a). As a result, individual grains with significantly lower or higher signals are averaged out, which may obscure the presence of heterogeneously bleached grains or mixed-age populations (Duller, 2008b; Wallinga et al., 2000; cf. Chapter 2.2.2). In heterogeneously bleached samples, at least some grains have not been exposed to sufficient sunlight. The degree of sunlight exposure might vary between the grains, resulting in different residual doses prior to burial. Consequently, their apparent ages do not reflect their last exposure to sunlight. Similarly, mixed-age populations arise when grains with different depositional histories are present in the same sample, for example due to post-depositional mixing. A few above-average old grains in a young grain population might lead to severe overestimation of the D_e. In contrast, single-grain measurements allow for the detection of heterogeneities in luminescence properties and bleaching history, enabling the identification and/or exclusion of poorly bleached or otherwise unsuitable grains (Duller, 2008a). This approach is therefore particularly beneficial in settings prone to heterogeneous bleaching, further explained in Chapter 2.2.2 (e.g. Duller, 2008b; Ventra and Clarke, 2018), or where grain-scale processes (e.g. sediment tracing) are of interest (e.g. Heimsath et al., 2002). However, single-grain measurements are significantly more time- and resource-intensive, requiring specialised equipment (e.g. laser stimulation systems; Truscott et al., 2000) and they have higher measurement uncertainty due to the lower signal intensity of individual grains. The choice between multi-grain and single-grain approaches should thus be guided by the expected complexity of the sample and the research objective (Duller, 2008a). The decision is also linked to the selected grain size. Commonly used grain size fractions include fine grains (e.g. 4–11 µm or 4–30 µm) and coarse grains (e.g. 63–90 µm, 90–125 µm, 212–250 µm) (e.g. Mahan et al., 2022). Fine grains have the advantage of a more uniform $\dot{D}$ and less self-dose effects (see Chapter 2.1.3), but are not suited for single-grain analyses and might be contaminated by other minerals. Coarse grains enable grain-specific signal assessment and are more appropriate for detecting

heterogeneous bleaching or reconstructing individual grain histories. Grain size selection is therefore dependent on mineral composition of the sample, equipment availability, and the study's specific objectives.

Depending on the mineral and stimulation method, different light wavelengths are used for OSL stimulation. Quartz is typically stimulated with blue light at wavelength of about 470 nm (LED) or 532 nm (laser), as its luminescence intensity increases with decreasing wavelength (Bøtter-Jensen et al., 1999, 1994; Huntley et al., 1985). In contrast, feldspar measurements rely on infrared stimulated luminescence (IRSL) at wavelength of about 830 nm (laser) or 850 nm (LED), corresponding to an energy of ~1.45 eV (Hütt et al., 1988; Krbetschek et al., 1997; Chapter 2.1.2). It has been shown that this stimulation energy corresponds with the strongest luminescence emission in feldspars (Kars et al., 2013; Krbetschek et al., 1997; Riedesel et al., 2019). An additional advantage of using infrared stimulation is that it does not excite quartz, thereby preventing excitation of potential quartz contamination within the samples (e.g. Krbetschek et al., 1997). Furthermore, the stimulation wavelength is chosen to far away from the detection wavelength (~365 nm for quartz, ~410 nm for feldspars), to prevent contamination of the luminescence signal by scattered stimulation light (Aitken, 1998). Additional light sources used include yellow-stimulated OSL for feldspars (Y-OSL; Lauer et al., 2012) and violet-stimulated luminescence for quartz (VSL; Jain, 2009). Stimulation is most often carried out using a continuous-wave stimulation (CW-OSL) with constant light intensity (Bulur, 1996). Alternative approaches include pulsed IRSL or time-resolved OSL (TR-OSL), where light is delivered in short pulses (Bailiff, 2000; Clark et al., 1997; Clark and Sanderson, 1994), and linearly modulated OSL (LM-OSL), in which the light intensity increases gradually during stimulation (Bulur, 1996; Bulur et al., 2002). A further method, infrared photoluminescence (IRPL), involves non-destructive stimulation of trapped electrons and enables spatially resolved investigations without emptying the traps (Prasad et al., 2017). The measurement protocol must be adapted to the type of stimulation and measurement scale (single- or multi-grain). This thesis focuses exclusively on feldspar IRSL measurements (see Chapter 2.1.2). Therefore, alternative optical stimulation modes are not discussed further.

Once luminescence measurements are completed, the D_e is usually derived by either using the software provided by the luminescence reader manufacturer (e.g. Analyst for Risø systems or LexStudio for Freiberg Instruments readers) or using an open-source environment such as R packages like Luminescence (Kreutzer et al., 2012) or numOSL (Peng et al., 2018). All tools provide the application of various fitting models for the dose-response curve, a variety of rejection criteria, visualisation of the data and further statistical analysis such as dose models.

Independent of the mineral, stimulation method, or measurement scale (multi- vs. single-grain), luminescence ages are typically derived from statistical dose models that interpret the D_e distribution obtained from individual multi- or single-grain measurements (e.g. Mahan et al., 2022; Rhodes, 2011). Different dose models aim to characterise different components of the D_e distribution. The dose model used should be chosen depending on the research question and the expected degree of scatter (Bailey and Arnold, 2006). The most commonly applied models include the Central Age Model (CAM; Galbraith et al., 1999), the Minimum Age Model (MAM; Galbraith et al., 1999), Finite Mixture Models (FMM; e.g. Galbraith and Green, 1990; Roberts et al., 2000), and the recently introduced BayLum R package for Bayesian analysis of OSL ages (Philippe et al., 2019). Within this thesis, only the CAM and MAM were applied, and therefore only these two are discussed in detail. The **CAM** assumes a single, log-normally distributed D_e distribution around a central value interpreted as the burial dose (Galbraith et al., 1999). This model is most appropriate when all grains are assumed to have been well bleached prior to deposition and the observed scatter arises from random uncertainties. A key parameter in the CAM is the overdispersion (σ_b), which quantifies the relative spread in the D_e values beyond the expected spread from analytical uncertainty alone. This spread may reflect natural variability in the sample, such as beta-dose heterogeneity during burial or intrinsic grain-to-grain variability in luminescence characteristics (Arnold and Roberts, 2009; Galbraith et al., 1999). In contrast, the **MAM** is applied when the D_e distribution is positively skewed, which may result from heterogeneous partial bleaching or post-depositional mixing (Galbraith et al., 1999). It targets the lower tail of the D_e distribution, aiming to identify the youngest grain population, which is assumed to represent the best bleached grains. It incorporates individual measurement uncertainties and an assumed value of overdispersion, which can be either estimated from well-bleached modern analogues or set based on prior knowledge.

2.1.2 Feldspar luminescence dating

Feldspars are a group of tectosilicate minerals which are the most abundant constituents of the Earth's crust and are frequently present in sedimentary deposits (Morad, 1978). Their general formula is MT_4O_8, with usually T being Al^{3+}, Si^{4+} corner-sharing tetrahedra connected via oxygen and with large cations Ca^{2+}, Ba^{+}, Na^{+}, K^{+} occupying the M sites (Deer et al., 2013). They are structurally classified within a ternary compositional system with the endmembers potassium (K) feldspars ($KAlSi_3O_8$, e.g. orthoclase and microcline), sodium (Na) feldspars ($NaAlSi_3O_8$, e.g. albite), and calcium (Ca) feldspars ($CaAl_2Si_2O_8$, e.g. anorthite) (Deer et al., 2013; Ribbe,

1983). At high temperatures (>980 °C), the feldspar group is divided into two solid solution series: plagioclase feldspars, ranging from albite to anorthite, and alkali feldspars, ranging from albite to K-feldspars (e.g. orthoclase and microcline). Exsolution of alkali feldspars during cooling leads to intergrowth textures referred to as perthite. Structural changes during cooling also affect tetrahedral site occupancy: high-temperature feldspars like sanidine have a monoclinic structure which is characterised by a random distribution of Al^{3+} and Si^{4+} across T sites. As temperature decreases, Al^{3+} becomes increasingly ordered, initially migrating to specific T1 sites and ultimately to a single site (T1(0)), inducing a symmetry change from monoclinic to triclinic (e.g. microcline) (Deer et al., 2013).

Prior to luminescence measurements of sand-sized grains, the desired feldspar fraction needs to be separated from the bulk sample through a series of physical and chemical treatments. Sample preparation is always carried out under subdued red to orange light conditions to avoid luminescence signal loss. Each laboratory follows a slightly different protocol. Yet, all of them include dry or wet sieving to isolate the desired grain size fraction, a treatment with hydrochloric acid (HCl; ~10 %) and hydrogen peroxide (H_2O_2; ~10 %) to remove carbonates and organic matter, respectively. Some laboratories include an additional treatment with disodium oxalate ($Na_2C_2O_4$; 0.01 N) to disperse the particles (e.g. Cordier et al., 2010; Hülle et al., 2009; this thesis). Often a density separation using heavy liquids (for example sodium polytungstate, Ollerhead et al., 1994) is applied to isolate the feldspar fraction, which typically floats at densities between 2.58 g/cm^3 (K-rich feldspars) and 2.62 g/cm^3 (K-rich and Na-rich feldspars) (Mejdahl, 1985). After each chemical treatment, samples are washed with deionised water, to remove any residues. Some laboratories also incorporate etching with hydrofluoric acid (HF), although this step is often avoided for feldspar samples due to the risk of grain alteration (Duller, 1992). Further steps, such as additional sieving if required, magnetic separation (usually applied only to quartz, Porat, 2006), or sample-specific chemical treatments, for example to remove calcium sulphate (Zinelabedin et al., 2022), may be included.

The luminescence properties of feldspars vary depending on their chemical composition and crystal structure. For example, the main luminescence emission from K-feldspars is at 3.0 eV (410 nm) while Na-feldspars have their main luminescence emission at 2.2 eV (570 nm) (Huntley and Baril, 1997; Krbetschek et al., 1996; Fig. 2.4). For luminescence dating, K-feldspars are generally preferred due to several assumptions[1]: **i)** their internal K-concentration is higher, which contributes

[1] The validity of the first three assumptions is discussed in detail in Chapters 3, 4, and 7.

significantly to the internal dose rate, wherefore other contributions to the dose rate become less relevant (Chapter 4); **ii)** the higher K-concentration is often believed to result in brighter luminescence signals (Chapter 3); **iii)** Na-feldspars and perthitic feldspars (intergrowth of K- and Na-feldspars) are thought to often exhibit weaker and less stable luminescence signals (Prescott and Fox, 1993; Sohbati et al., 2013; Tsukamoto et al., 2012, Chapter 3); **iv)** Ca-feldspars and plagioclase feldspars often have greater fading rates (Barré and Lamothe, 2010; Huntley and Lian, 2006) and suffer from low luminescence efficiency (Spooner, 1992). However, sample preparation techniques often fail to isolate pure K-rich feldspars (see Huntley and Baril, 1997; cf. Chapter 4). Hence, a specific filter combination, commonly referred to as the blue filter combination, is used during measurement to transmit only the blue emission centred around the K-feldspar emission peak at 410 nm (Fig. 2.4). In this thesis, the blue filter combination consists of a 4 mm Schott BG39 filter and a 3 mm Corning 7-59 filter. This combination allows light in the wavelength range of approximately 310 nm to 490 nm to pass into the photomultiplier tube, while effectively suppressing infrared stimulation light and longer-wavelength emissions (IR laser ~830 nm; IR LED ~850 nm).

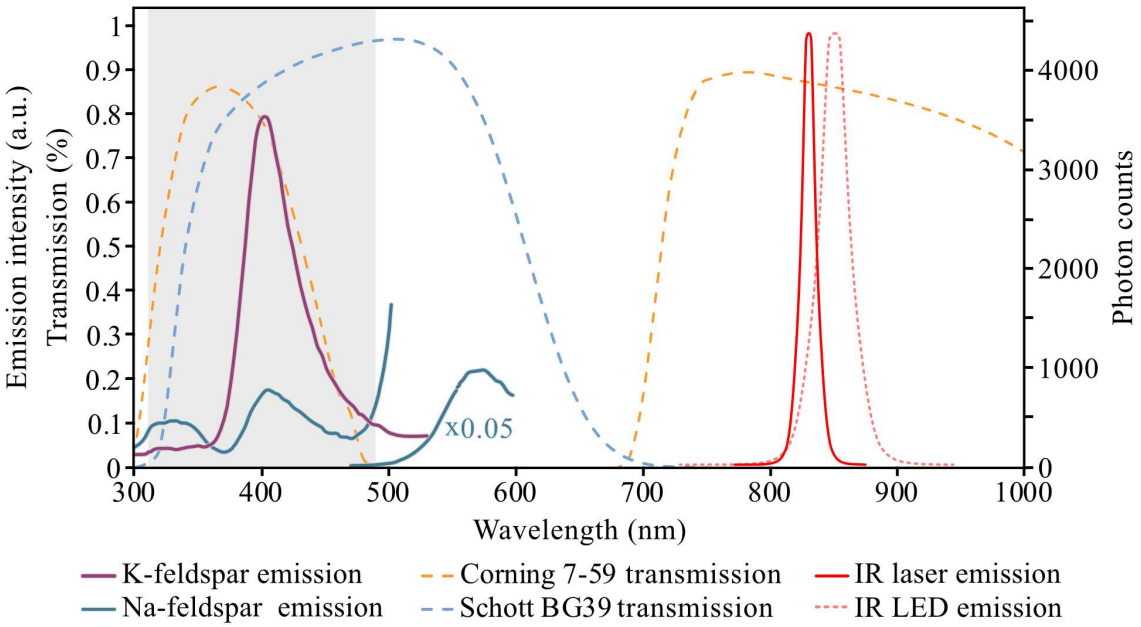

***Fig. 2.4**: Emission spectra of K- and Na-feldspar grains, transmittance curves of the Corning 7-59 and the Schott BG39 filters, and emission spectra from an IR laser and IR LEDs. The emission spectra of the feldspars are redrawn from Huntley et al. (1991). The main peak emission (~475 – 600 nm) of the Na-feldspar is drawn at x 0.05 of its original height. The transmission spectra for the Corning 7-59 was taken from Lo and Turk, (1982), the transmission spectra for the Schott BG39 and the IR LED emission spectra were taken from DTU Physics (2021), and the emission spectra for the IR laser was taken from Bøtter-Jensen et al. (2000). The grey bar highlights the transmission window of the blue filter combination between ~310 nm and ~490 nm.*

Since K-rich feldspars exhibit a dominant emission at around 410 nm (Huntley et al., 1991), they are expected to provide the strongest contribution to the detected

signal in multi-grain measurements (Huntley and Baril, 1997). In contrast, single-grain measurements present a greater challenge, as dim K-feldspar grains may be difficult to distinguish from other minerals that emit within a similar spectral range (Krbetschek et al., 1996), despite having different emissions peak positions. Na-feldspars, for example, exhibit a main emission around 570 nm along with two additional, but much weaker, emission peaks around 330 nm and 405 nm (cf. Fig. 2.4) (Huntley et al., 1991).

Compared to quartz, K-feldspars often yield stronger luminescence signals and saturate at higher doses, enabling the dating of samples beyond the upper limit of quartz OSL (Buylaert et al., 2012; Hütt et al., 1988). However, K-feldspars bleaches slower and less effective than quartz (Buylaert et al., 2012; Godfrey-Smith et al., 1988) and their luminescence signals are affected by anomalous fading, a process characterized by signal loss over time in the absence of light or heat exposure (Wintle, 1973). This signal loss is attributed to quantum-mechanical tunnelling of trapped electrons to recombination centres without the need for thermal or optical stimulation (Spooner, 1994). Anomalous fading leads to underestimation of luminescence ages if uncorrected. The fading rate is quantified as the g-value, which represents the percentage of signal loss per decade (Aitken, 1985a).

Due to fading, conventional IRSL signals from feldspars are often unsuitable for accurate age estimation unless fading corrections are applied (Huntley and Lamothe, 2001). To mitigate this limitation, the post-infrared infrared stimulated luminescence (pIRIR) protocol was developed (Thomsen et al., 2008). In this approach, a low-temperature IR stimulation (usually 50 °C) is first applied to remove the unstable, easily faded component of the IRSL signal. A subsequent stimulation at a higher temperature is then used to measure the more stable signal component, which is less affected by fading. Traditionally, the increasing stability of signals with increasing temperature was thought to result from progressive stimulation of deeper electron traps (Aitken, 1998; Murray and Wintle, 2000). However, more recent work suggests that the higher-temperature pIRIR signals do not originate from progressively deeper electron traps, but instead from recombination centres located at greater spatial separations from the trapped electrons (Jain and Ankjærgaard, 2011). Traps at a greater distance are less susceptible to quantum tunnelling and thus to fading, thereby enhancing the signal stability. Besides the charge in thermally stable electron traps targeted during the pIRIR measurement, some trapped charge resides in thermally unstable traps that are not stable over laboratory timescales. These thermally unstable traps can be emptied by applying a preheating step prior to the optical stimulation (Aitken, 1998; Murray and Wintle, 2000). Hence, a standard SAR protocol

for a pIRIR measurement includes the following steps to enhance the signal stability while reducing the fading probability (Murray and Wintle, 2000; Thomsen et al., 2008):

***Table 2.1**: Example of a standard SAR pIRIR protocol.*

Step	Treatment[a]	Observation
1	For L_x measurements: given dose D_i	
2	Preheat, 60s at temperature > step 4	
3	IRSL at 50°C	
4	IRSL at higher temperature	L_n or L_x
5	Given test dose D_t	
6	Preheat, 60s at temperature > step 8	
7	IRSL at 50°C	
8	IRSL at higher temperature	T_n or T_x
9	Return to step 1	

[a] given dose D_i [Gy]: depending on the expected D_e; test dose D_t [Gy]: usually ⅓ of expected D_e

It should be noted that for the first measurement cycle, where the natural signal is measured, step 1 is omitted. The size of the given dose D_i and the given test dose D_t as well as the number of cycles measured are sample dependent. A cycle with $D_i = 0$ Gy is typically included to assess recuperation, which refers to the amount of luminescence signal generated without irradiation. Replicate cycles with identical D_i values are usually included to evaluate if a dose can successfully be recovered (Murray and Wintle, 2000). In some cases, an additional "hot bleach" step (e.g. optical bleaching at elevated temperatures ≥290 °C) after step 8 is required to minimise residual signals (e.g. Buylaert et al., 2007; Li and Li, 2011; Murray and Wintle, 2003; Wallinga et al., 2007). In the context of single-grain measurements, Colarossi et al. (2018) implemented two hot bleach steps to reduce charge carry-over from L_x to T_x: one following the L_x measurement (step 4) and another after the T_x measurement (step 8). To further decrease anomalous fading, a modified version of the standard pIRIR protocol was developed by Li and Li (2011). In this so-called Multiple Elevated Temperature (MET) pIRIR protocol, IR signals are measured stepwise with progressively increasing stimulation temperatures at each step. By stimulating at higher temperatures, electrons in less stable, fading-prone traps are preferentially emptied, thereby isolating more thermally stable signal components that exhibit reduced fading (Li and Li, 2011).

To establish a robust pIRIR measurement protocol, several pre-tests are conducted to optimise measurement conditions and assess signal behaviour (Roberts, 2012; Wintle and Murray, 2006). These include a dose recovery test (DRT), a residual test, a fading test, and preheat plateau (PHP) tests. For each test, multiple multi-grain aliquots or single-grain discs per sample are bleached to reset their luminescence signals. In the **DRT**, a known D_i is administered, and the SAR protocol (cf. Table 2.1) is applied. To evaluate the reliability of the protocol, the ratio of recovered to

administered dose is assessed, which should ideally equal one. For the **residual tests**, no dose is administered in the first measurement cycle in step 1. The purpose of this test is to quantify how much signal remains in a sample after bleaching. Ideally, the residual doses measured should be close to zero. If considerable residuals are present, the natural signal measurements may require correction. The **fading test** measurements follow a modified SAR protocol. Like in a DRT, a D_i is administered in the first cycle. After the preheat (step 2) a pause is integrated before steps 3 to 8 are carried out. The delay varies from 0 seconds to longer time periods of 100,000 seconds or more. Each L_x measurement is then compared to the corresponding T_x measurement, which was measured without a pause. The L_x/T_x ratios are then plotted against the logarithm of storage time, and the g-value is calculated as the percent signal loss per decade (Fig. 2.5). If the fading test shows considerable fading (e.g. >2 % / decade, Fig.2.5a), fading corrections of the measurements are necessary (Huntley and Lamothe, 2001).

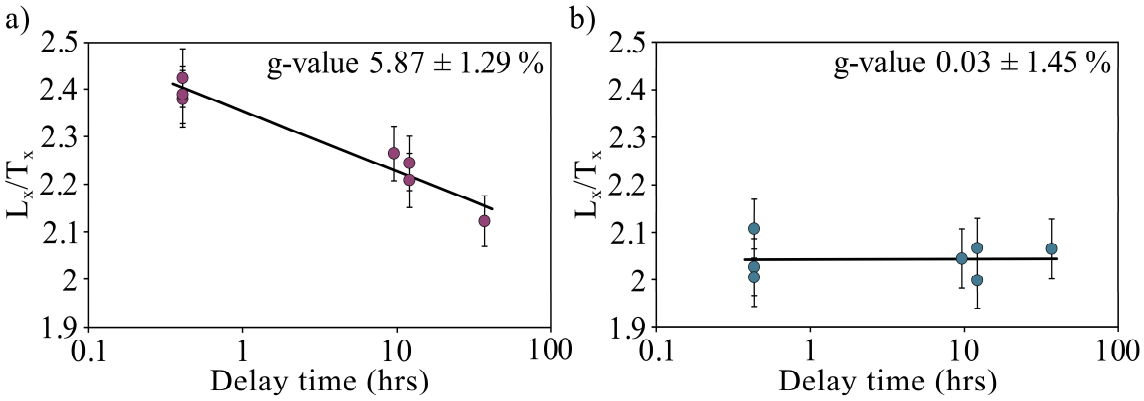

***Fig. 2.5**: pIRIR fading test results conducted on sample P5-4 (see Chapter 6), comparing **a)** pIRIR with a measurement temperature of 160° ($pIRIR_{160}$) and **b)** pIRIR with a measurement temperature of 225° ($pIRIR_{225}$) protocols. **a)** A preheat temperature of 190 °C was applied, the sample showed considerable fading with a g-value of 5.87 ± 1.29 %. **b)** A preheat temperature of 250 °C was applied, and the sample experienced negligible fading with a g-value of 0.03 ± 1.45 %.*

PHP tests are carried out to identify a suitable combination of preheat and stimulation temperatures. For this, a series of DRTs, residual tests, and fading tests are performed using different preheat temperatures, typically ranging from 190 °C to 320 °C, with stimulation temperatures adjusted accordingly. The preheat temperature is usually set 20 °C to 30 °C higher than the post-IR stimulation temperature in steps 4 and 8. The goal is to identify a temperature range where the recovered dose ratios are close to unity, and residual doses and fading rates are minimal. This range constitutes the "preheat plateau" and indicates stable measurement conditions. An appropriate protocol is subsequently selected based on all test measurements.

Not all measured multi-grain aliquots or single-grains yield reliable D_e estimates. Therefore, rejection criteria are applied to exclude poorly behaving multi-grain

aliquots or single-grains from the final age calculations. Commonly used criteria include: the T_n signal intensity compared to the background, the relative standard error (RSE) of the T_n signal, the RSE of the D_e, recuperation, a recycling ratio, and the goodness-of-fit of the dose response curve

The signal intensity of the T_n signal is usually rejected if it is <3σ above the background, since it is too dim to give a reliable signal. If the RSE of the T_n signal or the D_e is greater than a certain threshold (e.g. 25 % respectively 50 %), the multi-grain aliquot or single-grain is also rejected since the quality of the measurement is too low. For young samples, the RSE of the D_e is usually not considered. The RSE is calculated by dividing the absolute uncertainty (standard error of the D_e) by the D_e. Therefore, small absolute uncertainties in low D_e estimates can lead to large RSEs. Recuperation refers to the signal intensity after a zero-dose cycle ($D_i = 0$ Gy). High recuperation indicates thermal instability or contamination and may suggest incomplete signal resetting. The recycling ratio evaluates the reproducibility of a given dose by repeating a known regeneration dose during the SAR cycles. Acceptable recycling ratios typically lie within ± 10 % of unity. The goodness-of-fit of the dose-response curve is usually evaluated using the figure of merits (FOM) and/or the reduced Chi-square (χ^2) (Balian and Eddy, 1977). If FOM and χ^2 are above a certain threshold (e.g. 10 % for FOM and >1 for χ^2, Peng and Li, 2017), the aliquot or grain is rejected, as no reliable dose-response curve can be constructed.

Yet, even after careful protocol determination and rejection of unsuitable multi-grain aliquots, under some circumstances (e.g. heterogeneous bleaching, mixing), multi-grain feldspar measurements are still prone to additional uncertainties, as mentioned above in Chapter 2.1.1 and as will be further explained in Chapter 2.2.2.

2.1.3 Dose rate determination

The total dose rate (total $\dot{D}$) is the denominator in the luminescence age equation (Eq. 2.1). Therefore, the determination of the total $\dot{D}$ is just as important as the determination of the numerator, i.e., the D_e. The total $\dot{D}$ received by a sample comprises several components, which can be grouped into the cosmic dose rate ($\dot{D}_c$), the external dose rate ($\dot{D}_{ext}$), and the internal dose rate ($\dot{D}_{int}$) (e.g. Aitken et al., 1968). These components arise from four main types of ionizing radiation, alpha (α) particles, beta (β) particles, gamma (γ) rays, and cosmic rays (e.g. Aitken and Fleming, 1972; Houtermans et al., 1957). Their contribution may underly changes over time, as they are all influenced by external factors such as burial depth or water content in the surrounding sediment (e.g. Aitken, 1985a; Aitken and Fleming, 1972; Mejdahl, 1970), making $\dot{D}$ determination no less complex than D_e determination.

The $\dot{D}_c$ accounts for the contribution of cosmic rays to the total Ḋ, which is typically less than 10 % of the total Ḋ (Mahan et al., 2022), and can be divided into the soft component and the hard component (Nordheim, 1938). While the soft component only penetrates shallow depth of up to 167 g cm^{-2} [2] the hard component, which mainly consists of muons, is able to penetrate many tens of meters (Barbouti and Rastin, 1983; Prescott and Hutton, 1988). The intensity of the $\dot{D}_c$ is influenced by the longitude, latitude, and altitude from which a sample is taken, the thickness and density of the overburden of a sample, the strength of the geomagnetic field, and the intensity of the cosmic rays (Prescott and Hutton, 1988; Prescott and Stephan, 1982). While the overburden (i.e., thickness and density of sediment above the sample) may vary over time, which needs to be accounted for during $\dot{D}_c$ calculations, the longitude, latitude, and altitude usually do not change considerably during the timescales considered. The geomagnetic field and cosmic ray intensity have shown little variation over the past 500,000 years and are therefore also negligible and are hence irrelevant for most luminescence dating purposes (Prescott and Hutton, 1994).

The $\dot{D}_{ext}$ accounts for the α particles, β particles, and γ radiation emitted by the surrounding of a sample. These emissions originate primarily from the natural decay of radionuclides such as uranium (U), thorium (Th), potassium (K), and rubidium (Rb), which are commonly present in a wide range of geological settings (e.g. Aitken, 1985a). In particular, the decay chains of ^{238}U, ^{235}U[3], ^{232}Th, and the isotope ^{40}K are the main contributors to the $\dot{D}_{ext}$. To accurately determine the $\dot{D}_{ext}$, either *in situ* measurements of the radiation field are employed or $\dot{D}_{ext}$ calculations are based on lab-measured radionuclide concentrations (De Corte et al., 2007). In order to calculate $\dot{D}_{ext}$ from measurements, the radionuclide concentrations must be converted into α, β, and γ Ḋ using appropriate conversion factors (e.g. Adamiec and Aitken, 1998; Guérin et al., 2011; Liritzis et al., 2013). The use of conversion factors assumes that the sample is embedded in an infinite, homogeneous matrix (infinite matrix concept; Aitken, 1985a; Fano, 1954; Guérin et al., 2012), and that the decay chains of U and Th are in secular equilibrium (see Aitken, 1985a). The main principle of the infinite matrix concept is that, within a homogeneous infinite matrix, the energy emitted by radioactive decay per unit mass is equal to the rate of energy absorbed as dose per unit mass (Aitken, 1985a). In the context of luminescence dating, the infinite matrix

[2] g cm^{-2} is a measure of depth independent of the absorber and needs to be divided by the density of the absorber to calculate the penetration depth in cm. The density for a typical limestone with 10 % water content is 1.18 g cm^{-3} which would result in a penetration depth of the soft component of 141.5 cm. For sediments within this thesis (Chapter 6) a density of 1.8 g cm^{-3} is assumed resulting in a penetration depth of 92.8 cm.

[3] The ^{235}U decay chain is usually not analysed explicitly, as ^{238}U is much more abundant than ^{235}U (Duller, 2008a).

assumption is applied within a limited volume of approximately 30 cm surrounding the sample, as γ radiation has an effective range of about 30 cm in sediment, while α and β particles are absorbed within much shorter distances (Mahan et al., 2022). Therefore, it is assumed that the material within this 30 cm radius behaves as an infinite matrix, providing a uniform and isotropic radiation field for $\dot{D}_{ext}$ calculations. However, the surrounding of a sample within a 30 cm radius is not always homogeneous in natural settings, for example, if the sample is located near the surface or if a different sediment or rock layer lies within the 30 cm radius. Appropriate corrections must be applied to account for variations in density, composition, or geometry (e.g. Aitken, 1985a; Guérin et al., 2012; Riedesel et al., 2023; Riedesel and Autzen, 2020). Secular equilibrium within the U and Th decay chains is reached when all daughter isotopes decay at the same rate as the parent isotope, resulting in constant activity levels throughout the chain. However, disequilibrium may arise from processes such as the emanation of gaseous daughters (^{219}Rn, ^{220}Rn, and ^{222}Rn) or the leaching of radium isotopes by groundwater (e.g. Aitken, 1985a; Olley et al., 1996).

The $\dot{\mathbf{D}}_{\mathbf{int}}$ accounts for the α and β radiation emitted by radionuclides within the sampled mineral grain itself. While the $\dot{D}_{int}$ in quartz grains is typically negligible, feldspar grains possess a significant $\dot{D}_{int}$ component (Mejdahl, 1987). Since this study focuses exclusively on feldspars, $\dot{D}_{int}$ determination in quartz is not further considered. In K-rich alkali feldspars, which are the primary target mineral in feldspar luminescence dating, a major portion of the $\dot{D}_{int}$ arises from β emissions associated with the decay of the internal ^{40}K (Mejdahl, 1987). In addition, Rb, which is commonly present in alkali feldspars, also contributes to the β component of the $\dot{D}_{int}$ (Warren, 1978). The α and β contributions from U and Th are often considered negligible, although several studies have shown that they can significantly contribute to the $\dot{D}_{int}$ in specific cases (Mejdahl, 1987; Smedley and Pearce, 2016; Zhao and Li, 2005). In practice, $\dot{D}_{int}$ estimates are commonly based on published average K-concentrations (Maßon et al., in press; Chapter 4 this thesis). However, results from this thesis (Maßon et al., in press; Chapter 4) indicate that deriving $\dot{D}_{int}$ from literature-based K-concentration values should no longer be considered sufficient for routine dating due to the complex chemical composition of feldspars. Given that K and Rb typically occur in a ratio of approximately 270:1, Rb-concentrations are frequently inferred from the assumed K-concentration using the empirical relationship (Mejdahl, 1987):

$$Rb\ (ppm) = -9.17 + 38.13 * K\ (\%) \qquad \textit{(Eq. 2.2)}$$

As with the calculation of $\dot{D}_{ext}$, radionuclide concentrations must be converted into α and β $\dot{D}$ using appropriate conversion factors (Adamiec and Aitken, 1998; Guérin et al., 2011; Liritzis et al., 2013).

In addition to the radionuclide-specific parameters used to calculate the α, β, and γ components of the $\dot{D}_{ext}$ and $\dot{D}_{int}$, further factors influence how much of the total $\dot{D}$ is effectively absorbed by the mineral grain. Those variables are: the grain size, the alpha efficiency (a-value), the etching during sample preparation, and the water content (Aitken, 1985a).

Due to the limited penetration depths of α and β radiation, grains partially self-attenuate incoming radiation (e.g. Aitken, 1985a; Bell, 1980; Mejdahl, 1979). As a result, $\dot{D}_{ext}$ and $\dot{D}_{int}$ must be corrected for **grain-size**-dependent attenuation to avoid overestimating the absorbed dose. Attenuation factors have been calculated for both α and β radiation (e.g. Bell, 1980; Brennan, 2003; Brennan et al., 1991; Guérin et al., 2012; Mejdahl, 1979). These attenuation factors are derived under the assumptions that the dose absorbing grain is spherical, that the surrounding matrix is homogeneous (infinite matrix concept), and that the radionuclides are in secular equilibrium.

The limited range of α particles compared to β particles and γ radiation is due to their large mass and high ionising potential resulting in rapid energy loss as they pass through matter and is accounted for through grain-size attenuation factors. However, while α particles travel in nearly straight trajectories and ionise surrounding atoms, β particles and γ radiation interact more diffusely with the surrounding matrix (Knoll, 2000). To account for this reduced effectiveness, an α efficiency factor, the **a-value**, is applied. The a-value is typically defined as the ratio of luminescence produced per unit of absorbed α-dose to that produced per unit of absorbed β-dose (Aitken, 1985b; Aitken and Bowman, 1975). Reported a-values vary with mineralogy, grain size, and the experimental conditions under which they are measured. If not measured for the specific sample, commonly cited a-values in the literature for coarse grain K-feldspars are 0.11 ± 0.03, which is based on experimental measurements (Balescu and Lamothe, 1993) and 0.15 ± 0.05, which is based on an assumption about the absorbed α-dose rather than direct measurement (Balescu and Lamothe, 1994).

The influence of external α particles on quartz grains is typically minimized by **etching** the grain surfaces with HF. It is often assumed that HF etching on quartz grains removes an isotropic surface (e.g. Duval et al., 2018; Fleming, 1969), and thereby effectively eliminating their α-irradiated rims and potential feldspar contamination within the sample extract (Porat et al., 2015). In feldspars however, HF etching is known to results in an uneven surface removal (Duller, 1992), which is why it is rarely applied to eliminate the alpha-affected outer layer. Since etching alters the grain size, it must be taken into account during $\dot{D}$ calculations. Bell (1980) and Brennan et al. (1991) calculated etch attenuation factors.

Water within the sediment matrix attenuates α, β, and γ radiation throughout the burial period, reducing the effective Ḋ (Zimmerman, 1971). Therefore, the α, β, and γ $\dot{D}_{ext}$ have to be corrected based on assumptions about the long-term average water content. Zimmerman (1971) and Aitken and Xie (1990) introduced attenuation factors based on the assumed water content of the sediment matrix over time.

In practice, Ḋ are calculated by combining all contributing components using spreadsheet-based calculations, software tools such as DRAC (Dose Rate and Age Calculator; Durcan et al., 2015) or μRate (Tudyka et al., 2022), functions of luminescence-specific R packages such as the Luminescence package (Kreutzer et al., 2012) or the numOSL package (Peng et al., 2018), or a combination of these tools. Such tools integrate user-defined data on radionuclide concentrations, grain-size-dependent attenuation, a-values, water content, and other correction factors to compute sample-specific Ḋ and their associated uncertainties.

2.2 Alluvial deposits – implications for luminescence dating

2.2.1 Alluvial deposits in the Atacama Desert

Currently, the Atacama Desert is the driest non-polar desert on earth, receiving less than 2 mm of rainfall per year in its hyperarid core (Houston, 2006a). This hyperaridity results primarily from: **i)** the Atacama Deserts location within the sub-tropical high-pressure belt (Houston, 2006a), **ii)** subtropical atmospheric subsidence (e.g. Takahashi and Battisti, 2007a, 2007b), **iii)** temperature inversions driven by coastal upwelling of the cold Peru–Chile Current (Houston, 2006a), **iv)** the combined effects of continental distance from the Atlantic and a rain shadow imposed by the Andes (e.g. Houston and Hartley, 2003), and **v)** high evaporation rates (e.g. Houston, 2006b). As a result, present-day fluvial activity is very limited.

The prevailing hyperarid conditions are ideal to preserve landforms such as alluvial deposits, which are widespread across the Atacama Desert (e.g. Dunai et al., 2005; Evenstar et al., 2017; Haug et al., 2010; Nishiizumi et al., 2005). Some alluvial deposits developed during more humid phases millions of years ago, prior to the onset of the hyperaridity (e.g. Dunai et al., 2005; Evenstar et al., 2017; Rech et al., 2006). While other alluvial deposits preserve a record of episodic sediment transport and deposition under overall hyperarid climatic conditions since the Late Pleistocene (e.g. Bartz et al., 2020b, 2020a; Gayo et al., 2012; Haug et al., 2010; Nester et al., 2007; Walk et al., 2023). Deciphering the complex depositional and post-depositional histories of these sediments is therefore essential for reconstructing landscape evolution and past environmental changes, as well as assessing potential hazards for humans and their infrastructure (e.g. Harvey et al., 2005; Mather and Hartley, 2005). High-resolution

approaches, such as single-grain luminescence dating techniques, offer the potential to distinguish depositional from post-depositional processes and, ideally, to constrain the timing of both (Gliganic et al., 2015).

Climatic variability across the Atacama Desert influences sediment fluxes and the formation of alluvial deposits. Mean annual precipitation (MAP) outside the hyperarid core increases, especially to the south (26° to 29°S) (Navarro-González et al., 2003; Rundel et al., 1991). The limited amount of moisture that reaches the Atacama Desert originates from two main sources (Houston and Hartley, 2003). In the northeast, during the austral summer, northeasterly (monsoonal) airflows deliver convective precipitation from Amazonia (Garreaud, 1999). In contrast, the southwest is influenced by southerly (westerly) airflows, which bring frontal precipitation from extratropical cyclones during winter (Vuille, 1999).

Furthermore, the climatic conditions at the coast differ markedly from the inland. The humidity in coastal areas is generally higher, among other factors due to sea spray, and fog occurs frequently between ~300 and 1000 m a.s.l. (Cereceda et al., 2008a, 2008b, 2002; Schween et al., 2020). Stratocumulus clouds forming above the Pacific move inland, where they collide with the coastal cliff and thereby providing moisture in the form of advection fog, locally referred to as *Camanchaca* (Cereceda et al., 2002). Although MAP increases from north to south up to ~22 mm/a at 27.35 °S, the potential evapotranspiration exceeds 1500 mm/a throughout the entire region (Houston, 2006a; Trabucco and Zomer, 2019). Nevertheless, within the more humid coastal area, vegetation in the form of so called *loma formations* covers ≥50 % of the ground surface within the fog zone and <5 % of the coastal plain (Rundel et al., 1991). Loma formations within the Atacama Desert consist of almost 1400 different plant species (Gonzales et al., 2023). Within the research area in the Paposo transect around 120 different species are present and dominated by *Euphorbia lactiflua* and *Eulychnia iquiquensis*, both reaching heights of >2 m (Rundel et al., 1991).

In addition to regional moisture sources, the El Niño Southern Oscillation (ENSO) and other circulation anomalies might lead to localised intense rainfall and/or higher fog water yields (del Río et al., 2018; Vargas et al., 2006). When the amount of precipitation exceeds the infiltration capacity, surface runoff is generated.

Runoff can induce alluvial erosion as well as alluvial transport of eroded material, and ultimately result in deposition (Wainwright and Bracken, 2011). The recurrence interval of such events is highly variable, ranging from hours to centuries or even longer (Ortega et al., 2019, 2013, 2012; Vargas et al., 2006). In transport-limited systems, such as the studied Paposo transect, the geomorphological impact of such events largely depends on local controls, including slope morphology and channel

connectivity (Aguilar et al., 2020; Bovis and Jakob, 1999; Cabré et al., 2020; Carson and Kirkby, 1972). In transport-limited systems, sediment supply exceeds the transport capacity of runoff events. Consequently, the primary constraint on erosion and transport is the available energy of the runoff flow, rather than the available sediment supply. Given the abundant available sediment in the Paposo transect, the flow energy decreases rapidly, resulting in comparatively short transport and local sediment deposition (Davis, 1938; Mather, 2006).

Alluvial sediments in hyperarid regions are predominantly deposited through debris flows, sheet flows and sheetfloods, as well as hyperconcentrated flows (e.g. Hartley et al., 2005; Hogg, 1982).

Debris flows are sediment-dominated, unsorted mixtures of water, sediment matrix, and coarse clasts, with a water content <30 % (Harvey, 2011). The behaviour of debris flows is controlled by the water-to-matrix-to-clasts ratio and the transported grain sizes. Deposition occurs when the friction of the underlying surface hinders further transport, or when either the landscape gradient and/or the flow volume decreases. Debris flow deposits are usually poorly sorted, matrix supported clasts (Harvey, 2011; Pierson, 1980; Rust, 1977).

In contrast, **sheet flows** and **sheetfloods** are water-dominated, with a water content >60 % (Hogg, 1982; Mather, 2006). Sheetfloods are high-magnitude, turbulent flows, whereas sheet flows are low-magnitude, laminar flows (Hogg, 1982). Deposition occurs when the bed friction becomes too high or when the water depth and/or the landscape gradient decline (Harvey, 2011). Sheet flow and sheetflood deposits are generally more sorted than debris flow deposits and typically result in stratified deposits with a smooth surface topography (Harvey, 2011; Pierson, 1980).

Hyperconcentrated flows have an intermediate water-to-sediment ratio, with sediment contents of 40 % to 70 % and vice versa water contents of 30 % to 60 % (Mather, 2006). Consequently, hyperconcentrated flow deposits are better sorted and more stratified than debris flow deposits but less so than sheetflood or sheet flow deposits (Pierson and Scott, 1985; Wells and Harvey, 1987). During deposition, the water may drain downward, allowing the sediment to move below the surface rather than being deposited in between the clasts at the surface (Harvey, 2011; Wells and Harvey, 1987).

Although steep, confined catchments are generally debris-flow dominated and lower-gradient, larger catchments tend to be fluvially dominated, all three processes may occur simultaneously within a single section of a catchment (Harvey, 2011, 1984; Pierson and Scott, 1985). Moreover, within a single storm event, the water-to-sediment ratio can change rapidly at the same location, generating interbedded and mixed deposits (Cabré et al., 2020; Harvey, 2011; Wells and Harvey, 1987).

The processes responsible for the erosion, transport and deposition of sediments are termed primary processes (Blair and McPherson, 2009). In addition, secondary processes, such as pedogenesis, wind erosion, aeolian deposition, bioturbation, or weathering, affect the surfaces of alluvial deposits (Blair and McPherson, 2009; Harvey, 2011). The occurrence and intensity of these secondary processes are mainly governed by the climatic environment and the time frame considered (Ventra and Clarke, 2018).

Within hyperarid environments the formation of desert pavements constitutes a major secondary process. **Desert pavements** consist of a monolayer of interlocked clasts on top of a comparatively clast free sediment layer (Laity, 2011; McFadden et al., 1987). Their formation involves multiple simultaneous processes: **i)** fine-grained aeolian sediments become trapped between the clasts, **ii)** clast size decreases over time due to weathering, and **iii)** shrinking and swelling of the underlying fine-grained layer gradually transports clasts upward, where they can trap more fine-grained material (e.g. Dietze et al., 2016; Laity, 2011; McFadden et al., 1998, 1987; Ugalde et al., 2020; Wells et al., 1985). Over time, these processes smooth the surface topography, reduce clast sizes, and increases the thickness of the fine-grained layer (McFadden et al., 1998; Wells et al., 1985). Another often found characteristic of desert pavements is the development of desert varnish on the exposed clasts (Laity, 2011; Nash, 2011).

This thesis focuses on two types of alluvial deposits: **alluvial fans** and **ephemeral alluvial feeder channels** that are connected to alluvial fans (Fig. 2.6). Alluvial fans are typically cone-shaped depositional landforms that develop where the catchment slope decreases abruptly, resulting in a significant reduction of stream power (Harvey, 2011). Along the coast of the Atacama Desert, alluvial fans commonly occur side by side, merging to form extensive bajadas (Walk et al., 2020). In contrast, within the Coastal Cordillera, alluvial fans are typically smaller due to their overall smaller catchment sizes and lower gradients (Blair and McPherson, 2009; Lehmkuhl and Owen, 2024; Sun et al., 2023).

A typical alluvial fan consists of a feeder channel, an apex, and a depositional lobe (e.g. Blair and McPherson, 2009; Fig. 2.6). If a subsequent phase of alluvial activity occurs after the initial construction of a fan, earlier deposits may be incised downstream of the apex, and multiple generations of deposition and incision may be present within a single fan system.

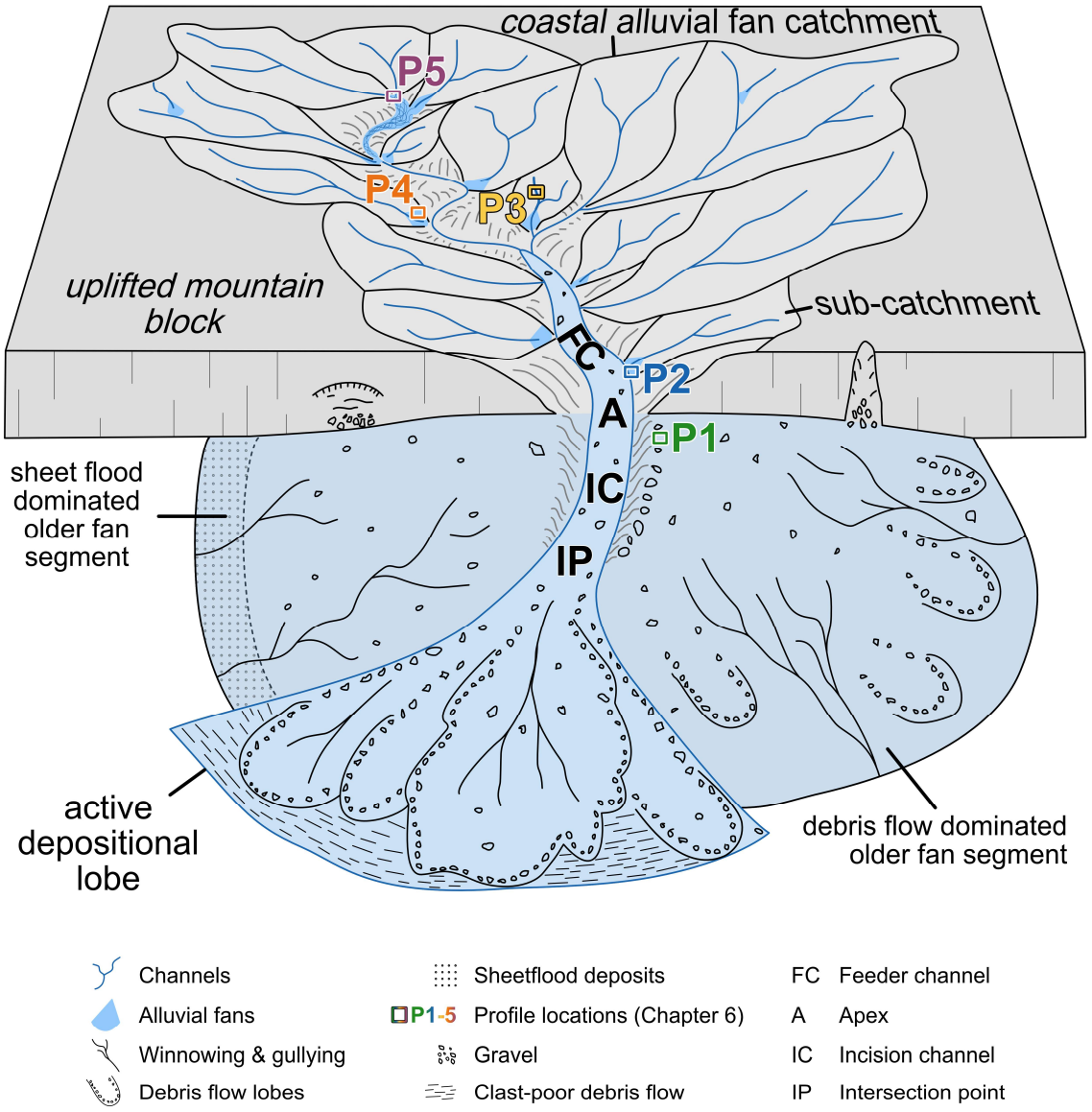

Fig. 2.6: *Schematic structure of an alluvial fan system in the Atacama Desert (modified from Walk, 2020, after Blair and McPherson, 2009). The sampling location of alluvial fans and ephemeral channels (Chapter 6) are indicated by coloured boxes and profile names (P1–P5). The abandoned left segment of the terminal alluvial fan is dominated by sheet floods, whereas the right abandoned segment and the active depositional lobe are dominated by debris flows.*

In this thesis, three alluvial fans were sampled: one located in the coastal plain and two within the Coastal Cordillera. The coastal plain alluvial fan is the largest, exhibiting several distinct depositional generations and incised channels (sampling location **P1**, Fig. 2.6). One of the Coastal Cordillera fans lies within the fog occurrence zone and displays less prominent generations (sampling location **P2**, Fig. 2.6). The second Coastal Cordillera fan is situated above the fog occurrence zone, featuring two distinct generations and a deeply (>1 m) incised channel in the younger generation of the fan (sampling location **P4**, Fig. 2.6).

In addition to the three alluvial fans, two ephemeral channels from the same catchment were sampled. The two channels are located at different topographic positions relative to their respective alluvial fan. The first is part of a ~1 km long

secondary feeder channel that confluences into a wider feeder channel ~200 m upstream of the lobe of a small alluvial fan (sampling location **P3**, Fig. 2.6). The second is part of the main drainage channel of the catchment, which ultimately feeds the coastal plain alluvial fan ~24 km downstream (sampling location **P5**, Fig. 2.6). The sampling site is located at the confluence of several braided ephemeral channels on a ~450 m wide plain. Downstream, the braided channels narrow down to a width of ~100 m within a distance of 500 m and further to a width of ~10 m within a distance of 1.5 km in respect to the analysed section.

Further details on the individual deposits and their local geomorphic settings are provided in Chapter 6 and its supplementary material in Appendix C-III.

2.2.2 Luminescence dating of alluvial deposits in the Atacama Desert

Luminescence dating of alluvial deposition or post-depositional processes in alluvial deposits is challenging due to heterogeneous bleaching during transport and deposition (Duller, 2008b; Gliganic et al., 2015; Wallinga, 2002). Heterogeneous bleaching refers to incomplete resetting of luminescence signals, which occurs to varying degrees among grains within one sample (Duller, 1994; "Type B" sediments). In alluvial deposits, heterogeneous bleaching is caused by the depositional process. In debris flows, the water content is low (<30 %), and sediment grains are transported in a dense mixture in which individual grains are frequently shielded from sunlight by other sediment particles or larger clasts (Berger and Leuternauer, 1987; Harvey, 2011; Rittenour, 2008). Even in hyperconcentrated flows, sheet flows, and sheetfloods, where water contents are higher and the flow is less dense, the turbulent flow characteristic and typically short transport distances often prevent sufficient light exposure of individual grains (Berger and Leuternauer, 1987; Mather, 2006; Rittenour, 2008). In all four settings, the involved water is further shielding light, yet the suspended load is the primary cause of insufficient light exposure (Berger, 1990; Ditlefsen, 1992). As a result, alluvial deposits can contain a mixture of three grain types: **i)** fully bleached grains, **ii)** unbleached grains, and **iii)** partially bleached grains with varying degrees of signal resetting (e.g. Duller, 2008b, 1994; Wallinga, 2002).

In a hypothetical scenario, if all grains had a D_e of 150 Gy prior to alluvial transport and deposition, heterogeneous bleaching could result in a grain population consisting of: a fraction with a D_e of ~0 Gy (fully bleached), a fraction retaining the original D_e of ~150 Gy (unbleached), and a fraction with intermediate D_e values between 0 and 150 Gy (partially bleached) (Fig. 2.7).

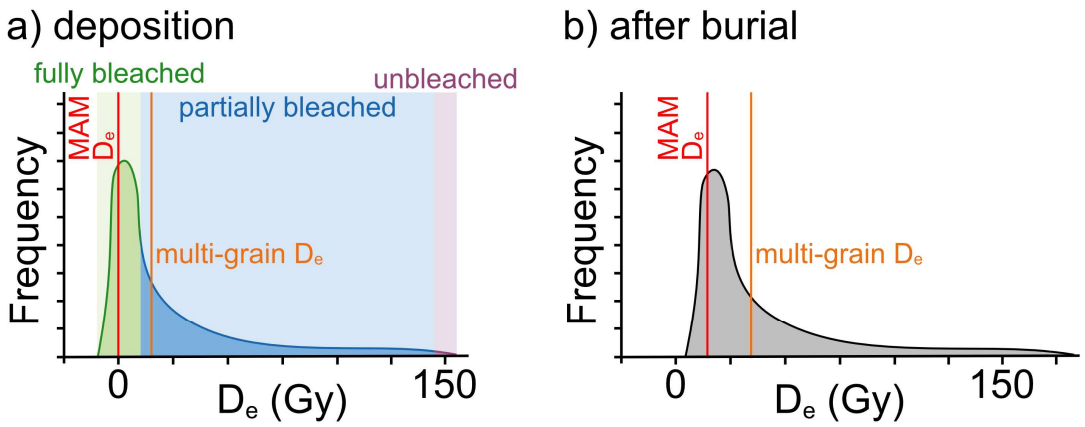

Fig. 2.7: *Single-grain D_e distribution of a hypothetical heterogeneous bleached sample:* ***a)*** *at time of burial, and* ***b)*** *after a period of burial.* ***a)*** ***Fully bleached*** *grains, exposed to sufficient sunlight prior to deposition, have a D_e around 0 Gy (green section).* ***Partially bleached*** *grains, which experienced limited sunlight exposure, have intermediate D_e values (blue section).* ***Unbleached*** *grains, completely shielded from sunlight, retain their original D_e of 150 Gy (purple section).* ***a, b)*** *The red line indicates the* ***MAM D_e*** *calculated based on single-grains. The orange line shows a theoretical D_e of a* ***multi-grain measurement*** *of the sample.* ***Note:*** *The peak of the distribution is slightly above 0 Gy because grains often retain a small residual dose even after adequate light exposure (e.g. Buylaert et al., 2009; Reimann et al., 2011). During the D_e calculations, each signal is background-corrected (signal – background). In cases where the net luminescence signal approaches zero, background noise can exceed the measured signal, resulting in small negative D_e values (e.g. Arnold et al., 2009; Galbraith and Roberts, 2012). After burial, microdosimetric effects cause a broadening of the D_e distribution (e.g. Murray and Roberts, 1997; Nathan et al., 2003; Olley et al., 1997).*

Fig. 2.7 illustrates how age estimates are influenced by heterogeneous bleaching. In the example presented, age estimates based on multi-grain measurements would lead to an overestimation of the true burial age, as they contain grains from all three fractions (fully bleached, partially bleached, and unbleached) (e.g. Duller, 2008b; Olley et al., 1999). In contrast, single-grain measurements would enable the identification of the youngest grain population (e.g. Duller, 2008b; Olley et al., 1999; Page et al., 2007). Statistical dose models, such as the MAM, are able to isolate this youngest grain population, which often represents the burial dose of a sample (Galbraith et al., 1999; Galbraith and Roberts, 2012).

In addition to the typical D_e distribution expected for heterogeneously bleached samples (Fig. 2.7), further characteristic shapes may occur in alluvial deposits (Fig. 2.8). The shape of single-grain D_e distributions can provide additional insights into the depositional and post-depositional history of a sample beyond simply identifying the youngest population as an indicator for burial (e.g. Bateman et al., 2003). Especially if local factors, such as climate, geomorphology, and stratigraphy, are considered, the shape of the D_e distributions may reveal characteristic patterns associated with specific processes (cf. Chapter 6.5).

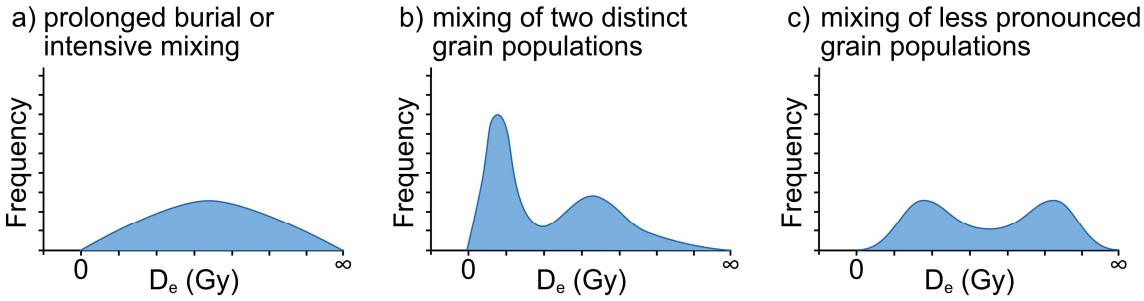

Fig. 2.8: *Hypothetical single-grain D_e distributions of samples in alluvial deposits within the Atacama Desert, illustrating different depositional and post-depositional scenarios.* ***a)*** *Unimodal broad distribution, potentially resulting from either prolonged burial, intensive mixing or a combination of both processes.* ***b)*** *Bimodal distribution with one dominant and one minor peak, typical of mixing between two distinct D_e populations.* ***c)*** *Bimodal distribution with broad, less pronounced peaks, characteristic of mixing between two less distinct D_e populations. Modified after Bateman et al. (2003).*

For instance, a sample with a broad unimodal distribution (Fig. 2.8a) in the fog-influenced zone of the Coastal Cordillera may be the result of intensive post-depositional mixing driven by bioturbation. In contrast, a similar shaped distribution in the hyperarid Coastal Cordillera, where vegetation is absent, may instead reflect prolonged burial with only minimal post-depositional disturbance. Likewise, in profiles affected by mixing (Fig. 2.8b, c), low D_e grains may not represent the burial age, but might be the effect of post-depositional transport of grains from the surface down to the sampled depth (Bateman et al., 2007).

Besides the evaluation of the distributions shape, further luminescence-based proxies were developed to quantify mixing processes. Single-grain luminescence dating has thereby become a valuable tool for tracing soil mixing processes in more humid regions with active geomorphic and pedogenic processes (e.g. Heimsath et al., 2002; Reimann et al., 2017; van Der Meij et al., 2025). Within this thesis, two soil- and sediment-mixing proxies based on single-grain luminescence are applied: *zero-dose grains* (Bateman et al., 2007) and *saturated grains* (Reimann et al., 2017). The **zero-dose grains** proxy is defined as the fraction of grains in a sample with a D_e indistinguishable from 0 Gy (Bateman et al., 2007). This fraction is used as an indicator of how many grains were transported from the surface down to the sampled depth. In this thesis, the original approach is modified to account for the residual dose typically observed in surface samples in the Atacama Desert (Chapter 6.3.3). Grains with a D_e equal to or lower than the MAM D_e of all surface samples (≤2.24 Gy) are classified as zero-dose grains. However, in recently deposited sediments the zero-dose grain fraction might only record the fraction of fully bleached grains during deposition, and not post-depositional mixing. Conversely, the **saturated grains** proxy is defined as the fraction of grains in a sample with a D_e in saturation (Reimann et al., 2017). This proxy is typically interpreted as indicating upward transport of grains. The saturated grains either originate from weathering bedrock at the base of the deposition or from

deposits older than the luminescence dating range. However, in the studied Late Pleistocene to Holocene alluvial deposits, their interpretive value is likely limited, as bedrock weathering beneath the analysed profiles is minimal and deeper depositional units may not have reached saturation.

While heterogeneous bleaching and post-depositional mixing pose significant challenges, luminescence dating in the Atacama Desert is further complicated by the available minerals themselves (cf. Chapters 1.3, 3, and 4). Quartz exhibits extremely low sensitivity and unstable signal components and is therefore excluded from this thesis (Bartz et al., 2020a, 2020b; del Río et al., 2019; May et al., 2015; Veit et al., 2015; Zinelabedin et al., 2022). Atacama Desert feldspars possess complex geochemical compositions (Chapter 3), making dose rate determinations intricate (Chapter 4). Additionally, only a small proportion of grains is giving suitable luminescence signals (~1 %; Zinelabedin et al., 2022).

Consequently, the analysis of complex alluvial deposits, affected by heterogeneous bleaching, multiple phases of deposition, and post-depositional reworking, requires a multi-method approach to reconstruct grain histories. Single-grain luminescence D_e distributions, dose model outputs, and derived luminescence proxies should be accompanied by geomorphological observations, geochemical analysis, granulometric data, and, where possible, further independent dating methods. Special precaution must also be taken during the $\dot{D}$ determination of the geochemical complex feldspars. When applied within such a framework, single-grain feldspar luminescence dating can be a powerful tool for deciphering the complex depositional and post-depositional histories of alluvial deposits in the hyperarid Atacama Desert.

Chapter 3

Testing the applicability of standardised growth curves (SGC) for chemically heterogeneous single-grain feldspars from the Atacama Desert, Chile

Linda A.E. Maßon[1*], Svenja Riedesel[1,2], Anja Zander[1], Mariana Sontag-González[3,4], Tony Reimann[1]

[1] Institute of Geography, University of Cologne, Germany
[2] Luminescence Physics and Technologies, Department of Physics, Technical University of Denmark, Denmark
[3] Institute of Geography, Justus-Liebig-University Gießen, Germany
[4] Department of Geosciences, Stony Brook University, NY 11794-2100, USA

Quaternary Geochronology 83 (2024) 101585
https://doi.org/10.1016/j.quageo.2024.101585

As outlined in Chapter 1.3, single-grain luminescence dating of feldspars from the Atacama Desert poses multiple challenges. In particular, typically only a small fraction of grains (~1 %) yields suitable luminescence signals for D_e estimation, and the grains exhibit considerable geochemical heterogeneity (Zinelabedin et al., 2022). The low number of suitable grains results in time-consuming measurements, and the geochemical heterogeneity may affect the internal dose rate calculations, and thereby the accuracy of luminescence ages, if the internal K-concentrations are not measured.

To achieve the overall aim of this thesis, which is to constrain chronologies of soil and surface process at high spatial and temporal resolution, it is necessary to improve both the efficiency and the reliability of single-grain feldspar luminescence dating. The following chapter addresses the efficiency issue by evaluating the applicability of the standardised growth curve (SGC) approach to feldspar samples from the Atacama Desert. The primary objective is to reduce measurement time while maintaining robust D_e estimates. In addition to Atacama Desert samples, a comparative dataset of feldspar separates from diverse geological and geographical settings was included in the study. This additional dataset was used to test whether an SGC constructed using non-Atacama Desert samples can yield reliable results when applied to Atacama Desert feldspars. If successful, this would provide a more practical and transferable protocol for future research.

Furthermore, the reliability issue is addresses through geochemical analyses at the single-grain level. These measurements were conducted to investigate potential correlations between elemental composition, particularly K-concentration, and luminescence properties such as signal intensity, D_e values, and dose recovery ratios. The purpose of these analysis is to assess whether the observed geochemical heterogeneity affects the suitability of feldspar grains for luminescence dating and whether it necessitates additional grain- or sample-specific considerations during internal dose rate calculations or the interpretation of luminescence data.

For a detailed statement on the contribution of the co-authors to the final manuscript, the reader is referred to the original text (Chapter 3.8). Linda Maßon contributed ~80% to the final publication (data acquisition – 75%; analysis and interpretation – 80%; visualisation – 95 %; manuscript writing – 70%).

Formatting and orthography of the publication are adapted to the dissertation style

Abstract

The Atacama Desert is generally considered the driest non-polar desert on Earth and is therefore an ideal study area for exploring the water and biota free endmember of Earth's Critical Zone (ECZ). Single-grain luminescence dating has successfully identified processes in the ECZ. However, single-grain luminescence dating of Atacama Desert feldspars is challenging and time consuming since only a small fraction of grains emits sufficient luminescence and their potassium (K) concentrations, needed for internal dose rate calculations, are highly variable. Here we present an adaption of the standardised growth curve (SGC) method adjusted to the conditions of Atacama Desert sediments and a correlation of single-grain geochemistry and luminescence properties.

To evaluate if SGCs are suitable for our study site and to determine the influence of the K-concentration on our luminescence age calculations, we used a set of five samples from the Atacama Desert and five chemically and structurally different feldspar sediment extracts from various geological origins worldwide. We performed a dose recovery test (DRT) using a post-infrared infrared stimulated luminescence (pIRIR) protocol and measured nine major element concentrations, including K, on a single-grain level using a scanning electron microscope (SEM) with energy-dispersive X-ray spectroscopy (EDX). The DRT dataset was then used to test the application of SGCs. The accuracy of Atacama Desert feldspar pIRIR measurements fitted onto SGCs frequently suffers from odd values in single measurement cycles, since the SGC approach developed for single-grain feldspar luminescence (Li et al., 2015b) uses one L_x/T_x measurement to project the L_n/T_n values onto an SGC. We investigate the influence of calculating a synthetic regenerative signal (sR) for SGC fitting, to reduce the effect of those odd values on individual grain measurements. Furthermore, we reduced the regenerative cycles (rc) used for our sR approach, to test if shorter protocols would result in equivalent dose (D_e) estimates in agreement with longer protocols. We then calculated Spearman rank correlations between the results obtained with our modified SGC and the SAR protocol, luminescence signal intensities, and the geochemical dataset.

Finally, we present a new method of fitting data onto an SGC which significantly decreases measurement time, without risking the inclusion of outliers. We furthermore show that the luminescence signal intensities, the D_e values and their dose recovery ratios obtained with our SGC method and a SAR protocol, are independent of the sample geochemistry.

3.1 Introduction

In the recent past the interrelationship of life and the evolution of Earth's surface has been subject to intensified research activities (e.g. Amundson et al., 2007; Starke et al., 2020). The outermost shell of our planet, in which rocks, soils, water, air and biota interact and thus where this interrelationship takes place, is often referred to as the Earth's Critical Zone (ECZ) (Giardino and Houser, 2015). The Atacama Desert in Chile, generally considered the driest non-polar desert on Earth, is an ideal study site to explore the dynamics of the water and biota free endmember of ECZ systems (e.g. Dietrich and Perron, 2006; Oeser et al., 2018; Tchakerian and Pease, 2015).

Single-grain luminescence dating has successfully been applied to infer sediment transport and mixing processes in the ECZ in various geological settings dissimilar to the Atacama Desert (Bonnet et al., 2019; Reimann et al., 2017; Román-Sánchez et al., 2019a, b). So far, optically stimulated luminescence (OSL) measurements carried out in the Atacama Desert were merely designed to determine the depositional age of sediments (e.g. Bartz et al., 2020a, b; Del Río et al., 2019; Diederich et al., 2020; May et al., 2020, 2015; Ritter et al., 2019; Veit et al., 2015) and dynamics inside a calcium sulphate wedge (Zinelabedin et al., 2022). Those studies revealed the unfavourable properties of Atacama Desert sediments especially regarding quartz OSL measurements. Quartz from the Atacama Desert has been shown to have a very low OSL sensitivity and unstable signal components (Bartz et al., 2020a; Del Río et al., 2019; May et al., 2015; Veit et al., 2015; Zinelabedin et al., 2022). Furthermore, a previous study on the applicability of luminescence dating of coarse grain feldspars from the Atacama Desert found highly variable potassium (K) concentrations within each sample and merely ~1 % of the measured feldspar grains gave a post-infrared infrared stimulated luminescence (pIRIR) signal suitable for dating (Zinelabedin et al., 2022). The heterogeneity of K-concentrations in feldspars poses a challenge in calculating internal dose rates and raises the question of whether the chemical composition of feldspars is related to luminescence properties.

Problematic quartz OSL properties have been reported previously and have been associated with the quartz source area (e.g. Bartz et al., 2020a; Sawakuchi et al., 2011; Tokuyasu et al., 2010), the depositional context of the sample (e.g. Fitzsimmons et al., 2010; Li and Wintle, 1992) or too few reworking cycles (e.g. Sawakuchi et al., 2011; Steffen et al., 2009). In some cases, coping strategies have been developed (Fuchs and Owen, 2008, Sawakuchi et al., 2011). So far, due to its unfavourable OSL properties, quartz has been discarded for luminescence dating of Atacama Desert sediments (e.g. Bartz et al., 2020a; Zinelabedin et al., 2022). Considerably fewer studies have addressed problematic feldspars. Single-grain measurements of feldspars can be challenging

and time-consuming, particularly when only a small percentage of grains emits suitable luminescence signals (e.g. Brill et al., 2018; O'Gorman et al., 2021b; Sontag-González et al., 2021; Zinelabedin et al., 2022). In such cases many single grain (SG) discs have to be measured before a sufficient number of grains has been obtained to calculate a robust palaeodose. This can result in such samples not being investigated further (Brill et al., 2018). Establishing a standardised growth curve (SGC) for single-grain feldspar pIRIR measurements reduces the measurement time considerably (Li et al., 2018). Sontag-González et al. (2021) showed that SGCs are also suitable for feldspars with unfavourable luminescence properties and a complex mineralogy.

Atacama Desert feldspars studied so far show highly variable K-concentrations with on average low K-concentrations (Zinelabedin et al., 2022). It is generally considered that a feldspar grain giving a luminescence signal has a K-concentration in the range of 8 to 13 % (12.5 ± 0.5 % Huntley and Baril, 1997 or 10 ± 2 % Smedley et al., 2012). Furthermore, Prescott and Fox (1993) (thermoluminescence) and Spooner (1992) (infrared stimulated luminescence) presented data for the whole composition range of the feldspar mineral group, showing a positive correlation of K-concentrations and signal intensity. In contrary, O'Gorman et al. (2021b) and Zinelabedin et al. (2022) not only showed that grains with lower K-concentrations may emit suitable pIRIR signals but also that the majority of grains in a sample, which are used for D_e calculations, may have K-concentrations much below the proposed literature values (<3 % and 3.9 ± 1 % respectively). Moreover Smedley et al. (2012) found no correlation between K-concentration and signal intensity on a single-grain level. In agreement with that Finch and Klein (1999) as well as Riedesel et al. (2021) proposed a different source for signal intensity levels in the blue emission by linking them to Al-O-Al bridges, whereas Garcia-Guinea et al. (1999) connected signal intensity to alkali ion leakages caused by prolonged heating. This raises the question of whether, in the case of Atacama Desert feldspars, single-grain K-concentrations have to be determined for dose rate calculation and if correlations exist between the chemical composition of the feldspars and their luminescence properties.

In this study we aim to establish a methodological framework for time-efficient single-grain luminescence-based analysis of feldspar samples from the Atacama Desert. We use a test dataset consisting of ten samples, five from the Atacama Desert and five chemically and structurally different feldspar sediment extracts from various geological origins from around the world. A dose recovery test ($pIRIR_{175}$) is performed on 500 grains per sample and the geochemistry of 300 out of the 500 grains is determined using a scanning electron microscope (SEM) equipped with an energy-dispersive X-ray spectrometer (EDX). With this dataset we test the applicability of SGCs for single-grain pIRIR equivalent dose (D_e) determination of Atacama Desert

feldspars, in order to reduce our measurement times and we use Spearman rank correlations to investigate the influence of geochemistry on luminescence properties and SGC performance.

3.2 Samples and instrumentation

3.2.1 Samples

Our sample suite consists of ten samples of different origin and chemical composition. Five samples (ARO-18-08-LP, CSA-1-2-2, LAGU-1-1, PAG-6-4b, PAG-6-6b) originate from the Atacama Desert. The remaining five samples originate from badlands in Canada (ABLR-1), lake sediments in Japan (HAM-5), a beach ridge in Chile ~1000 km south of the Atacama Desert (ISM-7), the Continental Deep Drilling (KTB) borehole in Germany (KTB-383-C) and the Mont-Blanc tunnel in Italy (MBT-I-2430). We chose the non-Atacama Desert samples to reflect a range of chemical and structural variations of feldspar. Basic information on the samples are summarised in Table 3.1.

Prior to luminescence measurements the samples were sieved and treated with HCl (10 %), H_2O_2 (10 %) and $Na_2C_2O_4$ (0.01 N), to remove carbonates and organics and to disperse the particles, respectively. Subsequently, samples were sieved again to obtain different grain size fractions (Table 3.1). A heavy liquid density separation was used to enrich the K-rich feldspar fraction (ρ <2.58 g/cm^3). Sample KTB-383-C feldspars were etched with HF afterwards (see Guralnik et al. (2015) for further details).

Table 3.1: *Sample description. Sample KTB-383-C was prepared in the laboratory of the University of Lausanne. Sample MBT-I-2430 was prepared at DTU-Risø. All other samples were prepared at the Cologne Luminescence Laboratory.*

Sample ID	Origin and subset affiliation	Coordinates		Grain size [µm]	Grain hole size [µm]	References
ARO-18-08 LP	Atacama Desert, Chile (A)	19°39'34.02" S	69°35'51.4" W	200 – 250	300	Zinelabedin et al., 2022
CSA-1-2-2	Atacama Desert, Chile (A)	19°36'20.17" S	70°5'52.12" W	100 – 200	250	This study
LAGU-1-1	Atacama Desert, Chile (A)	21°1'59.37" S	69°47'53.00" W	100 – 250	300	This study
PAG-6-4b	Atacama Desert, Chile (A)	21°32'31.7" S	69°54'47.9" W	100 – 200	250	Ritter et al., 2019
PAG-6-6b	Atacama Desert, Chile (A)	21°32'31.7" S	69°54'47.9" W	100 – 200	250	Ritter et al., 2019
ABLR-1	Badlands, Canada (X)	50°1'30.6" N	104°59'15.81" W	100 – 200	250	This study
HAM-5	Lake Hamana, Japan (X)	34°45'8.65" N	137°34'22.62" E	100 – 200	250	Riedesel et al., 2021, 2019
ISM-7	Beach ridge, Chile (X)	37°1'20.28" S	73°30'43.49" W	100 – 200	250	This study
KTB-383-C	KTB Borehole, Germany (X)	49°48'55" N	12°7'14" W	180 – 250	250	Guralnik et al., 2015
MBT-I-2430	Mount Blanc Tunnel, Italy (X)	45°50’07” N	6°55’59”E	180 – 212	250	Lambert, 2018

3.2.2 Luminescence

For the dose recovery tests the samples were loaded into standard single-grain discs under a microscope under daylight conditions, for grain hole sizes used see Table 3.1. A single hair was used to pick the grains ensuring that all 100 holes per disc were filled with one grain each. Despite this, for the samples CSA-1-2-2, HAM-5 and KTB-383-C it was sometimes unavoidable to have several grains in one hole. Prior to the dose recovery test, all mounted grains were bleached in a SOL2 solar simulator for 24 h.

An automated Risø TL/OSL-DA-20 reader equipped with a $^{90}Sr/^{90}Y$ beta source for irradiation, delivering a dose rate of ~0.08 Gy/s, was used for all luminescence measurements. A 150 mW 830 nm centred IR laser stimulated the grains, and the blue emission (~410 nm) was detected through a combination of two 2 mm Schott BG-39 filters and a 3 mm Corning 7-59 glass filter. A dose-rate map (Lapp et al., 2012), created by using radiosensitive film (GAFCHROMIC EBT2), showed a dose uniformity across the sample area of ~4.5 %. It is thus not expected to significantly contribute to the received doses of each grain. A dose recovery test (DRT, given dose = 150 Gy) was carried out employing a pIRIR protocol (Thomsen et al., 2008) with a preheat of 200 °C for 60 s and a pIRIR stimulation temperature of 175 °C (Madsen et al., 2011; Reimann et al., 2011). The IR_{50} and $pIRIR_{175}$ measurement times were 2 s and 3 s, respectively. For further details on the single-aliquot regenerative-dose (SAR) DRT protocol used see Table 3.2 (Reimann et al., 2017). All measurements were performed as dose recovery test using a given dose of 150 Gy. This allowed for direct comparison between the luminescence response of the samples. Furthermore, given the curvature of the dose response curve of the different samples, a dose of 150 Gy allowed for investigating the performance of the SGC in the non-linear, but non-saturation, part of the dose response curve.

Table 3.2: *Single-grain dose recovery test SAR measurement protocol. Heating rate for steps 2-4 and 6-8 2 °C/s.*

Step	Treatment[a]	Observation
1	Given dose D_i	
2	Preheat, 60s at 200°C	
3	IRSL, 2s at 50°C	
4	IRSL, 3s at 175°C	L_x
5	Given test dose D_t	
6	Preheat, 60s at 200°C	
7	IRSL, 2s at 50°C	
8	IRSL, 3s at 175°C	T_x
9	Return to step 1	

[a] given dose D_i [Gy]: 150, 0, 50, 150, 300, 500, 800, 0, 50, 150; test dose D_t [Gy]: 50

For signal integration the first 0.2 s minus a background of the last 0.4 s of stimulation was used. Five discs à 100 grains were measured per sample.

All D_e estimates and SGCs were derived using the numOSL R package (Peng et al., 2018) and the least-squares (LS)-normalisation approach following Li et al. (2016). A measurement error for the regenerative dose signal (L_x) and the corresponding test dose signal (T_x) of 2 % was used for calculations. Parameters used for growth curve fitting were: "exponential model", "not forced through origin" and "using a weighted procedure". Rejection criteria for the SAR and SGC approaches were as follows: test dose signal following natural dose measurement (T_n) >3σ above background, relative standard error (RSE) of T_n ≤25 %, recycling ratio = unity ± 10 % for all available recycling points, recuperation ≤10 % of the natural signal, recuperation ≤10 % of the maximum regenerative-dose signal, figure-of-merits (FOM) ≤10 % (Peng and Li, 2017), reduced chi square ≤10 %. The numOSL R package uses the recycling ratio ± two times the standard error to check if the recycling ratio is within unity ± 10 %. The FOM, a measure of goodness-of-fit, is calculated as follows: $\mathrm{FOM} = \sum|y_i^o - y_i^f| / \sum y_i^f * 100$ (Balian and Eddy, 1977). D_e with a RSE above 50 % were rejected after their calculation. A dose value of 150 Gy was used for SAR dataset re-normalisation in the pickSARdata() function.

3.2.3 Geochemistry (SEM-EDX)

Following the luminescence measurements double-sided sticky tape, on one side attached to a glass microscope slide, was placed on the top side of the SG discs. The undersides of the SG discs were lightly tapped with a piezoelectric ultrasonic cleaner (vibration frequency 30 ± 3 kHz) to transfer the grains onto the tape. About 80 % of the grains were extracted on average. Prior to disc removal from the tape the location of the disc position holes was marked on the tape. Subsequently the grains were embedded in colourless two-component epoxy resin (Araldit 2020, Huntsman), with position hole placement marked on the epoxy discs. The surfaces of the epoxy discs were sanded with a 1200 SiO_2 sandpaper and polished to ensure that no epoxy covers the grains.

The major element chemistry of individual grains was determined on a Zeiss Sigma 300-VP scanning electron microscope (SEM) with an energy dispersive spectroscopy (EDX) attachment. The working distance was set to 8.5 mm. The aperture diameter of 60 µm and an accelerating voltage of 20 kV resulted in an output count rate of ~45,000 cps. The chemical composition of individual feldspar grains was calculated based on the nine elements O, Na, Mg, Al, Si, K, Ca, Ti and Fe through stoichiometry.

Three out of five discs per sample were measured for their geochemical composition. For the samples ISM-7, LAGU-1-1 and MBT-I-2430 two discs were analysed.

3.2.4 Statistic

For data comparison Spearman rank correlations were used (Spearman, 1904), since they are nonparametric correlations and therefore less susceptible to outliers (Kendall et al., 1939; Zar, 2005). The results of a Spearman rank correlation, the Spearman's rank correlation coefficient (r_s), can range between -1 and 1, with -1 being a perfect negative correlation and 1 a perfect positive correlation. The closer the r_s value is to zero, the weaker the correlation. As there is no universally valid definition, we here define correlations with r_s values between 0 and ± 0.2 as very weak, between ± 0.2 and ± 0.4 weak, between ± 0.4 and ± 0.6 moderate, between ± 0.6 and ± 0.8 moderate to strong and between ± 0.8 and ± 1 strong. The significance of a correlation was tested using the cor.mtest() function of the corrplot() package (Wei and Simko, 2023). This test results in p-values for each correlation pair. If the p-value is >0.05, the correlation is not significant. Spearman rank correlations have the disadvantage that they do not take uncertainties of individual values into account. Nevertheless, we think that this does not affect our conclusions.

All errors given here for D_e values correspond to one standard deviation. Presented arithmetic means are always given with the corresponding standard error.

3.3 Standardised growth curve (SGC) application and modification

3.3.1 SAR and SGC

3.3.1.1 Procedure

To test the applicability of the SGC approach, first the dose response properties using the standard SAR approach were assessed. For further analysis the dataset was divided into two subsets, Atacama Desert (A) and external (X) samples (cf. Table 3.1). For each subset A and X one SGC was calculated using the numOSL R package and the rejection criteria mentioned in Chapter 3.2.2. Since the Atacama Desert samples are of main interest for this research, the SGC for subset A is hereafter called SGC. The SGC for subset X is referred to as xSGC and only used for direct comparison between SAR and SGC D_e values of dataset X to check its validity. The xSGC will be used in following sections for D_e calculation of grains from dataset A (see Fig. 3.1).

Following Li et al. (2015a) two SAR cycles are needed for the D_e calculation using an existing SGC. Besides the “natural” cycle (L_n/T_n), an additional regenerative cycle with a regenerative dose D_{r1} is required for the projection onto the existing SGC. According

to Li et al. (2015a) the size of D_{r1} should be close to the expected size of the D_e. Our expected dose is 150 Gy, which equals the regenerative dose of regenerative cycles R3 or R9. Unfortunately, the L_x/T_x values of regenerative cycles R3 and R9 of accepted grains often showed large deviations from the fitted growth curves of up to 44 % (see Fig. 3.2). Consequently, we decided to use regenerative cycle R8 (50 Gy) as D_{r1}.

3.3.1.2 Results & discussion

When using the standard SAR approach 657 grains out of 5000 analysed grains (13.1 %) passed the rejection criteria and resulted in a D_e. Most of the grains (56.7 %) were rejected due to T_n signals below 3σ above background. Another 15.6 % were rejected based on poorly-fitted growth curves and 11.6 % were rejected for a T_n with a RSE >25 %. Three additional grains were rejected due to their D_e value having a RSE >50 %. For details on rejected grains see Appendix A Table A1. The mean of the remaining 643 D_e values was 128 ± 1.42 Gy, which corresponds to a dose recovery ratio (DRR) of 0.85 ± 0.01. MBT-I-2430 was the sample giving the most D_e values (309 grains ≈ 47.2 %) and PAG-6-4b the one with the least (1 grain = 0.15 %).

From the Atacama Desert samples (subset A) merely 88 out of 2500 grains were accepted resulting in 87 D_e. Whereas from the external samples (subset X) 558 out of 2500 grains were accepted resulting in 556 D_e values. In each subset one sample was dominating the following results. In subset A grains from sample LAGU-1-1 make up 71.3 % of the total number of accepted grains. While in subset X 54.7 % of the accepted grains were from sample MBT-I-2430. The DRR of 0.89 ± 0.02 for subset A was slightly better than for subset X with a DRR of 0.85 ± 0.01. The generally observed underestimation of the given dose could be due to the protocol not being suitable for all samples. We also considered changes in sensitivity during the first measurement cycle (see Kars et al., 2014), but we could not find any indication for this (data not shown). Further investigations of the underestimation were not within the scope of this study.

The Atacama Desert samples are of main interest for this research, thus only D_e calculations for subset A are discussed in the following sections. Since the rejection criteria for the SAR and SGC methods were the same, 88 grains from subset A were used for the SGC construction and subsequent D_e calculation using the constructed SGCs. The LS-normalisation reduced the scatter between the grains in dataset A (see Appendix A Fig. A1). The D_e calculation with the SGC was possible for 87 out of 88 grains. The DRR of the remaining SGC-acquired D_e values was 0.84 ± 0.03. For further details on D_e distributions Abanico plots are provided in Appendix A Fig. A2. The overdispersion within the dose recovery D_e distribution calculated with the SAR

approach and the SGC method was 19.4 ±2.4 % and 19.6 ±2.4 % respectively, which is in a typical range for single-grain pIRIR measurements (Brill et al., 2018; Reimann et al., 2012).

It has been shown that the validity of the SGC can be tested by comparing the SAR and SGC D_e values ± their 2σ standard error, which should be in unity (e.g. Li et al., 2015a, b; Sontag-González et al., 2021). For 86 grains D_e values were calculated with both methods and were used for the comparison. All 86 grains were in unity at 2σ, therefore the SGC can be regarded as reliable.

When reporting luminescence ages, the 1σ standard error is commonly used (Mahan et al., 2022). The D_e values showed average RSEs of ~16 %, therefore the agreement within 1σ seems inappropriate to evaluate the precision between the SAR procedure and the SGC method. Therefore, we focus on the number of grains differing less than ± 10 % in their calculated D_e values (Fig. 3.1A) and on Spearman rank correlations.

Of the 86 comparable grains, 41 D_e values did not differ more than ± 10 %, 37 additional grains had indistinguishable D_e values at 1σ and 8 additional grains exhibited D_e values within 2σ. SAR and SGC results correlate with a r_s of 0.81, which can be regarded as the lower limit of a strong correlation.

Comparing the SGC and SAR D_e values, all 86 grains yielding a D_e value with the standard SAR procedure and the SGC approach are in unity within 2σ. However, only a low number of these grains yield D_e values with a good precision. There are several reasons why the SGC approach estimates D_e values which do not agree within ± 10 % with the SAR method. Firstly, the dataset for constructing the SGC is very small (n = 88). Secondly, even though D_{r1} was chosen to reduce the influence of odd L_x/T_x values, some L_{r1}/T_{r1} still showed deviation from the growth curve of up to 35 %. Thirdly, the overall large RSE of the dataset indicates poor luminescence properties.

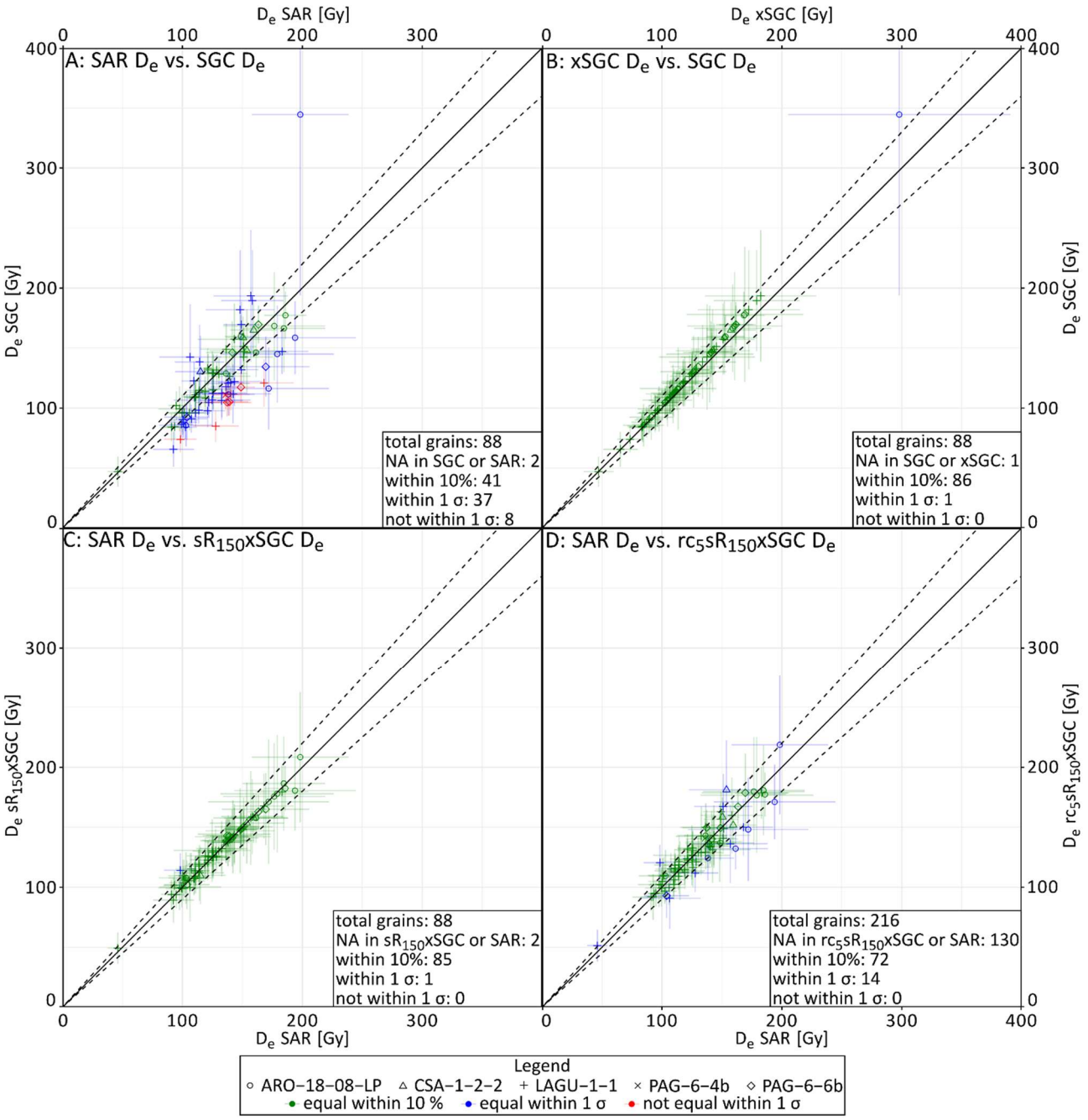

***Fig. 3.1**: Evaluation of SGC performance. **A)** comparison of D_e from samples of subset A (Table 3.1) obtained by the standard SAR procedure with D_e obtained using an SGC established with the same measurements, fitted with their L_{r1}/T_{r1} from the eighth regenerative SAR cycle with a D_{r1} of 50 Gy (Table 3.2); **B)** comparison of D_e from samples of subset A obtained by an SGC, established using the same samples, and obtained by a xSGC, constructed with data from subset X (Table 3.1); **C)** comparison of D_e from samples of subset A obtained by the standard SAR procedure with D_e obtained using the xSGC from B) and fitting the individual grains with L_{sR}/T_{sR} from an synthetic cycle with a D_{r1} of 150 Gy (sR_{150}xSGC); **D)** comparison of D_e from samples of subset A obtained by the standard SAR procedure with D_e obtained using the sR_{150}xSGC from C) and reducing the SAR-cycles for individual growth curve fitting to the "natural" 150, 0, 50, 500, 50 Gy cycles (rc_5sR_{150}xSGC).*

3.3.2 External SGC (xSGC)

3.3.2.1 Procedure

In future studies it seems more likely to use an already established SGC rather than constructing an SGC for every new sampling site. Therefore, the established SGC might be constructed from samples with different geographical and geological origin than the samples it is used for. To mimic this scenario, we test the performance of the xSGC, constructed with subset X, to analyse subset A. The xSGC was constructed in the same manner as the SGC (see Chapter 3.3.1.1). For shape of the xSGC see Appendix A Fig. A1. To test the validity of the xSGC the D_e values for dataset X acquired with the SAR method and the xSGC where compared. Out of 555 comparable grains 554 were in unity at 2σ, therefore the xSGC can be regarded as reliable (e.g. Li et al., 2015a, b). For the subsequent D_e calculation of dataset A the parameters of the xSGC were used in the calSGCED() function.

3.3.2.2 Results & discussion

Next the D_e results using the SGC and xSGC are compared in the same manner as SAR and SGC above (Fig. 3.1B). Using the xSGC, D_e values for all 88 grains could be calculated. A total of 87 mutual grains were used for the comparison between SGC and xSGC. All but one of them agreed within less than ± 10 %. If the SGC D_e is considered to be the true D_e, xSGC D_es all slightly underestimated with an average of 4.14 ± 0.56 Gy. The large uncertainty is caused by one grain not being within ± 10 % in unity. The correlation between both D_e results is perfect with a r_s of 1.

The one grain, which differed slightly more than 10 %, is still in agreement if the 1σ errors of the two D_e values are considered (cf. Fig. 3.1B). This particular grain had a L_x decay curve in the eight regenerative cycle (R8) with an unusual low net signal and a relatively high background. SGC and xSGC calculated unusually high D_e values based on this one L_x/T_x. With D_e values of 345 ± 151 Gy for the SGC and 298 ± 93 Gy for the xSGC, they were around twice as high as the given dose of 150 Gy. For comparison the SAR D_e for this particular grain was 198 ± 40 Gy, which demonstrates that outliers in individual measurement cycles can have a considerable effect on the SGC results if the outliers occur in the D_{r1} cycle.

In general, the deviation between D_e derived with the different SGCs increases with increasing L_n/T_n. As with the D_e calculation using a SAR growth curve, small changes in L_n/T_n result in larger changes in the D_e the closer to saturation they intersect the growth curve. L_n/T_n above $2D_0$ are therefore usually not considered (Murray et al., 2002).

The agreement between SGC and xSGC results confirms Li et al. (2015b) findings, that a 'global SGC' is suitable for feldspar samples and Mueller and Preusser (2022) observations that SGC results are not biased if the same input grains are used for SGC construction and application.

In our future studies in the Atacama Desert and elsewhere, the case of using a xSGC seems more likely because it is created with a larger dataset and might thus be more robust. Since the correlation between SGC and xSGC D_e values is perfect, all further data is generated with the xSGC.

3.3.3 Synthetic R (sR)

3.3.3.1 Procedure

When fitting a SAR growth curve using any function, in our case a single saturating exponential, all L_x/T_x points measured are considered by the fit. However, when interpolating data onto a constructed SGC only the natural signal and one regenerative dose point are used (Li et al., 2015a). Thus, in their original approach only those two cycles were measured for D_e estimation. We tested this approach and removed all measurement cycles from our dataset except for the "natural" signal and regenerative cycle eight (R8 = 50 Gy). Therefore, only the rejection criteria $T_n > 3\sigma$ above background, RSE of $T_n \leq 25$ % and RSE of the D_e above 50 % could be applied.

From the analysed 2500 grains from dataset A, 243 passed these rejection criteria (see Appendix A Table A2). Out of those 243 grains three grains were classified as saturated by the calSGC() function. The remaining 240 grains resulted in a finite D_e value, from which 86 D_e values could be compared to the D_e values achieved with the standard SAR approach. Although all 86 comparable grains were in unity within 2σ, we were not satisfied with the performance. As Appendix A Fig. A3 shows, the precision of the comparable D_e values was about the same as in Chapter 3.3.1 and the scatter in the not comparable grains was large. However, the mean D_e value of the not comparable grains is in unity within 1σ with the mean D_e value of the SAR approach.

If we would not have measured the full SAR cycle, we would not have known, that R8 has fewer odd L_x/T_x values than R2 and R3. As mentioned in Chapter 3.3.2.2 odd individual L_x/T_x values used as L_{r1}/T_{r1} can lead to pronounced over- or underestimation of the D_e values, when these values deviate significantly from the fitted growth curve (cf. Fig. 3.2A). The grain depicted in Fig. 3.2A for example passed all rejection criteria and had a D_e value of 154 ± 31 Gy calculated with the standard SAR approach. Using R8 as L_{r1}/T_{r1} it had a D_e of 142 ±31 Gy. Using either R2 or R3 as L_{r1}/T_{r1} the D_e values were estimated at 308 ± 89 Gy and 92.7 ± 19.9 Gy (cf. Fig. 3.2B). Due to the large errors they still agree with the SAR D_e with unity at 2σ.

We therefore introduce a new parameter and procedure for the projection of multiple L_x/T_x onto the constructed SGC. This parameter should ideally overcome the problem of including grains with unsuitable luminescence characteristics (e.g. too large recycling ratios or FOM >10%) and furthermore reduce the effect of odd individual L_x/T_x values. Instead of using a single L_x/T_x point as L_{r1}/T_{r1} we chose a L_x/T_x point, which we extracted from the fitted growth curve. We term this point synthetic regenerative dose (sR). For this we used the growth curves of each grain and reversed the process of D_e estimation from a growth curve. We chose an sR, for example 200 Gy (cf. Fig. 3.2A), and inserted it into our exponential function (Eq. 3.1). Thereby we projected the sR onto the growth curve whereby we calculated the point of interception with the growth curve to get the value on the y-axis of our synthetic L_{sR}/T_{sR} (Fig. 3.2).

$$\frac{L_{sR}}{T_{sR}} = a * \left(1 - exp^{(-sR*b)}\right) + c \qquad \textit{(Eq. 3.1)}$$

With a, b and c being the parameters a, b and c from the grain-wise exponential growth curve, calculated during the normal SAR procedure and sR a value in Gy. L_n/T_n and L_{sR}/T_{sR} were then used as input parameters for the function calSGCED() to calculate the D_e values.

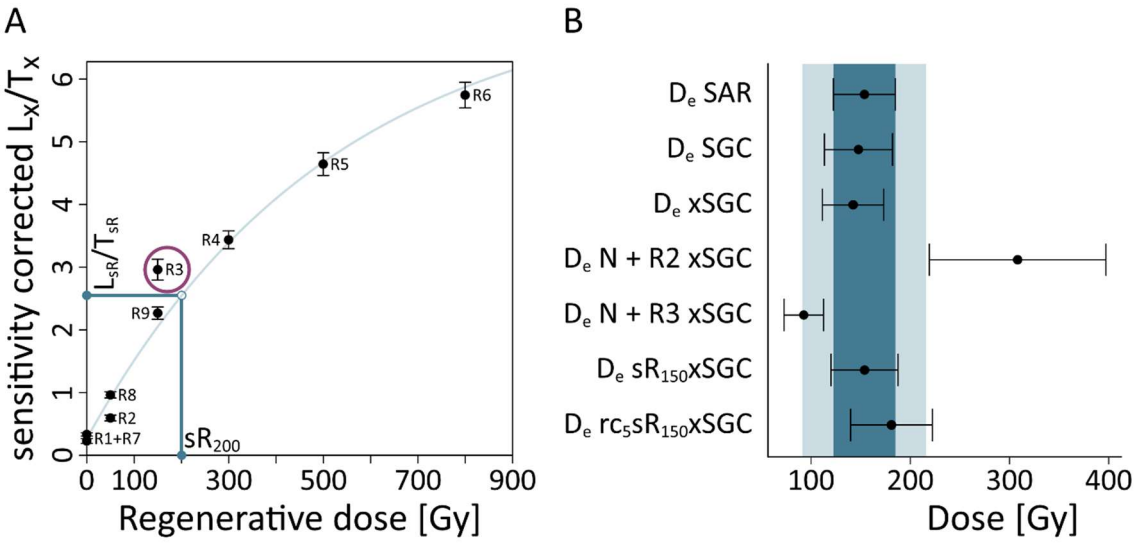

Fig. 3.2: *Influence of odd L_x/T_x values and the mitigation strategy of implementing (sR)* ***A)*** *Process of L_{sR}/T_{sR} determination with an sR of 200 Gy on an example exponential SG growth curve of the sample CSA-1-2-2 with an odd L_x/T_x value in the third regenerative SAR cycle (D_i = 150 Gy). The vertical line from the X-axes towards the growth curve illustrate the process of calculating the interception. The horizontal line from the growth curve towards the Y-axes illustrate the subsequent determination of L_{sR}/T_{sR}.* ***B)*** *Comparison of D_e values of the same grain estimated using different techniques with: SAR using the standard SAR approach, SGC using the SGC constructed with data from subset A and regenerative cycle R8 (50 Gy) used for projection onto the SGC, xSGC using the xSGC constructed with data from subset X and regenerative cycle R8 used for projection onto the xSGC, N + R2 xSGC using only the natural and regenerative cycle R2 (50 Gy) for the rejection process and using the xSGC constructed with data from subset X and regenerative cycle R2 used for projection onto the xSGC, N + R3 using the same procedure as N + R2 but using R3 (150 Gy) instead of R2, sR_{150}xSGC using the*

same procedure as xSGC but instead of using R8 for projection onto the SGC the sR method with a sR of 150 Gy was used, rc_5sR_{150}xSGC (introduced in Chapter 3.3.4) is using only regenerative cycles N, R1, R2, R4 and R8 (cf. Table 3.3) for the rejection process and the sR method with a sR of 150 Gy for projection onto the xSGC.

To evaluate if there is an influence of the size of sR on the resulting D_e and DRR we tested eight different sR values: sR_{50}, sR_{100}, sR_{125}, sR_{150}, sR_{175}, sR_{200}, sR_{300} and sR_{800}, with the subscript being the size in Gy.

3.3.3.2 Results & discussion

The results were evaluated in the same manner as SAR and SGC in Chapter 3.3.1.1 based on a comparison of D_e and DRR results of the SAR procedure and the $sR_{50\text{-}800}$xSGC procedures. For detailed results of all sR tested see Appendix A Table A3. For all sR sizes, except for 800 Gy, 86 D_e values for the 88 not rejected grains were calculated. With sR_{800} 87 D_e values were calculated. Since sR_{100}, sR_{125} and sR_{150} had the most grains within 10 % in unity with the SAR results, the other five sR values will not be discussed further. With sR_{125} all grains had D_e values within 10 % in unity with the SAR D_e values, whereas sR_{150} had one and sR_{100} three grains not within 10 %. With DRRs of 0.86 ± 0.02, 0.87 ± 0.02 and 0.89 ± 0.02 for sR_{100}, sR_{125} and sR_{150} respectively all three sR procedures showed an improved DRR compared to the above presented conventional SGC approach (0.84 ± 0.03). The correlation between the SAR D_e values and those achieved with sR_{100}, sR_{125} and sR_{150} was strong positive with Spearman's rank correlation coefficient (r_s) of 0.99 for all three sR values tested. The differences between sR_{100}, sR_{125} and sR_{150} were small, with sR_{125} having the most D_e results equal within 10 % with the SAR procedure but sR_{150} yielding the better DRRs.

Deviations of sR from the expected D_e (here 150 Gy) of ~30 % (± 50 Gy), do not cause major alterations in the D_e results in this data set. All sR ranging from 100 to 200 Gy have a strong positive correlation with the SAR procedure, with a minimum r_s of 0.94. In comparison with the SAR data, if the sR was slightly smaller than the expected D_e ($sR_{100,125}$), the method yielded better results than if the sR was slightly larger ($sR_{175,200}$). A cause for the better agreement with the SAR results might be the overall underestimation of the D_e with the SAR procedure. Since the differences between the best performing sR were very small and the sR_{150} had the same DRR as the SAR procedure, we chose an sR of 150 Gy for our further analysis (see Fig. 3.1C). Furthermore, the sR_{150} equals the recommended size for a D_{r1} (Li et al., 2015a). We therefore conclude that sR should be chosen to be the same size as the expected D_e. Nevertheless, considering that the D_e is normally unknown before measurement, it is reassuring that choosing an sR value within 30 % of the natural dose does not seem to have too great of an effect on final D_e calculations.

3.3.4 Reduction of SAR cycles (rc)

3.3.4.1 Procedure

Whilst the sR approach helps in making the interpolation onto the SGC more robust, it still requires the construction of a full growth curve for every grain and thus not saving any measurement time. Here we test which cycles can be removed to save time while still yielding robust D_e values with the sR_{150}xSGC method.

We carried out ten different reduced cycle (rc) scenarios, all containing the "natural" cycle and a zero-dose cycle (recuperation). Besides these two cycles, we tested if two additional cycles are enough to incorporate the sR method or if a third cycle, a recycling point, is needed as well. We also investigated which dose size yielded the best results. For the recycling point we could only test 50 Gy and 150 Gy since those were the only recycling doses in our SAR protocol. The ten tested rc scenarios are listed in Table 3.3 and afterwards abbreviated with their test number according to Table 3.3 as a subscript. The dataset used for xSGC establishment was not reduced.

Table 3.3: *Reduced cycle scenarios tested for subset A. The full SAR protocol used is given in Table 3.2.*

Abbreviation	Used cycles	D_i of used cycles [Gy]
rc_1	N + R1 + R2 + R4	150 + 0 + 50 + 300
rc_2	N + R1 + R2 + R5	150 + 0 + 50 + 500
rc_3	N + R1 + R2 + R6	150 + 0 + 50 + 800
rc_4	N + R1 + R2 + R3 + R8	150 + 0 + 50 + 150 + 50
rc_5	N + R1 + R2 + R4 + R8	150 + 0 + 50 + 300 + 50
rc_6	N + R1 + R2 + R5 + R8	150 + 0 + 50 + 500 + 50
rc_7	N + R1 + R2 + R6 + R8	150 + 0 + 50 + 800 + 50
rc_8	N + R1 + R3 + R4 + R9	150 + 0 + 150 + 300 + 150
rc_9	N + R1 + R3 + R5 + R9	150 + 0 + 150 + 500 + 150
rc_{10}	N + R1 + R3 + R6 + R9	150 + 0 + 150 + 800 + 150

3.3.4.2 Results & discussion

Reducing the number of SAR cycles used led to an increase of accepted grains, with fewer grains being rejected due to their poor growth curve fitting compared to when using full SAR cycles. For detailed rejection criteria and results of all tested rc see Appendix A Table A4 and A5.

The growth curves produced in rc_4 used for the sR method are not reliable since the highest given dose used for their calculation is still in the linear part of the growth curves constructed with the full set of SAR cycles. Many grains were falsely excluded as they appeared to be saturated. Furthermore, the results did not agree with the SAR

procedure (see Appendix A Table A4), thus rc_4 is not discussed further. All other tested rc were able to calculate ~200 D_e values out of the 2500 measured grains.

In a direct comparison to the SAR D_e values, all nine remaining tested rc had at least 85 common grains with the SAR results. All showed similar results (see Appendix A Table A5) with rc_5 and rc_6 showing the best performance. The other seven rc approaches are therefore not discussed further.

Rc_5 and rc_6 had the same setup for the cycle reduction, with remaining cycles being the "natural" cycle, a zero-dose cycle, a recovery dose of 50 Gy plus one additional dose. The additional doses of 300 Gy and 500 Gy, respectively, are between D_0 (284 Gy) and $2D_0$ (568 Gy) of the xSGC. Rc_6 was able to calculate eight D_e more than rc_5 but rc_5 had the best overall results. With rc_5 197 D_e values were calculated, of which 72 were equal with the SAR results within ± 10 % and the remaining 14 D_e were identical within the 1σ error (cf. Fig. 3.1D). The mean difference between the D_e values was 7.40 ± 0.70 Gy and the DRR of rc_5 was 0.9 ± 0.02, which is in unity within 1σ with the SAR-achieved DRR of 0.89 ± 0.02.

Compared to the approaches described in Chapters 3.3.1 and 3.3.2 (e.g. using the full SAR measurement for the rejection process and R8 for the projection onto the SGC or xSGC), the accuracy and the precision of the D_e values achieved with the rc_5sR_{150}xSGC compared to the D_e values estimated using the SAR procedure improved (cf. Fig. 3.1 and Appendix A Fig. A2). The scatter in the D_e values not comparable with SAR results was smaller using rc_5sR_{150}xSGC than using the natural and one additional L_X/T_X value for the rejection process and the projection onto the xSGC (cf. Appendix A Fig. A3). The mean D_e value of the not comparable grains was in unity within 1σ with the mean D_e value of the SAR approach.

All the grains yielding those extra D_e values, were rejected due to a FOM >10 % when using the full SAR procedure during the rejection process. Since the extra rc_5sR_{150}xSGC D_e values are in the same range and showing similar scatter as the rest of the rc_5sR_{150}xSGC D_e values which are comparable to the SAR results, we assume that those additional D_e values can be regarded as reliable.

Compared to the correlation of the sR_{150}xSGC results, with a r_s of 0.99, the correlation of the rc_5sR_{150}xSGC and the SAR approach is worse with a r_s of 0.94. Nevertheless, the rc_5sR_{150}xSGC approach is still an improvement compared to the conventional SGC approach (r_s = 0.81, DRR = 0.84 ± 0.03). Furthermore, it is possible to estimate more than twice as many D_e, resulting in fewer discs to be measured. The reduction of measurement cycles saves approximately 60 % of measurement time per disc.

We therefore recommend applying the rcsRxSGC approach when dealing with problematic single grain feldspars, with an sR in the size of the expected D_e and a rc

scenario with a recuperation point, a recycling point - smaller than the expected D_e -, and an additional dose point with a size of D_0 to $2D_0$ of the SGC used. If this approach is also applicable for expected D_e values with sizes greater than $2D_0$ needs to be evaluated.

3.3.5 Dose recovery ratio (DRR)

Since our dataset is based on a dose recovery test, another measure to test the performance of our approach is the dose recovery ratio. Overall, the given dose of 150 Gy is underestimated by all applied methods, including the standard SAR procedure. Fig. 3.3 shows a comparison of the D_e results achieved with the SAR procedure and the rc_5sR_{150}xSGC method. With the SAR procedure, 52 out of 87 grains yield a DRR within 1 ± 0.1 if their 1σ errors were considered and 35 grains differed more than ± 0.1 from a DRR of 1 even when their 1σ errors were considered. Out of the 197 D_e values calculated using the rc_5sR_{150}xSGC method, 134 grains had a DRR of 1 ± 0.1 if their 1σ errors were considered and 63 D_e values differed more than ± 0.1 from a DRR of 1 even when their 1σ errors were considered. Thus, using the rc_5sR_{150}xSGC method we observed a higher percentage of grains yielding a DRR within the desired 1 ± 0.1, contributing to an overall improved DRR.

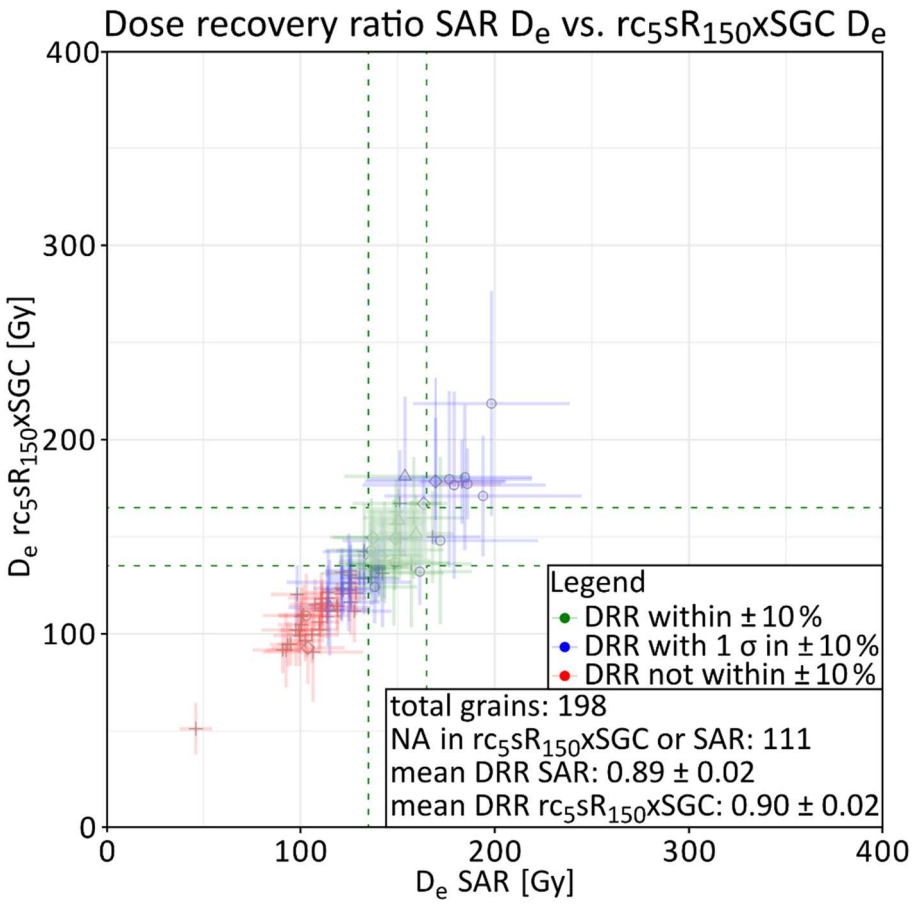

Fig. 3.3: *D_e values from grains of subset A, calculated with the standard SAR procedure (x-axes) and the rc_5sR_{150}xSGC method (y-axes). Colours of the horizontal and vertical 1σ error bars represent if the DRR calculated with SAR or rc_5sR_{150}xSGC are within unity ± 10 % (green), within 1 ± 10 % if the 1σ error is considered (blue) or if they are not within 1 ± 10 %. Shape of the datapoints indicates the sample allocation (cf. legend Fig. 3.2).*

3.4 Single-grain geochemistry (SEM-EDX)

3.4.1 Procedure

The SEM-EDX measurements were carried out at the Institute of Geology and Mineralogy of the University of Cologne, by defining regions of interests on the polished grain surfaces. These regions of interest were than mapped with a pixel size of 2 µm, resulting in average values for each region of interest. The elemental analysis results of each measured region were assigned to the individual grains on the basis of the maps of the measurements.

Unfortunately, SEM-EDX data could not be obtained for every grain. Some grains got lost during the transfer process from the discs to the tape, the position of others was slightly altered during embedding them in epoxy. If a grain was subsequently not clearly identifiable, its SEM-EDX results were not considered. For some grain positions (i.e., holes in the discs) more than one SEM-EDX result was obtained. This

was either due to multiple grains being located in one hole or due to breaking of the grains during the transfer process. For grains and holes with more than one SEM-EDX measurement result, the average was calculated.

3.4.2 Results

The results for the nine analysed elements are summarised in Fig. 3.4, for detailed measurement results see Appendix A Table A6. 2328 grains, out of the 5000 grains analysed for their luminescence characteristics, could be clearly identified on the SEM-EDX maps. From those 2328 grains, 250 gave suitable luminescence signals for D_e calculation with the SAR procedure and 492 with the rc_5sR_{150}xSGC method. Those grains are hereafter called luminescent grains. All luminescent grains from subset A (n = 65) contained O, Na, Al, Si and K, implying that no luminescent grain from the Atacama Desert was pure orthoclase. About half of them also contained Ca and Fe. From subset X (n = 434) most of the grains (>400) were also composed of O, Na, Al, Si and K, with 200 of them also having Ca and 15 of them being pure orthoclase, based on their geochemical composition.

The K-concentration of all luminescent grains varied between 0.06 wt% and 14.6 wt%, with a mean value of 7.04 ± 0.26 wt%. The coefficient of variation of all luminescent grains of 80 % indicates that luminescent grains can have a wide range of K-concentrations, supporting the findings from O'Gorman et al. (2021b) and Zinelabedin et al. (2022).

The SEM-EDX results presented in Fig. 3.4 suggest that there is no clear difference between the geochemical composition of luminescent and non-luminescent grains, neither for subset A nor subset X. Although, for example the median K-concentration of luminescent grains is higher than the median K-concentration of non-luminescent grains, this does not imply that all grains with low K-concentrations do not emit suitable luminescent signals nor that all grains with high K-concentration emit suitable luminescent signals.

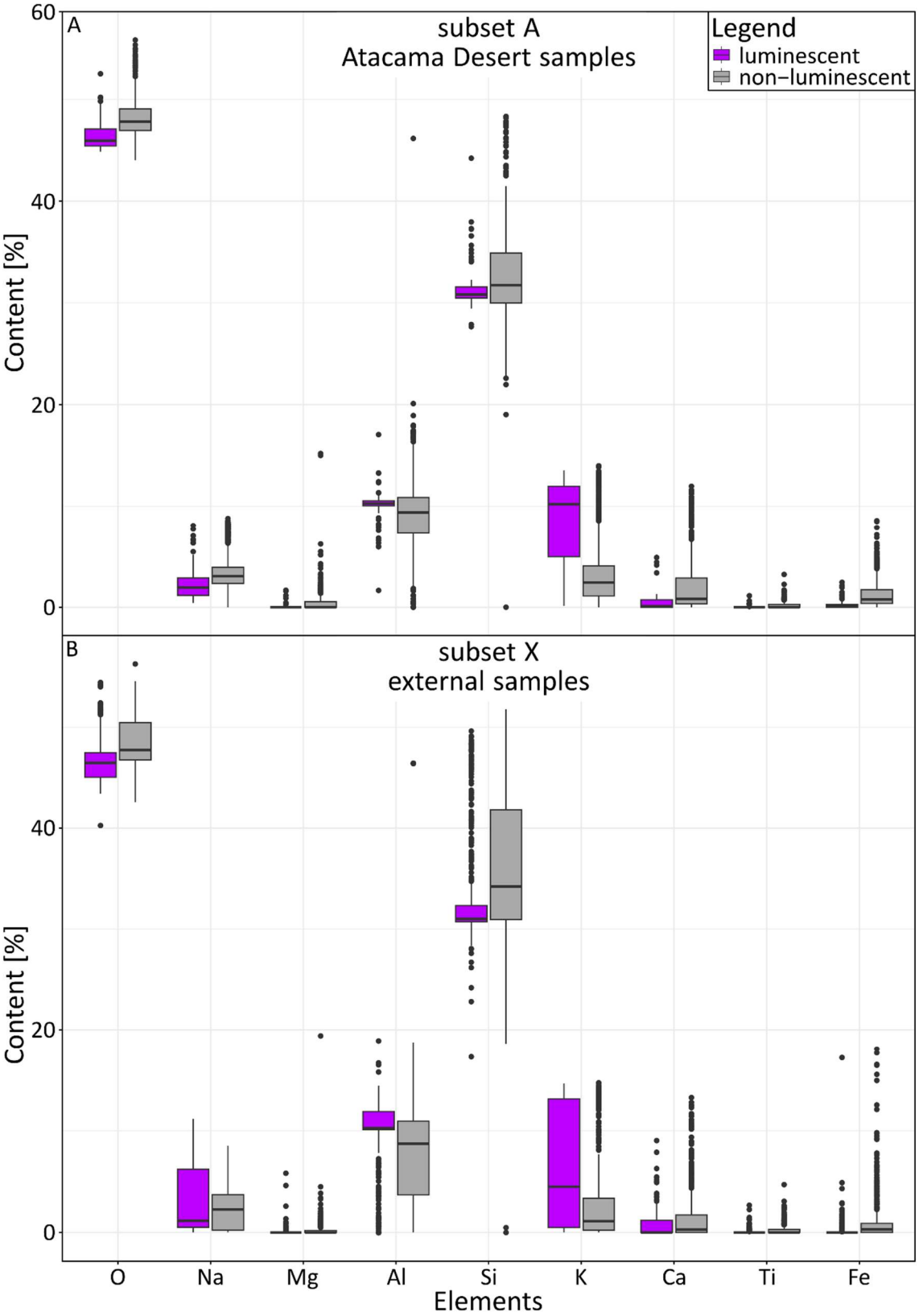

Fig. 3.4: *Statistical distribution of all measured element concentrations for* ***A)*** *the grains from subset A and* ***B)*** *the grains from subset X grouped into luminescent (purple) and non-luminescent grains (grey). The lower and upper hinges correspond to the first and third quartiles (the 25th and 75th percentiles). The upper whisker extends from the hinge to the largest value no further than 1.5 * IQR from the hinge (where IQR is the inter-quartile range, or distance between the first and third quartiles). The lower whisker extends from the hinge to the smallest value at most 1.5 * IQR of the hinge. Data beyond the end of the whiskers are called "outlying" points and are plotted individually. The horizontal bar represents the median.*

3.5 Correlation of luminescence characteristics and geochemistry

To evaluate whether signal intensity and K-concentration are linked and if there are further relationships within and between geochemistry and luminescence properties, we created nine correlation matrices. We performed Spearman rank correlations for the entire dataset and the two subsets. We then calculated six correlation matrices for these three categories by dividing them in luminescent and non-luminescent subgroups. In addition to the nine elements from the SEM-EDX analysis, the following luminescence properties were used as input variables: D_e and DRR determined with SAR, D_e and DRR determined by $rc_5sR_{150}xSGC$, to check whether high or low D_e or DRR are linked to geochemistry or signal intensity, L_n and T_n, to check whether there is a correlation between brightness of the grain and geochemistry. For better readability, only the correlation matrix of the entire data set is shown in Fig. 3.5. The eight remaining correlation matrices can be found in Appendix A Fig. A4.

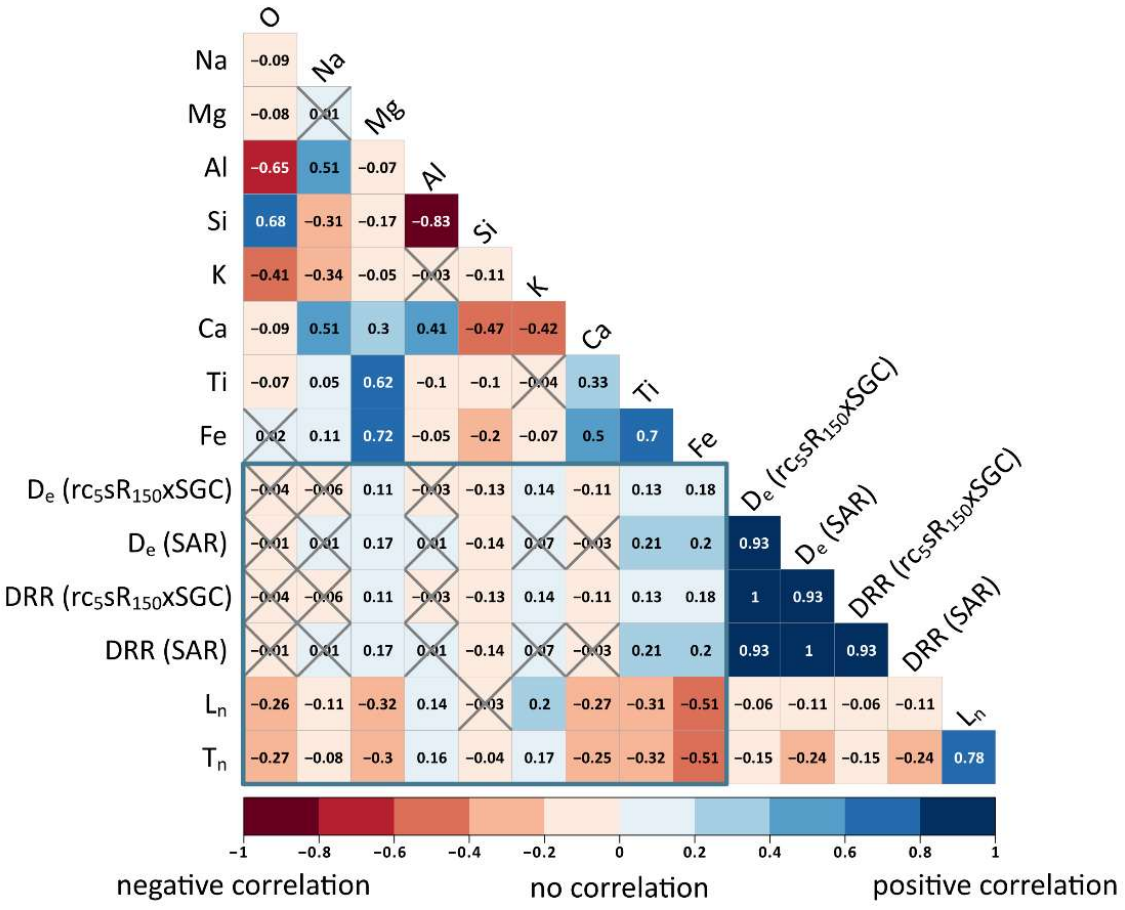

Fig. 3.5: *Correlation matrix of the complete dataset (subset A + X). Numbers in the squares represent Spearman's rank correlation coefficient values and their colour the strength of the correlation. For not significant correlations with a p-value above 0.05 % the squares are crossed out. The* ***turquoise square*** *surrounds the correlation between the geochemical data and the luminescence characteristics.*

No strong or moderate to strong correlation could be observed between any element and luminescence characteristics if the entire dataset is considered, as can be seen inside the turquoise square in Fig. 3.5. This also holds true regardless of whether the subset data or subgroups of the entire or subset data are considered. Furthermore, ~47 % of those correlations have a p-value >0.05 and are therefore not considered significant. The most significant correlation between SEM-EDX results and luminescence is the negative correlation observed between the Fe-concentration and the signal intensity (L_n and T_n) in the correlation matrix of all grains from subset X with a r_s of -0.57 and -0.56 for L_n and T_n respectively. The correlation between Fe-concentration and signal intensities in subset A is also negative but only very weak or weak, if significant at all. There is no significant correlation between K-concentration and the signal intensity (L_n and T_n) in subset A when only the luminescent grains are considered, but a weak negative correlation can be found in subset X. In contrast, the same correlation for the non-luminescent grains is very weak to weak positive in both datasets. In Fig. 3.5 these correlations between K-concentration and L_n respectively T_n are weak and very weak positive, since a greater number of non-luminescent grains contribute to the overall correlation in Fig. 3.5 (cf. Appendix A Table A6). Conversely, Na- and Ca-concentrations show a positive correlation with the signal intensity in the luminescent grains and a negative correlation in the non-luminescent ones (Appendix A Fig. A4B and C).

Within the luminescence characteristics there is no strong significant correlation between the signal intensity and the D_e or the DRR. Since the D_e values and DRRs determined with the same method have a perfect correlation, all correlations between D_es and DRRs determined with different methods yield the same r_s values within each correlation matrix. For subset A the r_s of these correlations is 0.94, for subset X and for both subsets combined it is 0.93. The correlation between L_n and T_n is almost perfectly positive if only the luminescent grains are considered, but substantially weaker if all or just non-luminescent grains are correlated.

Within the geochemical data the correlation values between the nine correlation matrices vary to a greater extent than within the luminescence characteristics. Correlations found between different elements reflect the general chemical characteristics of the feldspar mineral group, with Si:Al ratios differing between alkali feldspars and plagioclase and with a known miscibility gap between K- and Ca-feldspars. The strong negative correlation between Si- and Al-concentrations is particularly pronounced when only the non-luminescent grains are considered, but visible in all nine matrices. When only the luminescent grains are considered the correlations between K- and Na- as well as K- and Ca-concentrations are moderate to strong negative, while the correlations between Na- and Ca-concentrations are

moderate or very strong positive. None of the K-, Na- and Ca-concentration correlations is more than moderate in the non-luminescent correlation matrices but all are in the same directions as in the luminescent grains.

The luminescent grains from sample ARO-18-08-LP have a very strong negative correlation of -0.83 and -0.86 between their Fe-concentrations and the signal intensities L_n and T_n. Zinelabedin et al. (2022), investigating the same samples, suspected that the high Fe-concentrations might be caused by Fe-rich coatings of the feldspar grains. These iron layers around the sediment grains could on the one hand explain the high Fe-concentration of up to 8.8 % in luminescent grains and on the other hand the observed low luminescence intensities, since Fe coatings could cause absorption of the emitted luminescence (Kook et al., 2011). Geake et al. (1972) and Finch and Klein (1999) present alternative explanations for the negative correlation between Fe-concentration and L_n and T_n intensities. Ultimately, we cannot give a satisfactory explanation of the observed negative correlation between Fe-concentration and luminescence intensity at this stage.

The previously reported and generally accepted relationship of K-concentration and luminescence signal intensity is not supported by our data. The non-existing correlation between K-concentration and signal intensity in subset A confirms the findings of O'Gorman et al. (2021b) and thereby falsifies the common hypothesis of a positive correlation (e.g. Huntley and Baril, 1997; Prescott and Fox, 1993; Spooner, 1992) at least for our set of samples. The weak negative correlation in subset X is further evidence that a higher K-concentration is not the main determinant for a high signal intensity.

3.6 Conclusion

Atacama Desert feldspars are challenging for single-grain luminescence measurements for two reasons: firstly, only a small percentage of grains emits satisfactory luminescence signals (on average 3.52 %) and secondly their geochemical compositions are highly variable (on average 3.40 wt% K).

To obtain a sufficient number of accepted grains for palaeodose calculation, numerous discs have to be measured, resulting in a long overall measurement time. We therefore tested the application of the standardised growth curve (SGC) method (Li et al., 2015b) with a dose recovery test using a $pIRIR_{175}$ protocol on ten chemically different feldspar sediment extracts. With a perfect correlation between SGC and xSGC results, we confirmed that the geographical and geological origin of the samples, for which the D_e is estimated, can differ significantly from the geographical and

geological origin of the samples used for SGC construction and that the SGC is not biased if the same input grains are used for SGC construction and application.

We introduced a new and more robust method for interpolation of L_x/T_x values onto the SGC. The new sR (synthetic regenerative dose) method, reduces the influence of odd individual L_x/T_x values on the interpolation and D_e calculation. With the sR method a synthetic L_x/T_x, based on the growth curves of the individual grain, is used for D_e calculations with the SGC method. Since the sR method relies on the individual growth curves, no measurement time is saved. Therefore, we further tested how to reduce regenerative cycles (rc) to obtain a suitable growth curve for the sR method. With our new established rcsRxSGC method we were able to reduce our measurement time per disc by ~60 %. Furthermore, we were able to calculate around twice as many D_e per disc with the rcsRxSGC method than with the SAR procedure. Thus, potentially more measurement time can be saved, since fewer discs need to be measured to gain a sufficient amount of suitable grains.

We investigated the relationship of K-concentration and luminescence characteristics, as well as their implications for internal dose rate determination. Therefore, we measured the geochemical composition of the grains previously analysed for their luminescence properties using a costly and time-consuming scanning electron microscope (SEM) with energy-dispersive X-ray spectroscopy (EDX) attachment. Since no correlation between the K-concentrations and luminescence properties could be found, we conclude that for single-grain measurements in feldspars with heterogeneous K-concentrations the internal dose rate estimation should not be based on an average literature-based value. Further, we cannot recommend using SEM-EDX measurements to overcome the problem, since they are costly and time-consuming. Therefore, the internal dose rate determination for single-grain luminescence measurements remains a challenge.

When dealing with geochemically heterogeneous feldspars which give few suitable luminescence signals during single-grain pIRIR measurements, we recommend using the rcsRxSGC method with an sR in the size of the expected D_e and rc consisting of a recuperation point, a recycling point with a size smaller than the expected D_e, and an additional dose point with a size of D_0 to $2D_0$ of the xSGC. Yet a feasible solution for single-grain K-concentration measurements is still needed.

3.7 Acknowledgements

This project is affiliated to the Collaborative Research Centre 1211 “Earth – Evolution at the Dry Limit” (Grant-No.: 268236062) funded by the German Research Foundation (Deutsche Forschungsgemeinschaft, DFG), Germany. We would like to thank our colleagues who kindly supplied us with sample material. We thank Georgina E. King (Université de Lausanne) for MBT-I-2430, Benny Guralnik (Technical University of Denmark) for KTB-383-C, Dominik Brill (University of Cologne) for PAG-6-4b, PAG-6-6b and ISM-7, Simon M. May (University of Cologne) for CSA-1-2-2 and LAGU-1-1 and Aline Zinelabedin (University of Cologne) for ARO-18-08 LP. SR would like to thank Ulrike Hardenbicker for guidance in the field during which sample ABLR-1 was taken, and for hosting her at the University of Regina, Canada. We also thank Kathrin Jung (University of Cologne) for embedding our grains in resin and Hanna Cieszynski (University of Cologne) for the SEM-EDX measurements. SR acknowledges support by the European Union’s Horizon Europe research and innovation programme under the Marie Skłodowska-Curie grant agreement (RECREATE, grant no. 101103587) during co-writing and editing the manuscript. The sampling campaign during which sample ABLR-1 was sampled was financially supported by a Female Research Grant from the Faculty of Mathematics and Natural Sciences, University of Cologne, awarded to SR.

3.8 CRediT authorship contribution statement

Linda A.E. Maßon: Writing – review & editing, Writing – original draft, Visualization, Software, Methodology, Investigation, Formal analysis, Data curation. Svenja Riedesel: Writing – review & editing, Supervision, Methodology, Investigation, Conceptualization. Anja Zander: Writing – review & editing, Methodology, Investigation. Mariana Sontag-González: Writing – review & editing, Software, Methodology, Investigation, Conceptualization. Tony Reimann: Writing – review & editing, Supervision, Methodology, Investigation, Funding acquisition, Conceptualization.

3.9 Declaration of competing interest

The authors declare that they have no known competing financial interests or personal relationships that could have appeared to influence the work reported in this paper.

Chapter 4

How much K is OK? – Evaluating different methods for K-concentration determination and the effect of the internal K-concentration on feldspar luminescence dating

Linda A.E. Maßon[1*], Svenja Riedesel[1,2], Stephan Opitz[1], Anja Zander[1], Anthony Bell[3], Hanna Cieszynski[4], Tony Reimann[1]

[1] Institute of Geography, University of Cologne, Germany
[2] Luminescence Physics and Technologies, Department of Physics, Technical University of Denmark, Denmark
[3] Materials and Engineering Research Institute, Sheffield Hallam University, UK
[4] Institute of Geology and Mineralogy, University of Cologne, Germany

Geochronology 7 (4) (2025) 475-492
https://doi.org/10.5194/gchron-7-475-2025

The previous chapter demonstrated that no consistent relationship could be established between the internal K-concentration of individual feldspar grains and their luminescence characteristics. As a result, the internal dose rate cannot be reliably estimated based on signal intensity. Furthermore, while SEM-EDX analyses provided precise grain-specific K-concentration data, their high analytical cost and time demand make them impractical for routine application. These findings highlight a critical challenge in feldspar luminescence dating: the accurate determination of the internal dose rate remains unresolved, particularly for single-grain feldspar measurements of Atacama Desert samples where compositional heterogeneity is pronounced.

Building upon these results, the subsequent chapter investigates whether the measurement of the internal K-concentration is essential for robust internal dose rate determination and explores how different analytical approaches influence the resulting dose rate calculations. Four techniques for measuring the K-concentration will be systematically compared, and their impact on total dose rate estimations will be evaluated. This chapter aims to identify a method that achieves a balance between analytical accuracy and practical applicability in luminescence dating of feldspars not only in the context of this thesis but also for future research.

For a detailed statement on the contribution of the co-authors to the final manuscript, the reader is referred to the original text (Chapter 4.9). Linda Maßon contributed ~70 % to the final publication (data acquisition – 70 %; analysis and interpretation – 75 %; visualisation – 95 %; manuscript writing – 70 %).

- Formatting and orthography of the publication are adapted to the dissertation style -

Abstract

For luminescence dating of potassium-rich (K) feldspars, the presence of ^{40}K within the K-feldspar grains contributes significantly to the internal dose rate of the sample. Whilst it is common practice to determine uranium, thorium and potassium concentrations for external dose rate calculations, the vast majority of studies do not measure the internal K-concentration. Instead, most studies apply published K-concentrations of 10 ± 2 % (Smedley et al., 2012), 12.5 ± 0.5 % (Huntley and Baril, 1997) or 13 ± 1 % (Zhao and Li, 2005) to their samples. The use of these high literature-based K-concentrations is usually justified by two assumptions: **i)** only K-feldspar grains with high K-concentrations contribute to the luminescence signal significantly, and **ii)** we reliably exclude Na-feldspar luminescence signals using filters, with a narrow transmission window around the K-feldspar emission peak ~410 nm. However, these assumptions may not apply to all samples and assuming too high K-concentrations might result in significant dose rate overestimation.

To investigate the effect of the internal K-concentration on the dose rate and the validity of the above-mentioned assumptions, we determine the K-concentration of a set of ten density-separated sand-sized K-feldspar samples of different geological origin and chemical composition using four different techniques. We quantify their K-concentration on the bulk level using a wavelength dispersive X-ray fluorescence spectrometer and a beta counter, and on the single-grain level using a micro X-ray fluorescence spectrometer and a scanning electron microscope (SEM) with an energy dispersive spectroscopy (EDX) attachment. We use the SEM-EDX single-grain results to calculate two luminescence-weighted K estimates. These two estimates, effective K and luminescent grains, connect the K-concentration of a grain to its luminescence signal intensity.

Our experimental results show that **1.** There is a good agreement between bulk and average single-grain K-concentration measurements; **2.** Single-grain K-concentrations within one sample can be highly variable across the entire physically possible range of K-concentrations for feldspars; **3.** The blue luminescence emission is not dominated by K-rich feldspar grains. For most samples there are considerable differences between the published and the measured K-concentrations. These differences result in overestimation of the total dose rate of up to 34.6 % compared to dose rates calculated using measured K-concentrations. We therefore suggest to routinely measure the bulk K-concentration of each sample, complemented by additional single-grain K-concentration measurements.

4.1 Introduction

Optically stimulated luminescence (OSL) dating constrains the dose accumulated in mineral grains (in Gy) due to exposure to ionizing radiation and the rate at which this dose was received, termed dose rate (Ḋ), conventionally given in Gy ka^{-1}. The Ḋ can be divided into three parts: **i)** cosmic dose rate ($\dot{D}_c$), **ii)** external sediment dose rate ($\dot{D}_{ext}$) and **iii)** internal dose rate ($\dot{D}_{int}$). Total Ḋs may underly changes over time and are furthermore attenuated by water and sediment (e.g. Aitken et al., 1985; Bailiff and Aitken, 1980). The $\dot{D}_c$ is calculated based on the location of the sample (longitude and latitude, as well as altitude of the sampling location above sea level, and depth below the surface) (Prescott and Hutton, 1994). The $\dot{D}_{ext}$ and $\dot{D}_{int}$ depend on the abundance of certain radioactive elements and factors modifying the received doses, such as the grain size (e.g. Aitken et al., 1985; Bailiff and Aitken, 1980; Durcan et al., 2015).

Most commonly two minerals, quartz (SiO_2) and K-feldspar ($KAlSi_3O_8$), are used for OSL dating (e.g. Duller, 2008a; Preusser et al., 2008; Wintle, 2008). Although other minerals exhibit luminescence, these two minerals are preferred mainly due to the following reasons: **i)** their abundance in various geological settings, **ii)** their ability to store charge within defects in their crystal lattice, **iii)** their resistance to weathering compared to other luminescent minerals, **iv)** the bleachability of their luminescence signals, and **v)** the stability of their luminescence signals (e.g. Preusser et al., 2008; Rhodes, 2011). While the vast majority of dating studies used quartz OSL for the past decades the methodological development in general and the development of the post-infrared infrared stimulated luminescence (pIRIR) protocol in particular (Thomsen et al., 2008) led to an increased use of feldspars also for dating studies (see Chapter 4.2.2). The biggest difference for the dose rate determination between these two minerals is the internal dose rate (Aitken, 1998). Whilst the $\dot{D}_{int}$ in feldspars has been shown to arise from U, Th, K, and Rb within the mineral lattice (Mejdahl, 1987), in quartz, the $\dot{D}_{int}$ is believed to be negligible (Aitken, 1985a; Szymak et al., 2022). Especially, in K-rich feldspars the $\dot{D}_{int}$ can significantly contribute to the total Ḋ with internal K-concentrations of up to 14.05 % (Huntley and Baril, 1997; Smedley et al., 2012). The higher the internal K-concentration of a feldspar grain the greater the $\dot{D}_{int}$ (Huntley and Baril, 1997). In general, the smaller the grain size and the bigger the $\dot{D}_{ext}$ and $\dot{D}_c$, the less important is the $\dot{D}_{int}$ and therefore the K-concentration (Guérin et al., 2012). Especially in settings with predominantly coarse-grained (quartz-rich) sediments $\dot{D}_{int}$ can contribute more than 30 % to the total dose rate (e.g. Reimann and Tsukamoto, 2012, their Table 1) and could therefore lead to systematic errors for coarse-grain feldspar luminescence dating of the same magnitude.

It has been shown that laboratory sample preparation techniques based on density separation do not necessarily result in pure K-rich feldspar extracts in which all grains have a homogeneous K-concentration of ~14 % (e.g. Huntley and Baril, 1997; Woor et al., 2022). Therefore, the K-concentration used for $\dot{D}_{int}$ calculations of a sample should not automatically be assumed to be 14.05 %. Most of the time the K-concentration used for $\dot{D}_{int}$ calculations is based on literature values (see Chapter 4.2.2). The most cited studies measured single-grain and bulk sample K-concentrations and proposed K-concentrations ranging from 10 % to 13 % (Huntley and Baril, 1997; Li et al., 2008; Smedley et al., 2012; Zhao and Li, 2005). It is often assumed that there is a positive correlation between the K-concentration and the signal intensity, thus suggesting that predominately grains with a high K-concentration contribute to the measured luminescence signals (Huntley and Baril, 1997; Prescott and Fox, 1993; Spooner, 1992). It is further suggested that bright luminescence signals from Na-feldspars should not be transmitted by a blue filter combination, as their main emission peak is not within this region of the spectrum (Huntley and Baril, 1997; see Fig. 2.4). Yet, Smedley et al. (2012) found no correlation between single grain K-concentration and signal intensity. They therefore recommended a smaller mid-value of 10 % combined with an error of ± 2 % to account for grains with a lower K-concentration which still emit suitable signals. Further studies did not only disagree with the correlation between the K-concentration and the signal brightness but also showed that grains with K-concentrations below 6 % provide suitable luminescence signals (Maßon et al., 2024; O'Gorman et al., 2021b; Zinelabedin et al., 2022). These studies also showed that in some regions of the world (e.g. Indonesian archipelago or Atacama Desert) the majority of a density-separated feldspar extract might consist of feldspars with low K-concentrations and that these feldspars may even influence the bulk feldspar luminescence signal measured in the blue wavelength region. Assuming K-concentrations in the range of the proposed literature values for those grains or bulk signals that are dominated by these grains would very likely result in overestimations of the $\dot{D}_{int}$ and therefore the total $\dot{D}$. This strongly suggests that calculating $\dot{D}_{int}$ using K-concentrations based on literature values without analysing the geochemical composition of a sample can potentially lead to inaccurate feldspar luminescence ages (O'Gorman et al., 2021b). However, it should be noted that if the internal U- and Th-concentrations are high, they may partially counteract the overestimation effect caused by assuming a too high K-concentration (Smedley and Pearce, 2016; Zhao and Li, 2005). Nevertheless, in this study we focus on the internal K-concentration.

We therefore investigate the effect of the K-concentration on the $\dot{D}_{int}$ and the total $\dot{D}$ by exploring a suite of ten chemically different samples. Five samples originate from the Atacama Desert, and five samples are selected from study areas from

different geological environments from around the world. The K-concentrations of the ten samples are determined using four different techniques in different resolutions. We use a β-counter and a wavelength dispersive X-ray fluorescence spectrometer (WDXRF) to determine two average K-concentrations for each sample. Using a scanning electron microscope (SEM) with an energy dispersive spectroscopy (EDX) attachment and a μ-XRF device, we further determine the K-concentrations on the single-grain level of grains that have previously been analysed for their luminescence (cf. Chapter 4.3.2). The single-grain results are used to test whether there exists a correlation between the K-concentration and the brightness of a grain. Therefore, we calculate the following luminescence-weighted K estimates: average K-concentration of the grains resulting in a suitable luminescence signal (T_n signal >3σ above background) and the effective K of these grains (a signal-brightness weighted K-concentration). The single-grain data is also used to analyse the heterogeneity of the K-concentration within a sample. To investigate the effect on the total $\dot{D}$ and the $\dot{D}_{int}$ we calculate $\dot{D}$s based on the varying measured K-concentrations and luminescence-weighted K estimates. To place our results in the overall context, we conduct a literature review and compare our results with the three most frequently cited K-concentrations.

4.2 Feldspar luminescence dating

4.2.1 Feldspar characteristics

Feldspars form a group of aluminium framework minerals with the general formula MT_4O_8, with usually T being Al^{3+}, Si^{4+} and M being Ca^{2+}, Ba^{+}, Na^{+}, K^{+} (Deer et al., 2013). However, both M and T can be replaced by e.g.: Mg^{2+}, Pb^{2+}, or Fe^{2+} for M or Ti, Fe^{3+} or Fe^{2+} for T (Ribbe, 1983). Si^{4+} and Al^{3+} ions are linked by shared O^{2-} ions and thereby form a three-dimensional network. The interstitial spaces in this network are filled with the cations (Ca^{2+}, Ba^{+}, Na^{+}, K^{+}). The feldspar group can be divided into two solid solution series: plagioclase feldspars and alkali feldspars. Each subgroup has distinct endmembers, representing the pure chemical composition at the extremes of their solid solution series. Anorthite ($CaAl_2Si_2O_8$) and albite ($NaAlSi_3O_8$) are the endmembers of the plagioclase group and albite ($NaAlSi_3O_8$), orthoclase ($KAlSi_3O_8$) and microcline ($KAlSi_3O_8$) are the endmembers of the alkali feldspars. In alkali feldspars, potassium is usually included as a K^{+} ion. However, for dose rate calculations the elemental K-concentration is commonly used. We thus refer to the K-concentration as the concentration of the element K in these feldspars. The K-concentration within a feldspar can range between 0 % and 14.05 % based on stoichiometric calculations and the orthoclase/microcline formula ($KAlSi_3O_8$). The maximum K-concentration of

14.05 % can only be found in the alkali feldspar endmembers orthoclase or microcline. Typically, K-rich feldspars are the target mineral for feldspar luminescence dating. K-rich feldspars tend to have their emission peak at ~410 nm while Na-rich feldspars and plagioclases show a dominant emission ~570 nm (Krbetschek et al., 1996; Spooner, 1992; see Fig. 2.4). Filters are used to isolate the desired luminescence emission (Huntley and Baril, 1997).

4.2.2 Literature review

To get a more profound overview of how K-concentrations for $\dot{D}_{int}$ calculation in feldspar luminescence dating are usually determined, we conducted a systematic literature review. We used the search function of the web of science website (https://www.webofscience.com). By using the keywords “luminescence” and “feldspar” together with the setting “in all fields” we aimed to include all relevant studies. The search results totalled to 1664 to the search date (23.01.2024). Since the pIRIR method was first proposed in 2008 (Thomsen et al., 2008), we decided to include only studies published after 2008. The number of studies from 2009 to the search date amounted to 1076. Out of those 1076 merely 432 studies used feldspar for luminescence dating purposes. Most studies were discarded due to the following three reasons: **i)** the study applied rock surface, quartz or polymineral fine grain dating; **ii)** the study was methodological in nature and focussed solely on equivalent dose determination or other luminescence characteristics rather than the $\dot{D}_{int}$ or K-concentration; **iii)** the study used cathodoluminescence in order to analyse the composition of a sample and not optical luminescence dating.

Figure 4.1 shows the number of publications per year, filtered through our search criteria. A generally rising trend of publications can be recognised. In years following an International Luminescence and Electron Spin Resonance Dating conference (LED), a clear increase in published articles can be seen, presumably related to the LED special issues.

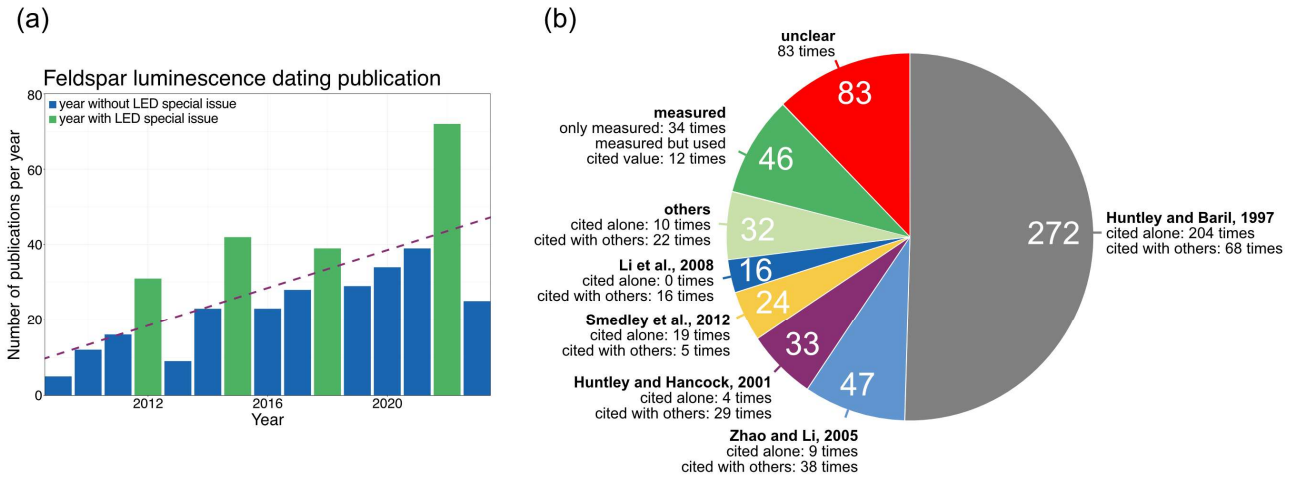

Fig. 4.1: *Summary of the literature review.* ***a)*** *Amount of published literature, covering the topic of dose rate determination for feldspar luminescence dating, per year from 2009 until 2023. Green bars represent years after a LED in which a LED special issue was published. The purple dashed line shows the trend of publication numbers per year over time.* ***b)*** *References given for used K-concentrations in the analysed 432 studies. The white numbers within the diagram show the total citation numbers. Note that the total sum exceeds the sum of 432 studies analysed since some studies cited several references. The "unclear" segment is the sum of studies who did not cite or mention a K-concentration, studies mentioning a value for the K-concentration without a reference, and studies vaguely giving information.*

The 432 selected studies can be divided into four groups regarding the K-concentration used for dose rate determination (cf. Appendix B Table B1 and Fig. B1). Group 1 used literature values, i.e., values that were measured or recommended in another publication (n = 302), group 2 measured the K-concentrations of their samples yet applied literature values (n = 12), group 3 measured the K-concentrations of their samples and used it subsequently for D_{int} calculations (n = 34), and group 4 did not provide enough information regarding the K-concentrations used or if the applied K-concentrations were based on literature values (n = 84) (cf. Appendix B Table B1 and Fig. B1).

A total of 20 different studies were cited for nominal K-concentration values. The five most frequently cited references were Huntley and Baril (1997, n = 272), Zhao and Li (2005, n = 47), Huntley and Hancock (2001, n = 33), Smedley et al. (2012, n = 23) and Li et al. (2008, n = 16) (Fig. 4.1b). In group four of the selected 432 studies 48 out of 84 papers did not mention any reference or measurement technique used and did not mention the K-concentration used. 18 out of the 84 papers mentioned a K-concentration value they used but did not cite a reference or mentioned a measurement technique they used to determine the K-concentration. Another 11 out of the 84 papers provided only vague information, such as that the internal dose rate was "taken into account", with six of them citing references which did not have any explicit information in them as well. Lastly, seven out of the 84 papers cited a reference without specifying the K-concentration they used (cf. Appendix B Fig. B1).

46 studies measured the K-concentration of their samples (Fig. 4.1b). Of those 46 studies, five studies did not clearly specify what K-concentration they used for dose rate determination (group 3), 29 studies used the measured values (group 3) and 12 studies used literature values instead of their measured results (group 2) (cf. Appendix B Table B1 and Fig. B1).

In practice, the majority (76 %) of studies based their $\dot{D}_{int}$ calculations on a literature value for the K-concentration, thus in this study we will compare our measured K-concentrations with the above mentioned most frequently used literature K-concentrations. We here give details about the techniques employed and the results obtained by the five most cited references. Huntley and Baril (1997) measured element concentration maps for 2,393 single-grains from 21 samples originating from seven geographically distinct areas using SEM. Using the element maps, they determined the proportion of K-feldspars per sample. They further analysed the K-concentration of a 0.3 g subsample of each of the 21 samples with commercial atomic-absorption analysis. Combining the determined K-concentration per sample with the proportion of K-feldspar per sample, they calculated the K-concentration of the K-feldspar fraction per sample. While they observed a cluster around 13 % K they argued that this value is probably too high due to their calculation methods used. Comparing their results with previous studies and assuming a correlation between the brightness of the luminescence signal and the K-concentration, they recommended to use a K-concentration of 12.5 ± 0.5 %. Furthermore, they noted that this value might not be true for all samples since two out of 21 samples had lower K-concentrations (8.4 ± 0.8 %, 6.5 ± 0.9 %).

Zhao and Li (2005) selected 16 grains and analysed their K-concentration using an electron microprobe. They reported measured single-grain K-concentrations between 13 % and 14 % and a K-concentration of 9.36 % for their bulk feldspar separate sample. Based on the assumption of a correlation between the signal brightness and the K-concentration and a good agreement of their results with the 12.5 ± 0.5 % from Huntley and Baril (1997) they decided to use a K-concentration of 13.5 ± 0.2 %. They did not recommend a K-concentration that should be used but are often cited as 13 ± 1 % K (cf. Appendix B Table B2).

Smedley et al. (2012) measured single-grain K-concentrations on the surface of 87 grains and in-depth profiles of 12 of the 87 grains using laser ablation inductively coupled plasma mass spectrometry. Even though they could not find a general correlation between the brightness of a signal and the K-concentration of a grain, the brightest signals were emitted by grains with a K-concentration of ~12 %. In total all grains with suitable luminescence signals had K-concentrations between 6 % and 13 %. Therefore, they suggested a K-concentration of 10 ± 2 %. The large error was

suggested as it covered a wide range of their K-concentrations measured within a 95 % confidence interval.

Huntley and Hancock (2001) did not measure a K-concentration nor did they recommend a specific K-concentration. They measured Rb-concentrations. Most of the papers citing Huntley and Hancock (2001) specify their K- and Rb-concentration used for $\dot{D}_{int}$ calculations in the same sentence. Therefore, the reference for the used K- and Rb-concentration end up in the same brackets at the end of the sentence. Since Huntley and Hancock (2001) are rarely cited alone and did not measure K-concentrations, we exclude them for our comparison.

Li et al. (2008) measured bulk K-feldspar samples on a beta counter for five different grain sizes for three different samples. They presented K-concentrations between 10 % and 14 %. They stated that there might be a contamination by Na-rich feldspars resulting in underestimation of the K-concentration of their luminescent sample. They therefore used a blue filter combination to isolate luminescence signals emitted by K-rich feldspars. To correct for the contamination during $\dot{D}_{int}$ calculations they assumed a K-concentration of 13 ± 1 % slightly larger than their measured minimum. Since Li et al. (2008) do not give recommendations, are never cited alone, and are mostly cited with the same K-concentration as Zhao and Li (2005), Li et al. (2008) will not be used for our comparison.

Unfortunately, in many feldspar luminescence studies the values cited for the internal K-concentration used, often do not match the referenced sources (cf. Appendix B Table B2). This is partly due to the fact that several sources that recommend different values are cited at once. In some cases, the used K-concentration does not fit any of the cited sources. It is noteworthy that most articles did not state why they used a specific value and why and how they changed the cited value. A detailed table of the five most cited sources, the K-concentration recommended, and the K-concentrations that other studies used despite giving a reference can be found in Appendix B Table B2. Only Huntley and Baril (1997), Zhao and Li (2005) and Smedley et al. (2012) are used for benchmarking purposes in this study. And given that Zhao and Li (2005) is usually cited as 13 ± 1 % K, we also use this value for our comparisons.

4.3 Sample details, instrumentation, and methods

4.3.1 Samples and sample preparation

We selected ten samples with differing chemical compositions and varying origins for our analysis. Maßon et al. (2024) previously analysed the same set of samples for their luminescence characteristics and single-grain K-concentrations based on SEM-EDX measurements (cf. Chapter 3). The first half of the samples were collected within the

Atacama Desert in Chile (ARO-18-08-LP, CSA-1-2-2, LAGU-1-1, PAG-6-4b, PAG-6-6b). The second half of the samples originate from different geological locations from around the world: badlands in Canada (ABLR-1), lake sediments in Japan (HAM-5), a beach ridge in Chile ~1000 km south of the Atacama Desert (ISM-7), the Continental Deep Drilling borehole in Germany (KTB-383-C), and the Mont-Blanc tunnel in Italy (MBT-I-2430). The non-Atacama Desert samples were chosen to capture the wider range of chemical and structural variations of the alkali feldspar solid solution series. These variations range from very low K-concentrations in sample KTB-383-C (~2.5 % K, Guralnik et al., 2015) to high K-concentrations in the sample MBT-I-2430 (~10.8 % K, Riedesel et al., 2021). Table 4.1 summarises general information on the samples.

Preceding the luminescence and K-concentration measurements, the samples underwent a series of preparatory treatments. The samples were sieved a first time, to remove fine (<63 µm) and coarse (>400 µm) material. Afterwards they were treated with HCl (10 %) to remove carbonates, with H_2O_2 (10 %) to dissolve organic material and with $Na_2C_2O_4$ (0.01 N) to disperse the particles. Subsequently, the samples were sieved a second time to obtain the desired grain size fraction (cf. Table 4.1). To enrich the K-rich feldspar fraction, a heavy liquid density separation was used (ρ <2.58 g/cm^3). Sample preparation for KTB-383-C and MBT-I-2430 differed slightly (see Guralnik et al., 2015 and Lambert, 2018 for further details), with the extracted feldspar fraction of KTB-383-C being etched with diluted HF. Both samples are rock samples; therefore, the light-exposed outer surface was removed prior to sample processing, and the remaining material was subsequently crushed. Neither sample was dispersed using $Na_2C_2O_4$.

Table 4.1: *Sample description. Sample MBT-I-2430 was prepared in the laboratory of the University of Lausanne. Sample KTB-383-C was prepared at Risø. All other samples were prepared at the Cologne Luminescence Laboratory.*

Sample ID	Origin	Geomorphic context	Grain size [µm]	Grain hole size [µm]	References
ARO-18-08 LP	Atacama Desert, Chile	Gypsisol in alluvial deposits, crack-filling in network of polygonal cracks	200 – 250	300	Zinelabedin et al., 2022
CSA-1-2-2	Atacama Desert, Chile	Gypsisol-type colluvial sediment, patterned ground	100 – 200	250	Maßon et al., 2024
LAGU-1-1	Atacama Desert, Chile	Gypsisol in lunette-type aeolian sediment	100 – 250	300	Maßon et al., 2024
PAG-6-4b	Atacama Desert, Chile	Mud pan; colluvium	100 – 200	250	Ritter et al., 2019
PAG-6-6b	Atacama Desert, Chile	Mud pan; colluvium	100 – 200	250	Ritter et al., 2019
ABLR-1	Badlands, Canada	Badlands	100 – 200	250	Maßon et al., 2024
HAM-5	Lake Hamana, Japan	Lake sediments	100 – 200	250	Riedesel et al., 2019, 2021
ISM-7	Beach ridge, Chile	Coastal sediments	100 – 200	250	Maßon et al., 2024
KTB-383-C	KTB Borehole, Germany	Bedrock; sillimanite-muscovite-biotite-gneiss	180 – 250	250	Guralnik et al., 2015
MBT-I-2430	Mount Blanc Tunnel, Italy	Bedrock; granite	180 – 212	250	Lambert, 2018

4.3.2 Luminescence measurements

The samples were brushed into standard single-grain discs (see Table 4.1 for grain hole size) under a microscope under white light conditions. A single hair was used to individually place grains into each of the 100 grain holes per disc, ensuring one grain per hole. In samples CSA-1-2-2, HAM-5 and KTB-383-C, however, occasionally two grains occupied a single hole. We administered the same dose to all samples in a single grain dose recovery test, to avoid a bias that could be attributed to a difference in the absorbed dose. Before performing single grain dose recovery tests, all mounted grains were exposed to a SOL2 solar simulator for 24 hours to reset the luminescence signal prior to administering a dose of 150 Gy. Per sample, three discs à 100 grains each were prepared and measured following the $pIRIR_{175}$ protocol outlined in Appendix B Table B3 in the supplementary material. Further details on the reader used for luminescence measurement, the measurement protocol, and the D_e estimation including the rejection criteria used are reported in Maßon et al. (2024).

4.3.3 Determination of K-concentrations in feldspars

For all methods, which determined the K-concentration in the oxide form (% K_2O), the results need to be converted to a non-oxide element concentration (% K) to compare them to the most cited literature values. This was done by multiplying the K_2O concentration results by a conversion factor of 0.830147 based on the molar masses of K (39.1 g/mol) and O (16.0 g/mol) (e.g. Prohaska et al., 2022). Therefore the weight of the element within the oxide (2*39.1 g/mol) is divided by the weight of the oxide (2*39.1 g/mol + 16.0 g/mol) (e.g. Al-Mishwat, 2016).

4.3.3.1 β-counter measurements of bulk material

For bulk K-concentration determination a low-level beta multicounter system (Risø, GM-25-5A Bøtter-Jensen and Mejdahl, 1988) with five sampling positions was used. The β-counter was surrounded by lead blocks and covered with blankets to shield the samples from external irradiation and from light, respectively. Each sampling position within the β-counter differs slightly in the measurement results. A position correction factor was therefore applied. For this purpose, the positions were calibrated in between measurements using a ^{36}Cl standard. The standard was measured for five minutes on each position and the counts per minute were afterwards normalised to position one. As the fifth position in the ^{36}Cl measurements always deviated significantly from the other four and showed considerable fluctuations, this position was not used.

For the measurements on the β-counter two sampling cups for each sample were prepared following Bøtter-Jensen and Mejdahl (1985). Only one cup of sample KTB-383-C could be prepared, as there was not enough sample material available. Under subdued red-light conditions 100 mg of the density-separated feldspar extract (see Chapter 4.3.1) sample material was distributed evenly on the bottom of an upside-down β-counter cup. A labelled piece of cling film was placed on top and secured with a plastic ring (cf. Appendix B Fig. B2). In the same way, one cup was loaded with a K-feldspar standard (FK-N bought via Service d'Analyse des Roches et des Minéraux, K_2O-concentration 12.81 %, Rb-concentration 860 ppm) and one cup with finely ground sucrose (icing sugar from the brand Ja!) to act as blank measurement. The first four positions of the β-counter were filled with two cups of a sample, one cup of the standard and one cup of finely ground sucrose. Each sample was measured for 96 h. After 48 h the position of the two cups with sampling material were switched. The counts per hour of each position were recorded. Although the β-counter is surrounded by lead blocks, there is a small amount of background radiation that penetrates to the detectors inside. As sucrose does not emit beta radiation, the background radiation was measured at the position of the sucrose cup. After the position correction of the hourly counts, the measured background per hour was subtracted from the other positions. Since the K-concentration of the standard is known, the counts of the sample cups were converted to K-concentrations using cross-multiplication. This was based on the assumptions that the ratio of K to Rb in our samples was close to the ratio within the standard and that all the counted beta radiation emitted came from the internal K and Rb of the samples. We neglected that a small proportion of the beta radiation may be emitted by internal U and Th. We used the average of all 192 hourly K-concentration values per sample as the β-counter K-concentration of each sample. We added a reproducibility error to our results in terms of the standard error of all 192 measurements.

4.3.3.2 WDXRF of bulk material

For measurements using the wavelength dispersive X-ray fluorescence spectrometer (WDXRF; Rigaku, ZSX Primus IV) 100 mg of each sample were ground to powder by hand in an agate mortar. A mixture of 100 mg of a cellulose binder ($C_6H_{10}O_5$) and 100 mg of sample material was spread on top of 2000 mg of cellulose binder in aluminium sample boat. This was then pressed at 20 tons using a Retsch PP40 press to make pressed pellet samples suitable for XRF. The spectrometer was equipped with a Rh anode X-ray source. The XRF spectra were measured over the element range of F to Cm. Each sample was measurement once for a duration of 17 minutes. The WDXRF

device calculates the results without specifying a measurement uncertainty. The software calculated the elemental composition based on the assumption that all elements, except chlorine (Cl), were present in the form of oxides.

Samples KTB-383-C and MBT-I-2430 were measured on a different WDXRF device (PANalytical MagiX PRO XRF) also equipped with a Rh anode X-ray source (see Riedesel et al., 2021 for MBT-I-2430). As there was insufficient sample material available, it was not possible to perform another measurement on the same device on which the other samples were measured. For those two samples pressed pellets were prepared as indicated above. Spectra were collected across ten distinct energy ranges and subsequently analysed to yield semi-quantitative results.

4.3.3.3 Single-grain SEM-EDX measurements

After conducting the luminescence measurements, double-sided sticky tape was affixed to a glass microscope slide on one side and then placed with the other side on the upper surface of the single-grain discs (cf. Appendix B Fig. B3). The grains were transferred onto the tape by gently tapping the bottom side of the discs with a piezoelectric ultrasonic cleaner (vibration frequency 30 ± 3 kHz). On average, approximately 80 % of the grains were successfully extracted. Before removing the discs from the tape, the positioning holes locations were drawn on the tape. To fixate the grains, a colourless two-component epoxy resin (Huntsman, Araldite 2020) was used. The location of the position holes was transferred onto the epoxy disc. Finally, it was ensured that no epoxy covered the grains. Therefore, the epoxy discs were sanded and polished with a 1200 SiO_2 sandpaper. All samples were carbon coated. For each sample, this process was applied to three single-grain discs. Only two usable epoxy discs were produced for the samples ISM-7, LAGU-1-1 and MBT-I-2430, as the grains in one disc each changed their position during the epoxy curing process.

A Zeiss Sigma 300-VP scanning electron microscope (SEM) equipped with an Oxford instruments energy dispersive spectroscopy (EDX) detector X-Max^N 80 was used to determine the major element chemistry of the individual grains. The SEM-EDX was operated at a working distance of 8.5 mm, with an aperture diameter of 60 µm and an accelerating voltage of 20 kV, resulting in an output count rate of approximately 45,000 cps. The penetration depth of the measurements depends not only on the measurement settings but also on the material being analysed and can therefore vary. However, it is generally on the order of a few micrometres (Kanaya and Okayama, 1972). The chemical composition of individual feldspar grains was determined through stoichiometric calculations based on the elements O, Na, Mg, Al, Si, K, Ca, Ti, and Fe (see Appendix B Table B4 for exemplary stoichiometric calculations and

Appendix B Fig. B4a for exemplary spectrum and fit). For this purpose, polygons were manually delineated over the individual grains, and the average composition within each polygon was subsequently calculated.

4.3.3.4 Single-grain µ-XRF measurements

One of the epoxy discs described in Chapter 4.3.3.3 per sample was also measured using an energy dispersive µ-XRF (Bruker M4 Tornado) equipped with a Rh anode and operating at 50 kV and 300 µA and a poly-capillary optic. With a beam spot size of 20 µm and a spatial resolution of 40 µm an element map of the whole disc was measured. Each measurement point was acquired with an integration time of 100 ms. The analyses were performed under a controlled vacuum environment maintained at 20 mbar to enhance sensitivity for light elements. Before measurement, an energy calibration for the Bruker Tornado M4 was carried out using a Mn standard. Data acquisition was facilitated by two silicon-drift detector systems, enabling high-resolution elemental mapping. The penetration depth depends on the material analysed but is generally greater than 1 mm, thus the collected signal originates from the entire grain, rather than just from its polished surface. For analysis the same elements as for the SEM-EDX measurement were selected (O, Na, Mg, Al, Si, K, Ca, Ti, and Fe). Afterwards, polygons were manually delineated over the individual grains, and the average composition within each polygon was subsequently calculated through stoichiometry (see Appendix B Table B4 for exemplary stoichiometric calculations and Appendix B Fig. B4b for exemplary spectrum and fit).

4.3.4 Calculations of the luminescence-weighted K estimates

It is often assumed that there is a correlation between the brightness of a grain and its K-concentration (Prescott and Fox, 1993; Spooner, 1992). Therefore, the K-concentration of a sample is expected to be higher for the brightest grains of a sample (Reimann et al., 2012; Smedley et al., 2012). To test this hypothesis, we calculated a luminescence-weighted K estimate for each sample: the *effective K*. The *effective K* is based on the K-concentration of single grains and a weighting factor based on the signal intensity of the T_n signal of the same grains. The *effective K* is calculated as follows:

1. Dismiss grains from a sample without SEM-EDX values
2. Dismiss quartz grains; e.g. grains consisting of pure SiO_2 (on average a sample contained 2.6 % quartz grains)
3. Sort the grains in descending order according to their background corrected T_n signal intensity

4. Set negative background corrected T_n signal values to zero
5. Sum up the background corrected T_n values to obtain the total background corrected T_n signal intensity
6. Calculate the percentage of each grain in the total background corrected T_n signal intensity
7. Multiply the percentage of the total background corrected T_n signal intensity by the K-concentration of the grain
8. Sum up the results from step 7 to obtain the *effective K*-concentration of the sample

We also calculated the average K-concentration for all "luminescent grains" per sample. We defined "luminescent grains" as grains with T_n signal intensities greater than three standard deviations above its background. For a better readability the average K-concentration for all luminescent grains will be referred to as the *luminescent grains*.

4.3.5 Dose rate calculations

The dose rate and age calculator (DRAC; Durcan et al., 2015) was used for all dose rate calculations. For each sample several total $\dot{D}$s including the corresponding $\dot{D}_c$, $\dot{D}_{ext}$ and $\dot{D}_{int}$ were calculated based on the different K-concentrations: One total $\dot{D}$ for each of the three most cited K-concentrations (10 ± 2 %, 12.5 ± 0.5 %, 13 ± 1 %), the measured WDXRF and β-counter K-concentrations, the average SEM-EDX and μ-XRF K-concentration, the *effective K*, and the *luminescent grains*. Since we are not yet able to calculate $\dot{D}_{ext}$ at a single-grain level, we have not calculated $\dot{D}$s at a single-grain level. Except for the K-concentration, the radionuclide concentrations factor, and the grain size attenuation factors the input values from the studies cited in Table 4.1 were taken. If a study did not contain all necessary input values for a sample, an attempt was made to use values that were as appropriate as possible. The accuracy of all input values except for the K-concentration is of secondary importance in this study, as the influence of the K-concentration on the total $\dot{D}$ is mainly to be considered. For further details on individual $\dot{D}$ calculation input variables cf. Appendix B Table B5.

4.4 Limitations and practicability

The sample selection of this study aimed at analysing a variety of different feldspars, with a focus on samples from the Atacama Desert in Chile. Therefore, our findings might not reflect the majority of samples analysed elsewhere. Although it has been shown that the $\dot{D}_{int}$ in feldspars arises from U, Th, Rb, and K (e.g. Smedley and Pearce,

2016), we focussed on the contribution of internal K concentrations to the $\dot{D}_{int}$, thus excluding the contribution of the internal alpha $\dot{D}$ to the total $\dot{D}_{int}$. This may result in an underestimation of the $\dot{D}_{int}$ in grains where the internal U- or Th-concentrations are unexpectedly high (see Smedley and Pearce, 2016; Zhao and Li, 2005).

Each of the presented methods to determine the K-concentration has its own limitations. Hence, before discussing the results, all methods need to be critically reviewed. All four methods are semi-quantitative and can therefore only result in approximate K-concentrations, which should not be compared directly. The most cited literature values are based on quantitative and semi-quantitative measurements. However, the values for the K-concentrations cited are in all three cases just estimates of the correct average K-concentration.

The β-counter method relies on the assumption that the ratio between K and Rb, Th, and U within a sample is the same as within the standard that is used for comparison. However, Buylaert et al. (2018) did not find a constant relationship between K and Rb and Smedley and Pearce (2016) found variability in the internal U and Th concentrations. Even though for most samples the K to Rb ratio should be similar and the internal U- and Th-concentrations should be negligible, this might introduce an error (Huntley and Hancock, 2001; Smedley and Pearce, 2016). Nevertheless, the β-counter method is a fast, cost-efficient, and easy way to obtain an estimate of the internal K-concentration of a sample. If the measurement can be conducted in the dark, the sample material can still be used for any subsequent luminescence measurements, and no sampling material will be lost.

With the WDXRF a wider range of elements can be measured simultaneously in a short amount of time. It requires additional sample preparation steps and thus a small proportion of the sampling material cannot be used for further luminescence measurements following WDXRF.

Incorrect estimates of the K-concentration can occur with both bulk material methods if a non-representative sub-sample is measured. This can become a problem especially with heterogeneous samples. If sufficient sample material is available, several sub-samples should therefore be measured.

For SEM-EDX single-grain measurements the grains need to be fixated in resin and polished afterwards. During this process entire grains might get lost, or polishing might result in the removal of parts of the grain. Alkali feldspars, often characterised by exsolution lamellae, can have a heterogeneous distribution of K^+ ions in their lattice. Removing part of the grain through polishing might therefore influence the measured overall K-concentration of the grain. Nevertheless, previous studies have shown that the outer surface of feldspar grains can differ in their elemental concentration compared to the interior of the grain (e.g. Smedley et al., 2012) as a

result of weathering processes (Parish, 1994). Therefore, polishing offers the advantage of avoiding a bias from potential surface coatings. It should also be noted that, due to the shallow penetration depth of SEM-EDX (on the order of a few micrometres), only elemental concentrations of the polished surface are captured, and any heterogeneity deeper within the grain remains undetected. It is further possible that not only the grain but also parts of the surrounding resin will be measured, due to inaccurate polygon selection, which can thus influence the average K-concentration of the grain. The preparation, measurement, and analysis process of SEM-EDX single-grain measurements is more time consuming and costlier than for the presented bulk measurements.

The μ-XRF method is most suitable for polished surfaces. Thus, for best results it requires the same sampling preparation steps as the SEM-EDX measurement inducing the same limitations as mentioned above. Since the penetration depth of μ-XRF measurements exceeds the grain diameter, parts of the epoxy resin below the grains will be measured as well. The epoxy resin used consists mainly of elements that cannot be detected with the μ-XRF device (H, O, C, N). As a result, the resin does not contribute to the measured spectrum, and the relatively deep penetration depth of the method is not problematic in this context. Furthermore, for the measurements, polygons have to be drawn onto the sample area of interest, to define regions of interest for the subsequent measurement. Dependent on the shape, colour and opacity of the grain, tracing the ideal grain shape was difficult, leading to measurements of only parts of the grains in some cases, or alternatively, resulting in measuring resin in addition to the actual grain. If a measurement point within a polygon falls entirely within the epoxy resin, it will influence the average value calculated for that polygon. Particularly in the measurements of sample CSA-1-2-2, epoxy resin was included in the analysed polygons, resulting in lower total K-concentrations in grains for which resin was included in the polygon shape. In all other samples the K-concentrations determined with the μ-XRF is higher compared to the SEM-EDX (cf. Chapter 4.5.2). Moreover, the embedding process is relatively time-consuming. For routine applications, a direct measurement of grains without resin embedding could be a practical alternative. This approach reduces preparation time but may decrease the measurement precision. However, it must be taken into account that the material on which the grains are mounted (e.g. a single-grain disc or adhesive tape) is also included in the μ-XRF measurement due to the large penetration depth of the μ-XRF method. The potential effect of this on the measured K-concentrations was not investigated in this study. Since the penetration depth of μ-XRF measurements exceeds the grain diameter, analyses of both polished, resin-embedded grains and unembedded grains can be affected by surface coatings. Nevertheless, this influence

is expected to be minimal because the surface layer constitutes only a small proportion of the total irradiated volume, and the signal is largely dominated by the grain interior. The μ-XRF device we used in this study is not effective in measuring light elements, including Na. Since Na is one of the major constituents of feldspar, not determining its correct concentration might lead to the overestimation of all element concentrations measured, including K. This could explain measurements yielding K-concentrations above the maximum possible K-concentration of 14.05 %. Both the SEM-EDX device and the μ-XRF were not specifically calibrated with feldspar standards for the measurements. Calibration with different feldspar standards could increase the accuracy of both methods.

Both single-grain-based geochemical methods are time consuming in terms of sample preparation, measurement preparation and data processing, even if the measurements themselves can be carried out overnight. However, O'Gorman et al. (2021a) developed a fast and automated K-concentration measurement method using a quantitative evaluation of minerals using energy dispersive spectroscopy (QEM-EDS) technique. Unfortunately, this method was not available to us.

The two bulk-sample measurement methods, on the other hand, are less laborious than the single-grain methods available to us. Yet, they provide no information regarding the heterogeneity of the samples.

4.5 Results and discussion

This chapter presents and evaluates results of the K-concentration determination on the bulk and average level (Chapter 4.5.1), as well as on the single grain level (Chapter 4.5.2). In Chapter 4.5.1 we compare K-concentrations obtained for bulk samples with averages obtained from single-grain-based measurements and the luminescence-weighted K estimates *effective K* and *luminescent grains*. Chapter 4.5.2 gives detailed information on the variation in K-concentrations found on the single grain level using SEM-EDX and μ-XRF measurements. Finally, in Chapter 4.5.3 we detail practical implications of our experimental observations.

4.5.1 Bulk sample measurements and sample average concentrations

Figure 4.2 presents all measurement results performed on bulk sample material (β-counter and WDXRF), the average values for the single-grain measurements (SEM-EDX and μ-XRF) and the calculated luminescence-weighted K estimates *effective K* and *luminescent grains*, and compares them to the three most commonly used literature values (cf. Chapter 4.2.2).

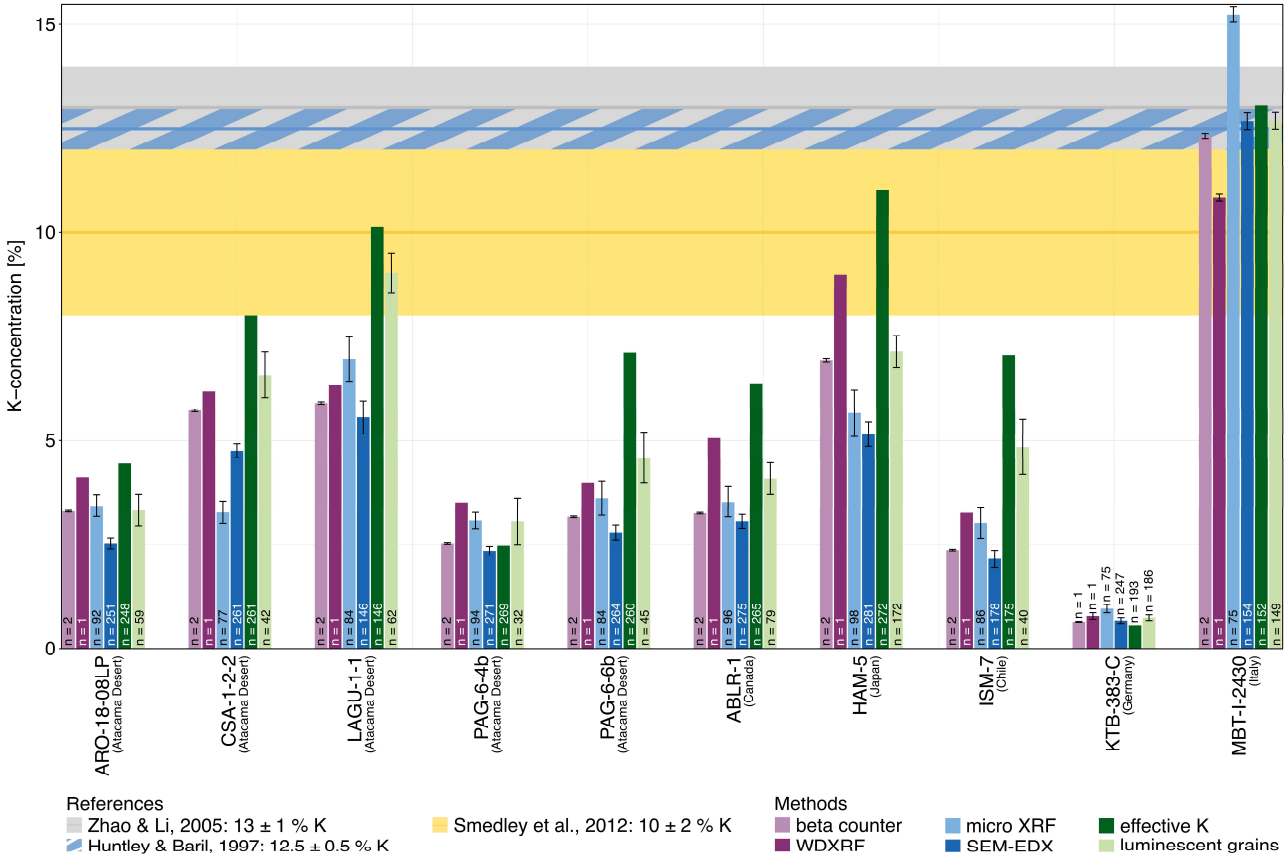

Fig. 4.2: *K-concentrations for each sample determined with different methods, respectively calculated from measured K-concentrations. For the single-grain measurements (μ-XRF and SEM-EDX), the averages are presented. The error bars represent the standard errors. Horizontal bars represent the most frequently used literature values for the K-concentration and their corresponding errors of 10 ± 2 %, 12.5 ± 0.5 % and 13 ± 1 %.*

Across all measurement techniques, MBT-I-2430 is the sample with the highest K-concentrations (10.8 % – 15.2 %) and KTB-383-C the sample with the lowest K-concentrations (0.6 % – 1.0 %). Considering the uncertainties reported, the literature values suggest K-concentrations from 8 % (lowest value by Smedley et al., 2012) to 14 % (highest value suggested by Zhao and Li, 2005). From our samples, measurement results of only two samples lie within this range. In case of HAM-5 the WDXRF results (9.0 %) and in case of MBT-I-2430 the β-counter results (12.3 ± 0.1 %), WDXRF (10.8 ± 0.1 %), and average SEM-EDX (12.7 ± 0.2 %) results are within the range of at least one of the proposed literature values. The average μ-XRF K-concentration for sample MBT-I-2430 (15.2 ± 0.2 %) is the only measured value above the suggested range. Potential reasons for this K-concentration being greater than the maximum possible K-concentration of feldspars (14.05 %) are discussed in Chapter 4.4. Measurements of all other samples are on average 55.6 % below the lowest value suggested by Smedley et al. (2012). The greatest total difference is 12.4 % K between the β-counter K-concentration of sample KTB-383-C with 0.6 ± 0.1 % K and the literature value from Zhao and Li (2005) with 13 ± 1 % K.

In each sample a different amount of grains was used for the calculation of each of the luminescence-weighted K estimates *effective K* and *luminescent grains* (cf. Fig. 4.2). The amount of grains used ranges from 32 grains for the calculation of the *luminescent grains* in sample PAG-6-4b up to 272 grains for the calculation of the *effective K* for sample HAM-5. Comparing the twenty calculated luminescence-weighted K estimates to the three most cited K-concentrations only five of them are within the suggested range of 8 – 14 % K. The five luminescence-weighted K estimates in the range suggested by the three most cited references are the *effective K* and the *luminescent grains* for the samples LAGU-1-1 and MBT-I-2430 and the *effective K* for sample LAGU-1-1. For all ten samples, apart from the sample KTB-383-C, these two luminescence-weighted K estimates, which are based on the single grain SEM-EDX results, are greater than the average SEM-EDX results. The *effective K* was calculated based on the assumption that K-feldspar separates might not only contain feldspar grains with a high K-concentration (Huntley and Baril, 1997; Smedley et al., 2012) but that the measured luminescence signal is dominated by grains with a high K-concentration. Therefore, it has been suggested that the heterogeneity of K-concentrations for a given sample is of low importance (Huntley and Baril, 1997; Prescott and Fox, 1993; Spooner, 1992). Following this assumption, the *effective K* for each sample should be in the range of the proposed literature values. In contrast to findings of Smedley et al. (2012), our data shows that also grains with a low K-concentrations contribute substantially to the overall luminescence signal (cf. Fig. 4.2 all samples except LAGU-1-1, HAM-5, and MBT-I-2430). Therefore, the assumption that the cumulative light sum curves are anyway dominated by K-rich feldspar grains and therefore the heterogeneity of the K-concentration within a sample is unimportant is not valid for the analysed samples.

Since all our measurement techniques are semi-quantitative it is impossible to provide an estimation of the most accurate representation of the internal K-concentration of a sample. However, we found that 85 % of our measurement results and the luminescence-weighted K estimates are not within the proposed range of the literature values (8 – 14 % K). Therefore, we conclude that using an often arbitrarily chosen literature value for the K-concentration (see literature review Chapter 4.2.2) can lead to a significant underestimation of the true sample-specific K-concentration.

4.5.2 Distributions of single-grain K-concentrations

Across all samples the single-grain K-concentrations vary from 0.0 % (eight out of ten samples) up to 14.7 % (MBT-I-2430) measured with the SEM-EDX and from 0.0 % (eight

out of ten samples) to 18.2 % (MBT-I-2430) measured with the μ-XRF (cf. Table 4.2). Within each sample the K-concentrations also show large ranges of up to 14.2 % K for SEM-EDX measurements (ABLR-1 0.0 % – 14.2 %) and 16.6 % K for μ-XRF measurements (HAM-5 0.0 % – 16.6 %). Sample MBT-I-2430 has the most homogeneous K-concentration distribution, with a coefficient of variation of 19.4 % for the SEM-EDX measurements and 10.9 % for the μ-XRF measurements. In contrast, samples KTB-383-C and ISM-7 have the most heterogeneous K-concentration distributions with coefficients of variation of 161.8 % for the SEM-EDX measurements (KTB-383-C) and 112.6 % for the μ-XRF measurements (ISM-7). Figure 4.3 shows the single-grain K-concentration measurement results in comparison to the literature values and the bulk measurements and the luminescence-weighted K estimates for ISM-7, one of the most heterogeneous sample, and MBT-I-2430, the most homogeneous sample. A complete comparison for all ten samples is provided in the supplementary material (cf. Appendix B Fig. B5).

From all grains measured with the SEM-EDX device, the K-concentration of only 15 % of all grains measured is within the range of the three proposed literature values (8 – 14 % K). In the case of the K-concentrations determined using the μ-XRF only 12 % of all grains have a K-concentration within the range of the three proposed literature values (8 – 14 % K). In total less than 14 % of the measured single-grain K-concentrations (including their uncertainties) are in agreement with the most cited literature values (cf. Fig. 4.3 and Appendix B Fig. B5). Moreover, fewer than 20 % of the measured single-grains have K-concentrations that align with any of the bulk measurements, the averaged single-grain measurements, or the luminescence-weighted K estimates (cf. Fig. 4.3 and Appendix B Fig. B5). This demonstrates that, due to the large spread of single-grain values, it is challenging to represent a sample's internal K-concentration with a single, representative value.

Table 4.2: *Summary of the single-grain K-concentration measurements, with CV being the coefficient of variation.*

Sample	SEM-EDX							μ-XRF						
	min [% K]	max [% K]	range [% K]	average [% K]	se	n	CV [%]	min [% K]	max [% K]	range [% K]	average [% K]	se	n	CV [%]
ARO-18-08-LP	0.0	11.5	11.5	2.5	0.1	251	79.4	0.2	11.4	11.2	3.4	0.3	92	72.3
CSA-1-2-2	0.2	13.5	13.2	4.8	0.2	261	56.2	0.0	12.0	12.0	3.3	0.3	77	71.5
LAGU-1-1	0.0	13.4	13.4	5.6	0.4	146	84.2	0.0	16.2	16.2	7.0	0.5	84	71.4
PAG-6-4b	0.0	11.9	11.9	2.3	0.1	271	77.4	0.0	12.0	11.9	3.1	0.2	94	62.5
PAG 6-6b	0.0	12.9	12.9	2.8	0.2	264	103.1	0.0	15.9	15.9	3.6	0.4	84	103.2
ABLR-1	0.0	14.2	14.2	3.1	0.2	275	95.1	0.0	15.0	15.0	3.5	0.4	96	101.6
HAM-5	0.0	13.7	13.7	5.2	0.3	281	93.9	0.0	16.6	16.6	5.7	0.6	98	96.5
ISM-7	0.0	13.0	13.0	2.1	0.2	178	130.4	0.0	15.1	15.1	3.0	0.4	86	112.6
KTB-383-C	0.0	8.2	8.2	0.7	0.1	247	161.8	0.0	4.1	4.1	1.0	0.1	75	88.6
MBT-I-2430	1.0	14.7	13.6	12.7	0.2	154	19.4	7.8	18.2	10.4	15.3	0.2	75	10.9

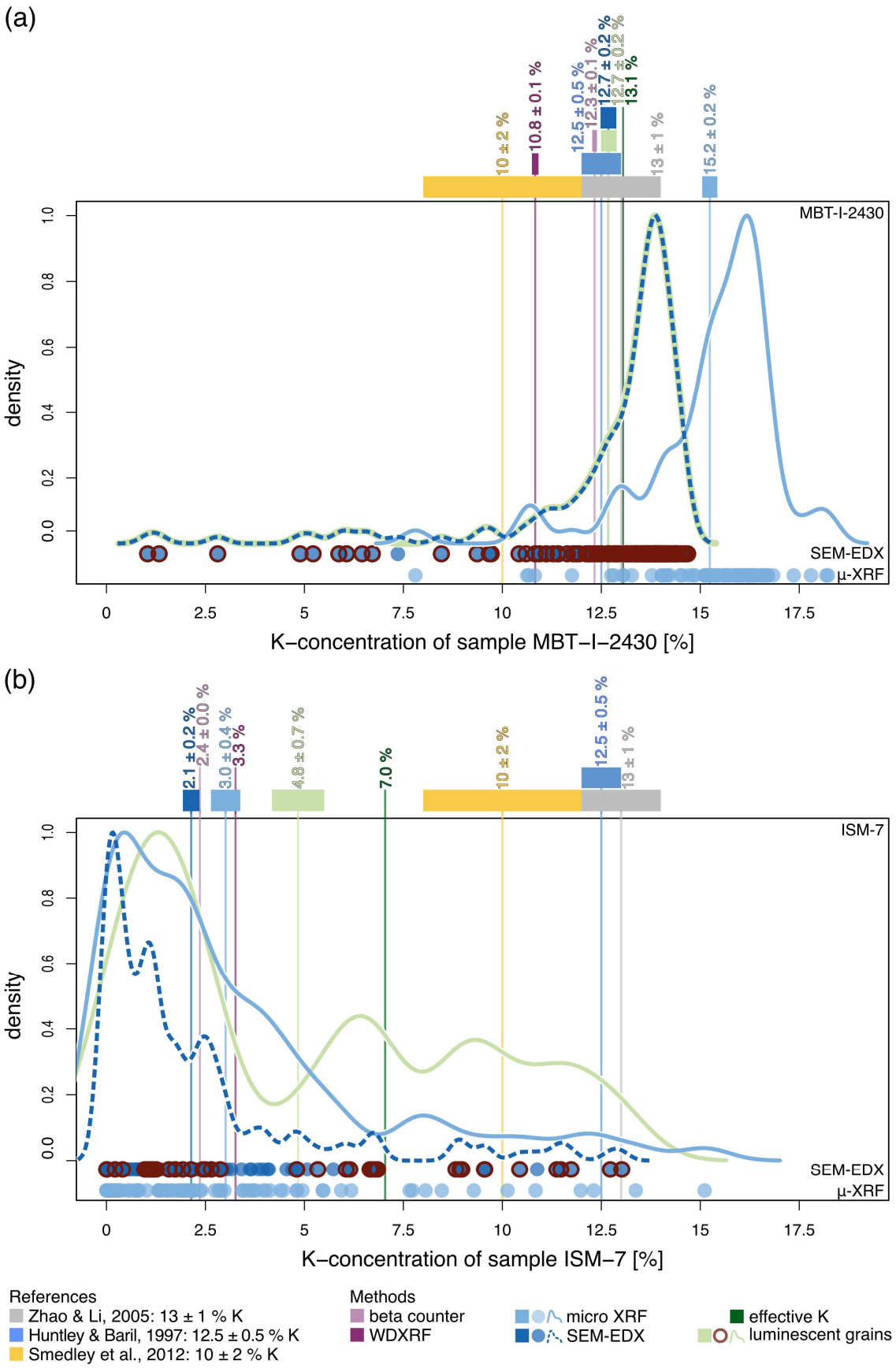

Fig. 4.3: *Single-grain K-concentrations for the overall most homogeneous sample MBT-I-2430 (**a**) and the most heterogeneous sample ISM-7 (**b**). The dark blue dashed density curves and dots are based on the SEM-EDX measurements and the light blue ones on the µ-XRF measurements. The red circles around the dark blue*

dots and the light green density curve represent the luminescent grains. The vertical lines represent the K-concentrations presented in Chapter 4.5.1, boxes above the graph representing their errors.

For the most homogenous sample MBT-I-2430, 69.1 % of the single-grain K-concentrations measured with the SEM-EDX are within the range of one of the literature values. However, 85.1 % of the single-grain K-concentrations determined by the µ-XRF for sample MBT-I-2430 are greater than the range covered by the literature values. Interestingly, 82.4 % of the single-grain µ-XRF K-concentrations for sample MBT-I-2430 are greater than the physically possible maximum K-concentration for pure feldspars of 14.05 %, which can likely be explained by limitations of the measurement procedure (cf. Chapter 4.4). For the heterogenous sample ISM-7 (Fig. 4.3b), which is representative for eight and thus the majority of the remaining samples (cf. Appendix B Fig. B5), the K-concentrations of most of the grains are not within the range of the most cited literature values (8 – 14 % K) and the single-grain distribution of the K-concentration is considerably right-skewed.

For the *luminescent grains* (T_n signal >3σ above background, see red circles in Figs. 4.3 and Appendix B Fig. B5) a similar picture appears: All samples exhibit *luminescent grains* with K-concentrations spanning the entire possible range of the respective sample. Even the most homogeneous sample MBT-I-2430 contains *luminescent grains* with K-concentrations as low as 1.0 %. However, whilst most (71 %) of MBT-I-2430's *luminescent grains* are within the range of K-concentrations suggested in the literature, all other samples show either right skewed distributions of *luminescent grain* K-concentrations (see for example ISM-7 in Fig. 4.3b), or multi-modal distributions, with the main peak located in the lower third of the possible K-concentration range (see for example CSA-1-2-2 in Appendix B Fig. B5b). We assume that the observed right-skewness in some of the distributions is primarily caused by the presence of a few luminescent grains with higher K-concentrations, while the majority of luminescent grains in these samples tend to have relatively low K-concentrations. This reflects the overall distribution of K-concentrations within the full grain population, which is also skewed in a similar way.

The *luminescent grains* are calculated based on the assumption that K-feldspar separates contain some Na-feldspar grains due to incomplete sample separation using heavy liquids (e.g. Huntley and Baril, 1997). The presence of Na-feldspar grains in the separate would lead to a lower bulk K-concentration. However, the luminescence signal emitted by these Na-rich feldspar grains is assumed to be removed by using a blue filter combination during the luminescence measurements (cf. Fig. 2.4). Thus, the blue luminescence emission recorded should be dominated by the K-rich feldspar grains, likely with concentrations in the range of 12.5 ± 0.5 % (Huntley and Baril, 1997). However, the results presented here show that luminescent grains occur over

the entire range of possible K-concentrations. Suggesting that **i)** Na-feldspars are still present within density separated K-feldspar separates, **ii)** the luminescence of Na-rich feldspars is not successfully removed using the blue filter combination, and most importantly **iii)** that sufficiently bright luminescent grains can be found across the entire alkali feldspar range. These observations are at odds with the current common practice of using relatively high K-concentration from the literature, which is based on the assumption that the luminescence emission in the blue is dominated by K-rich feldspar grains (cf. Chapter 4.2.2).

4.5.3 Practical implications

The results presented here are applicable to both single-grain and multi-grain coarse-grain feldspar luminescence dating. An exception to this is polymineral fine-grain luminescence dating, where usually grains with a diameter of 4-11 µm are considered. According to Guérin et al. (2012), the β self-dose of the internal K-concentration for this grain size fraction is as low as 0.007, which implies that the internal K-concentration does not significantly contribute to the $\dot{D}_{int}$ in this context. Importantly, it should be noted that none of the single-grain K-concentration distributions are normally distributed (Fig. 4.3, Appendix B Fig. B5), suggesting that the corresponding average value based on the arithmetic mean is not the optimal representation of the single-grain K-concentration for most of our samples. Furthermore, the experimental errors of all measurement methods are relatively small, leading to small uncertainties on the experimentally obtained averaged or bulk K-concentrations. This is in stark contrast to the often broad and/or skewed single-grain-based K-concentration distributions. Consequently, a single bulk or averaged measured value or one of the luminescence-weighted K estimates is therefore not representative of all grains in a sample. However, it seems impracticable to determine the K-concentration of all luminescent grains individually with the methods available to us. We propose to carry out a simple bulk measurement in a first step to determine the average K-concentration of the sample material. In a second step we furthermore suggest to perform single-grain K-concentration measurements (using SEM-EDX or µ-XRF) on a small number of individual grains to determine the heterogeneity of the sample. Based on the thus collected single-grain data an error estimate for the bulk measurement could be determined. This second step becomes particularly important when the bulk K-concentration is low, as single-grain measurements allow for a more informed assessment of the associated uncertainty. Low bulk values may either reflect consistently low K-concentrations across grains, requiring only a small error

estimate, or they may mask a wide internal variability, in which case a larger uncertainty would be more appropriate.

Since the β-counter is the easiest bulk measurement to implement and the μ-XRF provides the most efficient single-grain measurement, we tested this combination more in-depth. We found that 72.2 % of the K-concentrations of the individual grains lie within the sample-specific range for the K-concentration determined in this way (β-counter result ± sd of μ-XRF results).

4.6 Effect of the K-concentration on the dose rate

The internal K-concentration of a sample affects the size of the $\dot{D}_{int}$. For a sample with a large $\dot{D}_{ext}$ the K-concentration and thus the $\dot{D}_{int}$ will have a smaller effect on the total $\dot{D}$ compared to a sample where $\dot{D}_{int}$ is relatively large compared to $\dot{D}_{ext}$. The latter is often the case for relatively quartz-rich coarse sediments where $\dot{D}_{int}$ can contribute up to ~50 % to the total $\dot{D}$ (e.g. Reimann and Tsukamoto, 2012). Figure 4.4 illustrates the effect of the internal K-concentration on the total $\dot{D}$ of each sample, for dose rates based on the most-commonly used literature K-concentrations values (open symbols), our measured K-concentrations (filled symbols), and our luminescence-weighted K estimates (filled symbols). However, it should be noted that no measurements of internal U- and Th-concentrations were performed. High internal concentrations of U and Th could lead to an increased $\dot{D}_{int}$, which is not accounted for in our calculations (Smedley and Pearce, 2016; Zhao and Li, 2005). This may also apply to grains with elevated K-concentrations (Zhao and Li, 2005).

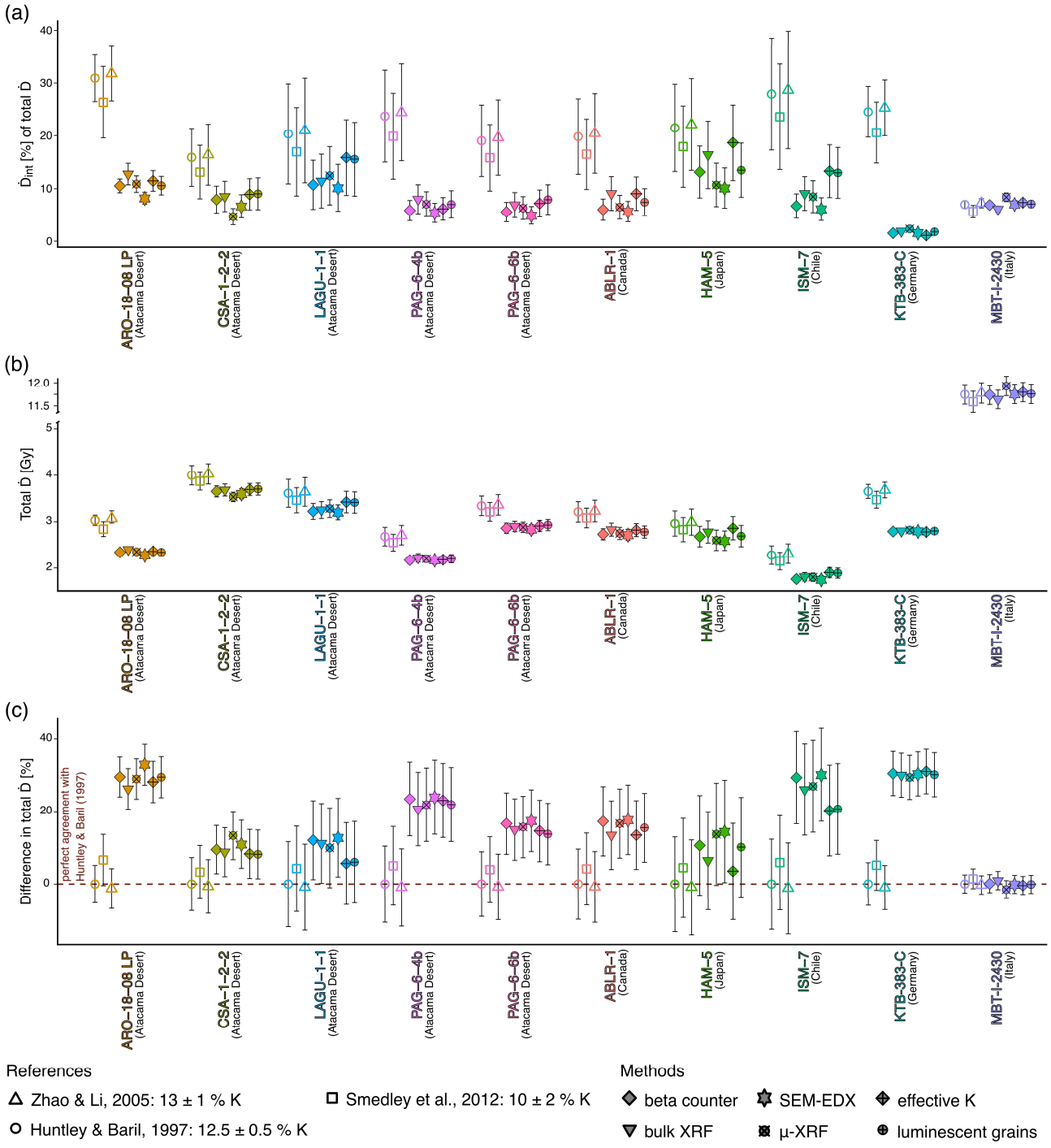

Fig. 4.4: *$\dot{D}$ results, with $\dot{D}_{int}$ and total $\dot{D}$ calculated with DRAC (Durcan et al., 2015) based on the different K-concentrations of the three most cited literature values (open symbols), the measured K-concentrations (filled symbols), and luminescence-weighted K estimates (filled symbols). All other input variables are described in Chapter 4.3.5.* ***a****) The proportion of the $\dot{D}_{int}$ in the corresponding total $\dot{D}$.* ***b****) The total $\dot{D}$.* ***c****) A comparison between the total $\dot{D}$ based on the K-concentration of 12.5 ± 0.5 % (Huntley & Baril, 1997) and the total $\dot{D}$ based on the measured K-concentrations and luminescence-weighted K estimates. The dashed line indicates a perfect agreement with the total $\dot{D}$ based on the K-concentration of 12.5 ± 0.5 % (Huntley & Baril, 1997).*

The large discrepancy observed between the literature values and the K-concentrations measured for each sample is also reflected in the proportion of the

$\dot{D}_{int}$ of the total $\dot{D}$ (Fig. 4.4a). Across all samples the proportion of the $\dot{D}_{int}$ in the total $\dot{D}$ varies between ~1 % and ~32 %. KTB-383-C and ARO-18-08-LP show the largest variations in the proportion of $\dot{D}_{int}$ observed within a sample, with $\dot{D}_{int}$ in KTB-383-C ranging from 1.1 % (based on the *effective K*) to 25.3 % (based on Zhao and Li, 2005) and in ARO-18-08-LP ranging from 8.2 % (based on mean SEM-EDX measurements) to 31.8 % (based on Zhao and Li, 2005). Sample MBT-I-2430 has the smallest variations within a sample, since, except for the mean µ-XRF K-concentration, all measured K-concentrations and luminescence-weighted K estimates are within the range of the proposed literature K-concentrations. Therefore, also all $\dot{D}_{int}$, except for the $\dot{D}_{int}$ based on the mean µ-XRF measurement, are in unity with each other when considering their uncertainties.

In nearly 60 % of the cases investigated here, the $\dot{D}_{int}$ estimates based on the proposed literature K-concentrations are not in agreement with the $\dot{D}_{int}$ calculated using measured K-concentrations or luminescence-weighted K estimates within uncertainties (compare open symbols to closed symbols in Fig. 4.4a). As this deviation is a one-directional systematic error for nine out of ten samples it will lead to an overestimation of the $\dot{D}_{int}$ in most samples. This error is particularly pronounced in the samples KTB-383-C and ARO-18-08-LP.

Figure 4.4b shows the effect of the different K-concentrations on the total $\dot{D}$. MBT-I-2430 exhibits the highest total $\dot{D}$s, ranging from 11.6 Gy ka^{-1} (WDXRF) to 11.9 Gy ka^{-1} (mean µ-XRF). Dose rates calculated for all other samples range between 1.8 Gy ka^{-1} and 4.0 Gy ka^{-1}. For all ten samples the total $\dot{D}$ based on the three proposed K-concentrations from the literature are in unity within their respective uncertainties (Fig. 4.4b open symbols) within each individual sample. In all cases, the total $\dot{D}$ based on the measured values and the luminescence-weighted K estimates are also in agreement within their uncertainties (Fig. 4.4b closed symbols) for each individual sample. However, $\dot{D}$s calculated using literature K-concentrations are only in agreement with total $\dot{D}$s calculated using experimentally obtained K-concentrations in 39 % of the cases, and this includes their respective uncertainties.

Figure 4.4c illustrates the differences between the total $\dot{D}$s based on the measured K-concentrations and luminescence-weighted K estimates for the K-concentration and the total $\dot{D}$ based on the K-concentration of 12.5 ± 0.5 % from the most cited reference (Huntley and Baril, 1997). A figure displaying the results in comparison to results obtained using the values by Smedley et al. (2012) and Zhao and Li (2005) can be found in the supplement (cf. Appendix B Fig. B6). With the exception of sample MBT-I-2430, the total $\dot{D}$ is systematically overestimated using a literature-based K-concentration (cf. Fig. 4.4c, Appendix B Fig. B6). The mean overestimation of the total $\dot{D}$ across all three literature values based on the remaining nine samples is 17.2 ± 8.1 %. The

maximum deviation can be found for the mean SEM-EDX result of sample ARO-18-08-LP: for Huntley and Baril (1997) the deviation is 32.9 % (Fig. 4.4c), for Zhao and Li (2005) the deviation is 34.6 % (Appendix B Fig. B6a) and for Smedley et al. (2012) the deviation is 24.7 % (Appendix B Fig. B6b).

In general, we observe a systematic one-directional deviation in the total $\dot{D}$ for nine out of ten samples when comparing literature value-based $\dot{D}_{int}$ to measurement-based $\dot{D}_{int}$ not incorporating $\dot{D}_{int}$ that might arise from high internal U- or Th-concentrations. Assuming that measured K-concentrations and calculated luminescence-weighted K estimates are more reliable than literature-based values, and that we do not have unusually high internal U- or Th-concentrations, this systematic overestimation of the total $\dot{D}$ would lead to a systematic underestimation of the luminescence age. Thus, we strongly recommend to base the decision on the K-concentration for the calculation of $\dot{D}_{int}$ on experimental data rather than literature values. Moreover, we find that all K-concentrations based on the four experimental methods used and the luminescence-weighted K estimates resulted in sample-wise total $\dot{D}$s agreeing with each other within uncertainties (cf. Fig. 4.4b). Therefore, we conclude that the measurement technique for the determination of the internal K-concentration is of minor importance for the total $\dot{D}$ of a sample, but that measuring the K-concentration of each sample results in more accurate dose rates compared to using literature-based estimates.

4.7 Conclusion

In feldspar luminescence dating studies, the internal K-concentration is often based on published K-concentrations. Furthermore, it is often assumed that the luminescence of feldspars predominantly arises from K-rich feldspar grains. In this study we thoroughly tested this critical assumption regarding the accuracy of feldspar luminescence dating and we made the following main observations:

- Our comprehensive literature review of 432 published studies, presenting feldspar luminescence dating results since 2009, revealed that 76 % of these studies use literature-derived K-concentrations. 96 % of these studies choose a literature value without any measurement of the sample-specific K-concentration.

- Our bulk sample analyses, averaged single-grain K measurements, and luminescence-weighted K estimates are in 85 % of the cases lower than the three most cited literature values (12.5 ± 0.5 % K Huntley & Baril, 1997; 13 ± 1 % K Zhao & Li, 2005; 10 ± 2 % K, Smedley et al., 2012).

- Our effective K-concentration calculations challenge the common assumption that the majority of the feldspar luminescence signal originates from high-K feldspar grains, as this holds true in only one out of ten samples investigated. Our single-grain analyses reveal considerable heterogeneity in K-concentrations, and that the blue luminescence emission is not dominated by K-rich feldspar grains. If uncertainties are considered only ~14 % of the single-grain K-concentrations are within the range of the literature values.

- Our data further shows that the overestimation of the K-concentration of the three most cited literature values in nine out of ten samples results in systematic one-directional errors in the $\dot{D}_{int}$ and therefore total $\dot{D}$ calculations for these samples of up to 34.6 %.

- Our comparison of the total $\dot{D}$ derived from the different K-concentration measurements and both associated luminescence-weighted K estimates agree with each other. Our data suggest that a sufficient agreement between bulk and average single-grain K-concentration measurements is achieved, yet they are not a good representation of all single grains.

Based on our findings, we strongly recommend routinely measuring the bulk K-concentration for each sample as a standard procedure of the $\dot{D}$ determination protocol. If the bulk measurements indicate low K-concentrations, thus potentially suggesting either heterogeneous K-concentrations or overall low K-concentrations, this routine should be complemented by targeted single-grain K-concentration analyses to assess intra-sample variability. This combined approach is essential for improving the accuracy of dose rate calculations and, ultimately, the accuracy of feldspar luminescence dating. Furthermore, spatially resolved luminescence measurements would be desirable to assess whether luminescence originates exclusively from K-rich domains within individual grains or from the entire grain, regardless of its K-concentration.

We also suggest that unless confirmed by measurements, future publications should refer to the dated mineral fraction as ‘feldspar dating’ rather than ‘K-feldspar dating’.

4.8 Data availability

Partly processed data is available on Zenodo https://doi.org/10.5281/zenodo.15533531.

4.9 Author contribution

LM: conceptualization, writing - original draft, formal analysis, investigation, visualisation; SR: conceptualization, writing – review & editing, supervision; SO, AZ, AB, and HC: investigation, writing – review & editing; TR: conceptualization, writing – review & editing, supervision, funding acquisition.

4.10 Competing interests

The authors declare that they have no known competing financial interests or personal relationships that could have appeared to influence the work reported in this paper.

4.11 Acknowledgements

This project is affiliated to the Collaborative Research Centre 1211 “Earth – Evolution at the Dry Limit” (Grant-No.: 268236062) funded by the German Research Foundation (Deutsche Forschungsgemeinschaft, DFG), Germany. We would like to thank our colleagues who kindly supplied us with sample material. We thank Georgina E. King (Université de Lausanne) for MBT-I-2430, Benny Guralnik (Technical University of Denmark) for KTB-383-C, Dominik Brill (University of Cologne) for PAG-6-4b, PAG-6-6b and ISM-7, Simon M. May (University of Cologne) for CSA-1-2-2 and LAGU-1-1, and Aline Zinelabedin (University of Cologne) for ARO-18-08 LP. SR would like to thank Ulrike Hardenbicker for guidance in the field during which sample ABLR-1 was taken, and for hosting her at the University of Regina, Canada. We also thank Kathrin Jung (University of Cologne) for embedding our grains in resin. SR acknowledges support by the European Union’s Horizon Europe research and innovation programme under the Marie Skłodowska-Curie grant agreement (RECREATE, grant no. 101103587). The sampling campaign during which sample ABLR-1 was sampled was financially supported by a Female Research Grant from the Faculty of Mathematics and Natural Sciences, University of Cologne, awarded to SR.

Chapter 5

Challenges in the application of SGCs to natural Atacama Desert samples

An approximate answer to the right question is worth a great deal more than a precise answer to the wrong question (John Tukey)

Or isn't it?

The aim of this dissertation is to decipher activity in Atacama Desert soils and surfaces using single-grain feldspar luminescence dating. As discussed in Maßon et al. (2024, Chapter 3 this thesis), single-grain luminescence measurements of Atacama Desert feldspars are extremely time-consuming. Therefore, in Maßon et al. (2024) we adapted the standardised growth curve (SGC) method (Li et al., 2018, 2015b) for Atacama Desert samples, achieving a 60 % reduction in measurement time while still obtaining robust results. In Maßon et al. (2024), we evaluated our modified version of the SGC method (rc_5sR_{150}xSGC) on Atacama Desert samples to calculate the equivalent doses (D_e) from a single-grain dose recovery test (DRT). However, when applying the rc_5sR_{150}xSGC method to determine the natural D_e, we encountered a problem. This chapter will outline the problem we faced and explain why we could not use the developed approach for our final analysis in Chapter 6.

To establish a SGC, we used a dataset consisting of single-grain $pIRIR_{225}$ measurements of ten samples from three different surface profiles in the Atacama Desert. For more information on the luminescence measurements and the samples used see Chapter 6 (Table 6.1 and Appendix C-II). We calculated the SGC in the same manner as the SGC described in Maßon et al. (2024). We therefore employed the complete SAR cycles for applying the rejection criteria. The rejection criteria we used differed slightly from Maßon et al. (2024), and were adapted to be suitable for expected recently bleached grains: test dose signal following natural dose measurement (T_n) >3σ above background, RSE of T_n ≤25 %, recycling ratio within unity ± 10 %, recuperation ≤20 % of the natural signal, recuperation ≤20 % of the maximum regenerative-dose signal, figure-of-merits (FOM) ≤10 %, reduced chi square ≤10 %. For growth curve fitting the parameters “exponential model”, “forced through origin” and “using a weighted procedure” were used.

According to the approaches mentioned in Maßon et al. (2024) the suitability of the SGC was assessed. There was a good agreement between SAR and SGC results (cf. Fig. 5.1A), the LS-normalisation successfully reduced the scatter (cf. Fig. 5.1B and C), and the agreement between the measured and expected L_x/T_x was sufficient (>80 % in unity within 2σ) (Li et al., 2015b).

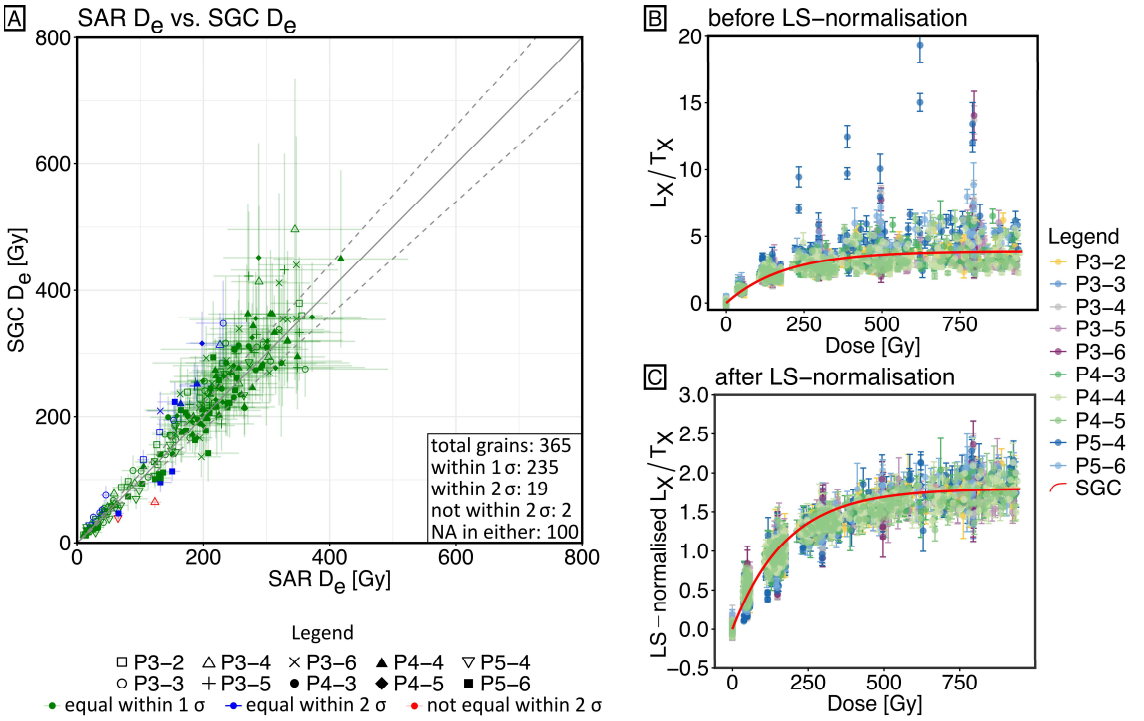

Fig. 5.1: *Evaluation of the SGC performance.* ***A)*** *comparison of D_e obtained by the standard SAR procedure with D_e obtained using the established SGC, fitted with their L_{r1}/T_{r1} from the fourth regenerative SAR cycle with a D_{r1} of 150 Gy.* ***B)*** *L_X/T_X values before LS-normalisation.* ***C)*** *LS-normalised L_X/T_X values.*

Subsequently, we tested whether our rc_5sR_{150}SGC approach yields robust results. We therefore reduced our measured SAR cycles within our dataset as proposed in Maßon et al. (2024, Table 3.3 this thesis: rc_5) and used a synthetic regenerative cycle with an sR of 150 Gy for fitting the data onto the established SGC.

Contrary to common practice, we compared not only the grains that yielded both a SAR D_e and a SGC D_e but also those for which a D_e could only be determined by one of the two method (either SAR or SGC). Those grains are hereafter termed unique SAR or unique SGC grains. When applying a SGC approach, one can expect to obtain a higher number of D_e values compared to a standard SAR approach. This is due to two main reasons: **i)** fewer rejection criteria can be applied, leading to an increased number of accepted grains, and **ii)** grains that would reach saturation on their individual growth curves in the SAR approach may not be in saturation when evaluated using the standardized growth curve due to its different trajectory (Li et al., 2018, 2017). The first reason should occur independently of the size of the D_e of a given grain, resulting in a uniform distribution of unique SGC D_e values across the entire D_e range. In contrast, the second reason is more likely to affect grains with high D_e values, potentially leading to a cluster of unique SGC D_e values in the upper range.

As shown in figure 5.2, we observed not only the expected grains which resulted in a rc_5sR_{150}SGC D_e but not in a SAR D_e (dark red symbols right of the graph), but also grains for which a SAR D_e could be calculated while a rc_5sR_{150}SGC D_e was not calculable (dark red symbols above the graph).

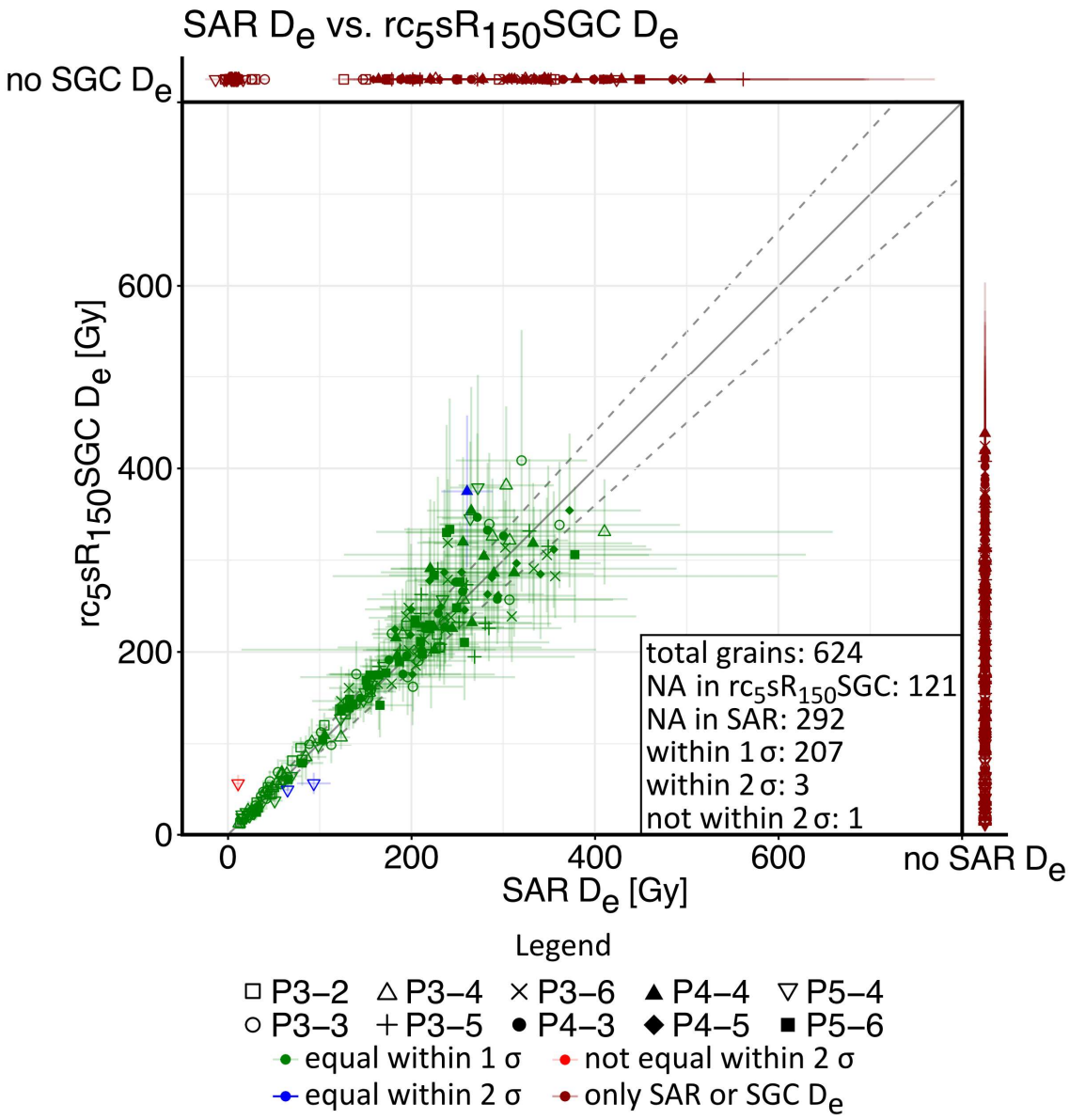

Fig. 5.2: *Evaluation of the rc_5sR_{150}SGC performance. Comparison of D_e results from a set of ten samples calculated using the SAR method (x-axis) and the rc_5sR_{150}SGC method (y-axis). The SGC was build using the same ten samples but using the full available set of SAR cycles for grain rejection and not the reduced set. Dark red symbols besides the x- and y-axis represent unique SAR and unique rc_5sR_{150} SGC D_e values, i.e., grains for which a D_e could only be determined by either the SAR or the rc_5sR_{150}SGC method.*

The distribution of the unique rc_5sR_{150}SGC D_e values is homogenously across the entire range. The expected cluster at higher D_e values is missing, since the rc_5sR_{150}SGC has a relatively flat shape with a low $2D_0$ value and therefore the individual growth curves of older grains often saturate at a higher value.

A notable issue with the unique SAR D_e values is that they are not uniformly distributed across the entire D_e range; a cluster forms at lower D_e values (<15 Gy) and a smaller cluster at higher D_e values (>300 Gy). The latter can be attributed to differences in the shape of the rc_5sR_{150}SGC relative to the individual growth curves, as the latter tend to saturate at higher doses than the rc_5sR_{150}SGC, resulting in saturation using the SGC method (Li et al., 2018, 2017).

For each sample and each method, a central age model (CAM) and a minimum age model (MAM) were calculated. The CAM doses were calculated using the calc_CentralDose() function from the R Luminescence package (Burow, 2024a; Galbraith et al., 1999; Kreutzer et al., 2012) and the MAM doses were calculated using the the calc_MinDose() function from the R Luminescence package (Burow, 2024b; Galbraith et al., 1999; Kreutzer et al., 2012). For all samples the unlogged version of the CAM was calculated. For samples with no negative D_e value, the log version of the MAM was used with a sigma b of 30 %. For samples in which negative D_e have been calculated the unlogged version was used. The sigma b was then chosen via an iterative approach. For a starting value for sigma b, 30 % of the CAM D_e were used. In the following iterations, 30 % of the previously calculated MAM D_e was used for sigma b until the difference between the last calculated MAM D_e and the newly calculated MAM D_e was marginal (old MAM / new MAM <0.001).

In the context of our research in the Atacama Desert, the cluster of unique SAR D_e values within the D_e distribution at lower values is more problematic than the those at higher values. This low D_e cluster has a significant impact on the calculation of the MAM, with discrepancies between the sample-specific SAR MAM D_e and the rc_5sR_{150}SGC MAM D_e exceeding 150 % in some cases (cf. Fig. 5.3). On average, the deviation of the SAR MAM and rc_5sR_{150}SGC MAM values is 43.5 %. In general, both unique SAR D_e and unique rc_5sR_{150}SGC D_e also lead to deviations between the SAR CAM D_e and the rc_5sR_{150}SGC CAM D_e, with a mean deviation of 11.6 %.

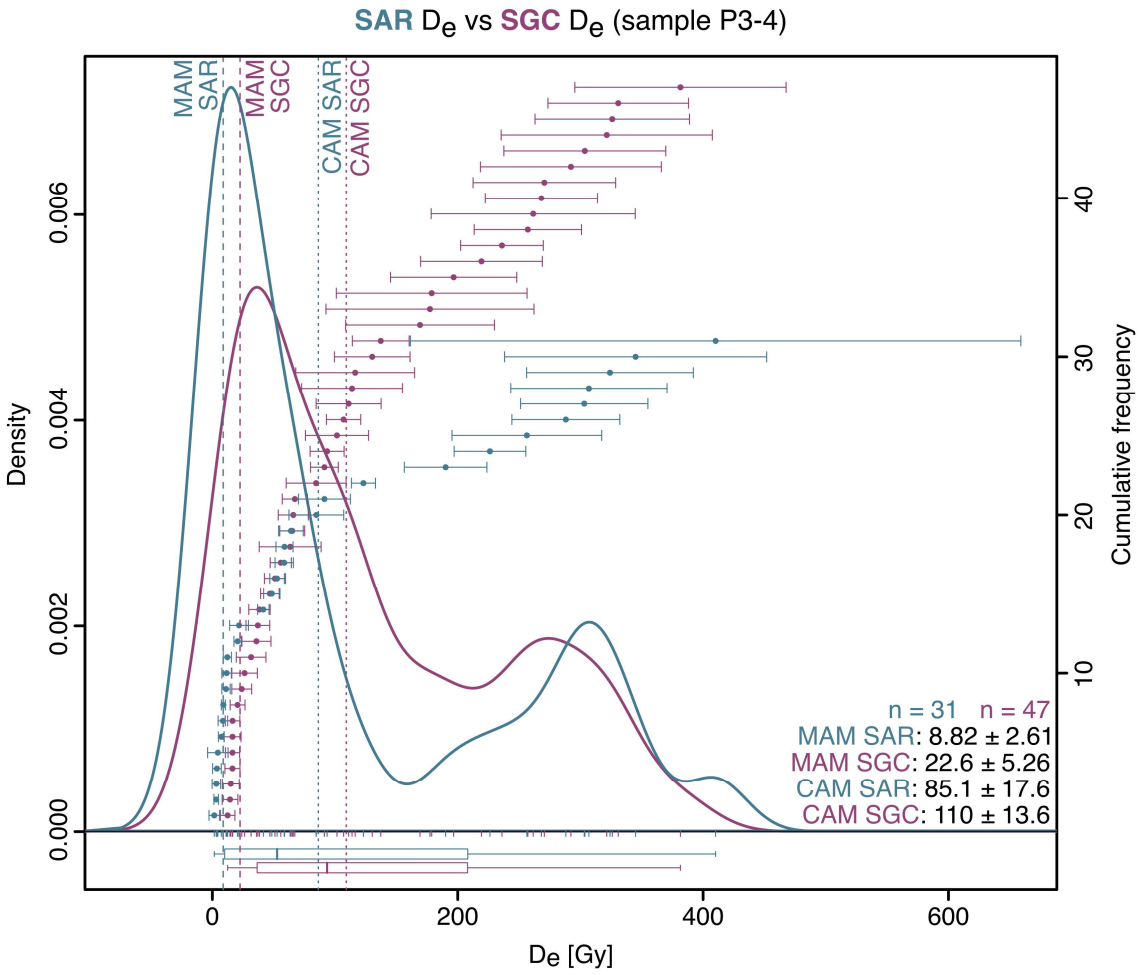

Fig. 5.3: *Kernel density plot of D_e calculated using the **SAR** approach and the **$rc_5sR_{150}SGC$** approach for sample P3-4. Dashed lines are the corresponding MAM D_e (calculated with the "Luminescence" R package, log = TRUE, sigma b = 0.3). Dotted lines are the corresponding CAM D_e (calculated with the "Luminescence" R package, log = FALSE)*

This discrepancy in the lower D_e range is likely linked to the rc_5sR_{150} method. The method developed by Maßon et al. (2024) is designed to tailor the measurement to the "expected magnitude" of a samples' D_e; for instance, the sR parameter is set to approximate the expected D_e, and the measured recycling cycles are intended to fall below that expected value. Because the Atacama Desert samples in Maßon et al. (2024) were bleached and then irradiated with the same dose under controlled laboratory conditions, all grains should have absorbed the same dose. This simplifies both, the choice of the size of sR, and the selection of the cycles to be measured. However, the natural Atacama Desert samples tested here exhibit highly heterogeneous D_e distributions, with values ranging from 0 to >500 Gy within a single sample. This makes it impractical to adjust the measurement cycles or sR for a sample, as the expected D_e varies significantly from grain to grain within the sample.

For future analysis, it might be possible to adapt the method developed by Maßon et al. (2024) to the goals of the analysis. For example, if merely the young population is of interest, it might be an option to design the reduced cycles and the sR around the

young population. Testing this option was unfortunately out of the scope of this study, since we could not re-measure all our samples using a different SAR protocol.

We could only test the change in the size of sR to a value below 150 Gy using the same set of reduced cycles. We tested the following four different values for the sR between the cluster of the low D_e values and the original 150 Gy: 15 Gy, 25 Gy, 50 Gy, and 100 Gy (Fig. 5.4).

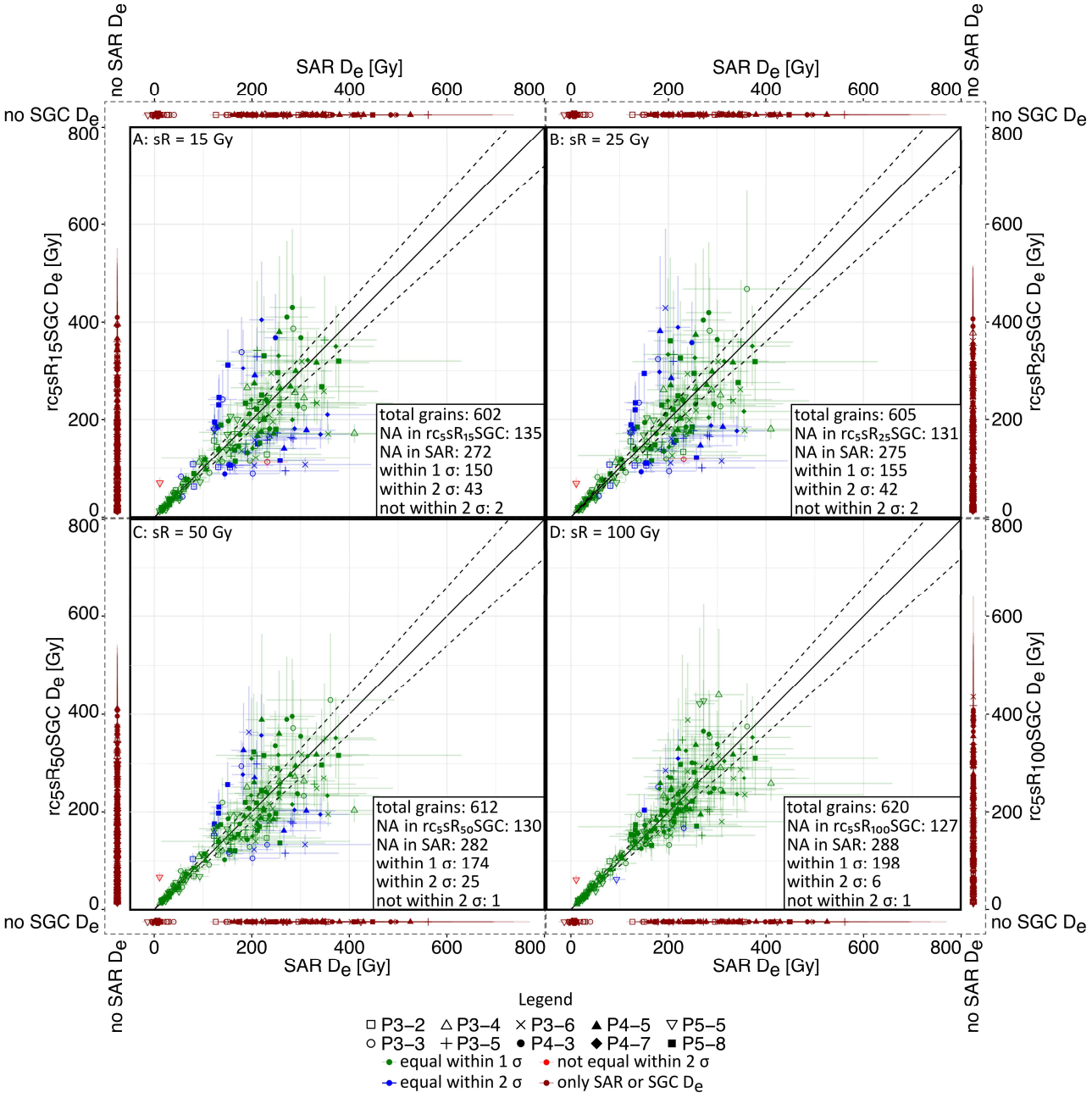

Fig. 5.4: *Evaluation of the $rc_5sR_{15\text{-}100}$SGC performance with differing sR values of 15 Gy in **A**, 25 Gy in **B**, 50 Gy in **C**, 100 Gy in **D**. **A-D**) Comparison of D_e results from a set of ten samples calculated using the SAR method (all x-axis) and the $rc_5sR_{15\text{-}100}$SGC method (y-axis). The SGC was build using the same ten samples but using the full available set of SAR cycles for grain rejection and not the reduced set. Dark red symbols besides the x- and y-axis represent unique SAR and unique $rc_5sR_{15\text{-}100}$SGC D_e values, i.e., grains for which a D_e could only be determined by either the SAR or the rc_5sR_{150}SGC method.*

Unfortunately, a lower sR value, without changing the measurement protocol, did not improve the results (Fig. 5.4). As shown by Maßon et al. (2024), the sR value must be adjusted not only to the resulting D_e values but also to the measurement protocol. For the tested smaller sR values, a larger number of grains yielded only a SAR D_e value, whereas the number of grains from which only a $rc_5sR_{15\text{-}100}$SGC D_e value could be calculated decreases. While grains that yield only a $rc_5sR_{15\text{-}100}$SGC D_e are evenly distributed across the entire D_e range regardless of the sR value, grains that yield only a SAR D_e consistently cluster at the lower end of the D_e distribution. As the sR value decreased from 150 to 15, the average deviation between the SAR and $rc_5sR_{15\text{-}150}$SGC MAM D_e increased from 43.5 % with a sR of 150 Gy to 74.5 % with a sR of 15 Gy. Similarly, the average deviation between the SAR and $rc_5sR_{15\text{-}150}$SGC CAM D_e increased from 11.6 % with a sR of 150 Gy to 17.4 % with a sR of 15 Gy.

Based on these findings, we decided to measure all samples using a full SAR protocol, despite not achieving the anticipated 60 % time-savings.

Chapter 6

Geomorphological activity and stability of surfaces and soils formed in hyperarid alluvial deposits (Atacama Desert, Chile)

Linda A.E. Maßon[1*], Simon M. May[1], Svenja Riedesel[1], Marijn van der Meij[1], Stephan Opitz[1], Andreas Peffeköver[1,2], Tony Reimann[1]

[1] Institute of Geography, University of Cologne, Germany

[2]Department of Earth Sciences, Simon Fraser University, Burnaby, Canada

Following the methodological developments (Chapters 3 and 4) and evaluations (Chapter 5) presented in the previous chapters, this chapter applies single-grain feldspar luminescence dating to reconstruct depositional and post-depositional processes in soils and surfaces along a climatic and elevation transect in the Atacama Desert. While the time-saving SGC approach developed in Chapter 3 proved unsuitable for the naturally irradiated samples analysed here (cf. Chapter 5), the internal K-concentration determination methodology established in Chapter 4 is employed to improve the accuracy of internal dose rate calculations.

In addition to luminescence dating, complementary geochemical and granulometric analyses, together with geomorphic field observations, are used to assess depositional and post-depositional characteristics of five soil and surface profiles distributed across different climatic regimes. The luminescence data is evaluated with respect to their suitability for identifying depositional versus post-depositional processes such as mixing, and their spatial variability across the transect is interpreted in light of the climatic gradient. Finally, the reconstructed chronostratigraphies and associated soil and surface processes are contextualised within the broader framework of regional palaeoenvironmental studies to contribute to an improved understanding of past climate variability and landscape evolution in one of the driest environments on Earth.

For a detailed statement on the contribution of the co-authors to the final manuscript, the reader is referred to the original text (Chapter 6.7). Linda Maßon contributed ~65 % to the final publication (field work – 80 %; data acquisition – 85 %; analysis and interpretation – 60 %; visualisation – 65 %; manuscript writing – 65 %).

- Formatting and orthography of the unpublished manuscript are adapted to the dissertation style -

Abstract

The hyperarid conditions of the central Atacama Desert, characterized by extremely low precipitation and high evaporation rates, create a unique environment where geomorphic stability is generally considered to be exceptionally high. Terrestrial cosmogenic nuclide-based surface exposure ages suggest that many surfaces underwent limited to no geomorphic changes since the Neogene or early Pleistocene. However, a number of recent studies reveal more recent landscape-scale geomorphic activity and link this to slightly wetter episodes during the Quaternary. In order to determine drivers of geomorphic activity, we performed a multi-proxy analysis of five profiles situated in alluvial deposits along a climatic transect from the coastal plain to the upper reaches of the Coastal Cordillera (~0–2000 m a.s.l.), combining single-grain feldspar luminescence dating with geochemistry, granulometry, and field observations. Alluvial deposits are prone to heterogeneous bleaching; therefore, we tested the bleachability of the feldspars and found a shallow effective bleaching depth (<2 cm) and high near-surface bleachability. The five profiles studied could be grouped into recently geomorphological active and stable sites, based on our multi-method approach. Profiles located on recently geomorphologically active surfaces show evidence of recent sediment deposition and, in one case, vertical grain transport. In contrast, recently stable surfaces preserve reworking signals relating to bioturbation at the coast and desert pavement formation in the hyperarid Coastal Cordillera. While no clear chronological trend along the west–east climatic gradient could be found, two phases of widespread geomorphic surface activity – ~50 ka and during the last ~5 ka – coincide with regionally wetter intervals compiled from other studies. Our findings highlight the value of single-grain luminescence data for reconstructing local sediment dynamics and soil reworking in hyperarid environments, and the need to account for both depositional and post-depositional processes in palaeoenvironmental interpretations.

6.1 Introduction

The Atacama Desert in northern Chile is one of the driest regions on Earth, with an extremely hyperarid core receiving less than 2 mm of rainfall per year (Houston, 2006a). Even though the timing of the onset of predominantly hyperarid conditions and their past variability remain highly debated (Ritter et al., 2019), these conditions have been more or less stable for millions of years (e.g. Dunai et al., 2005; Evenstar et al., 2017; Hartley and Chong, 2002; Nishiizumi et al., 2005; Rech et al., 2006). According to cosmogenic nuclide dating, the combination of hyperaridity and climatic stability is related to exceptionally low erosion rates (Jungers et al., 2013; Placzek et al., 2010),

supporting the notion that surface stability has persisted since the onset of hyperaridity (Nishiizumi et al., 2005). Nevertheless, wetter climatic episodes occurred during the Quaternary, related to the local activation and/or intensification of (water-driven) surface processes (e.g. Gayo et al., 2012; May et al., 2020; Medialdea et al., 2020; Nester et al., 2007; Pfeiffer et al., 2021, 2018; Ritter et al., 2019; Sáez et al., 2016). Climatic fluctuations during the Pleistocene and Holocene are documented in lake and wetland archives (Grosjean et al., 2001; Pfeiffer et al., 2018), rodent midden pollen records (Díaz et al., 2012; Maldonado et al., 2005), rodent midden faecal pallet size record (González-Pinilla et al., 2021), palaeosols (Veit, 1996), and fluvial and geoarchaeological evidence (Gayo et al., 2023, 2012; Latorre et al., 2013; Nester et al., 2007; Seeger et al., 2024; Vargas et al., 2006).

Most studies addressing fluvial and alluvial dynamics during the Late Pleistocene and Holocene focus on the Precordillera and the eastern desert margins, where Andean runoff exerts strong influence. More recently, Bartz et al. (2020a, 2020b), Haug et al. (2010) and Walk et al. (2020) have extended this work to coastal alluvial fan systems. Haug et al. (2010) showed the possibility of surfaces reactivation during El Niño events, whereas Walk et al. (2023) reported active soil processes that do not result in geomorphic changes of the landform. Yet, the timing and drivers of both depositional and post-depositional (i.e., soil) processes in the Coastal Cordillera remain poorly constrained, especially above the marine boundary layer, where fog and fog-depending loma vegetation are virtually absent (e.g. Diederich et al., 2020; Ritter et al., 2019; Vargas et al., 2006). To address this knowledge gap, we investigate soil and surface dynamics along a climatic transect spanning from the coastal plain to the hyperarid parts of the Coastal Cordillera. We focus on five profiles in alluvial deposits, combining stratigraphic observations, granulometry, geochemistry, and single-grain feldspar luminescence dating techniques.

In contrast to other dating methods, single-grain luminescence dating measures the burial time of individual sediment grains, which makes it a valuable tool for detecting both discrete depositional events and gradual reworking or soil mixing processes (e.g. Gliganic et al., 2016; Gray et al., 2019; Reimann et al., 2017; van der Meij et al., 2025). Although typically applied in more humid environments with highly active geomorphic and pedogenic processes, this method also holds promise for the Atacama Desert (Zinelabedin et al., 2022, 2025). Therefore, the aims of this study are **i)** to disentangle depositional and post-depositional sediment dynamics, and **ii)** to assess the applicability of single-grain luminescence dating as a sediment tracer and palaeoclimatic proxy in a challenging mineralogical and climatic environment. Ultimately, this work contributes to a better understanding of geomorphic surface

stability, sediment mixing, and soil formation in hyperarid landscapes, and their sensitivity to past climatic fluctuations.

6.2 Physical setting

6.2.1 Climate

The Atacama Desert is known for its hyperaridity, which results from subtropical atmospheric subsidence, coastal upwelling, the cold Humboldt current, and the Andean rain shadow (Garreaud et al., 2010; Houston, 2006a; Houston and Hartley, 2003). While hyperaridity has established around or before the mid-Miocene (de Porras et al., 2017; Dunai et al., 2005; Rech et al., 2019), several studies documented climatic fluctuations on more recent time scales (e.g. Latorre et al., 2013, 2002; Nester et al., 2007; Pfeiffer et al., 2018; Vargas et al., 2006; Veit, 1996). Fluctuations in fog and rainfall are controlled by the complex interplay of Eastern Pacific Sea Surface Temperatures (SSTs), Pacific Decadal Oscillation (PDO) and El Niño Southern Oscillation (ENSO), South American Summer Monsoon (SASM) patterns as well as moist northerlies (MN) and additionally depend on season, altitude and latitude (e.g. Garreaud et al., 2008, 2010; Jara et al., 2020; Latorre et al., 2011; Vicencio Veloso et al., 2024). These climatic drivers control the moisture supply and consequently vegetation occurrence, which affects surface processes such as alluvial activity and pedogenesis along the transect.

On a local level, more humid areas can be found. In the Paposo transect (Fig. 6.1), the Coastal Cordillera separates the narrow coastal plain from the broad Central Valley (Houston and Hartley, 2003). Marine fog frequently reaches elevations of up to ~1200 m a.s.l. (Cereceda et al., 2008a; del Río et al., 2018), supporting the occurrence of loma vegetation and microbial activity in the lower part of the transect (González et al., 2011; Jaeschke et al., 2024; Merklinger et al., 2020; Pinto et al., 2006; Sun et al., 2024). This creates a strong moisture gradient along the transect, with average relative humidity values ranging from 76.1 % at 160 m a.s.l. to 17.1 % at 1746 m a.s.l. (Table 6.1, Fig. C1).

Table 6.1: *Weather station data (Hoffmeister, 2018a, 2018b, 2018c). For location see Fig. 6.1a and b. Min and mean air temperature as well as mean rel. humidity were recorded between 01. May 2021 and 01. September 2023.*

Weather station number	Latitude	Longitude	Elevation a.s.l. (m)	Min. air temp	Mean air temp	Mean rel. humidity (air)
S31	-25.1151°	-70.458°	160	5.4 °C	14.9 °C	76.1 %
S32	-25.101°	-70.401°	1011	2.4 °C	15.5 °C	48.4 %
S33	-25.0916°	-70.2786°	1746	-5.2 °C	15.9 °C	17.1 %

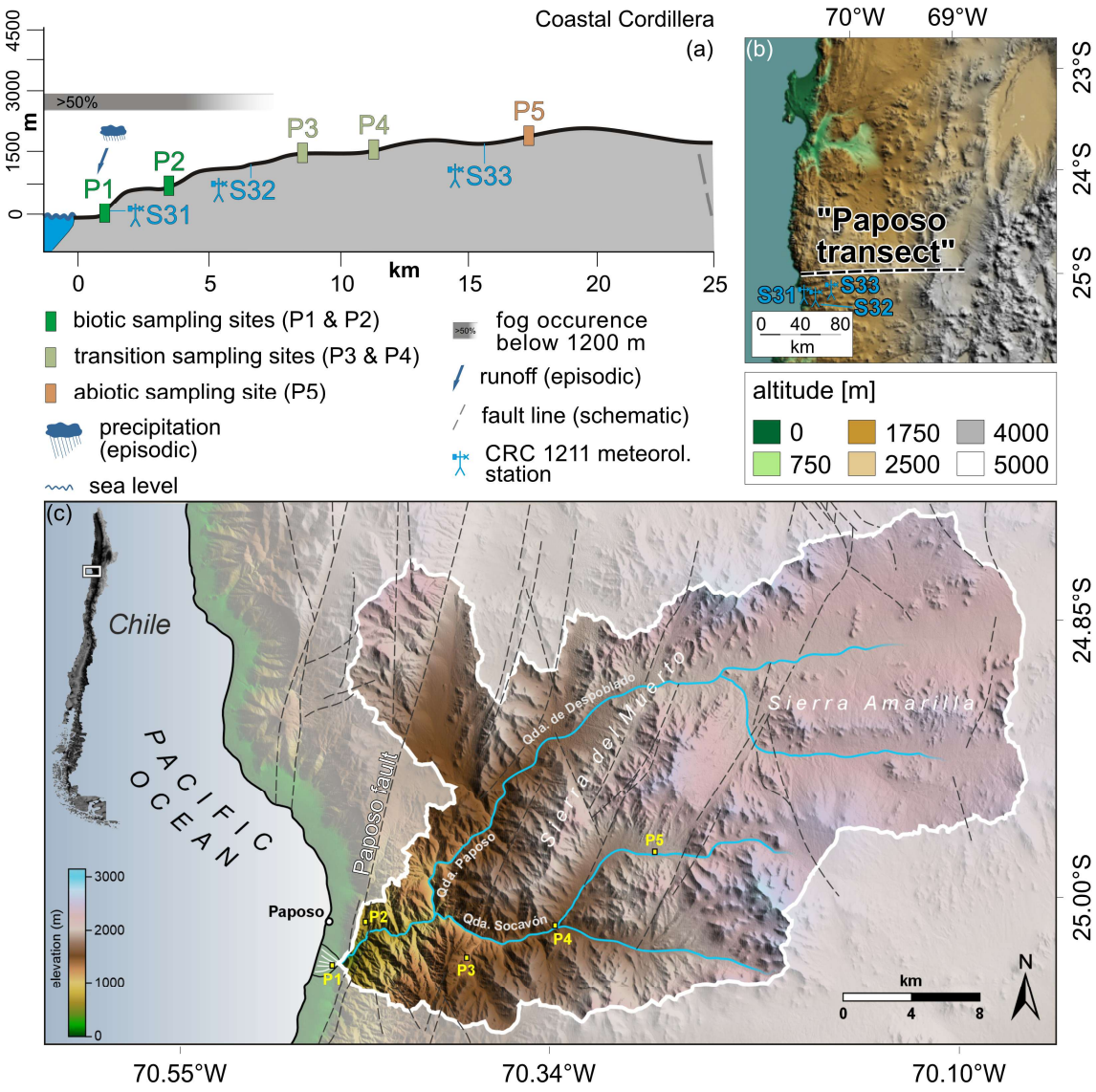

Fig. 6.1: a) *Topography along the Paposo transect, including sampling and weather station locations.* ***b)*** *overview map.* ***c)*** *Entire catchment of the Paposo Transect. Locations of the sampling sites (P1 – P5) are indicated by coloured (a) and yellow boxes (c). Fog occurrence (approx.) based on Cereceda et al. (2008a). Biotic sampling sites P1 and P2 (fog occurrence & loma vegetation) are located below, transitional sampling sites P3 and P4 and hyperarid sampling site P5 above the marine boundary layer.*

6.2.2 Geology and geomorphology

Given the extensive drainage basin of the studied transect (Fig. 6.1c), the lithological composition within the catchment is heterogeneous (Alvarez et al., 2016; Escribano et al., 2013). In the upper reaches, broad, shallow valleys are filled with semi-consolidated Miocene to Pliocene alluvial deposits, underlain by volcanic rocks of the La Negra Formation. In contrast, the central and lower parts of the catchment are primarily underlain by the Matancilla intrusive complex, composed predominantly of granodiorites and diorites of Middle to Upper Jurassic age. Additionally, Palaeozoic metasedimentary rocks of the Chañaral Epimetamorphic Complex crop out in the north-western sector of the catchment (Alvarez et al., 2016).

The study area is crossed by the Paposo fault, which is trending NNE–SSW to NE–SW and being a part of the Atacama Fault Zone, a principal tectonic structure stretching from 20°30'S at Iquique to 29°45'S at north of La Serena (Alvarez et al., 2016; Escribano et al., 2013; Hervé, 1987; Scheuber and Andriessen, 1990). Several other minor faults cross the research area trending in the same direction (Alvarez et al., 2016; Escribano et al., 2013). Except for **P2**, all field sites within our study are not directly intersected by active faults. The elevation profile of the transect is characterised by an abrupt transition from the coastal plain to the coastal cliff at about 110 m a.s.l (Fig. 6.1).

6.3 Methods

6.3.1 Field work

Field work was conducted during September 2022 and March 2023 and included geomorphological survey, site documentation, and sampling. In total five soil or surface profiles were dug along a climatic and altitude transect (see. Fig. 6.1b Paposo transect and Appendix C-III). All profiles were excavated in alluvial deposits in order to minimise the effects of different depositional processes on the profiles (cf. Fig. 6.2). The profile depths varied between 35 cm (**P5**) and 80 cm (**P4**) (cf. Fig. 6.3, Appendix C Table C1). Luminescence samples were collected under an opaque black plastic tarp under red light conditions. The sample material was carved out of the profiles into opaque black plastic bags. Each profile unit was further sampled under daylight conditions for dose rate determination. The retrieved samples, including their depths, are listed in Appendix C Table C1. Additionally, we used dust samples that were collected in an earlier study, from four different dust traps in the northern Atacama Desert installed at a height of 2 m (Wennrich et al., 2024).

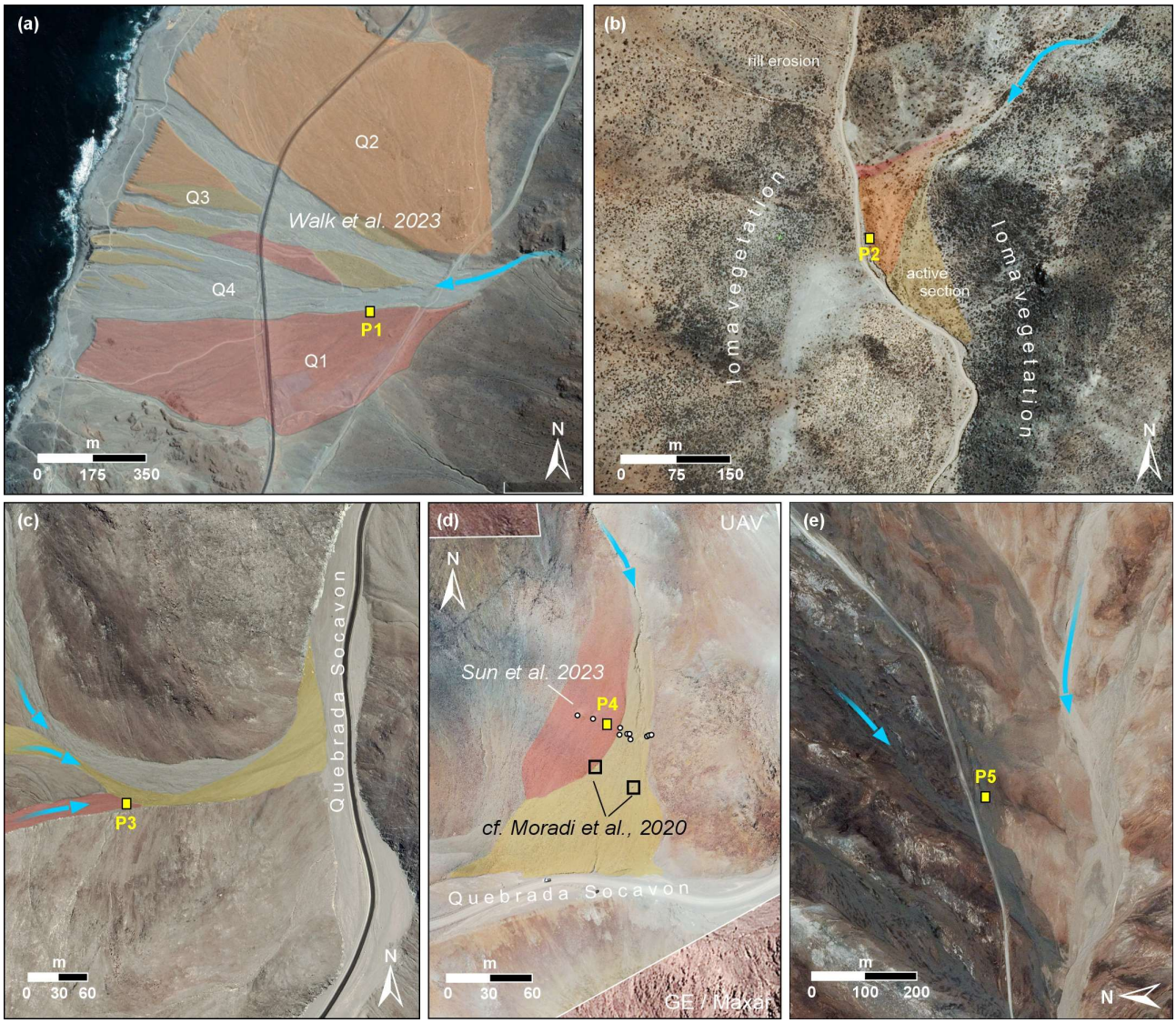

Fig. 6.2: *Satellite (a-e) and UAV (d) images of the study areas.* ***a)*** *Profile P1, located in the oldest alluvial fan generation (Q1) according to Walk et al. (2023) in direct adjacency to the erosional edge of the central alluvial channel, where subrecent to recent depositional activity occurs.* ***b)*** *Profile P2, located at the bottom edge in the centre of a small and steep alluvial fan at a natural outcrop exposed by lateral fluvial erosion; red area is assumed to represent the older fan section, whereas modern activity takes place in the yellow part.* ***c)*** *Profile P3, located within an alluvial channel (red) ~20 m upstream of the confluence of two further channels (yellow) and ~200 m upstream of a truncated alluvial fan.* ***d)*** *Profile P4, located in the older section of an alluvial fan (red) already described by Moradi et al. (2020) and Sun et al. (2023), using the profile pit from profile P9 of Sun et al. (2023); modern depositional activity is restricted to the yellow fan section.* ***e)*** *Profile P5, located in an alluvial channel deposit. The position of the sampled profiles within alluvial deposits are indicated by yellow boxes, flow directions are indicated by blue arrows.*

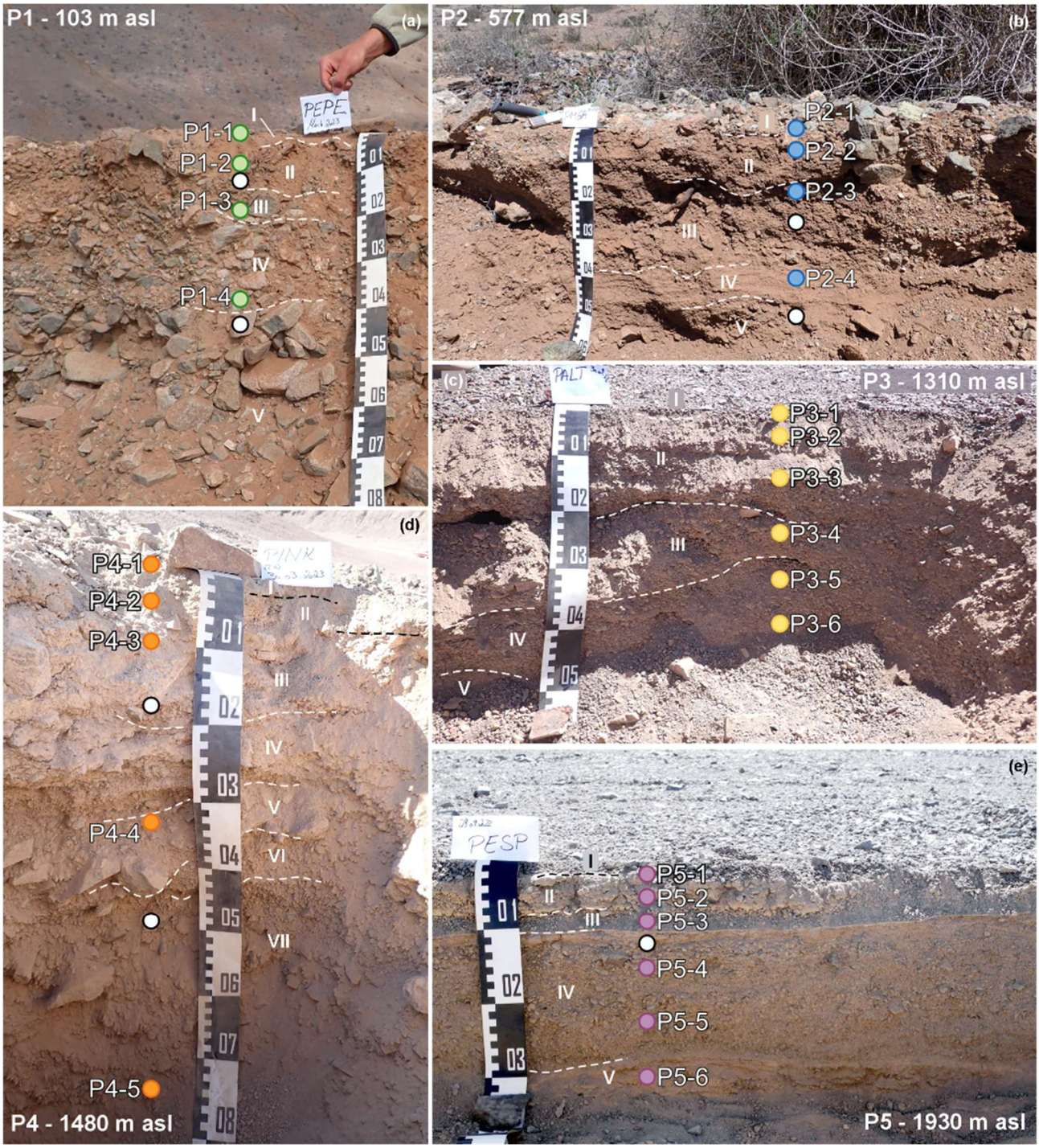

Fig. 6.3: *Photographs of the five investigated sampled profiles.* ***a)*** *Profile P1 (103 m a.s.l.),* ***b)*** *profile P2 (577 m a.s.l.),* ***c)*** *profile P3 (1310 m a.s.l.),* ***d)*** *profile P4 (1480 m a.s.l.), and* ***e)*** *profile P5 (1930 m a.s.l.). White circles indicate the depth of samples used for all analysis and coloured circle the depth of samples only analysed for their geochemistry and granulometry. The individual lithological units within each profile are marked by dashed lines and labelled using Roman numerals and are described in Appendix C-III. Profile units apply only to the respective profile and are not intended for correlations between profiles.*

6.3.2 Geochemistry and granulometry

Geochemical and granulometric analyses were conducted to characterise the sampled profiles and to identify potential indicators of depositional processes, sediment transport mechanisms, and pedogenic overprints. The material used for the analyses was generally taken from the luminescence samples. Where the available material was insufficient, additional samples for geochemical and sedimentological analyses were collected from the same sediment profiles but from different depths (Appendix C Table C1). Consequently, not all depths of the geochemical and sedimentological samples correspond exactly to those of the luminescence samples. Elemental concentrations were derived using the energy-dispersive X-ray spectrometer SPECTRO XEPOS (SPECTRO Analytical Instruments Ltd.) and for granulometric analyses a laser diffraction particle size analyser (Beckman Coulter LS13320) was used. For further details on sample preparation, measurement settings, and data analysis see Appendix C-I.

6.3.3 Feldspar luminescence dating

The luminescence samples were prepared in the Cologne Luminescence Laboratory (University of Cologne; CLL) under subdued red-light conditions. As the quartz from the Atacama Desert is not suitable for luminescence dating mainly due to its insufficient luminescence sensitivity (e.g. Bartz et al., 2020a; Del Río et al., 2019; Zinelabedin et al., 2022) the attention was shifted to feldspar luminescence dating. Automated Risø TL/OSL-DA-20 readers (Bøtter-Jensen et al., 2010) were used for single-grain measurements of the 200 – 250 µm fraction of feldspar separates. A single-aliquot regenerative-dose (SAR) post-infrared infrared stimulated luminescence (pIRIR) protocol (Thomsen et al., 2008), adapted for single grains (Reimann et al., 2012), with a preheat of 250 °C for 60 s, an IR stimulation temperature of 50 °C for 2 s, and a pIRIR stimulation temperature of 225 °C for 3 s ($pIRIR_{225}$; Buylaert et al., 2009) was used. All equivalent dose (D_e) estimates were calculated using the numOSL R package version 2.8 (Peng et al., 2018). A 2 % measurement error was used for the regenerative dose signals (L_x) and the corresponding test dose signals (T_x). The $pIRIR_{225}$ signal exhibits generally low fading rates, ranging from -0.7 ± 0.1 % to 1.9 ± 1.4 % per decade, with a mean fading rate of 1.1 ± 0.1 % per decade (± standard error, n = 21). Following Roberts (2012), no fading correction was applied to the $pIRIR_{225}$ ages.

Sample-wise uranium (U), thorium (Th), and potassium (K) concentrations were determined using an Ortec Profile MSeries GEM Coaxial P-type high-precision Germanium Gamma-Ray detector. The internal K-concentration was determined

using a Risø GM-25-5A beta multicounter system (Bøtter-Jensen and Mejdahl, 1985) and a Bruker M Tornado μ-XRF following the approach proposed by Maßon et al. (in press). Dose rates were calculated using the Dose Rate and Age Calculator (DRAC, Durcan et al., 2015). For further details on sample preparation, measurement protocol and its determination, OSL reader specification, luminescence data analysis, and dose rate calculations see Appendix C-II.

To obtain information about the depositional ages and post-depositional activity in the profiles, we applied different age models (Galbraith et al., 1999), which are implemented in the R Luminescence package version 0.9.25 (Burow, 2024a, 2024b; Kreutzer et al., 2012). Given the high dispersion in our D_e distributions caused by either heterogeneous bleaching and/or post depositional mixing, we applied the 4-parameter Minimum Age Model (MAM-4) to estimate the minimum dose (Galbraith et al., 1999; Galbraith and Roberts, 2012). When the MAM-4 failed to converge and to provide a reliable estimate, we used the more robust 3-parameter MAM (MAM-3) instead. In cases where both models were unable to provide a result, or when the models estimated that the fraction of grains contributing to the minimum dose component is very small (<10 %), we opted for a Central Age Model (CAM). Due to the occurrence of negative doses in the samples, we applied all age models on unlogged data (Arnold et al., 2009). The implementation of an unlogged MAM in the R Luminescence package requires a single value of natural overdispersion, called sigma-b (σ_b), in measured units (Gray) for all grains in a sample. As this will lead to a disproportionally large error for grains with near-zero doses and a negligible effect for grains with very high doses, we opted to add σ_b on a grain level instead of on a sample level. The grain-wise error was calculated by adding a σ_b of 30 % of the D_e to the measurement error in quadrature. This approach is consistent with the logged version of the MAM, where the relative σ_b is added to each individual relative measurement error.

To determine the final depositional age or the time of the last post-depositional mixing activity, we assessed whether **i)** the measured grains can be effectively bleached, meaning they do not retain significant residual doses after sunlight exposure, and **ii)** the bleaching depth does not extend far into the profile. Since the surface sample of each profile was taken from the uppermost two centimetres, it represents a mixture of grains exposed to sunlight and grains with up to two centimetres of overburden. These surface samples do not provide information about recent activity but instead serve as indicators of the natural bleaching characteristics of the profile. In addition, laboratory bleaching tests were conducted on a multi-grain and single-grain level using a SOL2 solar simulator for 24 h.

We further calculated two additional proxies to detect potential post-depositional mixing processes. These are **i)** the fraction of grains with a saturated luminescence signal (Reimann et al., 2017), and **ii)** the fraction of grains with D_e values near zero (Bateman et al., 2007). **Saturated grains**, originating from the bedrock or deposits older than the luminescence dating range, indicating upward transport when found in younger sediments in soil profiles. However, in late Pleistocene to Holocene alluvial deposits, their interpretive value appears to be limited, as deeper depositional units may not be in saturation. Conversely, grains with D_e values near zero in older deposits indicate downward transport (Bateman et al., 2007; Gliganic et al., 2016). We modified the "**zero-dose**" **grains** proxy by Bateman et al. (2007) and defined it as grains that agree within one standard deviation with the MAM-4 minimum dose of the surface samples (<2.24 Gy). Because our surface samples retain a small residual dose from incomplete bleaching during deposition, we use this value instead of a true zero dose. The use of this proxy is limited in recently deposited units, where the D_e value indicates the timing of deposition rather than downward transport, and in cases where D_e values >2.24 Gy have relatively large errors.

6.4 Results and interpretation

6.4.1 Geochemistry and granulometry

Most samples are sand-dominated. Only the samples **P4-1** and **P4-2** are dominated by very coarse silt (Fig. 6.4a). The dust samples (cf. Wennrich et al., 2024) are either mud or sandy mud, with comparatively low sand fractions of 3.2 % to 12.7 % (Fig. 6.4a). All samples are either poorly or very poorly sorted according to Folk and Ward (Blott and Pye, 2001; Folk and Ward, 1957). Exemplary grain size distributions from each profile and a mean distribution of the dust samples are shown in Fig. 6.4b. For detailed results on the grain size distributions see Appendix C-I Fig. C2.

Since common weathering indices are not suited for application in deserts (Chen et al., 2021), a ratio of mobile (Na, Mg, K, Ca) to immobile (Al, Ti) elements was calculated based on elemental concentrations obtained by XRF analysis ($\sum E_m/\sum E_{im}$, Fig. 6.5a). In general, smaller ratios indicate leaching of mobile elements. Due to the geochemical differences in the parent material, a comparison between different profiles is not possible. The biggest intra-profile differences occur in **P1** and **P4** (Fig. 6.5a green respectively orange line).

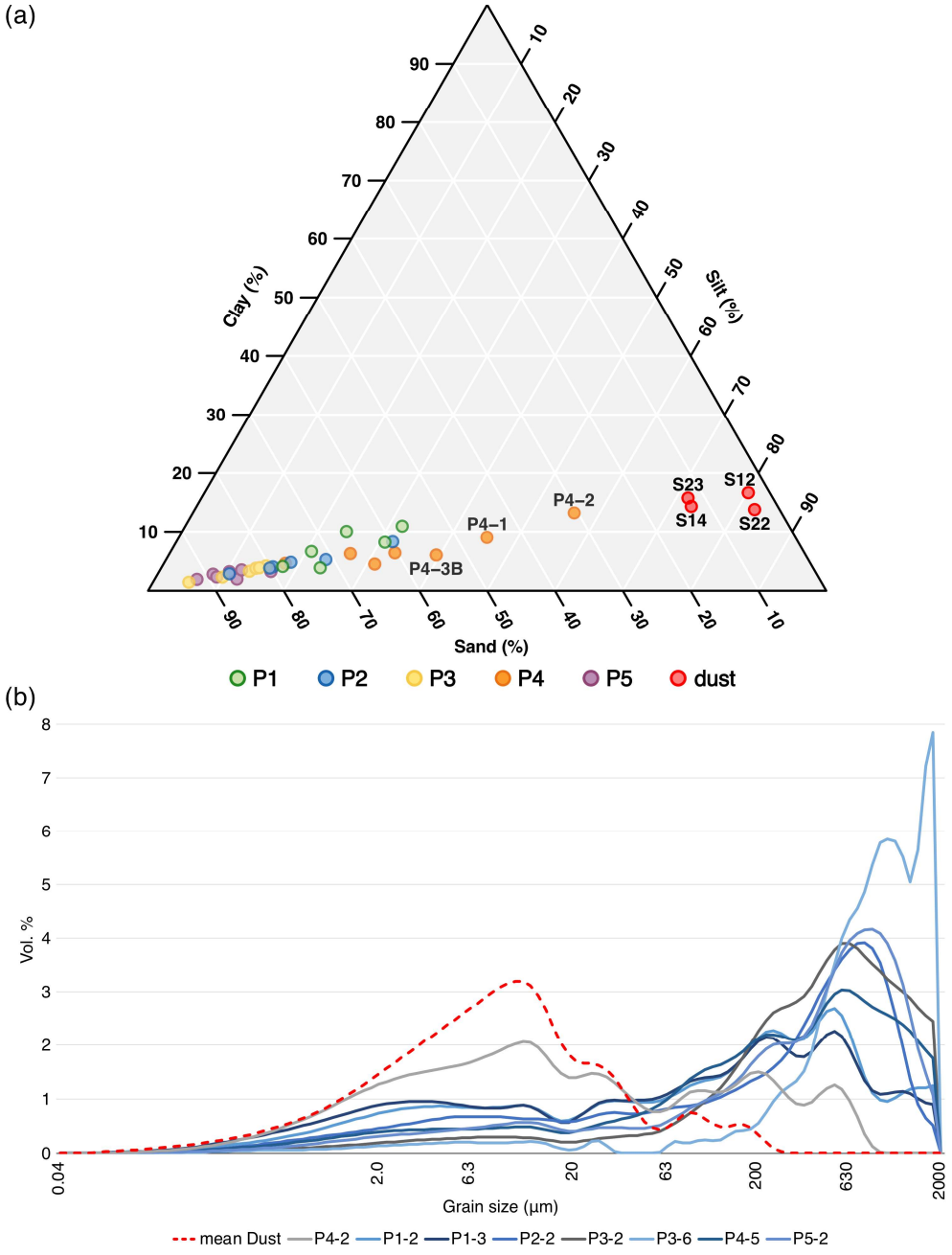

Fig. 6.4: a) *Soil texture triangle of all sediment samples and the four dust samples, and* ***b)*** *grain size distributions of exemplary samples including the mean values for the four dust samples (red dotted line).*

To allow for a comparison of the geochemical composition and granulometric results among the profiles and to assess the degree of weathering, a principal component analysis (PCA) was conducted. The input data included grain size parameters (sand, silt, and clay fractions), concentrations of relatively immobile and weathering-resistant elements (Al, Ti), concentrations of relatively mobile and weathering-susceptible elements (K, Na, Ca, Mg, Si), as well as the Fe-concentrations (Fig. 6.5b). The first two principal components (PC1 and PC2) explain 41.1 % and 28.2 % of the total variance, respectively, thereby accounting for ~70 % of the variability of the dataset. While PC1 is primarily influenced by the granulometric properties, PC2 is mainly influenced by the geochemical components. The PCA

reveals a distinct separation of samples by profile rather than by degree of weathering. In the biplot, samples from **P1** and **P4** plot in the positive PC1 half, associated with higher Mg-concentrations and fine grain contents (silt and clay). Along PC2, the samples of **P1** (negative half) and **P4** (positive half) are primarily separated due to their differing Al-, Si-, Fe-, K-, Ca-, and Ti- concentrations. Samples of **P2**, **P3**, and **P5** plot mostly in the negative half of PC1, with the exceptions of sample **P2-3B** (no equivalent luminescence sample available) and **P3-4**. Their separation along PC2 is primarily caused by their differing concentrations of Al, Si, Fe, K, Ca, and Ti.

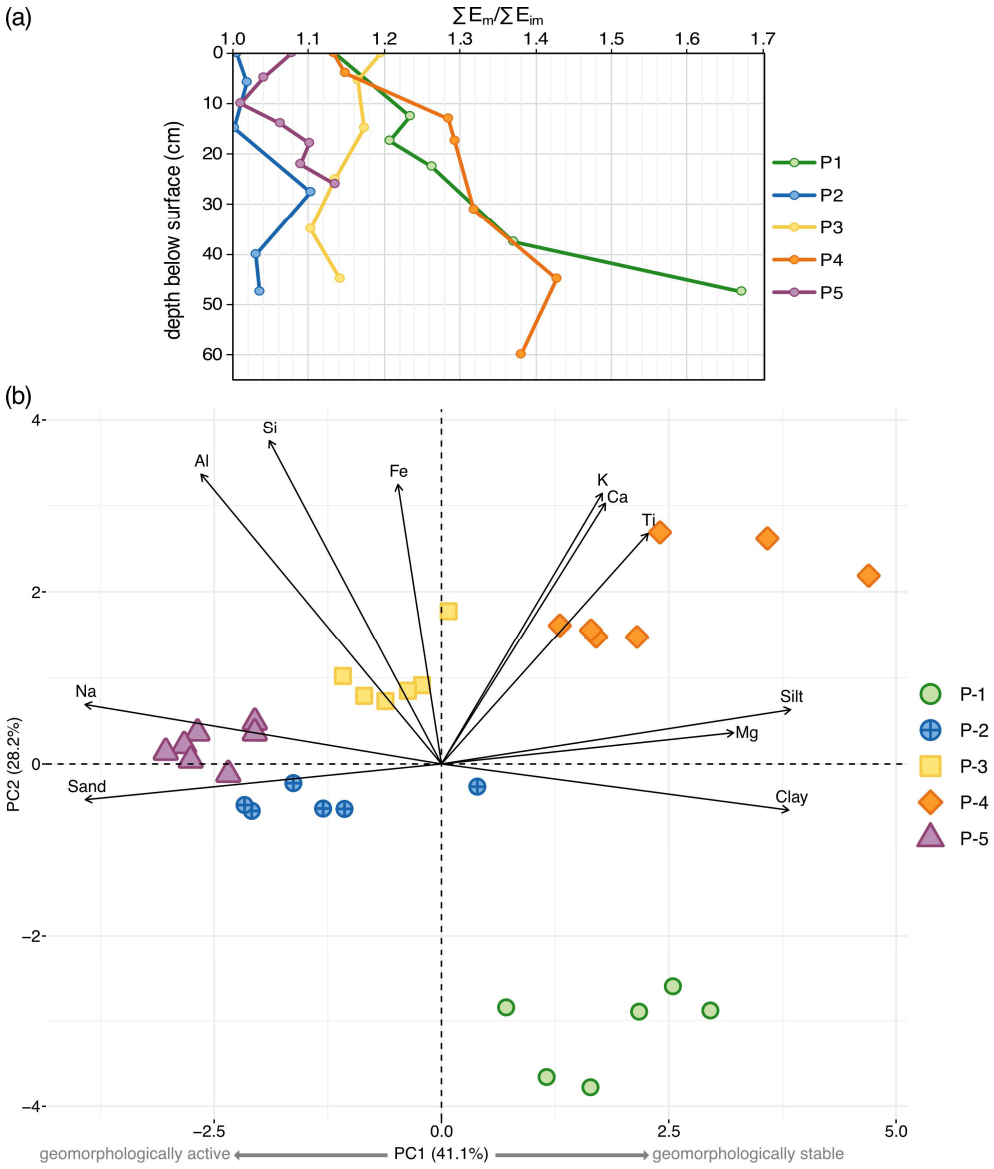

Fig. 6.5: a) *Mobile to immobile ratio ($\sum E_m/\sum E_{im}$) against depth. Smaller ratios indicate the leaching of mobile elements and therefore weathering.* ***b)*** *Biplot of the PCA of all sediment samples based on grain size parameters and elemental concentrations.*

6.4.2 Feldspar luminescence ages

All surface samples (**P1-1**, **P2-1**, **P3-1**, **P4-1**, and **P5-1**) show a mixture of recently bleached grains <5 Gy and grains with D_e >50 Gy (Appendix C-III Fig. C5-9). This indicates that under natural conditions **i)** grains at the immediate surface are sufficiently bleached, and **ii)** bleaching ceases already at very shallow depths, i.e., within the uppermost 2 cm. Therefore, in the following (Chapters 6.4.3 – 6.5.2 and the figures therein), only the ages of the underlying sedimentary units within each profile are discussed, yet all ages and dose rate-relevant elemental concentrations can be found in Tables 6.2 and Appendix C-II Table C5. On average, residuals in the laboratory bleaching tests were found to be <2 Gy for multi-grain analysis and <1 Gy for single-grain tests, which further demonstrates the potential of the samples to be effectively bleached (Appendix C-II Fig. C3e and Fig. C4a-g).

The single-grain $pIRIR_{225}$ D_e distributions of most samples are broad, spanning from 0 Gy up to saturation in some cases (Fig 6.6). While samples close to the surface show a unimodal right skewed distribution, deeper samples in the profiles **P2**, **P3**, and **P5** display more complex distributions. The total dose rates range from 2.41 Gy ka^{-1} (**P5-2**) to 5.00 Gy ka^{-1} (**P4-4**). **P2** and **P5** have the lowest and **P4** the highest dose rates. Sub-surface zero-dose grains range from 0 % to 66.2 %, usually gradually decreasing downward (Table 6.2). Sub-surface saturated grains range from 0 % to 47.2 %, usually gradually increasing downward (Table 6.2).

Table 6.2: *Luminescence results, including the dose model used for calculation of the D_e, the D_e, the total dose rate ($\dot{D}$), the age, the fraction of zero-dose grains and the fraction of saturated grains per sample.*

Sample	Unit (profile-wise)	Model used	D_e (Gy)	$\dot{D}$ (Gy ka^{-1})	Age (ka)	Zero-dose grains (%)	Saturated grains (%)
Profile P1							
P1-1	I	MAM-4	1.60 ± 0.17	3.85 ± 0.50	0.42 ± 0.07	79.5	0
P1-2	II	MAM-4	10.9 ± 1.45	3.91 ± 0.62	2.78 ± 0.57	2.07	3.45
P1-3	III	CAM	106 ± 5.02	3.77 ± 0.59	28.07 ± 4.55	0	3.37
P1-4	IV	CAM	107 ± 2.77	3.71 ± 0.69	28.71 ± 5.37	0.64	2.88
Profile P2							
P2-1	I	MAM-4	1.52 ± 0.55	2.35 ± 0.25	0.65 ± 0.24	74.2	1.08
P2-2	II	MAM-4	1.05 ± 0.57	2.50 ± 0.28	0.42 ± 0.23	66.2	1.54
P2-3	II	MAM-4	2.73 ± 0.46	2.54 ± 0.29	1.08 ± 0.22	56.2	0
P2-4	IV	MAM-4	1.83 ± 1.02	2.52 ± 0.35	0.73 ± 0.42	33.3	0
Profile P3							
P3-1	I	CAM	4.93 ± 0.63	3.16 ± 0.35	1.56 ± 0.26	43.2	2.11
P3-2	II	MAM-4	2.94 ± 0.74	3.36 ± 0.51	0.87 ± 0.26	19.8	5.81
P3-3	II	MAM-4	3.96 ± 1.11	3.43 ± 0.54	1.16 ± 0.37	10.2	7.63
P3-4	III	CAM	6.31 ± 5.68	3.43 ± 0.54	1.84 ± 1.68	9.78	9.78
P3-5	IV	CAM	184 ± 12.2	3.48 ± 0.59	53.0 ± 9.59	1.12	30.3
P3-6	IV	CAM	208 ± 12.8	3.60 ± 0.59	57.9 ± 10.07	0	36.7
Profile P4							
P4-1	I	MAM-4	4.72 ± 0.26	4.28 ± 0.49	1.10 ± 0.14	30.3	0.90
P4-2	II	CAM	29.5 ± 2.69	4.51 ± 0.56	6.55 ± 1.01	1.33	10.0
P4-3	III	CAM	205 ± 13.0	4.92 ± 0.72	41.7 ± 6.65	0.72	46.4
P4-4	V	CAM	224 ± 10.6	5.00 ± 0.70	45.0 ± 6.65	1.52	41.4
P4-5	VII	CAM	227 ± 11.9	4.53 ± 0.89	50.1 ± 10.17	0.62	47.2
Profile P5							
P5-1	I	MAM-3	2.92 ± 0.34	2.26 ± 0.25	1.29 ± 0.21	58.0	2.76
P5-2	II	MAM-4	3.42 ± 0.44	2.41 ± 0.28	1.42 ± 0.25	50.5	1.77
P5-3	III	MAM-3	4.39 ± 0.59	2.48 ± 0.29	1.77 ± 0.31	36.6	3.23
P5-4	IV	MAM-4	9.65 ± 1.07	2.44 ± 0.35	3.95 ± 0.71	15.6	8.89
P5-5	IV	MAM-3	10.8 ± 1.49	2.46 ± 0.35	4.41 ± 0.87	7.58	4.55
P5-6	V	MAM-4	45.0 ± 3.42	2.52 ± 0.39	17.9 ± 3.06	0	7.61

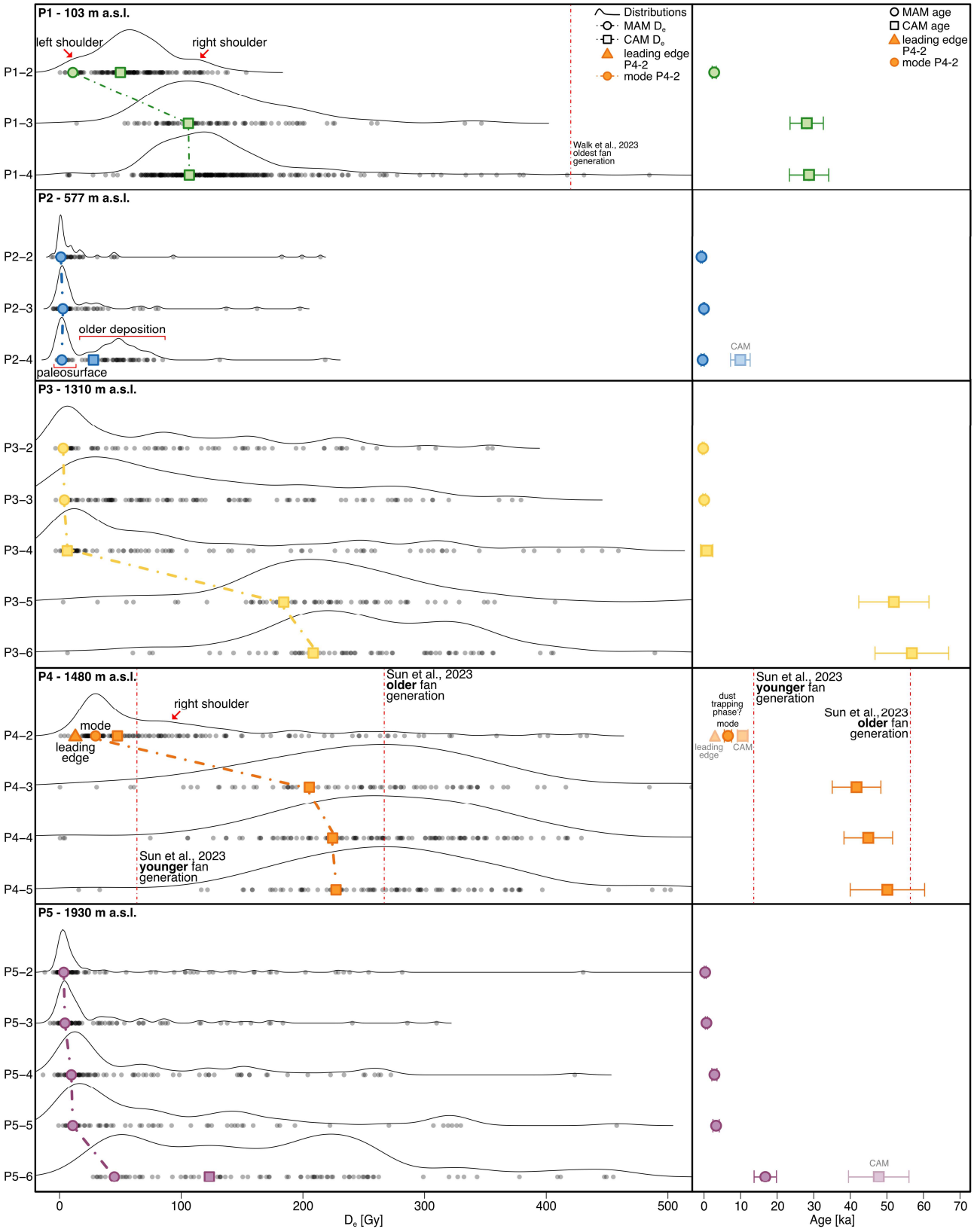

Fig. 6.6: *D_e distributions and corresponding MAM (circle) or CAM (square) D_e in Gy (left) and ages in ka (right) of all five sampled profiles, excluding the surface samples. Ages from earlier studies referenced in the main text, are shown as dotted red lines. Their conversion into D_e was based on an average dose rate of the corresponding profile. The x-axis for the D_e distributions is truncated at 500 Gy to facilitate visualisation.*

6.4.3 Interpretation of profile genesis

Profile P1 – 103 m a.s.l.

P1 is located on the surface of the oldest depositional generation (Q1, Walk et al., 2023) of a large coastal alluvial fan just south of Paposo (Fig.6.2a, Appendix C-III, Fig. C5). The deposition of this alluvial fan generation was previously dated to 111 ± 20 ka (i.e., MIS 5) based on ^{10}Be exposure ages of boulders at the fan surface (Walk et al., 2023). Based on various soil proxies, these authors also suggested that weathering processes on this surface have resulted in the evolution of a well-developed soil horizon. A clear downward trend is also evident in our geochemical data for **P1**, suggesting that mobile elements were depleted from the top layers, as generally expected for top soil layers (Fig. 6.5a). Further, the silt and clay fractions of units II, III and the upper part of IV are slightly increased, which potentially indicates initial weathering and soil forming processes as well (Fig. 6.4a, Appendix C-III Fig. C5). Unit I is the only unit extensively penetrated by roots, with diameters reaching up to 5 mm while in unit II, only a few fine roots are present, and their abundance decreases with depth. Starting from unit III, no roots are observed. Yet, none of the grains in sample **P1-2** and merely 2.3 % of the grains in sample **P1-3** respectively 4.6 % in sample **P1-4** have a D_e in agreement with the depositional age (111 ± 20 ka = ~420 ± 75 Gy) according to Walk et al. (2023). Recent to subrecent material exchange between the surface and deeper profile units IV and V is unlikely, as zero-dose grains are absent or rare (<1 %) in samples **P1-3** and **P1-4** (Table 6.2). Moreover, the D_e peak in **P1-2** (CAM D_e 50.1 Gy) is largely absent in the distributions of **P1-3** and **P1-4**, and only minor portions of their peaks appear in the right shoulder of **P1-2**. We therefore interpret that **P1-3** and **P1-4** belong to a depositional phase around ~28 ka, rather than being the result of post-depositional vertical mixing. However, in the uppermost ~10 cm, post-depositional mixing may be inferred from the D_e distribution of sample **P1-2**. Although **P1-2** contains only 2 % zero-dose grains, the shoulder on the left flank of the distribution might represent material mixing in the form of vertical grain transport from the surface (**P1-1**) to the depth of **P1-2**. This portion of the D_e distribution of **P1-2** is reflected in the MAM-4 age of 2.78 ± 0.56 ka indicating that mixing processes were active at least until that time. The CAM age, in contrast, indicates a depositional phase around 13 ka for sample **P1-2**. Bioturbation caused by the observed roots and the initial soil processes indicated by our granulometric and geochemical analysis support this interpretation. The discrepancy between the luminescence inferred depositional age presented here, and the cosmogenic nuclide-based ages reported by Walk et al. (2023) may be explained by: **i)** a younger phase of fluvial reworking or resurfacing (cf. Haug et al., 2010) on top of the older alluvial fan generation; **ii)** cut-and-fill processes and lateral

sedimentation associated with the formation of the fourth and youngest alluvial fan generation inside the main channel, which may have reworked or reactivated surface sediments of the oldest fan surface, incorporating younger material; or **iii)** inherited age in the cosmogenic nuclide ages reported by Walk et al. (2023).

Profile P2 – 577 m a.s.l.

The profile is located within the marine boundary layer and thus in a zone of high fog occurrence and abundant loma vegetation (Cereceda et al., 2008a; del Río et al., 2018; Appendix C-III, Fig. C6). Unit I of profile **P2** is penetrated by both fine and thick (~2 cm in diameter) roots, extending into unit II. No roots are observed in unit III, yet fine roots occur again in underlying unit IV. The grain size analysis shows an overall downward increase of grain size and only little variation is visible in the geochemical parameters (Fig. 6.4a, Fig. 6.5a, Fig C6). The D_e distributions of samples **P2-2** and **P2-3** show a peak in a low dose range and a short tail towards the higher doses (>25 Gy) (Fig. 6.6). Saturated grains are virtually absent (Table 6.2), which might indicate the recent deposition of heterogeneously bleached grains and/or intense post-depositional mixing processes. A combination of deposition and post-depositional mixing seems to agree with **i)** the presence of an active fault line (Paposo fault) in the direct adjacency, and **ii)** the location within the marine boundary layer that is presumably linked to higher moisture availability enabling bioturbation as a mixing process. The MAM-4 ages of samples **P2-2** (0.42 ± 0.23 ka) and **P2-3** (1.08 ± 0.22 ka) and their position within the same unit (unit II) suggest deposition of the upper profile within the last ~1200 years. Additional post-depositional mixing is indicated by **i)** a decreasing fraction of zero-dose grains from 74 % (**P2-1**) to 56 % (**P2-3**) (Table 6.2), and **ii)** a widening of the D_e peak bases from **P2-1** to **P2-3** (Fig. 6.6, Appendix C-III Fig. C6). The downward decline in zero-dose grains suggests a depth-dependent reduction in post-depositional vertical mixing processes, likely caused by root-related bioturbation. This aligns with the lithology, as unit II appears heterogeneous and contains numerous roots. The broader D_e peaks in **P2-2** and **P2-3** likely reflect mixing with adjacent sediment layers, where more old grains are incorporated in proximity to older underlying layers. The high root density supports bioturbation as the dominant process driving this vertical grain movement.

The lowermost sample **P2-4** (unit IV) contains two distinct grain populations with a CAM age of 11.0 ± 2.7 ka and a MAM age of 0.73 ± 0.42 ka (Fig. 6.6). The younger population is consistent with the overlying samples, suggesting possible synchronous deposition with **P2-2** and **P2-3**. The older grain population could reflect intensive post-depositional mixing or reworking of older sediments during the deposition of all four

units. However, synchronous deposition with the overlying units is unlikely. Roots are present in unit IV but absent in unit III (no age available), indicating that unit IV formed a palaeosurface with limited vegetation cover. As sample **P2-4** comprises the uppermost 10 cm of unit IV, the older D_e peak likely reflects grains from deeper within the unit, and thus the deposition of unit IV >11 ka, whereas the younger D_e peak likely reflects grains near the palaeosurface, recording the burial of unit IV and deposition of unit III ~700 years ago.

Profile P3 – 1310 m a.s.l.

Similar to **P2**, the grain size of the brown-yellowish matrix in **P3** shows an overall downward increase (Appendix C-III; Fig. C7). All units are dominated by the coarse to very coarse sand fractions, and the mobile to immobile element ratios reveal minimal differences between the individual profile units (Fig. 6.4a, Fig. 6.5a). The MAM-4 and CAM ages from the uppermost units in **P3** (**P3-2**, **P3-3**, **P3-4**) suggest that the most recent bleaching activity, likely related to deposition, took place during the past 2000 years. Although located in elevations above the upper limit of the marine boundary layer, the presumed depositional age is similar to **P2** (Fig. 6.6). In contrast to **P2**, however, the single-grain D_e distributions of these uppermost samples of **P3**, including surface sample **P3-1**, are very broad (Fig 6.6, Appendix C-III Fig. C7). Broad peaks, together with the occurrence of saturated grains and zero-dose grains, suggest heterogeneous bleaching as well as the erosion and reworking of both surface sediments and previously buried older material during deposition (Table 6.2, Fig. 6.6). Below, samples **P3-5** and **P3-6** display broad unimodal D_e distributions, likely indicating a rather long burial time. Together with the high proportion of saturated grains (>30 %) and the absence of surfaced grains (≤1 %) (Table 6.2), the CAM ages of samples **P3-5** and **P3-6** provide evidence of a much older depositional period or event at **P3**, that took place around 55 ka (**P3-5**, 53.0 ± 9.6 ka; **P3-6**, 57.9 ± 10.1 ka).

Profile P4 – 1480 m a.s.l.

P4 is located on the surface of an older alluvial fan generation earlier described by Moradi et al. (2020) and Sun et al. (2023). The alluvial fan is situated several 100 metres above the upper limit of the marine boundary layer and thus outside the zone of frequent fog occurrence and loma vegetation (Appendix C-III; Fig. C8). As in **P2** and **P3**, profile **P4** shows an increase in average grain size with depth, transitioning from a silt-dominated upper unit to sand-dominated layers below (Fig. 6.4a, Appendix C-III Fig. C8). The mobile to immobile element ratio likewise increases, particularly from unit II (**P4-2**) to unit III (**P4-3**), whereas only small variations are visible in the deeper

units III-VII (Fig. 6.5a). The D_e distribution of **P4-2** is right skewed, peaking around 30 Gy (Fig. 6.6). For this sample, no MAM age could be calculated and the CAM age (10.6 ± 1.5 ka) corresponds to the beginning of the shoulder on the right flank rather than the peak or leading edge. The peaks mode is ~29.5 Gy (6.6 ka), and the leading edge is estimated at ~13 Gy (3 ka) (Fig. 6.6). Below, samples **P4-3** to **P4-5** are characterised by **i)** the virtual absence of zero-dose grains (<2 %; Table 6.2), **ii)** >40 % of saturated grains, and **iii)** broad unimodal D_e distributions, altogether likely indicating long-term burial (Fig. 6.6). Saturated grains presumably reflect incomplete bleaching due to the steep and confined catchment area of **P4**.

The absence of zero-dose grains and the broad unimodal distribution of the lower samples **P4-3** to **P4-5** suggest that the CAM ages of these samples represent a depositional period between 50.1 ± 10.2 ka (CAM **P4-5**) and 41.7 ± 6.7 ka (CAM **P4-3**). Those CAM ages agree within 2σ with the proposed depositional age of 56.4 ± 2.8 ka for this fan generation proposed by Sun et al. (2023) (Fig. 6.6). In addition, these authors date the deposition of the adjacent younger fan generation to ~13.6 ± 1.8 ka, which agrees with the CAM age of 10.6 ± 1.5 ka of sample **P4-2**, that was taken from the uppermost sub-surface unit in **P4**. However, surface characteristics at **P4**, including varnished and rubified clasts, planar topography, and partly indurated bedding, rather suggest a longer period of depositional inactivity. By contrast, the younger fan section is characterised by grey clasts, distinct bar-and-swale topography, and loose bedding (Sun et al., 2023). To explain the young CAM age and long tail of the distribution of **P4-2**, it may be assumed that unconcentrated sheet wash events, likely contemporaneous to the alluvial activity in the younger fan generation, have led to the successive accumulation of fine-grained unit II on top of the older fan section. More likely, processes related to the evolution of desert pavements, i.e., the trapping of (aeolian) fine sediment below the gravel-covered surface, may explain the young peak including its left shoulder (Dietze et al., 2016; Ugalde et al., 2020; Williams and Zimbelman, 1994). **P4-2**'s grain size distribution also more closely resembles that of dust samples from the northern Atacama Desert than any other sample (Fig. 6.4b), supporting this hypothesis. The D_e distribution may thus reflect intensified dust trapping and desert pavement development between ~7 and 3 ka that occurred on top of an older (40-50 ka) alluvial fan surface.

The absence of both the peak and the assumed leading edge of the D_e distribution of **P4-2** (~30 Gy, ~13 Gy) in underlying D_e distributions suggests little or no vertical mixing between units II and III. In addition, the very low zero-dose grains fraction in **P4-2** (<2 %) further implies negligible downward transport from **P4-1** at present (Table 6.2). Accordingly, present day post-depositional mixing at **P4** appears limited, which

agrees with the fact that vegetation-related bioturbation and maybe even desert pavement evolution is impeded under present environmental conditions.

Profile P5 – 1930 m a.s.l.

Overall, in **P5**, no consistent trend in grain size with depth is observed and all units are dominated by coarse to very coarse sand (Fig. 6.4a, Appendix C-III; Fig. C9). The ratio of mobile to immobile elements does not vary significantly across the profile (Fig. 6.5a). All single-grain D_e distributions show large scatter (Fig. 6.6). Samples **P5-2** to **P5-5** show unimodal, right-skewed D_e distributions with progressively broader peaks towards the base of the profile, whereas sample **P5-6** lacks a clearly defined peak. While the fraction of saturated grains is small throughout the entire profile (2-9 %) and not increasing consistently with depth, the fraction of zero-dose grains constantly decreases with depth from 50 % in **P5-2** to 0 % in **P5-6** (Table 6.2). However, due to the young MAM-3 and -4 ages of the samples the zero-dose grains more likely reflect recent deposition rather than post-depositional mixing. The MAM-4 and -3 ages of the upper two sample **P5-2** (1.42 ± 0.25 ka) and **P5-3** (1.77 ± 0.31 ka) from units II and III agree within 1σ, indicating a deposition during the last 2 ka, like the upper units of **P2** and **P3** (Fig. 6.6). Unit IV likely belongs to a period of deposition between ~3 and 5 ka (**P5-4,** 3.95 ± 0.71 ka; **P5-5,** 4.41 ± 0.87 ka, Fig. 6.6). In addition, sample **P5-6** from unit V displays a markedly different D_e distribution compared to the overlying samples (Fig. 6.6). Its MAM-4 age (17.9 ± 3.1 ka) also deviates significantly from the overlying samples. Based on our ambiguous data, we cannot identify the processes responsible for the D_e distributions in sample P5-6, and therefore cannot interpret the age of unit V.

6.5 Discussion

6.5.1 Profile chronology and formation

The luminescence data obtained from all five profiles reveal characteristic patterns of both depositional and post-depositional processes. In all profiles, the single-grain D_e distributions range from narrow unimodal to very broad and occasionally multimodal shapes, suggesting varying degrees of bleaching prior to deposition and post-depositional disturbances (Fig. 6.6). Alluvial deposits are generally prone to heterogeneous bleaching of the luminescence signal, since they are usually the result of fast but intense discharge events with high sediment-to-water ratios that prohibit bleaching of all sediment grains (Duller, 2008b; Ventra and Clarke, 2018). In this context, it is therefore important to perform single-grain analyses, as the averaging effect of single-grain signals in multi-grain measurements can obscure important age

components (Duller, 2008b). We observe D_e distributions with a distinct peak around a low dose ~2.24 Gy and a long tail reaching into a higher dose region >50 Gy in all our surface samples as well as in samples **P2-2** and **P2-3** (cf. Fig. 6.6, Appendix C-III Fig. C5-C9), which is a typical characteristic of heterogeneous bleaching in fluvial transport (Guibert et al., 2017) (Fig. 6.7b).

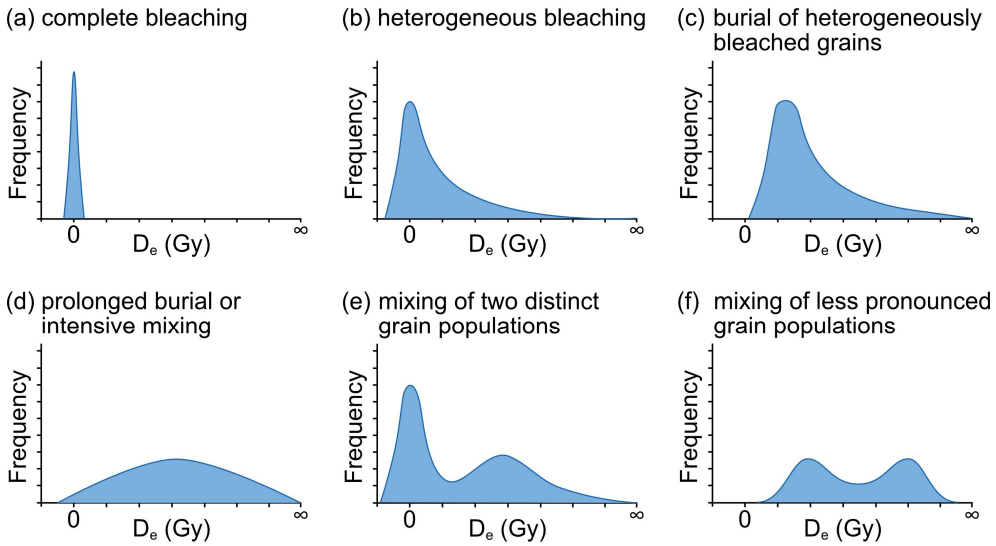

Fig. 6.7: *Theoretical D_e distributions adapted from Bateman et al. (2003): **a)** complete bleaching with a narrow normal distributed D_e distribution around a dose of 0 Gy, **b)** heterogeneously bleached grains with a distinct peak in a low dose region and a tail towards higher doses, **c)** heterogeneously bleached grains after burial, broadening the low dose peak and shifting it to the right, **d)** prolonged burial or intensive mixing of heterogeneous grain populations represented by a unimodal normal distributed D_e distribution, **e)** mixing of two distinct grain populations resulting in a bi-modal distribution with the older grain population being broader than the recently buried one, **f)** mixing of two less pronounced grain populations.*

The length of the tail represents the inherited dose that was accumulated in the individual grains prior to alluvial transport and the associated bleaching period. In samples **P3-2** to **P3-4**, **P4-2**, and **P5-2** to **P5-5**, the D_e distributions likewise exhibit a long tail to the right yet their peaks are broader and in slightly higher dose regions (Fig. 6.6 and 6.7c). This indicates a burial phase of heterogeneously bleached samples, where the entire distribution will shift towards higher doses and will disperse due to differences in micro-dosimetry and potentially mixing (Bateman et al., 2003; Cunningham et al., 2015, Fig. 6.7c). Broad unimodal distributions are observed in samples **P1-2** to **P1-4**, **P3-5**, and **P4-3** to **P4-5** (Fig. 6.6 and 6.7d). Those broad unimodal distributions suggest either prolonged phases of burial, where effects like micro-dosimetry and/or mixing lead to a substantial broadening of the peak, or intense mixing after burial (Fig. 6.7c). In turn, if a heterogeneously bleached sediment layer remains at the surface and therefore experiences bleaching over a longer time period, the peak will become more pronounced and the tail will vanish over time (Duller, 2008b; Fig. 6.7a). However, in this study we took surface samples ranging up to 2 cm in depth. Therefore, we incorporated grains into our surface samples that have not

been exposed to light at the present surface. Since the D_e distributions of all surface samples have grains reaching into high doses (~100 Gy for **P1-1** up to ~600 Gy for **P5-1**, Appendix C-III Fig. C5-C9 similar to Fig. 6.7b) we can infer that the bleaching depth within Atacama Desert soils and surfaces is less than 2 cm. Nevertheless, almost 85 % of the grains in the surface samples can be considered as well bleached (p0 of the MAM-4 of all surface samples = 0.85). Finally, bimodal distributions occur in samples **P2-4, P3-6**, and **P5-6** (Fig. 6.6). Bi- or multimodal D_e distributions may indicate post-depositional mixing processes, such as bioturbation caused by roots or burrowing organisms. These processes result in the appearance of one or more additional peaks alongside the original (heterogeneously bleached) component (Bateman et al., 2003; Fig. 6.7e and f). Alternatively, such distributions may also reflect the input of sediment from multiple sources with distinct inherent luminescence signals that were not reset during deposition.

The different shapes of D_e distributions offer insights into depositional and post-depositional processes on a sample level. Yet, it is not possible to definitively determine whether each sample was shaped by either depositional or post-depositional processes. For their interpretation, D_e distributions should always be accompanied by stratigraphy, field observations, sediment properties and additional proxies such as saturated and zero-dose grains. Unfortunately, the PCA based on geochemical and granulometric parameters mainly provided site-specific characteristics (Fig. 6.5b), indicating that sediment source and local environmental conditions have a stronger effect on the sediment properties than weathering, post-depositional mixing or depositional processes. Nevertheless, based on the combination of D_e distributions, field observations, elemental ratios, grain size properties and the PCA, we can distinguish two main types of profiles: **i)** profiles that are associated with recently **geomorphologically active** surfaces (**P2**, **P3**, **P5**, left part of the PCA biplot, Fig. 6.5b), and **ii)** profiles that are associated with recently **geomorphologically stable** surfaces (**P1** and **P4**, right part of the PCA bi-plot, Fig. 6.5b). The sediments and chronologies of the profiles associated to recently **geomorphologically active** surfaces are dominated by recent to sub-recent depositional processes, mainly in the form of alluvial activity. In contrast, recently **geomorphologically stable** surfaces are affected by post-depositional *in-situ* weathering and mixing processes in the absence of active geomorphic processes, as they lie outside of areas affected by subrecent or modern alluvial activity.

A key feature of recently geomorphologically active profiles is the relatively high proportion (10-66 %) of zero-dose grains up to depth of 30 cm or more (Table 6.2, Appendix C-III Fig. C6, C7, C9). This suggests that, despite the dominance of

geomorphic processes, recently bleached grains are incorporated into the subsurface layers. This may result from post-depositional mixing or from erosion of modern surfaces and/or young depositional units within the catchment during deposition. The root penetration in **P2** indicates a post-depositional mixing component, while the supposed palaeosurface (**P2-4**) indicates recent deposition of the upper three profile units. Given the absence of vegetation at the sites of **P3** and **P5**, bioturbation as a post-depositional process can be excluded for these profiles. The downward decrease in zero-dose grains in these profiles is thus more likely the result of mixing during recent deposition.

In contrast to recently geomorphologically active profiles, the recently stable profiles were sampled from older alluvial fan surfaces. In both fans, the older surfaces are lying on higher terrace-type levels than the recent depositional activity, creating a topographic barrier. **P1** is located in the coastal plain, which has a considerably higher relative air humidity (Table 6.1) and – though still hyperarid – generally receives higher precipitation amounts compared to the Coastal Cordillera above the marine boundary layer. These local climatic conditions promote weathering and vegetation growth, which in turn enhances bioturbation. In contrast, **P4** is positioned in the Coastal Cordillera above the fog-influenced zone without the presence of vegetation. Mixing in **P4** likely results from desert pavement dynamics under persistently hyperarid conditions (Dietze et al., 2016; Ugalde et al., 2020; Williams and Zimbelman, 1994). Although both profiles are situated in distinctly different climatic settings and are affected by different mixing processes, they exhibit evidence of post-depositional mixing restricted to the uppermost ~10 cm of the soil. This shallow mixing depth in both profiles is consistent with previous findings of limited downward translocation of salts and water-soluble colloids in Atacama Desert soils (Ewing et al., 2006; Sun et al., 2023).

6.5.2 Palaeoclimatic significance

Across the ~70 ka period covered by our data we identify two main phases of alluvial activity (Fig. 6.6). The first occurs around 50 ka during Marine Isotope Stage 3 (MIS 3) and is consistently recorded in profiles above the marine boundary layer (**P3**-**P5**). The second phase of alluvial activity covers the last ~5 ka and is evident in the profiles from recently geomorphologically active settings (**P2**, **P3**, **P5**). The data also reveals three distinct intervals with no alluvial activity (Fig. 6.6). In the Coastal Cordillera, the first interval starts ~35 ka and ends at ~14 ka. In contrast, the profile in the coastal plain (**P1**) shows a phase of activity within this interval (~34–23 ka), effectively subdividing the period of alluvial inactivity into two shorter phases: a minor one from

~35–34 ka and a more extended one from ~23–14 ka (Fig. 6.6 right). The third period of alluvial inactivity is evident across the entire transect from ~8.4–5.3 ka (Fig. 6.6 right).

The first alluvial active phase at ~50 ka coincides with a marked reduction in regional aridity indicated by the aridity index of by Stuut and Lamy (2004; Fig. 6.8a, g). It further aligns with previously reported activity patterns from alluvial deposits in the coastal plain located further north (Bartz et al., 2020a, 2020b; Vargas et al., 2006; Fig. 6.8f), suggesting a broader climatic control on sediment mobilisation during MIS 3. According to Stuut and Lamy (2004), this more humid phase reflects the effect of precessional forcing of the Milankovitch cycle, which influenced the tropics and thereby the latitudinal position of Southern Westerlies.

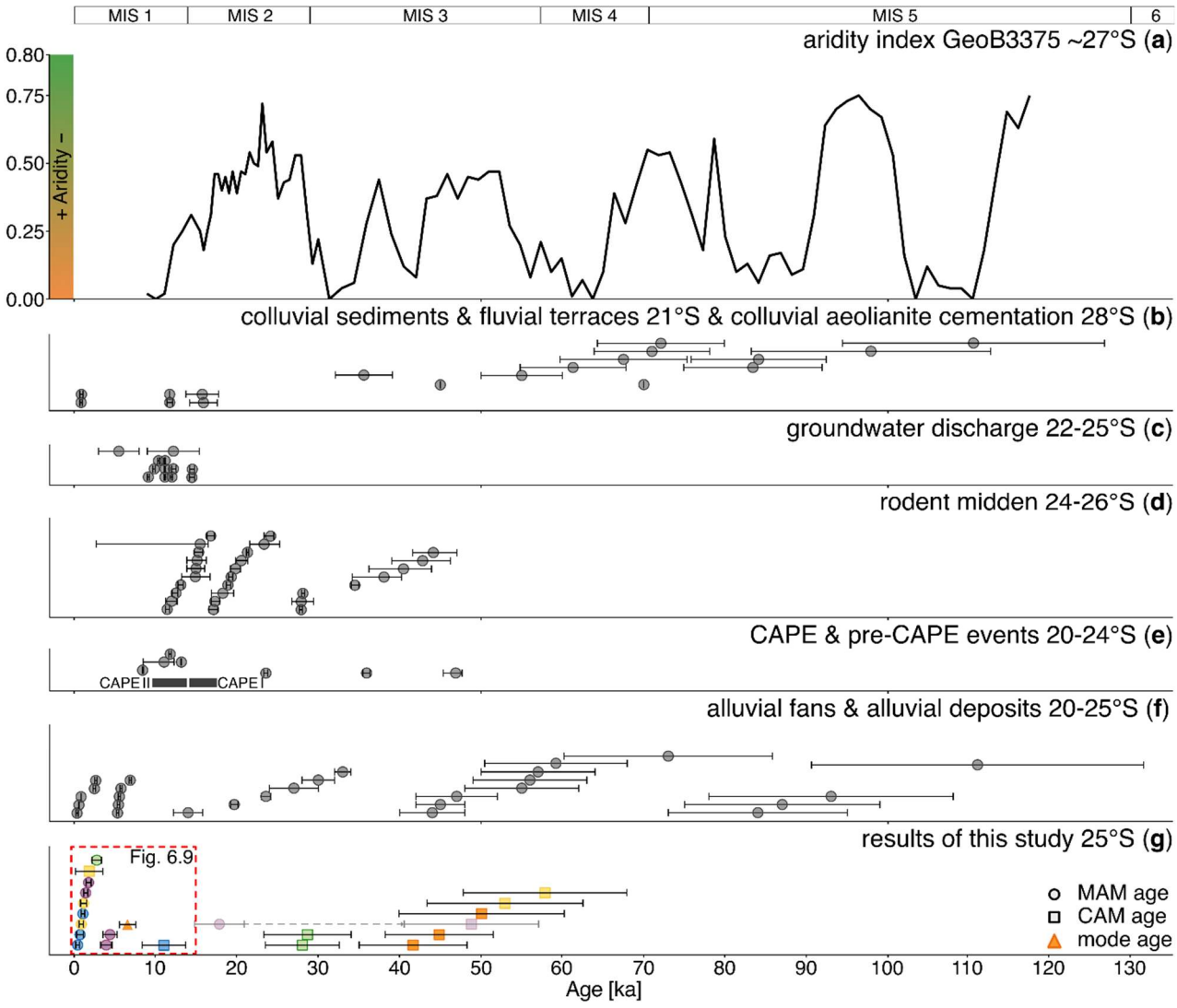

Fig. 6.8: *Regional proxies for humid phases:* ***a)*** *Aridity Index ~27 °S (Stuut and Lamy, 2004),* ***b)*** *humid phases based on colluvial sediments ~21 °S (Medialdea et al., 2020), colluvial aeolianite cementation ~28 °S (Nash et al., 2018), fluvial terraces ~21 °S (Gayo et al., 2023; Nester et al., 2007),* ***c)*** *humid phases based on groundwater recharge ~22-25 °S (Rech et al., 2002; Sáez et al., 2016),* ***d)*** *humid phases based on rodent middens ~24-26 °S (Díaz et al., 2012; Maldonado et al., 2005),* ***e)*** *pre-CAPE and CAPE events ~20-24 °S (de Porras et al., 2017; Gayo et al., 2012; Pfeiffer et al., 2018; Quade et al., 2008),* ***f)*** *alluvial fan active phases from other studies ~20-25 °S (Bartz et al., 2020a, 2020b; Vargas et al., 2006; Vásquez et al., 2018; Walk et al.,*

*2023), **g)** MAM ages (circles) and CAM ages (squares) within alluvial deposits this study ~25 °S; different colours represent the five different profiles (cf. Fig. 6.3-6.6), for sample P4-1 the mode is shown, MAM-4 and CAM ages of P5-6 are slightly transparent since their associated process is ambiguous.*

The second and most recent phase of alluvial activity, recorded in profiles **P2**, **P3**, and **P5**, corresponds to an interval of both intensified and highly variable El Niño activity (cf. Fig. 6.9) starting at ~5 ka, which likely promoted an increased frequency of extreme rainfall events (Rein et al., 2005, 2004).

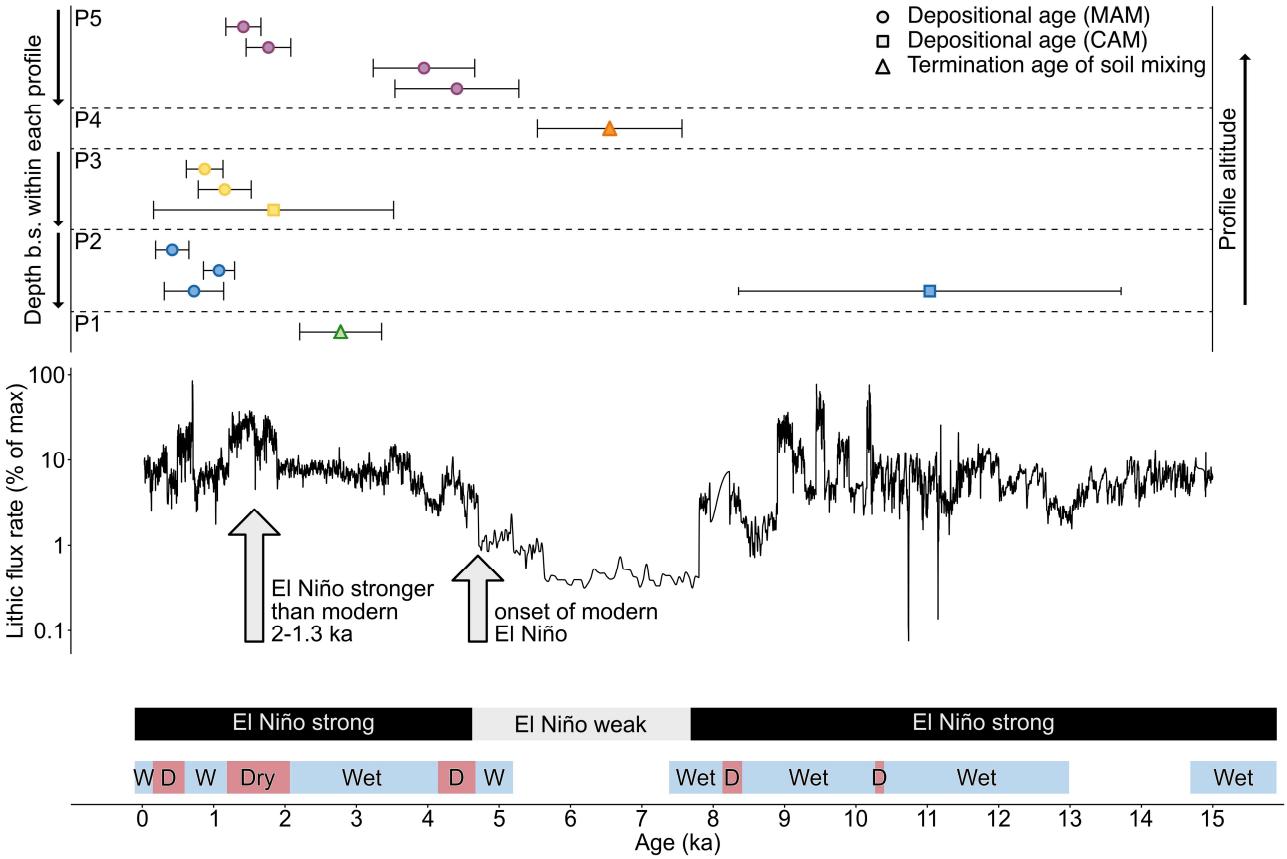

***Fig. 6.9:** Comparison of the luminescence ages (top) of all five profiles during the last 15 ka to independent proxies (bottom). MAM and CAM ages of recently geomorphic active surfaces are depicted as circles and squares respectively. Ages of recently geomorphic stable surfaces are depicted as triangles, with the MAM-4 age for P1-2 and the mode for P4-2. The lithic flux rate, as an indicator for El Niño activity (Rein et al., 2005, 2004), and wet and dry phases, based on the A. cinerea pellet diameters from palaeo-middens in the Atacama Desert (González-Pinilla et al., 2021), are provided as well.*

Besides these two main phases, additional evidence for alluvial activity is found in **P1**, **P2**, and **P5**:

In **P1**, the ages of samples **P1-3** and **P1-4** are interpreted to reflect secondary depositional activity on top of the oldest alluvial fan generation at the onset of MIS 2. These findings contradict the findings of Walk et al (2023), who suggested a MIS 5 depositional age for the same fan generation based on cosmogenic nuclide dating of surface clasts. This discrepancy may be explained by local reworking and surficial sediment redistribution through low-intensity sheet-wash. However, surface clasts

might contain inherited cosmogenic nuclide concentrations. This is particularly true in transport-limited cascading systems, in which short episodes of geomorphic activity are separated by long phases of geomorphic stability (Anderson et al., 1996; Walk et al., 2023). Based on our luminescence ages of the oldest fan generation, we consider an overestimation of this fan generation by Walk et al. (2023) likely. Although the reasons for this discrepancy remain ambiguous, our findings underline the need to use complementing chronometers (e.g. cosmogenic nuclide and feldspar luminescence dating). Using multiple chronometers enables more robust chronologies and ultimately helps to detect possible dating biases. This is particularly true for complex geomorphic settings, where different dating techniques are affected by different types of errors (i.e., inheritance and heterogeneous bleaching).

Further contemporary depositional activity at the onset of MIS 2, as found for **P1**, was not observed elsewhere along the transect. Local climatic differences between the coastal plain and the Coastal Cordillera during this period are difficult to constrain based on our data. However, localised runoff on coastal alluvial fans may occur independently of regional climate variability and is not necessarily related to alluvial activity within the Coastal Cordillera. Other studies reported alluvial deposition (Bartz et al., 2020a), activity in alluvial fans (Bartz et al., 2020b) and in alluvial terraces (Vargas et al., 2006) along the coastal zone during this interval (Fig. 6.8f). In addition, pollen analysis from rodent middens close to our study site indicate the occurrence of plants, and hence elevated humidity, in the Coastal Cordillera (Díaz et al., 2012) and at higher elevations of 2670 m a.s.l (Maldonado et al., 2005) during the same period (Fig. 6.8d). The aridity index shows a trend towards more humid conditions during this phase, following an extremely arid period recorded toward the end of MIS 3 (Stuut and Lamy, 2004; Fig. 6.8a). Together, this suggests that the localised signals in **P1** may reflect broader climatic trends throughout the entire Coastal Cordillera, although Coastal Cordillera profiles studied here lack evidence of activity during this period.

In sample **P2-4**, two distinct phases of alluvial activity were identified. The younger phase corresponds to an interval of enhanced El Niño variability starting at ~5 ka. The older phase aligns with an earlier period of intensified El Niño activity beginning ~13 ka (Rein et al., 2005, 2004; Fig. 6.9). Both phases also coincide with wet conditions inferred by González-Pinilla et al. (2021; Fig. 6.9) and with the formation of fluvial terraces (Gayo et al., 2023; Nester et al., 2007; Fig. 6.8b). The younger phase is further supported by evidence of alluvial deposition both along the coast (Vargas et al., 2006; Fig. 6.8f) and within the Cordillera (Vásquez et al., 2018; Fig. 6.8f). The older phase corresponds to debris-flow activity at a coastal alluvial fan (Bartz et al., 2020a; Fig. 6.8f). Additional indicators for the older phase include the Central Andean Pluvial

Event (CAPE) II and pre-CAPE events (de Porras et al., 2017; Gayo et al., 2012; Pfeiffer et al., 2018; Quade et al., 2008; Fig. 6.8e), regional groundwater discharge (Rech et al., 2002; Sáez et al., 2016; Fig. 6.8c), and pollen records from rodent middens in the Cordillera (Maldonado et al., 2005; Fig. 6.8d). These observations suggest that both phases of alluvial activity were likely driven by increased frequencies of extreme rainfall events linked to shifts in ENSO dynamics affecting the entire region. This highlights the strong influence of climatic variability on sediment fluxes in the region.

The broad and multimodal D_e distribution of sample **P5-6** and the granulometric and geochemical characteristics do not allow for identifying particular processes such as alluvial depositional activity or post-depositional mixing. However, its MAM-4 age of 17.8 ± 3.1 ka indicates that bleaching of sediments in this unit ceased during the comparatively humid late MIS 2 (Stuut and Lamy, 2004; Fig. 6.8a). The CAM age of 48.9 ± 8.3 ka is consistent with the older depositional phases observed in profiles **P3** and **P4**, both situated above the marine boundary layer. Thus, the CAM age may reflect depositional activity under regionally wetter climatic conditions during MIS 3. Between the CAM and MAM-4 ages, multiple phases of increased humidity are evident in the aridity index (Stuut and Lamy, 2004; Fig. 6.8a), and are corroborated by all other regional proxies analysed in this study (Fig. 6.8b–f). Nonetheless, the processes associated with this D_e distribution and the MAM-4 and CAM ages remains ambiguous.

Against the background of these results, past and present alluvial depositional activity along the here presented climatic transect appears to be primarily controlled by site-specific conditions. These include whether the sampling site is located within a recently geomorphologically active (**P2**, **P3**, and **P5**) or recently geomorphologically stable (**P1**, **P4**) segment of the respective alluvial deposit. The transect spans from the coastal plain (**P1**) through the fog-influenced zone of the Coastal Cordillera (**P2**) to the upper part of the Coastal Cordillera (**P3-P5**), where fog is virtually absent and rainfall frequency extremely low. We observe no systematic spatial pattern in geomorphic activity related to the geographic position of a profile within the climatic transect. This is consistent with the characteristics of transport-limited alluvial systems, where sediment supply exceeds the transport capacity of the system (Bovis and Jakob, 1999). In such settings, local controls such as slope morphology, channel connectivity, or sediment availability play a more significant role in determining depositional timing and surface reworking than external drivers alone. Consequently, deposition or alluvial reworking can occur within a spatially confined area without necessarily affecting downstream locations within the same catchment.

However, the present climatic gradient along the Paposo transect is indeed reflected by post-depositional processes in **P1**, **P2** and **P4**. In the lower elevations of the transect (**P1**, **P2**), post-depositional processes are likely related to bioturbation, while at higher elevations above the marine boundary layer (**P4**) they are presumably related to desert pavement formation. The probably bioturbation-related most recent phase of post-depositional mixing in **P1** falls within a wetter climatic interval characterised by a comparatively strong El Niño (González-Pinilla et al., 2021; Rein et al., 2005, 2004; Fig. 6.9). Evidence for depositional activity in profiles **P3** and **P5**, as well as phases of alluvial fan accumulation in more northern parts of the Coastal Cordillera (Vargas et al., 2006; Fig. 6.8f) support this interpretation. In contrast, post-depositional processes plausibly related to the development of a desert pavement (Ugalde et al., 2020) in **P4** coincide with a phase of prevailing hyperarid conditions between ~8 and ~5 ka and weak and relatively stable El Niño activity (González-Pinilla et al., 2021; Rein et al., 2005, 2004; Fig. 6.9). Moreover, de Haas et al. (2014) emphasised that desert pavements cannot form under wet conditions which lead to intensified weathering and surface reworking by runoff events. The absence of deposition during the last ~5 ka in **P1** and **P4** likely reflects the presence of younger alluvial fan segments and not dry climatic conditions. Surface runoff and associated sediment transport were redirected toward these adjacent, more active younger sections, resulting in the bypassing of older depositional surfaces. Consequently, **P1** and **P4** lack evidence of late Holocene fluvial activity, despite supposedly continued sedimentary dynamics within their fan systems.

Overall, our results support the growing body of evidence that, even under persistent hyperarid conditions, episodic increases in moisture availability were sufficient to drive localised alluvial processes. These findings emphasise the importance of integrating geomorphic, geochemical, granulometric, and chronometric data at high spatial resolution to understand landscape dynamics in extreme hyperarid environments. The high spatial resolution is of particular importance where geomorphological active and stable surfaces occur in direct vicinity. The identified post-depositional processes highlight that geomorphological stable surfaces can retain climatic and geomorphic signals valuable for palaeoenvironmental reconstruction. Moreover, careful interpretation of single-grain D_e distributions can be used as a palaeoclimatic proxy for the late Pleistocene and Holocene.

6.6 Conclusions

The combined analysis of luminescence dating, stratigraphy, geochemistry, granulometry and field observations of five profiles in a climatic transect in the Atacama Desert reveals a complex interplay between depositional and post-depositional processes in Atacama Desert soils and surfaces.

Although heterogeneous bleaching is a ubiquitous feature in alluvial deposits, the high proportion of well-bleached grains at the surface implies a good bleachability in our samples, if grains are at the immediate surface, and a shallow effective bleaching depth (<2 cm). The different shapes of the single-grain D_e distributions underscore the importance of interpreting luminescence ages in the context of surface stability and disturbance regimes, rather than associating age signals exclusively to the moment of deposition. It further emphasises that single-grain dating is capable of distinguishing between depositional and post-depositional processes, which is not possible with multi-grain dating or terrestrial cosmogenic nuclide dating, due to their lower spatial and temporal resolution.

Along the investigated climatic transect, stratigraphic patterns are primarily governed by local geomorphic controls rather than regional climatic patterns. This results in spatially heterogeneous surface evolution and varying degrees of soil and surface activity and stability. Recently geomorphological active profiles (**P2**, **P3**, **P5**) show recent sediment accumulation and signs of vertical grain transport in **P2**. In contrast, recently geomorphological stable profiles (**P1**, **P4**) preserve evidence of reworking superimposed upon longer-term landscape stability. Despite contrasting environmental settings, post-depositional mixing in **P1** and **P4** remains shallow, suggesting that soil processes in the Atacama Desert are depth-limited regardless of the presence of vegetation.

The overall timing of soil and surface activity and stability aligns with a compilation of regional climatic reconstructions from other studies. Especially the relatively strong and variable El Niño episode during the last ~5 ka and a relatively humid phase around 50 ka are evident throughout the entire transect. This highlights the importance of integrating local-scale sediment dynamics and post-depositional processes when interpreting luminescence data for palaeoenvironmental reconstructions in hyperarid landscapes and shows the potential of single-grain luminescence dating as a high-resolution climatic proxy.

6.7 Author contributions

LM: conceptualization, writing - original draft, data curation, formal analysis, investigation, visualisation
SM: conceptualization, writing - original draft, investigation, visualisation
SR: writing – review & editing, investigation, supervision
WM: writing – review & editing, formal analysis
SO: writing – review & editing, investigation
AP: writing – review & editing, investigation
TR: conceptualization, writing – review & editing, supervision, funding acquisition

6.8 Competing interests

The authors declare that they have no known competing financial interests or personal relationships that could have appeared to influence the work reported in this paper.

6.9 Acknowledgements

This project is affiliated to the Collaborative Research Centre 1211 “Earth – Evolution at the Dry Limit” (Grant-No.: 268236062) funded by the German Research Foundation (Deutsche Forschungsgemeinschaft, DFG), Germany. We would like to thank Andreas Peffeköver his assistance during fieldwork. We further thank Sarah Spengeler, Johanna Steiner, and Johanna Schreiber for their contributions to the laboratory analyses. LM is also grateful to Eduardo Campos as well as Bárbara Blanco Arrué and her team for their kind help when we stranded along Ruta 5 without accommodation.

Chapter 7

Discussion of the research questions

It's a funny old world.
(Margaret Thatcher)

This thesis investigates Earth's surface evolution and fluctuations of the palaeoclimate under overall hyperarid conditions in the Atacama Desert in Chile, primarily based on single-grain luminescence dating of alluvial deposits. In order to decipher depositional and post-depositional dynamics using luminescence-based inventories, the used method required adaptation to the specific challenges posed by Atacama Desert sediments. Subsequently, a geochronological framework was established for five soil and surface profiles along a climatic elevation transect. All findings were contextualised both locally and regionally, contributing to a broader understanding of Late Pleistocene to Holocene climate variability and landscape evolution in the Coastal Cordillera of the Atacama Desert, Chile.

As this thesis aims to address multiple research questions, to contribute to the understanding of geochemically complex feldspar samples as well as landscape evolution and palaeoclimatic fluctuations in the Atacama Desert, the following chapters present the corresponding answers.

7.1 Method refinement and geochemical properties of feldspar

Q1: Can standardised growth curves (SGCs) be applied to determine single-grain Atacama Desert feldspar equivalent doses and how does intra-sample geochemical variability relate to observed luminescence characteristics, such as equivalent dose, dose recovery ratio, and signal brightness? (Chapters 3 and 5)

Objective 1a: *Construct a standardised growth curve (SGC) with Atacama Desert feldspar separates.*

Chapter 3 demonstrates that an SGC can be successfully constructed using a dataset consisting of dose recovery tests on five Atacama Desert samples. The standard quality controls for an SGC were met (SAR D_e = SGC D_e, reduction of scatter, measured L_x/T_x = expected L_x/T_x) (Fig. 3.1 and Appendix A Fig. A1).

Chapter 5 further showed that an SGC can also successfully be constructed using a dataset consisting of measurements of the natural luminescence signal from ten Atacama Desert samples. The standard quality controls for an SGC were met (Fig. 5.1).

Hence Atacama Desert samples have been proven to be suitable for SGC construction. This result confirms earlier studies by Sontag-González et al. (2021), who tested the SGC application on geochemically complex feldspar samples from Indonesia.

Objective 1b: *Construct an additional SGC with feldspar separates from outside of the Atacama Desert and applying both curves to Atacama Desert samples.*

A second SGC, hereafter referred to as **xSGC**, was successfully established using a dataset consisting of dose recovery tests on five feldspar samples from various geological and geographical contexts in Chapter 3. All standard quality controls for an SGC were met (Appendix A Fig. A1). Subsequently, D_e values were calculated for a set of five Atacama Desert samples using both the xSGC and the SGC constructed with the same set of Atacama Desert samples (cf. Objective 1a). The grain-wise comparison of the two sets of D_e values showed a good agreement (Fig. 3.1). Nevertheless, the xSGC consistently produced slightly lower D_e values than the SGC. This discrepancy increased with increasing L_n/T_n. As with the D_e estimation using a SAR growth curve, small changes in L_n/T_n result in disproportionately larger changes in the D_e the closer to saturation they intersect the growth curve.

Despite these deviations, the successful application of the xSGC to Atacama Desert samples demonstrates that an SGC can be constructed from samples of different origin than those for which it is applied. The agreement between SGC and xSGC results confirms the observations by Li et al. (2015b), who reported that a 'global SGC' can be suitable for feldspar samples across diverse environments, and are consistent with Mueller and Preusser (2022), who found that SGC-based D_e estimates remain unbiased when the same grains are used for both SGC construction and SGC application for D_e calculation.

The results from Objective 1a and 1b were promising, but they did not lead to any reduction of measurement time. When an SGC is used for D_e determination, the number of measurement cycles is typically reduced to the L_n/T_n and one further L_x/T_x measurement cycle. Many commonly used rejection criteria cannot be applied when measurement cycles are reduced to those two measurement cycles. Since no full SAR sequence is available, neither recycling ratios nor recuperation can be determined. Additionally, no grain-wise growth curve is constructed, which means that criteria based on the goodness of the growth curve fit, such as the figure of merit (FOM) or the reduced chi-square, cannot be calculated. The reduction in applicable rejection criteria results in a higher number of accepted grains for D_e determination. The D_e values of grains that were only accepted when using a single L_x/T_x cycle exhibited a high scatter. The scatter was markedly higher compared to the scatter in the SGC- and SAR-based D_e values when all SAR cycle and therefore all rejection criteria were used (Appendix A Fig. A2).

A further limitation of using only a single L_x/T_x cycle was the occurrence of significant deviations of some L_x/T_x values from the grain-wise fitted dose response

curve established from all measured cycles (cf. Fig. 3.2A). If all SAR cycles were used, most of those odd L_x/T_x cycle were filtered out by the growth curve fitting rejection criteria, which cannot be applied if only one measurement cycle is used. If one of those odd L_x/T_x cycles is chosen for the SGC approach the resulting D_e might not be in unity with the SAR D_e. To address this issue, a new parameter, the synthetic regenerative dose (**sR**) was introduced. This parameter allows the projection of multiple L_x/T_x onto the constructed SGC. The sR is inserted into the grain-specific exponential growth function (Eq. 3.1) to derive a synthetic L_x/T_x value (L_{sR}/T_{sR}), which, together with L_n/T_n, serves as input for D_e calculation; its influence was tested using eight sR values ranging from 50 to 800 Gy. An sR of 150 Gy yielded the best agreement with D_e values obtained from the SAR approach. However, this approach alone does not save measurement time either.

Therefore, in a subsequent step, the cycles used for D_e calculations with the sR_{150}xSGC approach were reduced. The best-performing set of reduced measurement cycles (**rc_5**; Table 3.3) included a recuperation point, a recycling point smaller than the expected D_e, and an additional dose point between D_0 and $2D_0$ of the applied SGC. This **rc_5sR_{150}xSGC** approach saved ~60 % of the measurement time and resulted in more than twice as many calculable D_e values. The increased number of calculated D_e values further reduces overall measurement time, as fewer discs need to be measured.

After developing the rc_5sR_{150}xSGC technique using dose recovery tests in Chapter 3, it was applied to natural luminescence signals in Chapter 5. Even though the successful construction of the SGC was possible, its application to natural signals did not yield reliable D_e estimates. In Chapter 5, full $pIRIR_{225}$ SAR protocols were measured for ten samples, and the resulting dataset was subsequently reduced to include only measurement cycles according to the rc_5 approach from Chapter 3. As expected, fewer grains were rejected when using the reduced dataset, resulting in some grains having only SGC-derived D_e values and no SAR D_e (referred to as unique SGC grains). However, numerous grains also yielded SAR D_e values but no SGC D_e values (referred to as unique SAR grains) (Fig. 5.2).

Unfortunately, these unique SAR grains were not homogeneously distributed across the entire range of D_e values but were instead clustered in the low D_e region. This is problematic, as for most samples the Minimum Age Model (MAM) should be applied, which specifically targets the lower D_e grain population. The inability of the rc_5sR_{150}SGC approach to determine D_e values for grains in this region introduces a bias in the comparison of SAR- and SGC-based MAM results (Fig. 5.3).

The rc_5sR_{150}SGC method is dependent on the expected D_e and thus performs best when the D_e values of all measured grains are relatively uniform. Therefore, its

application to potentially heterogeneously bleached or mixed samples seems limited. Since remeasuring the ten samples using a protocol tailored specifically to low-dose grains was not possible within the frame of this thesis, refinement of the rc_xsR_xSGC approach was limited to adjusting the size of the sR parameter. However, changes in sR did not lead to improved results (Fig. 5.4). Thus, the rc_xsR_xSGC method could not be used to reduce the measurement time for the analysis of the Atacama Desert samples within this thesis.

Objective 1c: *Identifying statistical correlations between elemental composition and luminescence properties, including equivalent dose, dose recovery ratio, and signal brightness.*

No statistically significant correlations were found between the elemental composition of the ten investigated samples and their luminescence properties, namely their signal brightness, size of the D_e, and their dose recovery ratio (Fig. 3.5 and Appendix A Fig. A4). As expected, the grains from the Atacama Desert exhibited substantial geochemical variability (Fig. 3.4A). However, similarly high variability was also observed in three out of five comparison samples originating from outside the Atacama Desert (Fig. 3.4B). No systematic difference in the geochemical composition was identified between grains that yielded suitable luminescence signals and those that did not (Fig. 3.4).

In particular, no correlation was observed between the internal K-concentration and any of the assessed luminescence properties (Fig. 3.5 and Appendix A Fig. A4). Given the heterogeneity of geochemical compositions, the internal K-concentration used for dose rate determination requires further investigation. However, the method applied (SEM-EDX) was time-consuming and costly, making it impractical for routine application in luminescence dating. These limitations led to the development of the subsequent research question **Q2**.

Overall, SGCs currently do not provide robust single-grain D_e estimates for naturally irradiated Atacama Desert feldspar samples. Nevertheless, methodical refinements may potentially address the identified limitations. Furthermore, intra-sample geochemical variability does not correlate with luminescence properties such as signal brightness, D_e, or dose recovery ratio. Therefore, while SGCs hold promise, particularly with methodological optimisation, the influence of internal K-concentration on dose rate calculations in geochemically heterogeneous samples remains an issue requiring further investigation, which is the focus of the following discussion.

Q2: Is the measurement of the internal K-concentration in feldspar grains essential for accurate internal dose rate calculations? In particular: what level of detail is necessary in those measurements and what effect do different K-concentration determination approaches have on the calculated total dose rate of a sample. (Chapter 4)

Objective 2a: *Reviewing current literature on how the internal K-concentration is determined and used in internal dose rate calculations.*

A systematic literature review of 432 publications on feldspar luminescence dating revealed that 76 % of the studies used a literature-derived value to determine the $\dot{D}_{int}$. In 96 % of these cases, the literature values were chosen without any investigations of the sample-specific K-concentration. The study by Huntley and Baril (1997) was the most frequently cited, referenced by approximately half of all reviewed publications. The three most cited K-concentration values were 12.5 ± 0.5 % K (Huntley and Baril, 1997; n = 272), 13 ± 1 % K (Zhao and Li, 2005, n = 47), and 10 ± 2 % K (Smedley et al., 2012, n = 23) (Fig. 4.1b). Notably, 84 out of the 432 publications failed to report the applied K-concentration in line with good scientific practice, thereby conflicting with established standards of scientific transparency. While some studies did not mention the K-concentration at all, others reported a value without citing a reference or mentioning a measurement technique used. The analysis also indicated a steady increase in the number of publications related to feldspar luminescence dating over time. Consequently, the question of whether measuring the internal K-concentration is essential for accurate $\dot{D}_{int}$ determination becomes increasingly relevant.

Objective 2b: *Comparing K-concentration results obtained using four different analytical methods.*

In Chapter 4, four analytical techniques were evaluated to determine the internal K-concentration of feldspar separates, using the same set of ten samples as in Chapter 3 (**Q1**). Two of these methods were applied at the multi-grain level (β-counter and WDXRF), and two at the single-grain level (μ-XRF and SEM-EDX). The single-grain SEM-EDX results were also used to calculate two luminescence-weighted K estimates per sample: the *effective K* and the *luminescent grains*. Firstly, the multi-grain measurements, average values of the single-grain measurements, and the luminescence-weighted K estimates were compared to each other and to the three most cited literature values of 10 ± 2 % K (Smedley et al., 2012), 12.5 ± 0.5 % K (Huntley and Baril, 1997) and 13 ± 1 % K (Zhao and Li, 2005) (Fig. 4.2). The ten samples had K-concentrations between 0.6 % and 15.2 %. The majority (85 %) of both measured

K-concentrations and the calculated luminescence-weighted K estimates fell outside the range of the three most cited literature values (8 – 14 %). This demonstrates that the use of often arbitrarily selected literature values for the internal K-concentration (cf. Objective 2a) may significantly overestimate the true sample-specific K-concentration, potentially resulting in erroneous dose rate estimations (cf. Objective 2c).

Intra-sample variability at the single-grain level was substantial, with K-concentration ranges of up to 14.2 % K (SEM-EDX) and 16.6 % K (μ-XRF). The grain-wise results per sample have been compared to the sample-wise results and the three most cited literature values (Fig. 4.3 and Appendix B Fig. B5). Fewer than 14 % of the single-grain values agreed with the literature values, and fewer than 20 % matched the bulk measurements, the averaged single-grain measurements, or the luminescence-weighted K estimates. The large variability within the samples makes it difficult to represent all individual values within a sample with a single representative K-concentration.

Two luminescence-weighted K estimates were calculated: the *effective K* and *luminescent grains* (all grains with $T_n > 3\sigma$ background). Both were based on the common assumptions that the signal intensity correlates with the K-concentration (Prescott and Fox, 1993; Spooner, 1992) and that K-rich feldspars emit more strongly in the 410 nm spectral region than Na-rich feldspars (e.g. Huntley et al., 1991; Fig. 2.4). The *effective K* was higher than the average of the underlying single-grain values in nine out of ten samples. However, it remained below the literature values in seven out of ten cases. The *luminescent grains* showed a similar behaviour and were additionally analysed on a single-grain level. It was shown that sufficiently bright luminescent grains occur across the entire range of measured K-concentrations. Given that the widespread use of comparatively high literature K-concentration values is based on the two assumptions above, the findings further highlight the risk of overestimating the internal K-concentration when applying arbitrarily chosen, non-sample-specific literature values.

While answering this objective three main conclusions could be drawn: **i)** literature values might significantly overestimate the K-concentration; **ii)** *luminescent grains* can have K-concentrations over the entire possible range and thereby confirming the non-existing correlation between the geochemical composition and luminescence properties found in Chapter 3 (**Q1**); **iii)** none of the sample-wise K-concentration values measured or calculated can represent the majority of single-grain K-concentration values within the same sample. Hence, the central question remains which K-concentration should be used for accurate $\dot{D}_{int}$ determination.

Objective 2c: *Assessing the influence of the different methods for the K-concentration determination on internal and total dose rate estimates.*

While in 85 % of our measurement-based K-concentration values significantly differ from the commonly used literature values, this does not necessarily imply a corresponding impact on the total Ḋ. Therefore, in Chapter 4, $\dot{D}_{int}$ and total Ḋ were calculated for each sample using different K-concentrations: multi-grain measurement results, averaged single-grain measurement results, luminescence-weighted K estimates, and the three most frequently cited literature values. In nearly 60 % of the cases the $\dot{D}_{int}$ results based on literature values were not in agreement with the measurement-based $\dot{D}_{int}$ results (Fig. 4.4a). For nine out of ten samples, literature-based $\dot{D}_{int}$ values overestimated $\dot{D}_{int}$ values based on measurements. Therefore, this deviation can be regarded as a systematic one-directional error.

A similar pattern was observed for the total Ḋ values. The literature-based total Ḋ values per sample were in unity, and measurement-based total Ḋ values per sample were also in unity. However, only 39 % of the measurement-based total Ḋ values were in agreement with the corresponding literature-based values for the same sample (Fig. 4.4b). In 61 % of the cases the literature-based total Ḋ values overestimated the measurement-based ones. Excluding sample MBT-I-2430, where all measurement- and literature-based total Ḋ values are in unity, the mean overestimation was >17 % (Fig. 4.4c and Appendix B Fig. B6).

This suggests that the use of literature-based K-concentrations may lead to a systematic overestimation of the total Ḋ, and consequently to an underestimation of the luminescence age. Although all tested measurement techniques yielded internally consistent total Ḋ values per sample, none of them adequately captured the full variability of K-concentrations observed at the single-grain level (cf. Objective 2b). Thus, while the choice of measurement method appears to have little influence on the total Ḋ value, it remains unclear which approach is best suited to represent geochemically heterogeneous feldspar samples for Ḋ assessments.

Objective 2d: *Evaluating the practicality and reliability of each method for routine application in luminescence dating.*

All four tested measurement techniques are semi-quantitative. Hence, the true internal K-concentration of a sample, whether on the multi- or single-grain level, remains unknown. The two multi-grain techniques are less time-consuming but provide no information on the variability of the K-concentrations. Single-grain techniques appear more accurate, yet the measurements are time-consuming and sample preparation can be laborious. The µ-XRF analysis tested here has an additional

limitation: the device has a limited sensitivity to the Na, which leads to systematic overestimation of the K-concentration. In some cases, the measured K-concentrations exceed the physically possible maximum of 14.05 % K.

Nevertheless, none of the analysed bulk or averaged measurements, including the K estimates, reflects the heterogeneity observed in single-grain K-concentrations. Therefore, it seems necessary to incorporate single-grain analysis in cases where variability in the grain-wise K-concentrations is likely. However, the total $\dot{D}$ should not be calculated at the single-grain level, as micro-dosimetry effects on the $\dot{D}_{ext}$ can currently not be resolved.

A pragmatic solution is needed for the multi-grain vs. single-grain measurement dilemma. The main downside of multi-grain-based techniques is the lack of information on the K variability. The main limitations of the analysed single-grain techniques are their time demands, and, in the case of the μ-XRF, the systematic overestimation of the K-concentration due to poor Na detection. A feasible solution combining the strength of both methods while avoiding their limitations would start with a time-efficient multi-grain measurement. If this measurement results in a K-concentration outside the range of the most cited literature values, high K-concentration variability is likely. In such cases, a small number of grains should be analysed for their single-grain K-concentration to assess the variability within the sample. The observed variability in the single-grain measurements can then be used to estimate the uncertainty of the multi-grain K-concentration. Because only a small number of grains are analysed, the additional sample preparation effort is minimised. Further, potential K overestimations are less problematic, since only a measure of variability is obtained from the single-grain analysis.

This hybrid approach offers a time- and cost-effective solution that may help avoid systematic underestimation of luminescence ages in future feldspar dating studies. Nevertheless, it would be desirable to include a single-grain technique to evaluate the internal U-, Th-, and Rb-concentrations as well, since they might also significantly influence the $\dot{D}_{int}$.

In Chapter 6, the $\dot{D}_{int}$ was calculated using this combined approach: the mean K-concentration was derived from β-counting, and the associated uncertainty was estimated from the variability observed in single-grain measurements using a μ-XRF device. The internal K-concentrations of the samples from the Paposo transect in Chapter 6 were on average 3.69 ± 0.33 % K (min = 1.61 % K in **P2-3**; max = 7.45 % K in **P1-1**; Appendix C-II Table C5). The uncertainty based on single-grain measurements was 3.01 % K and was used for all samples. To further evaluate the results from Chapter 4, $\dot{D}$ values for samples from Chapter 6 based on the approach from

Chapter 4 are compared to Ḋ values and ages based on the three most cited literature values. The measured K-concentrations from only six of the twenty-five samples fell within the proposed K-concentration range by Smedley et al. (2012; 10 ± 2 % K), and none of the samples were in the range of the values proposed by Huntley and Baril (1997; 12.5 ± 0.5 % K) or Zhao and Li (2005; 13 ± 1 % K).

Although in 63 % of the cases, the total Ḋ values based on the measured K-concentrations agreed with those based on the literature values (Fig. 7.1a), still a systematic one-directional error is visible. On average, the total Ḋ was overestimated by 21.4 ± 1.0 % (Fig. 7.1b) with a maximum overestimation of 36.8 ± 9.0% (**P2-1** based on Zhao and Li, 2005).

When comparing the ages derived from the different total Ḋ values, all ages for each sample were statistically indistinguishable due to the large associated uncertainties. Deviations reach up to 10.2 ± 12.2 ka (sample **P3-6**, based on Zhao and Li, 2005) (Table 7.1). On average, the ages differ by 17.2 ± 0.7 %. The maximum relative deviation amounts to 26.9 ± 46.7 % (sample **P2-1**, based on Zhao and Li, 2005) (Table 7.1). Despite the statistical agreement of the age estimates, a systematic underestimation of age occurred when the $\dot{D}_{int}$ was based on literature values for the K-concentrations. This bias can be mitigated by applying the hybrid approach introduced in Chapter 4.

Table 7.1: *Age underestimation of samples from Chapter 6 based on three most cited literature values, compared to the combined multi-grain/single-grain approach from Chapter 4. Results are given in absolute values (ka, left) and relative values (%, right).*

absolute age under-estimation (ka)	Smedley et al., 2012	Huntley and Baril, 1997	Zhao and Li, 2005
mean	1.53	2.06	2.16
sd	2.17	2.86	2.99
se	0.43	0.57	0.60
min	0.02 ± 0.09	0.04 ± 0.09	0.04 ± 0.09
max	7.61 ± 12.61	9.80 ± 12.20	10.20 ± 12.15

relative age under-estimation (%)	Smedley et al., 2012	Huntley and Baril, 1997	Zhao and Li, 2005
mean	14.23	18.32	19.09
sd	5.36	5.81	5.89
se	1.07	1.16	1.18
min	5.66 ± 21.65	9.82 ± 20.33	10.61 ± 22.38
max	21.37 ± 41.46	26.02 ± 38.87	26.9 ± 46.67

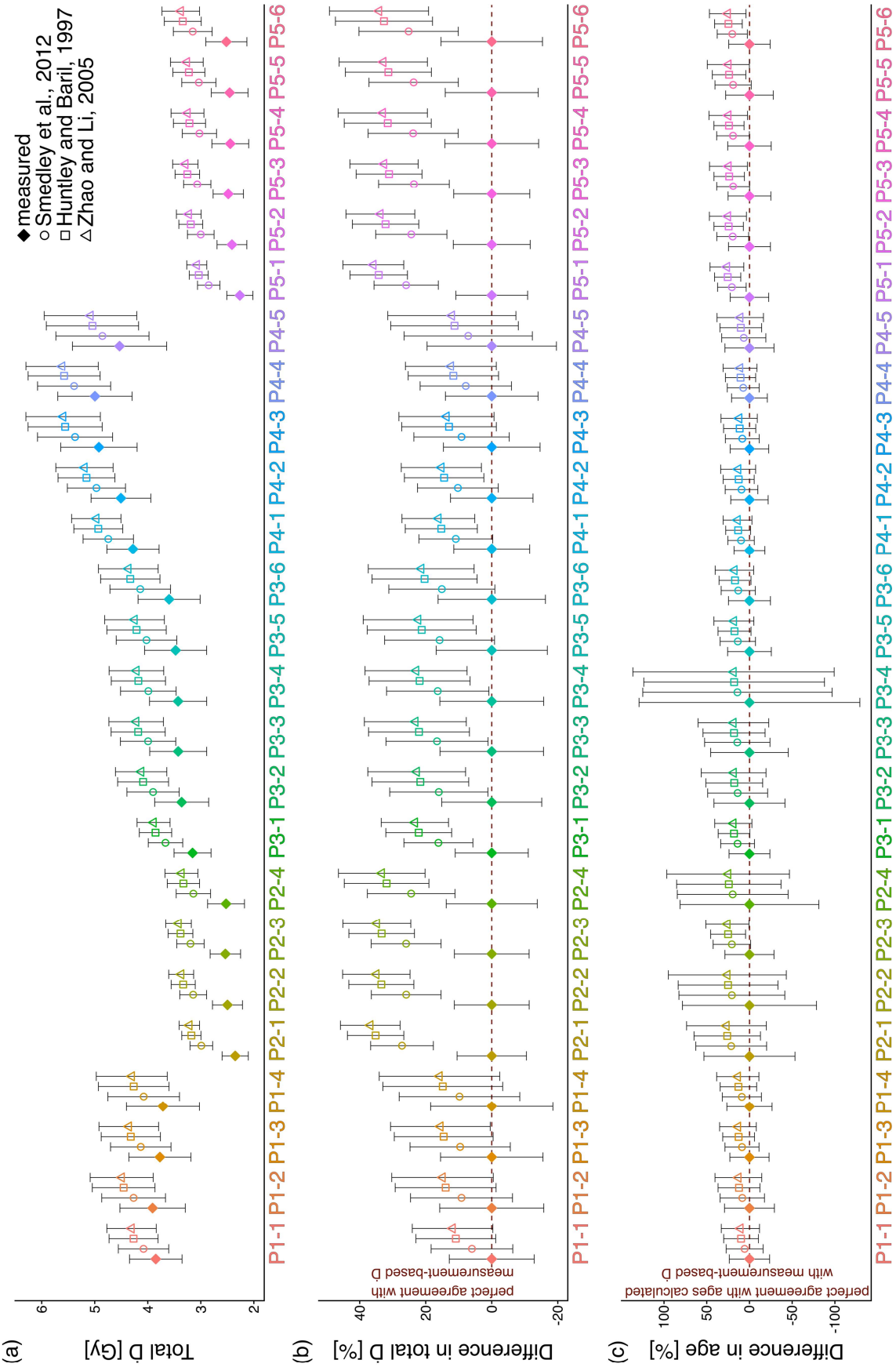

Fig. 7.1: *Total Ḋ and age comparison.* ***a)*** *Total Ḋ results per sample, with $\dot{D}_{int}$ and total Ḋ calculated with DRAC (Durcan et al., 2015) based on measured K-concentrations (filled symbols) and on the three most cited literature values (open symbols) (Huntley and Baril, 1997; Smedley et al., 2012; Zhao and Li, 2005). All other input variables are described in Chapter 6 and Appendix C-II and Appendix C Table C5.* ***b)*** *A comparison of*

the percentage deviation between the total Ḋ based on the measured K-concentration and the total Ḋ based on the three most cited literature values. ***c)*** *A comparison of the percentage deviation between the ages calculated with total Ḋ based on the measured K-concentration and the ages calculated with total Ḋ based on the three most cited literature values.*

Overall, the measurement of the internal K-concentration of feldspar grains is essential for accurate dose rate determination. Assuming a K-concentration based on literature values may lead to a systematic overestimation of the total Ḋ. Although an age calculated from a literature-based K-concentration may be consistent with an age based on a measurement, it still has a systematic one-directional error. As single-grain K-concentration measurements of each luminescent grain are not practical for routine application, first a multi-grain measurement should be performed. In addition, a small subset of grains should be measured at the single-grain level to assess the variability within a sample. The two results can then be combined. The multi-grain result is used as the K-concentration, while the variability from the single-grain measurement is used as the uncertainty of the K-concentration. Testing this approach on 25 samples from the Atacama Desert in Chapter 6 further supported the conclusions from Chapter 4: **i)** literature values may result in a systematic underestimation of the age, and **ii)** the combined approach is both time- and cost-efficient.

7.2 Method application

Q3: Can individual grain histories, determined with single-grain luminescence dating techniques, reveal sample-specific, site-specific, and transect-wide patterns of deposition and post-depositional mixing in soils and surfaces along a climatic elevation transect in the Atacama Desert, and how can these findings contribute to the understanding of regional palaeoclimatic fluctuations? (Chapter 6)

Objective 3a: *Evaluate the applicability of feldspar single-grain luminescence dating techniques to reconstruct depositional and post-depositional processes of soils and surfaces in the Atacama Desert.*

This objective addressed three specific aims: **i)** assessing the luminescence characteristics of the feldspar samples, **ii)** evaluating the D_e distributions in order to differentiate depositional from post-depositional processes, and **iii)** integrating the luminescence results with geomorphological, granulometric, and geochemical data.

Luminescence characteristics:

A total of 307 single-grain discs were measured for age determination in Chapter 6. These were supplemented by measurements on 30 single-grain discs and 153 2 mm multi-grain aliquots for protocol testing and bleaching experiments. Based on multi-

grain pre-heat plateau tests measuring residuals, dose recovery ratios, and fading behaviour, a $pIRIR_{225}$ protocol was chosen for D_e measurements.

For the interpretation of D_e distributions it is necessary to evaluate the bleaching behaviour of the samples. Therefore, selected samples were bleached for 24 h in a SOL2 solar simulator to quantify their residual doses after bleaching. Multi-grain measurements on 2 mm aliquots showed residuals <2 Gy, while single-grain measurements yielded residuals of <1 Gy (Appendix C-II Fig. C3e and Fig. C4a-g). It can be concluded, that samples from the Atacama Desert can be bleached efficiently under laboratory conditions.

To assess the bleaching behaviour and depth under natural conditions, the D_e distributions of the surface samples were analysed. All surface samples included material from the uppermost two centimetres of the profile. Although all surface samples contained grains with doses >50 Gy, the majority of grains were well bleached (p0 of the MAM-4 of all surface samples = 0.85). Thus, under natural conditions grains are successfully bleached at the direct surface. The presence of grains with significant residuals suggests a bleaching depth limited to <2 cm below surface. The direct comparison of naturally and laboratory bleached surface samples demonstrates that grains can be effectively bleached under natural conditions (Fig. 7.2). Their density plots peak within the same range as their laboratory bleached counterparts, with only samples **P3-1** and **P4-1** appearing slightly less effectively bleached in nature.

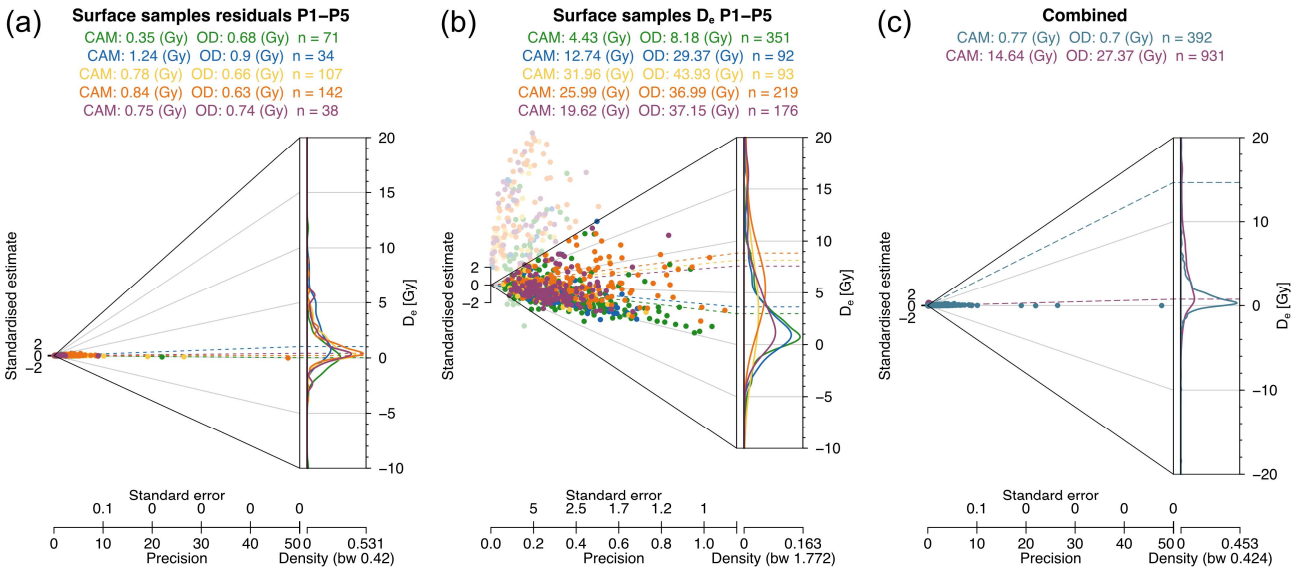

Fig. 7.2: *Abanico plots of* ***a)*** *single-grain residual test D_e values from surface samples after 24 h of laboratory bleaching;* ***b)*** *single-grain D_e values of the surface samples without laboratory bleaching; and* ***c)*** *comparison of the residual test D_e values (turquois) and the surface sample D_e values (purple). Colours in a) and b) correspond to the different profiles: **P1**, **P2**, **P3**, **P4**, and **P5**. Dotted lines in all Abanico plots indicate the weighted mean. In b), D_e values outside the z-axis range (-10 – 20 Gy) are shown semi-transparent.* ***Note:*** *the x-axes for standard error, precision, and density are scaled differently in a), b), and c).*

Of the 30,700 measured grains, 3,297 grains passed all rejection criteria (Table 7.2). Even though the SGC approach could not be applied (Chapter 5), the proportion of

suitable grains (~10 %) was higher than in previous studies in the Atacama Desert (~1 % Zinelabedin et al., 2022; 3.52 % Maßon et al., 2024). This improvement likely results from adding a magnetic separation step during sample preparation. Most rejected grains (70 %) were dismissed due to their low sensitivity (T_n signal <3σ of the background signal), consistent with previous observations on feldspars in the Atacama Desert (Bartz et al., 2020a, 2020b; Maßon et al., 2024; Zinelabedin et al., 2022).

Table 7.2: *Overview of rejection criteria applied to the single-grain dataset, with the corresponding number of grains rejected for each criterion.*

	Number of grains
Total number of analysed grains	30700
Rejection criterion: T_n below 3σ background	21497
Rejection criterion: RSE of T_n exceeds 25 %	4282
Rejection criterion: recycling ratio 1 outsides [0.8 – 1.2]	72
Rejection criterion: recycling ratio 2 outsides [0.8 – 1.2]	3
Rejection criterion: recuperation 1 exceeds 20 %	155
Rejection criterion: recuperation 2 exceeds 20 %	0
Function fitGrowth(): improper input argument	0
Function fitGrowth(): failed in growth curve fitting	13
Rejection criterion: FOM of growth curve exceeds 15 %	1381
Total number of rejected aliquots (grains)	27403
Total number of accepted aliquots (grains)	3297

<u>D_e distributions:</u>

Surface samples were excluded from further analysis as they are constantly bleached by sunlight and therefore do not record depositional or post-depositional processes. Due to the occurrence of negative D_e, unlogged dose models needed to be applied for all age calculations.

Most samples displayed D_e distributions with a low-dose peak and a long tail towards higher doses (Fig. 6.6). Such patterns may either result from heterogeneous bleaching prior to burial (Fig. 6.7b, c) or from post-depositional mixing of the sub-surface sample with recently bleached grains (similar to Fig. 6.7e). Seven samples had broad unimodal D_e distributions, which may either reflect long burial or, less likely, intensive mixing (Fig. 6.6 and 6.7c). Three samples showed bimodal D_e distributions, indicating possible post-depositional disturbance (Fig. 6.6 and 6.7e, f). Yet, one of the peaks may reflect the depositional age.

The statistical characteristics of the D_e distributions, including their shape and the calculated ages, are insufficient on their own to distinguish depositional from post-depositional processes. Since heterogeneous bleaching is likely in all samples, the luminescence results need to be interpreted within a multi-method framework, considering the geomorphological context. Ages interpreted solely from luminescence characteristics cannot provide reliable results.

Integrating independent characteristics:

Field observations, and geochemical as well as granulometric analysis were integrated into the D_e distribution interpretation.

D_e distributions with a **low dose peak and a tail towards higher doses** were observed in profile **P2**, **P3**, **P4** and **P5**. In **P3** and **P5**, these distributions are likely caused solely by heterogeneous bleaching prior to deposition. In contrast, profile **P2** and sample **P4-2** show additional influence from post-depositional processes. In **P2-2** and **P2-3**, the young depositional age (<2 ka) prevents clear distinction between grains fully bleached prior to deposition and grains transported downward from the surface. Nevertheless, post-depositional mixing is likely, as indicated by the decreasing number of zero-dose grains and the vegetation cover. The D_e distribution of sample **P4-2** shows a broad right shoulder, presumably indicating its burial age ~11 ka. The profile is situated in an old fan generation, with desert varnish developed on surface clasts, indicating long-term surface stability. Sun et al. (2023) dated the last depositional activity of the younger fan segment to the same age as the right shoulder of the D_e distribution, supporting this interpretation. **P4-2**'s grain size distribution resembles dust samples, and the mobile-to-immobile element ratios show leaching in the upper profile units. Thus, the low-dose peak in **P4-2** between ~7-3 ka is likely indicative of a desert pavement formation during prolonged surface stability.

All **unimodal** D_e distributions, except for sample **P1-2**, indicate long burial. The absence of vegetation and other turbation drivers, the prevailing hyperarid climate, and the low proportion of surfaced grains (<2 %) contradict intensive mixing as a plausible cause of the observed distribution patterns. The D_e distribution of sample **P1-2** showed left and right shoulders. Together with the mobile to immobile element ratios of the profile and the occurrence of roots, the left shoulder likely reflects post-depositional mixing caused by bioturbation. Whereas the right shoulder indicates mixing with underlying sediments during or after deposition

Bimodal D_e distributions do not have a universal interpretation. In sample **P2-4**, the younger peak likely records the deposition of the overlying profile units, while the older peak reflects the deposition of the respective profile unit. In sample **P3-6**, the younger peak likely reflects the depositional phase of the respective profile unit, whereas the older peak may result from a combination of mixing during deposition, micro-dosimetric effects, and heterogeneous bleaching. In sample **P5-6**, the processes responsible for the D_e distribution could not be identified.

When integrated into a multi-method framework, single-grain feldspar luminescence dating can, most of the time, resolve depositional and post-depositional histories in complex alluvial deposits in hyperarid environments.

Objective 3b: *Analysing patterns inferred from geochemistry, granulometry, and single-grain feldspar luminescence measurements (cf. Objective 3a) in the context of the climatic and elevation transect.*

Geochemistry and granulometry

Both geochemical and granulometric analyses were used as proxies for weathering and post-depositional mixing. Although all profiles were sampled within the same catchment, the lithological composition is heterogeneous (Alvarez et al., 2016; Escribano et al., 2013). In the upper reaches of the catchment (**P5**), broad, shallow valleys are filled with semi-consolidated Miocene to Pliocene alluvial deposits, underlain by volcanic rocks of the La Negra Formation. The central and lower parts of the catchment are mainly underlain by the Matancilla intrusive complex (**P1**-**P4**), composed predominantly of granodiorites and diorites of Middle to Upper Jurassic age. Additionally, Palaeozoic metasedimentary rocks of the Chañaral Epimetamorphic Complex crop out in the north-western sector of the catchment (potentially **P1**) (Alvarez et al., 2016). Grain size distributions in alluvial deposits are generally not well sorted and highly depend on the source area (cf. Chapter 2.2). As therefore expected, the PCA of major element concentrations and grain size fractions revealed a clear separation by profile rather than by the degree of weathering of a sample. Nevertheless, the two profiles, showing signs of weathering (**P1**) and post-depositional mixing (**P1**, **P4**), were separated along PC1 from the profiles **P2**, **P3**, and **P5**.

Consequently, neither geochemical nor granulometric data are adequate for a transect-wide comparison of individual samples. The climatic conditions along the transect are not reflected in the analysed data. However, at a profile scale, the geochemical data indicate initial weathering and a long-term absence of deposition, which results in leaching of mobile elements in two profiles (**P1**, **P4**; Fig. 6.5). The grain size distributions of **P4-1** and **P4-2**, resembling those of dust samples, further indicate aeolian deposition atop of the alluvial deposits (Fig. 6.4, Appendix C-I Fig. C2d).

Single-grain feldspar luminescence

Two phases of geomorphic activity indicating wetter phases were identified by comparing the timing of deposition and post-depositional processes along the transect. The first phase around 50 ka was only visible in the three profiles above the marine boundary layer (**P3**-**P5**; Fig. 6.8g). It is highly likely that below the sampled profile sections, evidences for fluvial activity can also be found in **P1** and **P2**. This would indicate a wetter phase affecting the entire transect.

The second phase of geomorphic activity, from around 5 ka to present, is evident in profiles **P2**, **P3**, and **P5** (Fig. 6.9). Both **P1** and **P4** lie within older fan generations,

which are typically bypassed during fan re-activation (cf. Chapter 2.2). In such cases, erosion and deposition occur primarily on younger fan segments, leaving no datable trace on the geomorphic stable surfaces of older generations. Nevertheless, **P1** also shows post-depositional activity during this second phase. As the coastal plain is generally more humid, this may reflect enhanced plant growth during a wetter phase, causing bioturbation. Alternatively, a sufficiently intense rain event may have been capable of re-activating the abandoned fan segment. **P4** is therefore the only profile without evidence for a wetter episode or event during the last 5 ka. However, evidence for a wetter period may be preserved in the adjacent younger fan segment. Hence, this second phase also indicates wetter climatic conditions affecting the entire transect.

In addition to the supposedly transect-wide wetter conditions, **P1** records a geomorphic active phase ~29 ka, absent in **P2**-**P5**, and **P2** records a wetter phase ~11 ka, absent in all other profiles. The lowest sample in **P2** is significantly younger than the 29 ka observed in **P1** (CAM = 11.0 ± 2.7 ka), hence evidence for a wetter period ~29 ka may exist below the sampled profile section in **P2**. Without further evidence, this indicates a wetter episode solely in the coastal plain and possibly in the fog-influenced part of the Coastal Cordillera. The depositional activity ~11 ka detected in **P2-4** may further indicate a wetter phase restricted to the fog-influenced zone.

Despite the presumably local wetter phases ~29 ka and ~11 ka as well as the climatic dependence of processes driving post-depositional mixing, no systematic spatial pattern is evident that corresponds to the present-day climatic gradient from profile **P1** to profile **P5**. Instead, the wetter conditions affected the entire transect simultaneously, and the observed patterns reflect local geological and geomorphological settings. In addition, post-depositional mixing processes remain shallow, independent of the climatic conditions driving them.

Objective 3c: *Integrate the site-specific and transect-wide luminescence-based interpretations (Objectives 3a and 3b) into the broader regional geomorphological and (palaeo-) environmental framework of the Atacama Desert.*

The luminescence-based chronostratigraphies, supported by field observations, granulometric and geochemical data, reveal both site-specific and transect-wide consistent sedimentary responses to late Quaternary climate variability in the Atacama Desert. Two phases of alluvial activity were identified across the entire transect: an early phase ~50 ka and a recent phase since ~5 ka.

The early phase aligns with previous reports of alluvial activity in the northern coastal plain and lower Coastal Cordillera (Bartz et al., 2020a, 2020b; Vargas et al., 2006) and with a period of reduced regional aridity (i.e., more humidity) during MIS 3 (Stuut

and Lamy, 2004). This indicates a broader regional climatic control on sediment mobilisation, even though, at the Paposo transect evidence for this phase was only found above the marine boundary layer.

The more recent geomorphic active phase since ~5 ka was observed as depositional processes in profiles **P2**, **P3**, and **P5**. Post-depositional activity in **P1** and **P2** (presumably caused by bioturbation) also indicate wetter conditions. This phase correlate with the onset of modern El Niño (i.e., intensified El Niño), associated with the occurrence of extreme rainfall events (Rein et al., 2005, 2004).

Despite these regional signals, the profiles also demonstrate spatial heterogeneity. Localised depositional or post-depositional processes were not always synchronised across the transect. This underscores the strong influence of catchment-scale variability of local geomorphological settings. For instance, profiles **P1** and **P2** record wetter episodes at ~29 ka (**P1**) and ~11 ka (**P2**), which are absent from the other profiles, suggesting very localised wetter periods or events.

However, the wetter phase in **P1** (~29 ka) is also evident in alluvial deposition along the coastal plain (Bartz et al., 2020a, 2020b; Vargas et al., 2006) and in pollen records above the Coastal Cordillera (2670 m a.s.l.) (Maldonado et al., 2005). Although no evidence was found in profiles **P2**-**P5**, pollen analysis close to the Paposo transect indicated elevated humidity in the Coastal Cordillera (1550-1900 m a.s.l.; Díaz et al., 2012). The aridity index based on an offshore drill core also shows a marked increase (i.e., less arid, more humid) (Stuut and Lamy, 2004).

Additionally, the presumably wetter phase in **P2** (~11 ka) coincides with an interval of strong El Niño activity (Rein et al., 2005, 2004). Further evidence for a wetter phase was found in palaeo-middens (González-Pinilla et al., 2021; Maldonado et al., 2005), a coastal alluvial fan (Bartz et al., 2020a), and regional groundwater discharge (Rech et al., 2002; Sáez et al., 2016). This phase further corresponds to the CAPE II and several pre-CAPE events (de Porras et al., 2017; Gayo et al., 2012; Pfeiffer et al., 2018; Quade et al., 2008). The offshore record confirms an elevated yet decreasing aridity index (Stuut and Lamy, 2004). The absence of visible activity in any of the other profiles, suggests that this phase (or event) may have been relatively weak. After a prolonged period of geomorphic stability, only the profile located in the transect's zone of highest present-day water availability responded.

Even though in both cases evidence for wetter phases was only found in one profile, the integration into the existing palaeoenvironmental framework suggests regional instead of localised climatic fluctuations.

Additionally, **P4** preserved evidence for an arid phase without alluvial activity. The post-depositional activity in **P4** at ~6.6 ka (desert pavement formation) indicates a

possibly prolonged dry phase. This phase coincides with a potentially very dry phase recorded in palaeo-middens (González-Pinilla et al., 2021) and with a phase of weak El Niño (Rein et al., 2005, 2004), further supporting the presumably dry conditions.

Overall, wet and dry phases inferred from geomorphologically active and stable episodes at the Paposo transect fit well into the regional palaeoenvironmental framework. Integrating the transect-wide findings into the regional context emphasises the importance of combining locally limited datasets, such as the five studied profiles, with broader records. Without this integration, some localised findings could be misinterpreted as purely local rather than regional effects. The results further highlight that even under long-term hyperarid conditions, episodic increases in moisture availability were sufficient to trigger both deposition and post-depositional surface reworking.

In summary, single-grain feldspar luminescence dating of soil and surface profiles in the Atacama Desert is a valuable tool within a multi-method approach. It allows differentiation between depositional and post-depositional processes and reveals patterns of wetter and arid phases from sample-specific to regional scales.

7.3 Concluding remarks

Even though the methodological development reveals further open questions, it paves the way for a more robust determination of feldspar luminescence ages in settings with geochemical heterogeneous samples. The SGC method showed high potential for analysing homogeneously bleached samples. Furthermore, a refinement of this method might lead to the reduction in measurement time for heterogeneously bleached samples. The lack of correlation between luminescence properties and the geochemical composition of feldspars is challenging fundamental assumptions made in most feldspar luminescence studies. Nevertheless, a method was developed to time- and cost-effectively determine the internal K-concentration of feldspars for the dose rate determination. This technique enabled a more accurate age calculation for soil and surface profiles in the Atacama Desert. The developed luminescence framework proofed capable of deciphering grain histories in complex alluvial deposits in a hyperarid environment, if integrated into a multi-method approach and the regional palaeoclimatic context.

Chapter 8

Conclusion and outlook

Make a thing as simple as possible but no simpler.
(Albert Einstein)

© Simon Schablack

8.1 Conclusion

In conclusion, this thesis demonstrates that single-grain feldspar luminescence dating can be a valuable tool for deciphering particle histories in hyperarid alluvial landforms in the Atacama Desert, if certain requirements are met. These requirements include adapted sample preparation, accurate determination of the internal K-concentration, and a multi-method approach to interpret luminescence results.

The results presented in this thesis confirm that it is possible to construct a standardised growth curve (SGC) with geochemical heterogeneous, dim feldspar grains. Yet, applying such an SGC to natural feldspar samples is not straightforward. The method was improved by extending the original SGC measurement protocol from two to five measurement cycles and by introducing a new parameter, the synthetic regenerative dose (sR) (Chapter 3). For the method development laboratory-irradiated feldspars were used. Nevertheless, this approach yielded unreliable results when applied to naturally irradiated feldspars (Chapter 5). Consequently, no method was developed to reduce the measurement time in the luminescence reader or to increase the number of accepted grains by SGC application. However, by using magnetic separation during sample preparation, the number of luminescent grains per disc increased from 3.52 % (Chapter 3) to ~10 % (Chapter 6).

The internal K-concentration is an important component of the total $\dot{D}$ in feldspars. It is often assumed that the K-concentration is correlated to luminescence signal intensity. Thus, the brightest grains are supposed to have the highest K-concentration. Correlation analyses between single-grain luminescence characteristics and single-grain geochemical composition showed that the internal K-concentration is independent of the signal intensity, underscoring the need for accurate K-concentration determination (Chapter 3). Subsequently, four measurement techniques to determine the K-concentration and two luminescence-weighted K-estimates were analysed and systematically compared to the three most cited literature K-concentration values (Chapter 4). It was shown that choosing a usually high literature-based K-concentration (8 – 14 % K) without any knowledge about the true K-concentration, might introduce one-directional systematic errors into the $\dot{D}$ determination. A systematic overestimation of the total $\dot{D}$ inevitably results in a systematic underestimation of the luminescence age. Although the resulting ages may be in unity within their error margins, the one-directional systematic nature of the bias remains problematic.

Consequently, a cost- and time-efficient approach was developed that combines a fast and inexpensive bulk measurement with a single-grain measurement on a small subset of grains. The bulk measurement results in a sample-wide K-concentration, while the single-grain measurement captures the spread within a sample. The standard deviation of the single-grain measurement is therefore used as the error for the bulk K-concentration.

This method was applied for the $\dot{D}$ calculations of 25 samples from five soil and surface profiles along a climatic and elevation transect near Paposo in the Atacama Desert (Chapter 6). The measured bulk K-concentrations for the 25 samples ranged between 1.61 % K and 7.45 % K (Appendix C-II Table C5). If one of the three most cited literature values for the K-concentration had been used, the resulting luminescence ages would have been underestimated by an average of 17.2 %.

Within the complex alluvial settings of the five profiles, luminescence ages were interpreted using a multi-method framework. This approach combined luminescence ages, D_e distributions, luminescence-based proxies (zero-dose grains, saturated grains), field observations, geochemical data, and granulometric analysis of both soil and surface samples as well as dust samples. Combining all methods allowed the palaeo-reconstruction on different scales: from individual grain histories, to sample-level, profile-level, and transect-level interpretations. It was thus possible to differentiate between depositional and post-depositional processes. Post-depositional mixing in terms of bioturbation, reworking during deposition, and desert pavement formation was identified. Furthermore, evidence for wetter phases around 50 ka and since 5 ka was found along the transect. Additionally, two wetter phases were recorded ~29 ka within the coastal plain (**P1**) and ~11 ka in the fog-influenced Coastal Cordillera (**P2**). One profile (**P4**) further recorded a period of prolonged geomorphic stability under presumably very dry conditions ~6 ka. All findings are consistent with regional palaeoenvironmental studies, which highlight the influence of (ENSO-related) weather anomalies in the southern Atacama Desert. Nevertheless, the chronostratigraphy developed for the profile in the coastal plain (**P1**) did not align with a previously published cosmogenic nuclide-based chronology.

Overall, this thesis demonstrates that when dealing with complex alluvial landforms, prone to heterogeneous bleaching, and heterogeneous chemical compositions of the dated feldspars, special precautions are required. The $\dot{D}$ must be accurately determined, with a special focus on internal K-concentrations. Further, luminescence results must be interpreted holistically, considering the shape of D_e distributions, ages, and luminescence proxies, rather than focussing on a single age per sample. Finally, a multi-method approach should be applied when interpreting

the luminescence results to distinguish deposition from post-depositional processes. Once these requirements are met, single-grain feldspar luminescence dating provides a robust tool to reconstruct the palaeoenvironment and thereby advance the understanding of Quaternary landscape evolution in the hyperarid Atacama Desert.

8.2 Outlook

Although this thesis contributes to the methodological toolkit for luminescence dating in complex alluvial systems in hyperarid environments, several open questions remain. Some of these questions arise as a consequence of new findings presented in this thesis and offer important starting points for future research.

Method refinement

Single-grain measurements in complex settings, such as those investigated in this thesis, are necessary but time consuming. Refining the sample preparation protocol by introduction a magnetic separation step increased the proportion of grains giving a suitable luminescence signal from ~1 % (Zinelabedin et al., 2022) to ~10 %. Nevertheless, the average measurement time remained long, at ~22.5 h per disc depending on the reader. Reducing the measurement time should therefore be a primary aim of methodological development.

As shown in Chapter 5, the rc_xsR_xSGC approach developed in Chapter 3 is not directly applicable to the Paposo transect. The broad D_e distributions were not ideal for the rc_xsR_xSGC approach, which relies on measurement protocols tailored to an expected D_e. For a substantial fraction of grains, especially in the low dose region <50 Gy, only SAR D_e values and no SGC D_e values could be calculated. Adjusting the size of sR without modifying the measurement protocol was not effective. Future work should test the performance of measurement protocols with reduced cycles and sR values optimised for low-dose grains. However, such adjustments may compromise the analysis of older samples, where low-dose grains are scarce. A functioning SGC could improve the measurement efficiency and potentially reduce the measurement time by at least 60 % (Chapter 3).

Since the total $\dot{D}$ contributes 50 % of the age equation in luminescence dating, accurate determination is essential. Chapter 4 addressed the internal K-concentration in feldspars for $\dot{D}_{int}$ calculations. Yet, the internal K-concentration is not the only relevant factor controlling the $\dot{D}_{int}$ (Mejdahl, 1987). Most studies analysed in Chapter 4.2.2 assumed either a fixed K:Rb ratio of 270:1 (Mejdahl, 1987) or a constant Rb-concentration of 400 ± 100 ppm (Huntley and Hancock, 2001). They further considered the influence of U and Th are negligible (cf. Smedley and Pearce, 2016).

However, Buylaert et al. (2018) found no correlation between K and Rb and showed that Rb-concentrations often deviated from the proposed 400 ± 100 ppm. Several studies further highlight the variability of U and Th in feldspars (e.g. Mejdahl, 1987; Smedley and Pearce, 2016; Zhao and Li, 2005). The approach of K-concentration determination proposed in Chapter 4 could potentially be combined with Rb-concentration measurements. Buylaert et al. (2018) used the same μ-XRF device to measure the Rb-concentration that is proposed here for the error determination of the K-concentration. Measuring both simultaneously could provide information on the variability of the Rb-concentration within a sample. In addition, the ratio of K:Rb within a sample could be calculated, which would improve the reliability of the β-counter measurement of the K-concentration (cf. Chapter 4.4). Overall, future work should focus on developing a time- and cost-efficient method to also routinely determine the internal U- and Th-concentrations in feldspars alongside with the K- and Rb-concentrations.

Post-depositional processes

In addition to the methodological refinements, a better understanding of post-depositional processes in the Atacama Desert is required. Previous studies suggest that hyperconcentrated flows may result in downward migration of grains during deposition (e.g. Harvey, 2011; Wells and Harvey, 1987). However, neither the proportion of migrating grains nor the depth of their displacement have been systematically quantified in the Atacama Desert. Both parameters are critical for the interpretation of single-grain luminescence D_e distributions. Therefore, future research could address this knowledge gap through controlled field experiments, for example by tracking coloured surface grains that are mobilised during artificial hyperconcentrated flows.

A typical soil in the central Atacama Desert is enriched in salts, including nitrates, chlorides, iodates, and sulphates (e.g. Ericksen, 1981; Ewing et al., 2006). These soils are characterised by three horizons: a salt-cemented surface layer (*costra*), a white horizon rich in soluble sulphates (*chuca*), and a thick halite-rich horizon (*caliche*) at the transition to the underlying regolith (*conjelo* or *coba*) (Ericksen, 1981). The presence of salts throughout these horizons indicates that haloturbation, in addition to processes identified in Chapter 6, may represent an important post-depositional process in the central Atacama Desert (Zinelabedin et al., 2025).

So far, only a single calcium sulphate wedge in the Aroma transect (**T1**; Fig. 1.1) has been analysed in detail using single-grain feldspar luminescence dating (Zinelabedin et al., 2022). The Aroma transect provides the opportunity to investigate post-

depositional processes along a climatic gradient, ranging from ~20 % relative humidity at the lowest section (~1360 m a.s.l.) up to ~33 % relative humidity at the highest section (~2640 m a.s.l.) (Hoffmeister, 2018d, 2018e). While haloturbation is likely the dominant post-depositional mixing process at the lower elevations, bioturbation and fluvial surface-reactivation may also contribute to post-depositional mixing at higher elevations. However, systematic investigations of these processes are methodologically considerably more challenging than those presented in this thesis, as the presence of calcium sulphate impedes the sample preparation for luminescence dating and granulometric analysis.

Testing inheritance in cosmogenic nuclide dating

As discussed in Chapters 6 and 7.2, palaeoenvironmental reconstructions in complex environments, such as the landforms analysed in this thesis, are best tackled with a multi-method approach. Ideally, luminescence dating should be complemented by an independent dating technique. Beside luminescence dating, the most widely used methods to constrain Quaternary evolution of alluvial deposits in the Atacama Desert are radiocarbon dating (if organic material is available) and terrestrial cosmogenic nuclide dating, such as ^{10}Be (e.g. Hartley et al., 2005; Ortlieb et al., 2011; Vargas et al., 2006; Vásquez et al., 2018; Walk et al., 2023, 2022).

However, it was shown in Chapter 6 that ^{10}Be exposure ages of surface clasts, used as proxies for the timing of last depositional activity, deviated substantially from luminescence-based results. The coastal alluvial fan in the Paposo transect therefore provides an ideal study site to investigate inheritance in ^{10}Be dating within a cascading system. Given that the overall ^{10}Be chronostratigraphy of the fan (i.e., from youngest to oldest generation) appears consistent with field observations and soil proxies, systematic comparison with luminescence-based ages may reveal characteristic patterns of inheritance. Such combined investigations could further contribute to the regional palaeoenvironmental framework.

In conclusion, to advance future dating of alluvial deposits in the Atacama Desert, progress in three coherent research areas is essential: luminescence methodology, post-depositional process understanding, and the integration of multiple dating techniques. A further refinement of the D_e and $\dot{D}$ determination in single-grain luminescence dating will improve both the efficiency and precision of the method. Improved understanding of post-depositional processes is essential for the interpretation of D_e distributions and resulting ages. Finally, the understanding and integration of an independent dating technique will enhance the robustness of local and regional chronostratigraphies.

Appendix

Without data, you're just another person with an opinion.

(W. Edwards Deming)

Appendix A (Chapter 3)

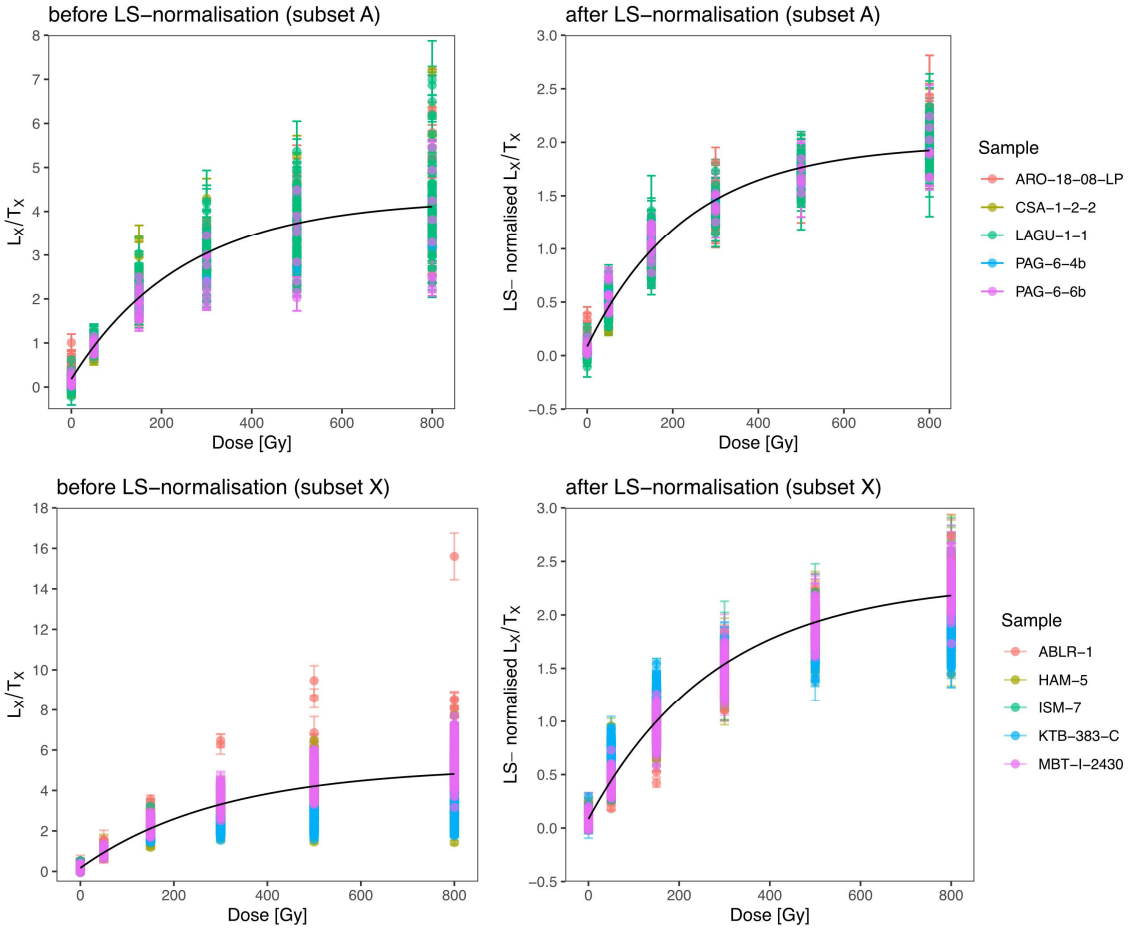

Fig. A1: *comparison of L_X/T_X values before and after LS-normalisation for subset A (**top**) and subset X (**bottom**).*

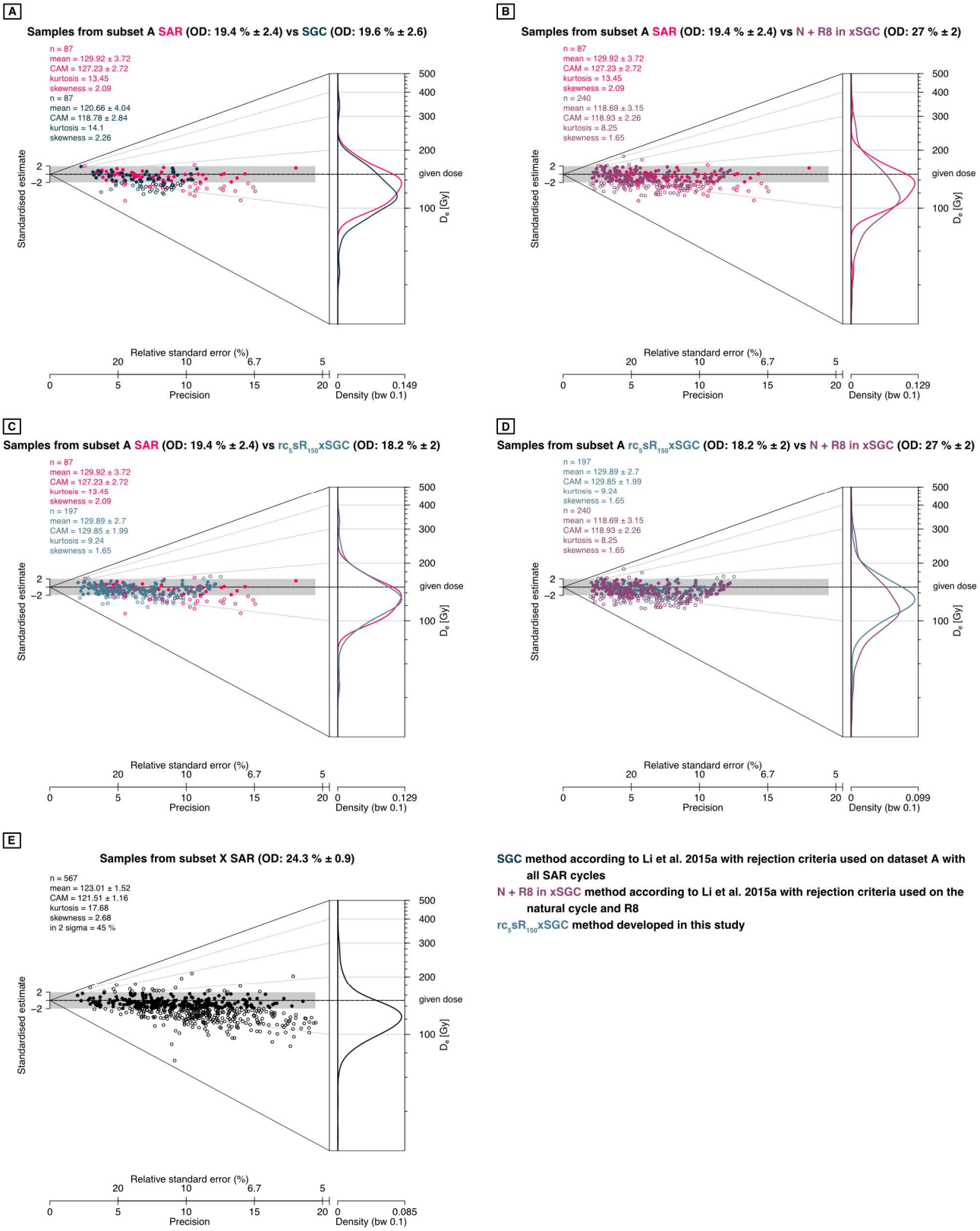

Fig. A2: *Abanico plots of D_e distributions resulting from dose recovery experiments, with a given dose of 150 Gy. Filled circles are within 2σ of the given dose, empty circles differ more than 2σ from the given dose. The overdispersion was calculated using CAM.* ***A-D*** *show D_e distributions of subset A and E from subset X. The* ***SAR*** *D_e values were calculated using the standard SAR approach. The* ***SGC*** *D_e values were calculated following Li et al. 2015a and using the natural cycle (N) and the eighth regenerative cycle (R8) for projection onto a SGC, constructed with data from subset A, while applying the rejection criteria to the full SAR dataset. The* ***N + R8 xSGC*** *D_e values were calculated following Li et al. 2015a and using N and R8 for projection onto the*

xSGC, constructed with data from subset X, while applying the rejection criteria to a dataset only consisting of the N and R8. The ***rc_5sR_{150}xSGC*** *D_e values were calculated with the new method developed in this paper.*

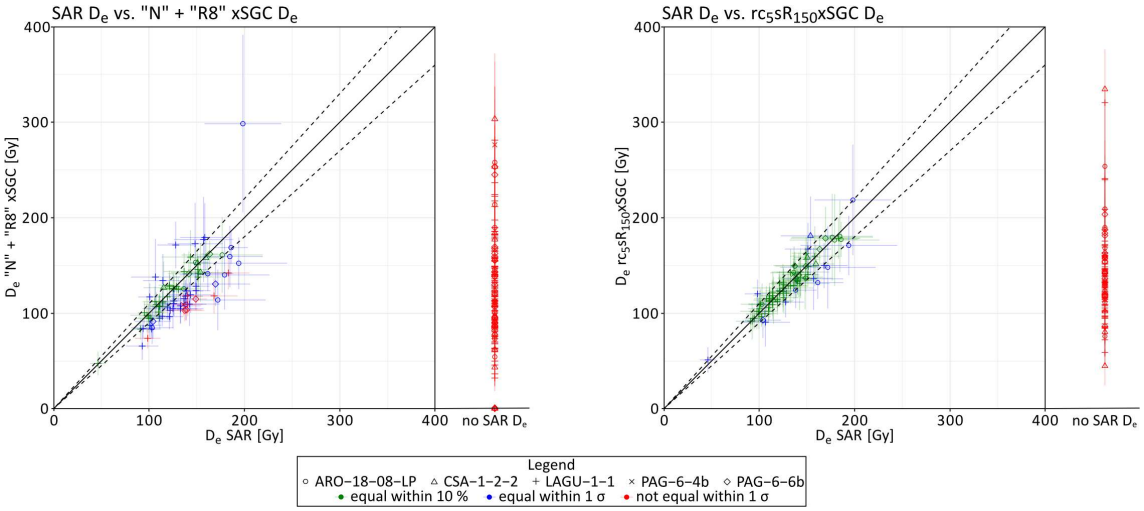

Fig. A3: *evaluation of SGC performance.* ***Left*** *comparison of D_e from subset A obtained with the standard SAR procedure with D_e obtained using the xSGC, established with data from subset X, and rejection criteria applied for a reduced dataset from subset A including only the "natural" SAR cycle plus the eighth SAR cycle (R8 = 50 Gy), where R8 used as L_{r1}/T_{r1} to scale and interpolate L_n/T_n onto the xSGC.* ***Right*** *comparison of D_e from samples of subset A obtained by the standard SAR procedure with D_e obtained using the sR_{150}xSGC and reducing the SAR-cycles for individual growth curve fitting to the "natural" 150, 0, 50, 500, 50 Gy cycles (rc_5sR_{150}xSGC). Both show the D_e values of the used SGC approaches on a separate axis that yielded no corresponding D_e value when estimating the D_e with the standard SAR procedure. For Abanico plots including both, the D_e with corresponding SAR D_e and those without, see Fig. A2B, C and D.*

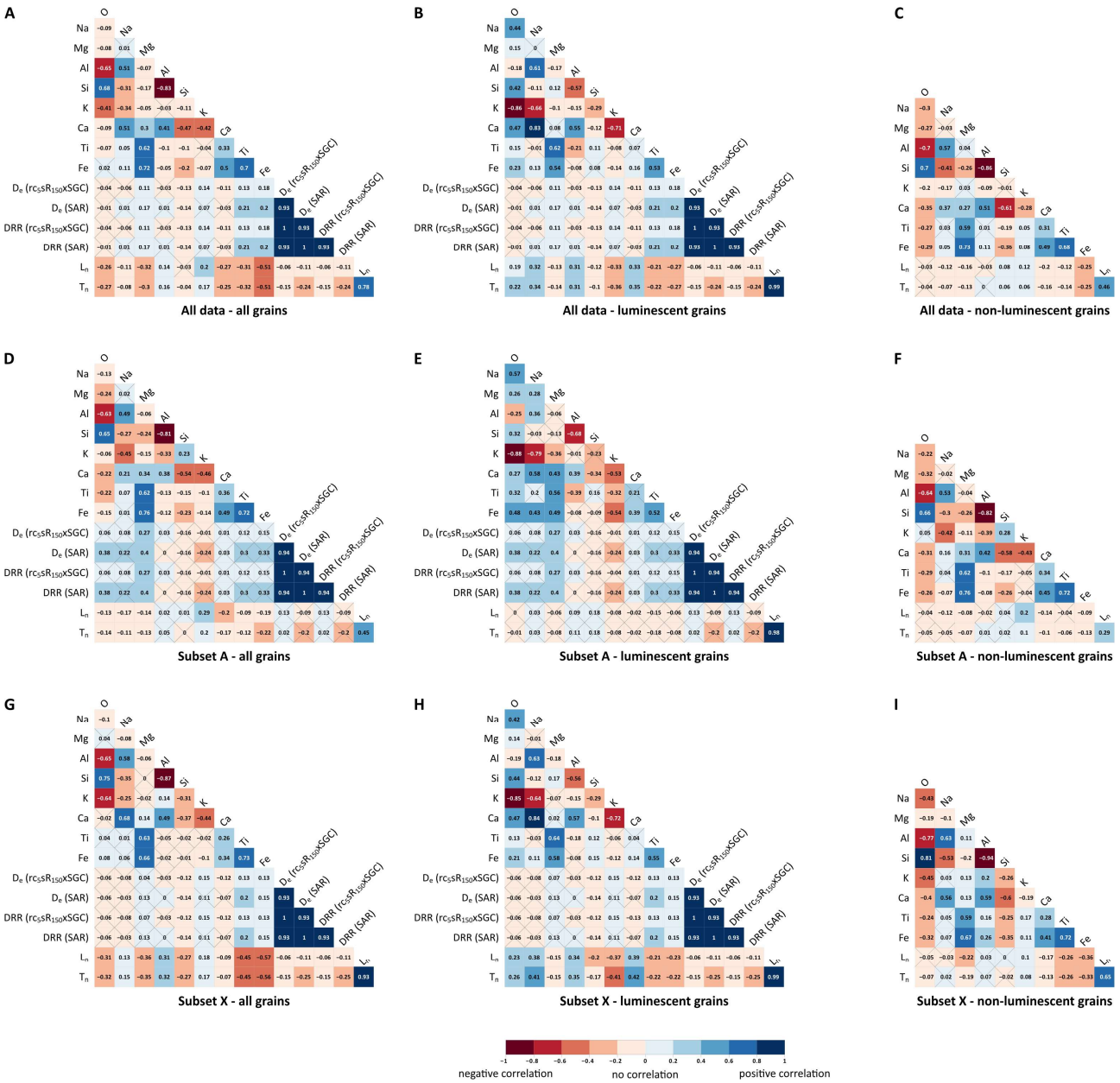

Fig. A4: *correlation matrices of the complete dataset (subset A + X) in the* ***first row****, subset A in the* ***second row*** *and subset X in the* ***third row****, for all grains in the first column, luminescent grains in the second column and non-luminescent grains in the third column. Numbers in the squares represent Spearman's rank correlation coefficient values and their colour the strength of the correlation. For not significant correlations with a p-value above 0.05 % the squares are x-ed out.*

Table A1: *Summary of grain rejection for all ten samples for the SAR procedure, the SGC method (samples 1-5) and the xSGC method (samples 6-10) for the full data sets using all SAR cycles.*

Description	ARO-18-08-LP	CSA-1-2-2	LAGU-1-1	PAG-6-4b	PAG-6-6b	ABLR-1	HAM-5	ISM-7	KTB-383-C	MBT-I-2430
Total number of analysed grains	500	500	500	500	500	500	500	500	500	500
Rejection criterion: Tn below 3 σ BG	385	421	268	433	416	314	173	360	62	3
Rejection criterion: RSE of Tn exceeds 25 %	75	52	67	58	52	104	65	74	29	4
Rejection criterion: recycling ratio 1 outsides [0.9:1.1]	3	1	9	1	2	8	13	2	43	52
Rejection criterion: recycling ratio 2 outsides [0.9:1.1]	0	0	0	0	0	0	4	2	0	5
Rejection criterion: recycling ratio 3 outsides [0.9:1.1]	0	0	0	0	0	0	0	0	0	0
Rejection criterion: recuperation 1 exceeds 10 %	0	0	0	0	1	1	1	0	6	0
Rejection criterion: recuperation 2 exceeds 10 %	0	0	0	0	0	0	0	0	0	0
Function fitGrowth(): improper input argument	0	0	0	0	0	0	0	0	0	0
Function fitGrowth(): failed in growth curve fitting	0	0	0	1	0	3	0	0	1	0
Rejection criterion: FOM of growth curve exceeds 10%	23	22	90	6	11	41	65	31	62	74
Rejection criterion: RCS of growth curve exceeds 10	1	0	4	0	10	5	75	1	201	58
Total number of rejected grains	487	496	438	499	492	476	396	470	404	196
Total number of accepted grains	13	4	62	1	8	24	104	30	96	304
Rejection criterion: RSE of SAR D_e exceeds 50%	0	0	0	0	1	0	0	1	1	0

Table A2: *Summary of grain rejection for all samples from dataset A for the SGC approach using only the "natural" SAR cycle and SAR cycle R8 (50 Gy).*

Description	ARO-18-08-LP	CSA-1-2-2	LAGU-1-1	PAG-6-4b	PAG-6-6b
Total number of analysed grains	500	500	500	500	500
Rejection criterion: Tn below 3 σ BG	385	421	268	433	416
Rejection criterion: RSE of Tn exceeds 25 %	75	52	67	58	52
Function fitGrowth(): improper input argument	0	0	0	0	0
Function fitGrowth(): failed in growth curve fitting	2	1	1	1	0
Rejection criterion: FOM of growth curve exceeds 10%	0	0	0	0	0
Rejection criterion: RCS of growth curve exceeds 10	0	0	0	0	0
Total number of rejected grains	462	474	336	492	468
Total number of accepted grains	38	26	164	8	32
Rejection criterion: RSE of SAR D_e exceeds 50%	5	8	8	1	3

Table A3: *Summary of the results for dataset A using the sRxSGC approach, in relation to the D_e calculated with the SAR approach and to a dose recovery ratio (DRR) of 1. The DRR is calculated for all grains yielding a D_e with the sRxSGC approach and for "common grains", which yield a D_e with the SAR and the sRxSGC approaches.*

synthetic regenerative dose (sR) size used in the sRxSGC approach	50	100	125	150	175	200	300	800
n D_e	88	88	88	88	88	88	88	88
n D_e common grains sRxSGC & SAR	86	86	86	86	86	86	86	87
In unity within 10 %	69	83	86	85	76	69	36	11
In unity within 1 σ	16	3	0	1	10	16	36	24
In unity within 2 σ	1	0	0	0	0	1	12	28
Not in unity	0	0	0	0	0	0	2	24
NA in either sRxSGC or SAR	2	2	2	2	2	2	2	1
Differences in D_e								
Min	0.37	0.00	0.00	0.03	0.01	0.02	0.07	1.58
Max	46.63	25.10	19.31	16.53	25.31	34.31	87.21	282.54
Mean	9.36	3.86	2.42	2.65	4.81	7.48	19.61	59.99
sd	9.84	4.96	3.16	3.10	4.74	7.00	16.42	50.05
CV	1.05	1.29	1.31	1.17	0.99	0.94	0.84	0.83
DRR (all grains)								
DRR between 0.9-1.1	25	20	26	30	30	33	29	15
DRR with 1 σ error between 0.9-1.1	28	35	31	26	30	28	34	20
DRR with 1 σ error not between 0.9-1.1	33	31	29	30	26	25	23	52
Mean DRR	0.87	0.86	0.87	0.89	0.9	0.91	0.98	1.19
DRR (common grains)								
DRR between 0.9-1.1	25	20	26	30	30	33	29	15
DRR with 1 σ error between 0.9-1.1	28	35	31	26	30	28	34	20
DRR with 1 σ error not between 0.9-1.1	33	31	29	30	26	25	23	52
Mean DRR	0.87	0.86	0.87	0.89	0.9	0.91	0.98	1.19
Correlation with SAR (r_s values)	0.9	0.99	0.99	0.99	0.97	0.94	0.76	0.21

Table A4: Summary of grain rejection for all ten samples for the SAR procedure, the SGC method (samples 1-5) and the xSGC method (samples 6-10) for reduced dataset using the cycles of rc_5.

Description	ARO-18-08-LP	CSA-1-2-2	LAGU-1-1	PAG-6-4b	PAG-6-6b	ABLR-1	HAM-5	ISM-7	KTB-383-C	MBT-I-2430
Total number of analysed aliquots (grains)	500	500	500	500	500	500	500	500	500	500
Rejection criterion: Tn below 3 sigma BG	385	421	268	433	416	314	173	360	62	3
Rejection criterion: RSE of Tn exceeds 25%	75	52	67	58	52	104	65	74	29	4
Rejection criterion: recycling ratio 1 outsides [0.9:1.1]	3	1	9	1	2	8	13	2	43	52
Rejection criterion: recycling ratio 2 outsides [0.9:1.1]	0	0	0	0	0	0	0	0	0	0
Rejection criterion: recycling ratio 3 outsides [0.9:1.1]	0	0	0	0	0	0	0	0	0	0
Rejection criterion: recuperation 1 exceeds 10%	0	0	0	0	1	1	1	0	6	0
Rejection criterion: recuperation 2 exceeds 10%	0	0	0	0	1	0	0	0	0	0
Function fitGrowth(): improper input argument	0	0	0	0	0	0	0	0	0	0
Function fitGrowth(): failed in growth curve fitting	0	0	0	1	0	2	0	0	0	0
Rejection criterion: FOM of growth curve exceeds 10%	7	9	12	1	2	11	9	5	3	4
Rejection criterion: RCS of growth curve exceeds 10	0	0	0	0	1	0	7	1	27	7
Total number of rejected aliquots (grains)	470	483	356	494	475	440	268	442	170	70
Total number of accepted aliquots (grains)	30	17	144	6	25	60	232	58	330	430

Table A5: *Summary of the results for dataset A using the rcsR$_{150}$xSGC approach, in relation to the D$_e$ calculated with the SAR approach and to a dose recovery ratio (DRR) of 1. The DRR is calculated for all grains yielding a D$_e$ with the rcsR$_{150}$xSGC approach and for "common grains", which yield a D$_e$ with the SAR and the rcsR$_{150}$xSGC approaches. Headers indicating the size of the dose (D$_i$) of the used cycles, with the first 150 being the "natural" cycle. The abbreviations refer to Table 3.3.*

Reduced cycles used (sR = 150 Gy)	150-0-50-300	150-0-50-500	150-0-50-800	150-0-50-150-50	150-0-50-300-50	150-0-50-500-50	150-0-50-800-50	150-0-150-300-150	150-0-150-500-150	150-0-150-800-150
Abbreviation	**rc$_1$**	**rc$_2$**	**rc$_3$**	**rc$_4$**	**rc$_5$**	**rc$_6$**	**rc$_7$**	**rc$_8$**	**rc$_9$**	**rc$_{10}$**
n D$_e$	219	226	229	142	198	206	212	186	200	208
n D$_e$ common grains rcsR$_{150}$xSGC & SAR	86	86	87	59	86	86	87	85	86	86
In unity within 10 %	68	53	48	41	72	69	64	62	63	63
In unity within 1 σ	18	33	38	18	14	17	22	22	22	22
In unity within 2 σ	0	0	1	0	0	0	1	1	1	1
Not in unity	0	0	0	0	0	0	0	0	0	0
NA in either rcsR$_{150}$xSGC or SAR	133	140	142	83	112	120	125	101	114	122
Differences in D$_e$										
Min	0.11	0.10	0.48	0.15	0.03	0.17	0.43	0.22	0.21	0.21
Max	45.08	92.96	163.44	38.78	29.37	66.85	72.05	33.63	33.63	33.63
Mean	9.00	12.21	15.33	8.70	7.40	8.74	11.43	9.98	9.85	9.85
sd	8.25	12.93	19.67	8.02	6.51	9.45	10.45	7.57	7.61	7.61
CV	0.92	1.06	1.28	0.92	0.88	1.08	0.91	0.76	0.77	0.77
DRR (all grains)										
DRR between 0.9-1.1	58	50	46	25	54	57	47	59	65	66
DRR with 1 σ error between 0.9-1.1	85	82	73	36	80	66	66	63	68	71
DRR with 1 σ error not between 0.9-1.1	75	93	110	53	63	82	99	62	66	67
Mean DRR	0.91	0.88	0.88	0.78	0.9	0.89	0.87	0.95	0.98	0.99
DRR (common grains)										
DRR between 0.9-1.1	21	18	17	13	23	24	21	32	32	32
DRR with 1 σ error between 0.9-1.1	34	28	25	17	33	22	18	26	26	26
DRR with 1 σ error not between 0.9-1.1	31	40	45	29	30	40	48	27	28	28
Mean DRR	0.88	0.87	0.86	0.79	0.87	0.85	0.84	0.91	0.9	0.9
Correlation with SAR (r$_s$ values)	0.92	0.9	0.9	0.84	0.94	0.94	0.95	0.89	0.89	0.89

Table A6: *Summary of the SEM-EDX measurement results for the nine elements measured. For each element the results are given for subset A, subset X and the complete dataset. The table is further divided in all grains (upper third), luminescent grains (middle third) and the non-luminescent grains (bottom third).*

All	O			Na			Mg			Al			Si			K			Ca			Ti			Fe		
Element	subset A	subset X	total	subset A	subset X	total	subset A	subset X	total	subset A	subset X	total	subset A	subset X	total	subset A	subset X	total	subset A	subset X	total	subset A	subset X	total	subset A	subset X	total
n measurements	1193	1135	2328	1193	1135	2328	1193	1135	2328	1193	1135	2328	1193	1135	2328	1193	1135	2328	1193	1135	2328	1193	1135	2328	1193	1135	2328
n (without 0)	1193	1135	2328	1158	978	2136	531	258	789	1185	1067	2252	1193	1135	2328	1152	1002	2154	1046	658	1704	519	325	844	1071	562	1633
Min [%]	44.04	42.55	42.55	0	0	0	0	0	0	0	0	0	12.22	18.63	12.22	0	0	0	0	0	0	0	0	0	0	0	0
Min (without 0) [%]	44.04	42.55	42.55	0.32	0.13	0.13	0.07	0.08	0.07	0.34	0.25	0.25	12.22	18.63	12.22	0.06	0.06	0.06	0.07	0.03	0.03	0.04	0.04	0.04	0.08	0.07	0.07
Max [%]	55.37	56.25	56.25	8.51	9.02	9.02	15.00	6.68	15.00	30.93	23.84	30.93	48.19	49.02	49.02	13.98	14.68	14.68	11.97	13.27	13.27	3.22	4.71	4.71	8.57	17.69	17.69
Mean [%]	48.02	47.70	47.87	3.33	2.65	3.00	0.39	0.14	0.26	9.33	8.54	8.94	32.29	34.94	33.58	3.40	4.21	3.80	1.80	1.09	1.45	0.16	0.13	0.15	1.28	0.60	0.95
sd [%]	1.74	2.25	2.01	1.84	2.35	2.13	0.78	0.39	0.63	2.73	3.95	3.40	3.72	5.99	5.13	3.01	4.88	4.05	2.18	1.83	2.05	0.26	0.32	0.29	1.39	1.44	1.46
Coefficient of variation	0.04	0.05	0.04	0.55	0.89	0.71	2.01	2.90	2.40	0.29	0.46	0.38	0.12	0.17	0.15	0.89	1.16	1.07	1.21	1.68	1.41	1.61	2.42	1.97	1.08	2.42	1.53

luminescent	O			Na			Mg			Al			Si			K			Ca			Ti			Fe		
Element	subset A	subset X	total	subset A	subset X	total	subset A	subset X	total	subset A	subset X	total	subset A	subset X	total	subset A	subset X	total	subset A	subset X	total	subset A	subset X	total	subset A	subset X	total
n measurements	65	434	499	65	434	499	65	434	499	65	434	499	65	434	499	65	434	499	65	434	499	65	434	499	65	434	499
n (without 0)	65	434	499	65	402	467	6	29	35	65	420	485	65	434	499	65	410	475	36	209	245	6	28	34	37	88	125
Min [%]	44.88	43.86	43.86	0.42	0	0	0	0	0	1.65	0	0.00	27.66	28.02	27.66	0.24	0	0	0	0	0	0	0	0	0	0	0
Min (without 0) [%]	44.88	43.86	43.86	0.42	0.13	0.13	0.22	0.12	0.12	1.65	0.59	0.59	27.66	28.02	27.66	0.24	0.06	0.06	0.10	0.06	0.06	0.27	0.07	0.07	0.09	0.08	0.08
Max [%]	52.53	54.42	54.42	7.7	9.015	9.015	1.67	2.31	2.31	17.05	14.44	17.05	44.23	48.72	48.72	13.33	14.63	14.63	4.42	5.46	5.46	1.13	1.34	1.34	2.45	8.81	8.81
Mean [%]	46.5	46.63	46.62	2.44	2.87	2.82	0.06	0.03	0.03	9.91	9.74	9.76	31.86	33.03	32.88	8.38	6.84	7.04	0.48	0.73	0.69	0.04	0.02	0.02	0.28	0.11	0.13
sd [%]	1.48	1.95	1.89	1.64	2.66	2.55	0.26	0.15	0.17	1.95	2.99	2.87	2.58	4.48	4.30	3.97	5.81	5.62	0.79	1.06	1.03	0.16	0.12	0.13	0.51	0.51	0.51
Coefficient of variation	0.03	0.04	0.04	0.67	0.93	0.91	3.94	5.66	5.32	0.20	0.31	0.29	0.08	0.14	0.13	0.47	0.85	0.80	1.63	1.47	1.49	3.84	5.46	5.13	1.82	4.72	3.93

non-luminescent	O			Na			Mg			Al			Si			K			Ca			Ti			Fe		
Element	subset A	subset X	total	subset A	subset X	total	subset A	subset X	total	subset A	subset X	total	subset A	subset X	total	subset A	subset X	total	subset A	subset X	total	subset A	subset X	total	subset A	subset X	total
n measurements	1128	701	1829	1128	701	1829	1128	701	1829	1128	701	1829	1128	701	1829	1128	701	1829	1128	701	1829	1128	701	1829	1128	701	1829
n (without 0)	1128	701	1829	1093	576	1669	525	229	754	1120	647	1767	1128	701	1829	1087	592	1679	1010	449	1459	513	297	810	1034	474	1508
Min [%]	44.04	42.55	42.55	0	0	0	0	0	0	0	0	0	12.22	18.63	12.22	0	0	0	0	0	0	0	0	0	0	0	0
Min (without 0) [%]	44.04	42.55	42.55	0.32	0.15	0.15	0.07	0.08	0.07	0.34	0.25	0.25	12.22	18.63	12.22	0.06	0.10	0.06	0.07	0.03	0.03	0.04	0.04	0.04	0.08	0.07	0.07
Max [%]	55.37	56.25	56.25	8.51	8.46	8.51	15	6.68	15	30.925	23.84	30.925	48.19	49.02	49.02	13.975	14.68	14.68	11.97	13.27	13.27	3.22	4.71	4.71	8.57	17.69	17.69
Mean [%]	48.1	48.37	48.21	3.39	2.51	3.05	0.40	0.20	0.33	9.29	7.79	8.72	32.31	36.12	33.77	3.11	2.59	2.91	1.87	1.32	1.66	0.17	0.20	0.18	1.34	0.90	1.17
sd [%]	1.71	2.17	1.91	1.84	2.12	2.00	0.79	0.47	0.69	2.76	4.27	3.50	3.78	6.48	5.32	2.68	3.27	2.93	2.21	2.15	2.20	0.26	0.38	0.31	1.40	1.73	1.55
Coefficient of variation	0.04	0.04	0.04	0.54	0.85	0.66	1.96	2.33	2.12	0.30	0.55	0.40	0.12	0.18	0.16	0.86	1.26	1.01	1.18	1.63	1.33	1.56	1.89	1.73	1.04	1.92	1.32

Appendix B (Chapter 4)

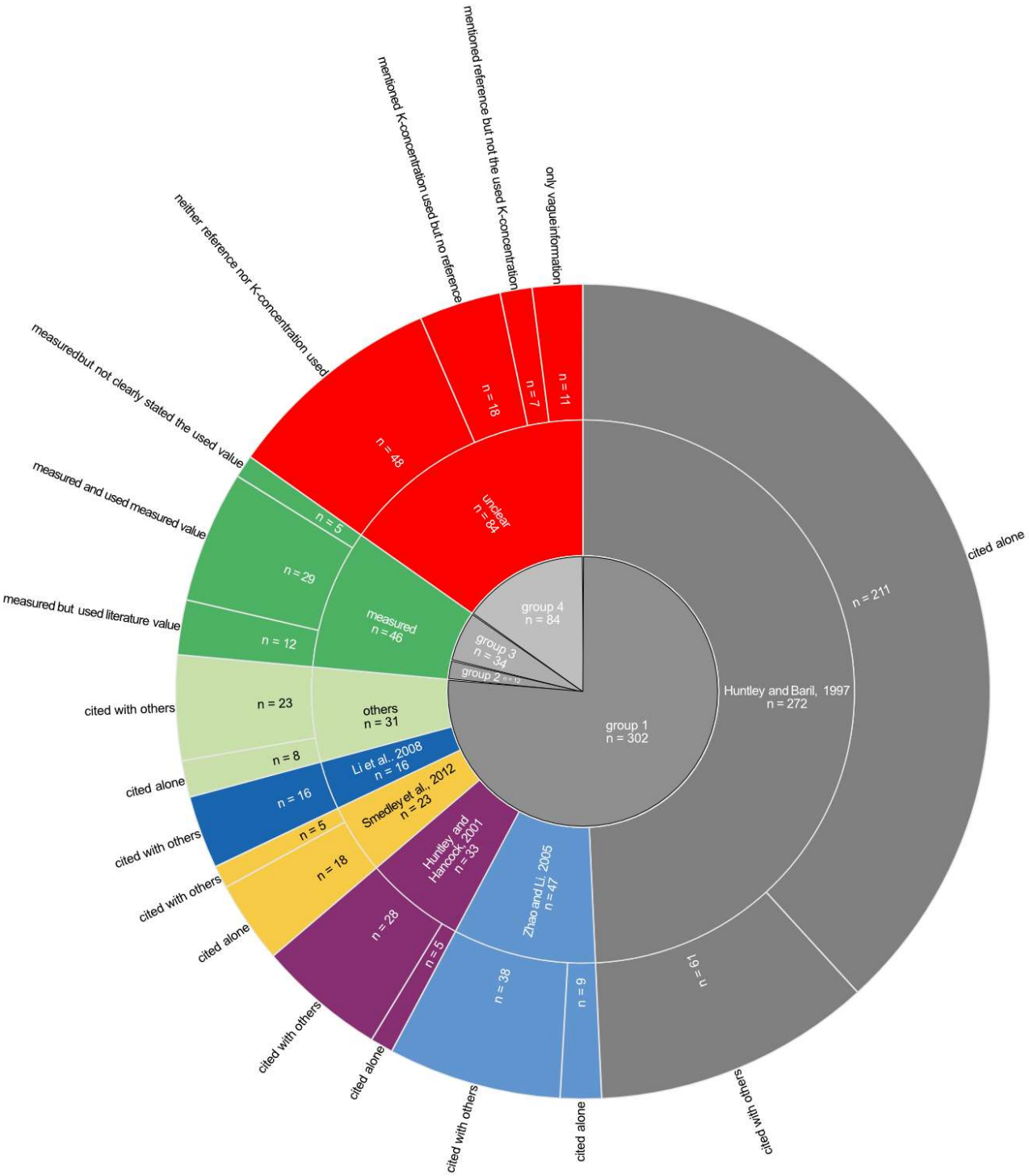

Fig. B1: *Detailed summary of the literature review.* ***Inner circle****: allocation of the 432 articles into four groups, where group 1 used one or more literature values for the K-concentration, group 2 measured the K-concentration of their samples but used a literature value instead, group 3 measured the K-concentration of their samples and used it, group 4 did not clearly state what K-concentration they used or where the used K-concentration came from.* ***Middle circle****: numbers of citations per source for the five most cited literature sources, number of citations of all other sources, number of articles that performed measurements and number of articles that provided only inaccurate information on K concentration.* ***Outer circle****: detailed information on the categories from the middle circle.*

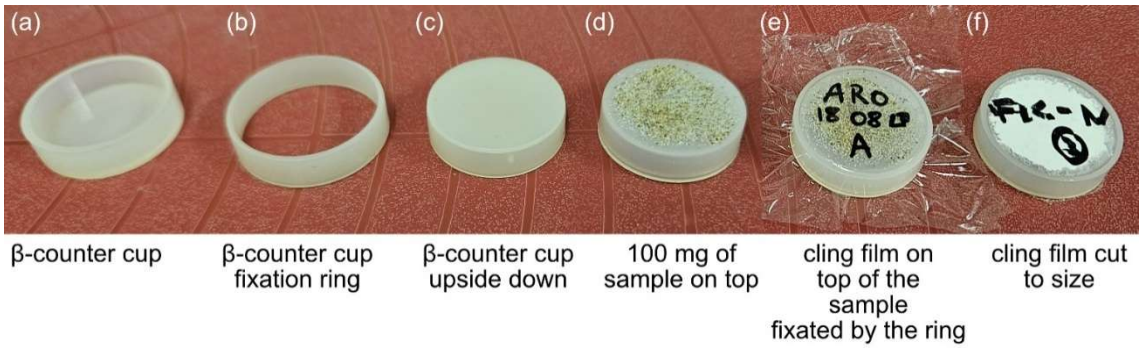

Fig. B2: *Preparation of feldspar samples for measurements in the β-counter.* ***a)*** *A plastic β-counter cup in its normal position.* ***b)*** *A plastic ring with a slightly larger diameter than the β-counter cup.* ***c)*** *A plastic β-counter cup in the upside-down position.* ***d)*** *100 mg of feldspar sprinkled onto the upside-down β-counter cup.* ***e)*** *A piece of cling film labelled with the sample name is placed on top of the sample material on the upside-down β-counter cup and secured by the plastic ring.* ***f)*** *The same as shown in e) but with the excess cling film cut off.*

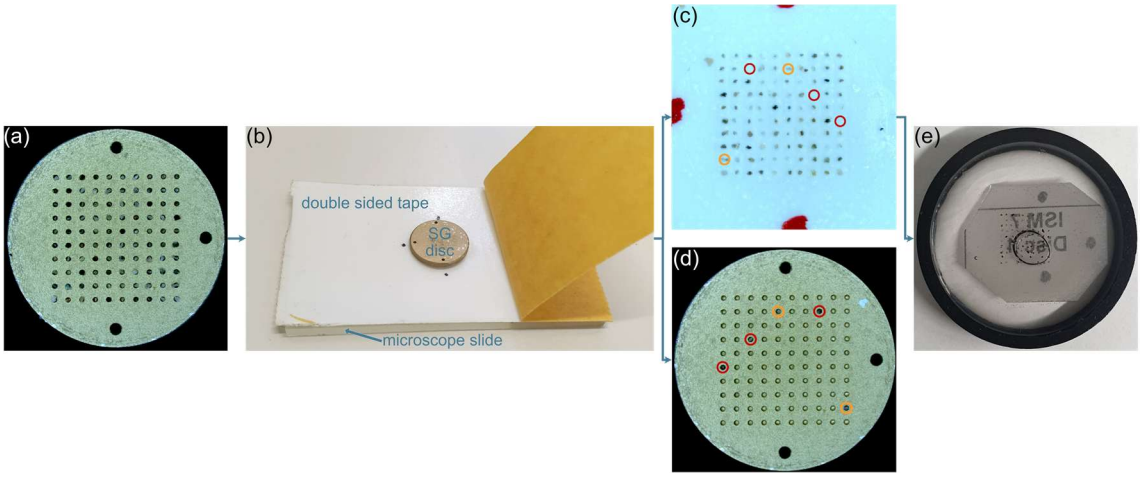

Fig. B3: *Sample preparation for the single grain SEM-EDX and μ-XRF measurements.* ***a)*** *A single grain (SG) sample disc after luminescence measurements filled with all 100 grain holes filled.* ***b)*** *SG disc facing downward onto double sided sticky tape. The tape is attached to a glass microscope slide on the other side. The directions of the three positioning holes are marked on the tape.* ***c)*** *Grains on the sticky tape after disc removal. Red circles show locations where no grain was transferred and yellow circles show locations where only parts of a grain where transferred while still parts stuck in the SG disc.* ***d)*** *SG disc after removal from sticky tape. Red circles show position of grains still within grain holes, corresponding to the red circles in c), and yellow circles show part of grains still within grain holes, corresponding to the yellow circles in c).* ***e)*** *Grains fixated in resin with a polished surface.*

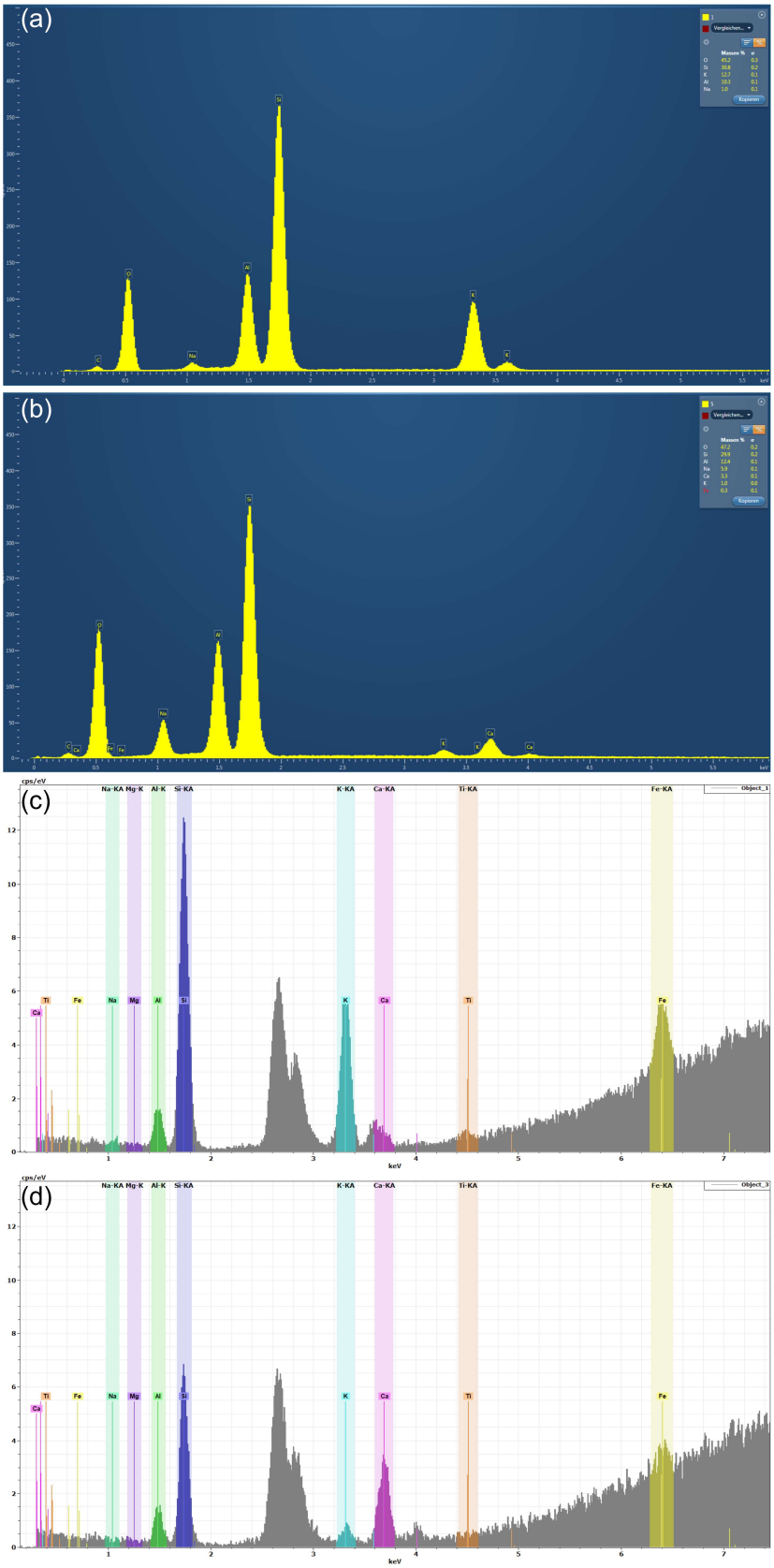

Fig. B4: *Exemplary spectra including peak fits for selected elements (Na, Mg, Al, Si, K, Ca, Ti, and Fe).* ***a)*** *SEM-EDX spectrum of a grain with ~8 wt% K.* ***b)*** *SEM-EDX spectrum of a grain with ~2 wt% K.* ***c)*** *µ-XRF spectrum of the same grain depicted in a) with ~8 wt% K.* ***d)*** *µ-XRF spectrum of the same grain depicted in b) with ~2 wt% K. The peak observed between ~2.5–3 keV in c) and d) originates from the Rh anode of the µ-XRF instrument. Note that oxygen concentrations are not measured directly in either method but are inferred from the stoichiometry of the detected elements assuming their oxide forms.*

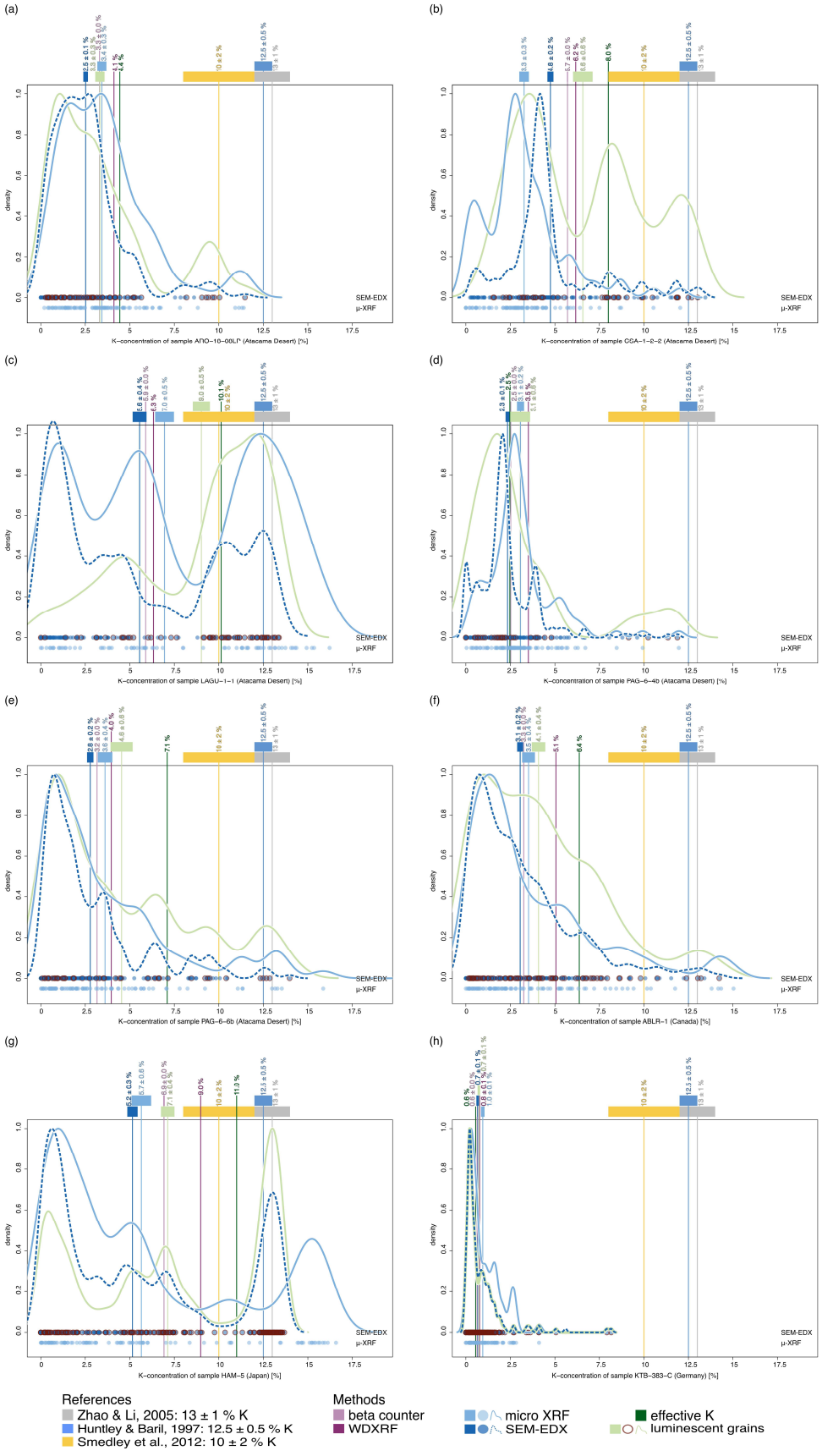

Fig. B5: *Single-grain K-concentrations for the eight samples not depicted in Fig. 4.3 of the main text. The dark blue dotted density curves and dots are based on the SEM-EDX measurements and the light blue ones on the µ-XRF measurements. The red circles around the dark blue dots and the light green density curve represent the luminescent grains. The vertical lines represent the K-concentrations presented in Chapter 4.4.1, boxes above the graph representing their errors.*

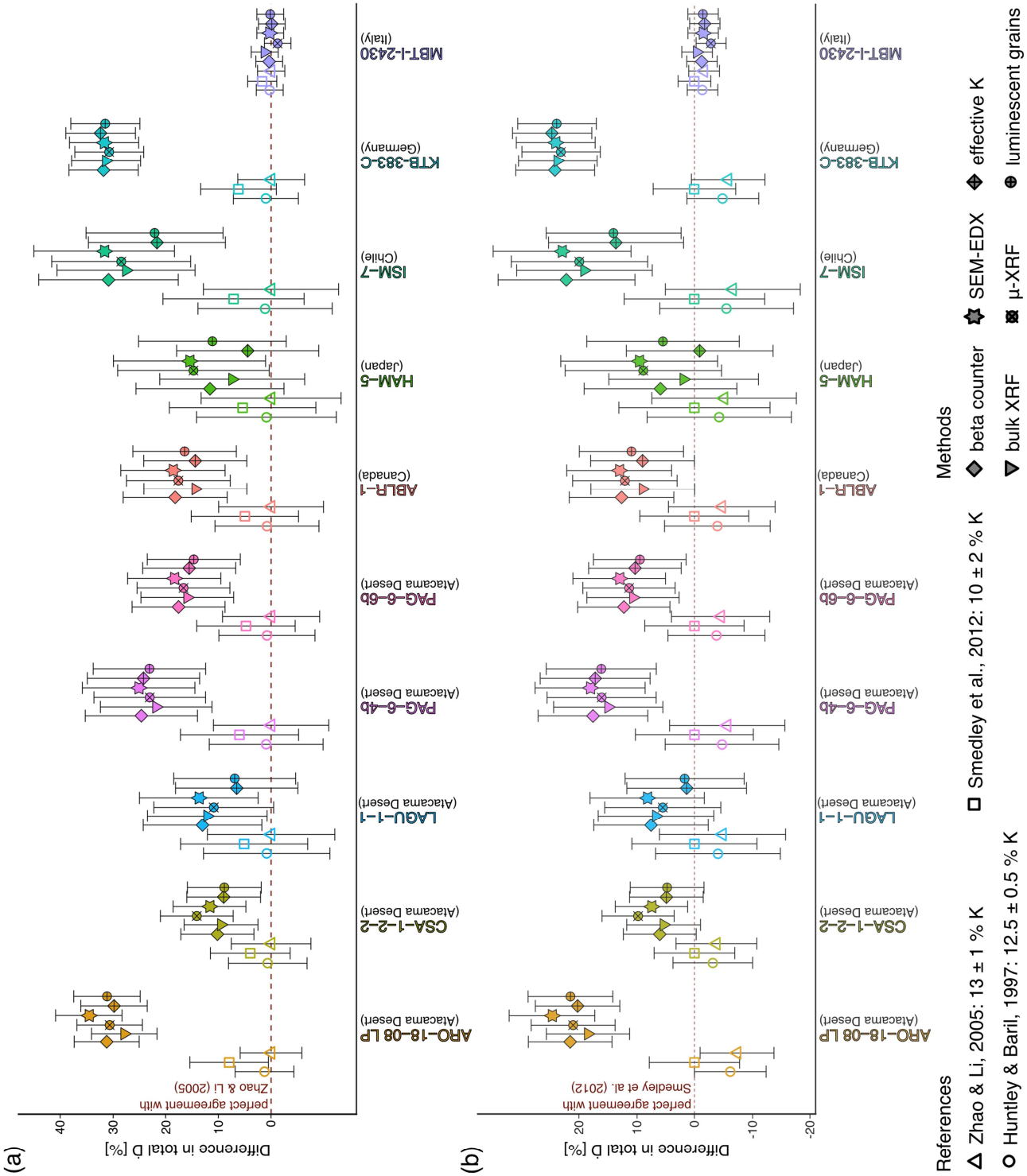

Fig. B6: *Ḋ results.* ***a)*** *A comparison between the total Ḋ based on the K-concentration of 13 ± 1 % (Zhao & Li, 2005) and the total Ḋ based on the measured K-concentrations and luminescence-weighted K estimates.* ***b)*** *A comparison between the total Ḋ based on the K-concentration of 10 ± 2 % (Smedley et al., 2012) and the total Ḋ based on the measured K-concentrations and luminescence-weighted K estimates. The dashed lines indicate a perfect agreement with the total Ḋ based on the K-concentration of 13 ± 1 % (Zhao & Li, 2005) in a) and of 10 ± 2 % (Smedley et al., 2012) in b).*

For Table B1 and B5 see digital Appendix Table B1 and Table B5 file.

Table B2: *Overview of the K-concentrations with which the five most frequently cited sources were quoted.*

Reference	recommended/mentioned K-concentration	cited as	Frequency
Huntley and Baril, 1997	12.5 ± 0.5 %	12.5 ± 0.5 %	204
		12 %	2
		12 ± 1 %	2
		12 ± 2 %	1
		12 ± 0.5 %	7
		12.5 ± 1 %	12
		12.5 ± 2.5 %	2
		12.5 %	8
		13 ± 1 %	25
		12.5 ± 5	1
		12.5 ± 0.12 %	2
		not mentioned	7
Zhao and Li. 2005	13 - 14 %	13 ± 1 %	35
		13 ± 0.5 %	1
		13.5 ± 0.2 %	1
		12.5 ± 0.5 %	7
		12.5 ± 1 %	2
		12.5 %	1
Huntley and Hancock, 2001*	No recommendation but used 12.5 ± 0.5 %	12.5 ± 0.5 %	12
		12.5 ± 2 %	1
		13 ± 1 %	15
		12.5 ± 1 %	2
		not mentioned	3
Smedley et al., 2012	10 ± 2 %	10 ± 2 %	17
		10 ± 3 %	3
		12 ± 0.5 %	2
		not mentioned	2
Li et al., 2008	No recommendation but used 13 ± 1 %	13 ± 1 %	14
		12.5 ± 0.5 %	2

*this paper refers to the ratio of K-concentration and Rb-concentration and was three times cited alone without an additional citation

Table B3: *Single-grain dose recovery test SAR measurement protocol. Heating rate for steps 2–4 and 6–8 2 °C/s.*

Step	Treatment[a]	Observation
1	Given dose D_i	
2	Preheat, 60 s at 200 °C	
3	IRSL, 2 s at 50 °C	
4	IRSL, 3 s at 175 °C	L_x
5	Given test dose D_t	
6	Preheat, 60s at 200 °C	
7	IRSL, 2 s at 50 °C	
8	IRSL, 3 s at 175 °C	T_x
9	Return to step 1	

[a] given dose D_i [Gy]: 150, 0, 50, 150, 300, 500, 800, 0, 50, 150; test dose D_t [Gy]: 50

Table B4: *Example of stoichiometric calculations of elemental concentrations for SEM-EDX and μ-XRF measurements. First the spectral peaks of each target element get fitted to the acquired spectrum (see Fig. B4). Next, the net peak areas (= net counts) under each fitted peak are summed per element and converted to mass concentrations (wt %). Oxygen concentrations are then derived from these oxide formulations rather than measured directly. Finally, these mass concentrations are normalised to 100 %.*

Element	∑ net counts	Mass concentration (wt %)	Normalised concentrations (wt %)
O	-	8.41	50.09
Na	17	0	0
Mg	0	0	0
Al	642	1.38	8.22
Si	6513	5.81	34.6
K	3784	1.08	6.43
Ca	224	0.04	0.24
Ti	88	0.01	0.06
Fe	2298	0.06	0.36
Sum	13566	16.79	100

Appendix C (Chapter 6)

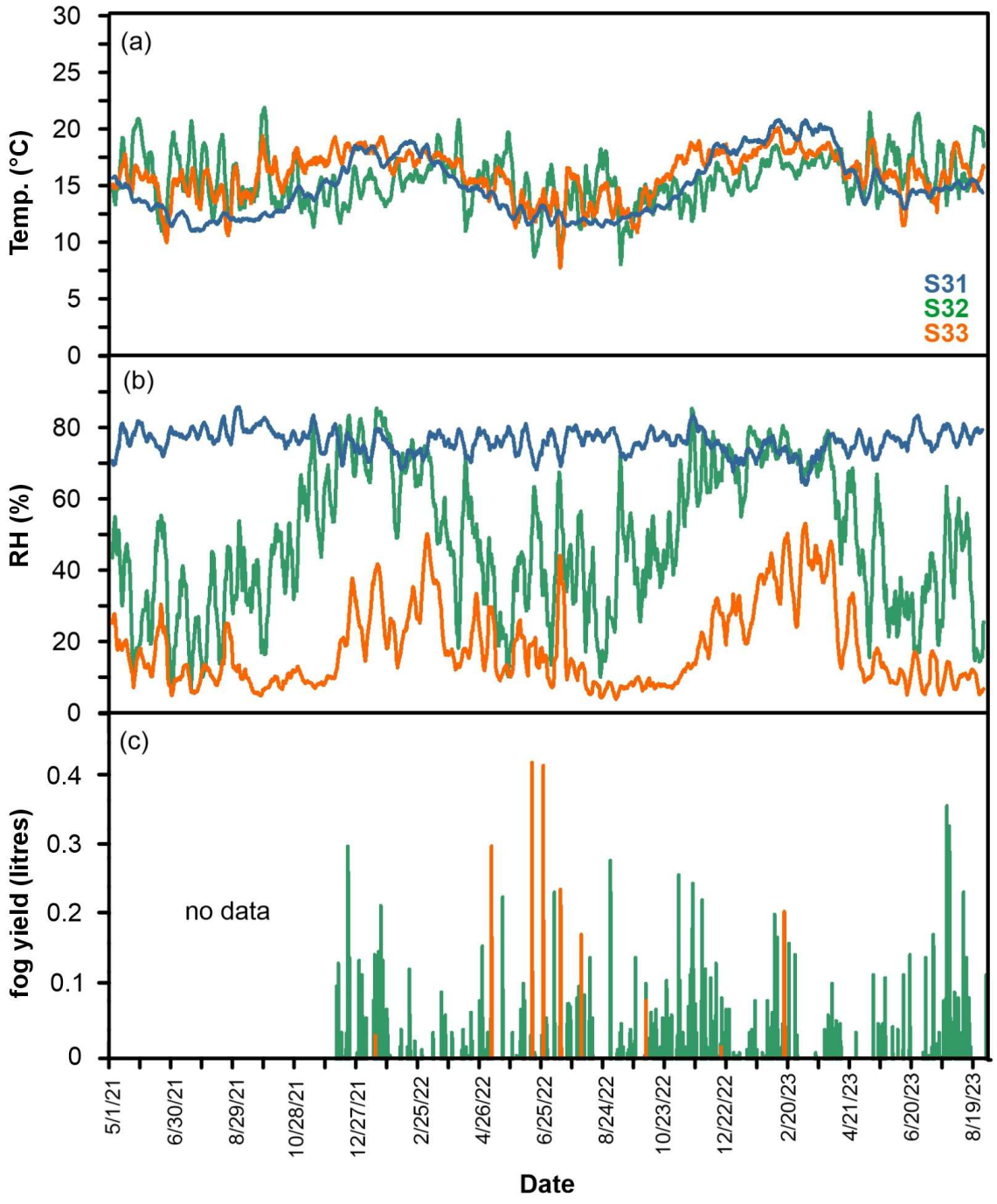

Fig. C1: *Weather station data from 1. May 2021 to 19. August 2023 of the three weather stations* ***S31****,* ***S32****, and* ***S33*** *situated a few km south of the studied Paposo transect (Hoffmeister, 2018a, 2018c, 2018b). Values represent weekly running averages derived from 10-minute data.* ***a)*** *Air temperature at 2 m above ground.* ***b)*** *Relative humidity (%) of the air at 2 m above ground.* ***c)*** *Fog yield (litres) at 2 m above ground.*

Table C1: *D_e measurements, internal and external dose rate determination, geochemistry analysis and granulometric analysis.*

	Depth below surface (cm)				
Sample	D_e measurements	External dose rate	Internal dose rate	Geochemistry	Granulometry
P1					
P1-1	0-5	0-5	0-5	0-5	0-5
P1-2	5-15	5-15	X	10-15	10-15
P1-2B	X	X	X	15-20	15-20
P1-3	20	20-40	20	20-25	20-25
P1-4	40	20-40	X	35-40	35-40
P1-5	X	X	X	45-50	45-50
P2					
P2-1	0-2	0-2	0-2	0-2	0-2
P2-2	2-10	2-20	X	2-10	2-10
P2-3	10-20	2-20	10-20	10-20	10-20
P2-3B	X	20-35	X	20-35	20-35
P2-4	35-45	35-50	35-45	35-45	35-45
P2-5	X	35-50	X	45-50	45-50
P3					
P3-1	0-1	0-1	0-1	0-1	0-1
P3-2	1-10	1-20	X	1-10	1-10
P3-3	10-20	1-20	10-20	10-20	10-20
P3-4	20-30	20-50	X	20-30	20-30
P3-5	30-40	20-50	X	30-40	30-40
P3-6	40-50	20-50	40-50	40-50	40-50
P3-7	X	>50	X	X	X
P4					
P4-1	0-2	0-6	0-2	0-2	0-2
P4-2	2-6	0-6	X	2-6	2-6
P4-3	6-15	6-20	6-15	6-15	6-15
P4-3B	X	6-20	X	15-20	15-20
P4-4	28-34	28-34	X	28-34	28-34
P4-4B	X	40-80	X	40-50	40-50
P4-5	70-80	40-80	70-80	70-80	70-80
P5					
P5-1	0-2	0-2	0-2	0-2	0-2
P5-2	2-8	2-8	X	2-8	2-8
P5-3	8-12	8-12	8-12	8-12	8-12
P5-3B	X	12-28	X	12-16	12-16
P5-4	16-20	12-28	X	16-20	16-20
P5-5	24-28	12-28	X	24-28	24-28
P5-6	28-35	28-35	28-35	28-35	28-35

Appendix C-I – Geochemistry and granulometry

Geochemical and granulometric analyses were conducted to characterize the sampled profiles and to identify potential indicators of depositional processes, sediment transport mechanisms, and pedogenic overprints. The material used for the analyses was generally taken as subsamples from the luminescence samples. Where the available material was insufficient, additional samples for geochemical and sedimentological analyses were collected. Consequently, not all depths of the geochemical and sedimentological samples correspond exactly to those of the luminescence samples (cf. Table C1). For geochemical analyses ~50 mg sampling material was hand-pestled to break up larger aggregates. The material was then sieved to <2 mm and ground in a ball mill (Retsch MM 400) for one minute at 30 vibrations per second. Subsequently, the powder-fine sample material was mixed with wax binder (Cereox Hoechst wax) in a ratio of 5:1 (5 g sample material to 1 g wax binder) and placed in an overhead mixer overnight to ensure even distribution of the wax binder throughout the whole sample. In a final step, the samples were pressed into round pellets (32 mm diameter, 3.4 mm thickness) at a pressure of 15 tonnes. The pressed pallets were then analysed utilising the energy dispersive-XRF spectrometer SPECTRO XEPOS (SPECTRO Analytical Instruments Ltd.) in a helium gas atmosphere with a 50 W/60 kV X-ray tube. Every sample was measured twice for 600 s and the concentrations of major and trace elements from Na to U were determined simultaneously. The measured concentrations (mg/kg) were adjusted to sample weight (6 g). The pellets were not rotated between the two measurements. Subsequently, the arithmetic mean of the two measurements for each detected element per sample were calculated and used for all further analysis. Oxides, as well as their molar proportions, of the elements used in the subsequent data analysis, were calculated by applying element specific conversion constants (Samsonov, 2013) (cf. Table C2).

Table C2: *Element specific conversion constants according to Samsonov (2013).*

Element	Oxide	Oxide conversion factor	Molar mass conversion factor
Na	Na_2O	1.348	61.979
Mg	MgO	1.658	40.309
Al	Al_2O_3	1.889	101.960
Si	SiO_2	2.139	60.084
P	P_2O_5	2.291	141.945
Cl	ClO_2	1.903	67.450
K	K_2O	1.205	94.199
Ca	CaO	1.399	56.077
Ti	TiO_2	1.668	79.865
Fe	Fe_2O_3	0.699	159.687

For granulometric analyses were performed on the same set of samples and on the four samples from the dust traps (Wennrich et al., 2024). Before measuring organic matter of two grams of sampling material <2 mm was dissolved using hydrogen peroxide (H_2O_2; 15 %). Subsequently the calcium sulphate was dissolved with sodium bicarbonate (Na_2CO_3; 210 g/l, 12 h at 60 °C) (Ritter et al., 2019) and the calcium carbonate was dissolved with hydrochloric acid (HCl; 10 %). Tetrasodium pyrophosphate ($Na_4P_2O_7$; 55.7 g/l) was used to disperse the sample. Finally, the sample was diluted with distilled water until a sample concentration of 10 % was reached. The samples were measured with a laser diffraction particle size analyser (Beckman Coulter LS13 320) and the data was analysed with the GRADISTAT software (Blott and Pye, 2001). Grain size statistics were calculated after Folk and Ward (1957). In addition to the exemplary grain size distributions in the main text (Fig. 6.4b), Fig. C2 shows profile-wise grain size distributions including the mean distribution of the dust samples (Fig. C2a-e) and the grain size distribution of each dust sample (Fig. C2f).

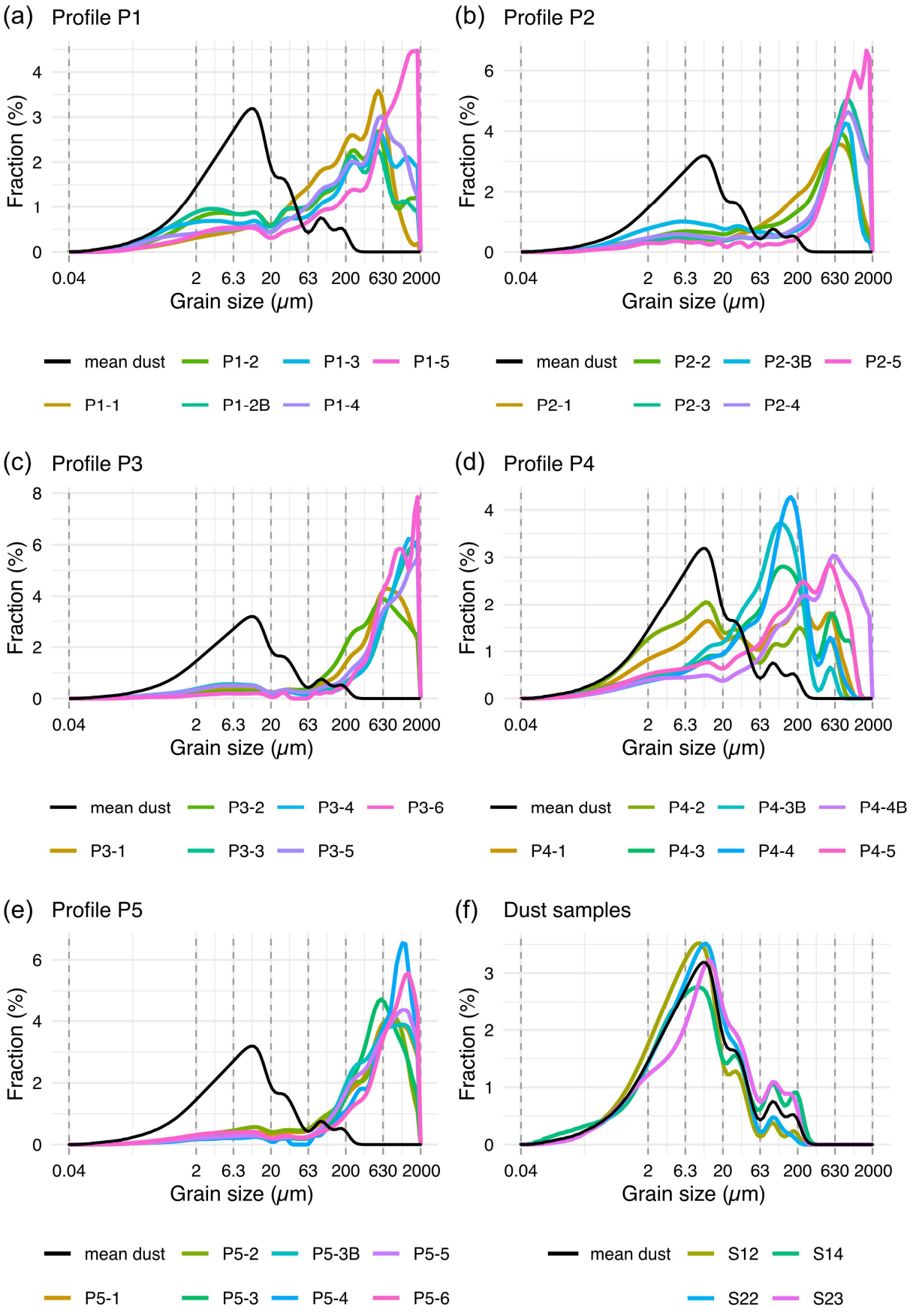

Fig. C2: *Profile-wise grain size distributions of* ***a)*** *P1,* ***b)*** *P2,* ***c)*** *P3,* ***d)*** *P4,* ***e)*** *P5, all including the mean distribution of the four dust samples as a reference (black line).* ***f)*** *grain size distribution of the four dust samples.*

Table C3: *Geochemistry and grain size results. Geochemical results are expressed as the ratio of mobile to immobile elements ($\sum E_m/\sum E_{im}$) and for the grain sizes the fraction of the grain size classes sand, silt, and clay are shown.*

Sample	Unit (profile-wise)	$\sum E_m/\sum E_{im}$	Sand fraction (%)	Silt fraction (%)	Clay fraction (%)
Profile **P1**					
P1-1	I	1.13	72.66	23.43	3.91
P1-2	II	1.23	60.94	30.79	8.27
P1-2B	III	1.21	57.05	32.00	10.95
P1-3	IV	1.26	65.72	24.22	10.05
P1-4	IV	1.37	72.56	20.76	6.69
P1-4B	V	1.67	78.08	17.78	4.14
Profile **P2**					
P2-1	I	1.01	79.56	16.37	4.07
P2-2	II	1.02	71.13	23.56	5.31
P2-3	II	1.00	80.13	16.00	3.86
P2-3B	III	1.10	59.75	31.89	8.36
P2-4	IV	1.03	76.52	18.62	4.85
P2-4B	V	1.03	86.56	10.55	2.89
Profile **P3**					
P3-1	I	1.19	83.40	13.28	3.32
P3-2	II	1.16	87.89	9.80	2.31
P3-3	II	1.17	80.50	15.27	4.23
P3-4	III	1.13	82.20	13.96	3.83
P3-5	IV	1.10	81.62	14.46	3.92
P3-6	IV	1.14	93.27	5.29	1.44
Profile **P4**					
P4-1	I	1.13	45.50	45.43	9.07
P4-2	II	1.15	30.56	56.22	13.22
P4-3	III	1.29	60.38	33.18	6.45
P4-3B	III	1.29	54.46	39.44	6.09
P4-4	V	1.32	64.31	31.15	4.54
P4-4B	VII	1.43	77.44	17.90	4.66
P4-5	VII	1.38	67.01	26.66	6.32
Profile **P5**					
P5-1	I	1.08	85.90	12.10	1.99
P5-2	II	1.04	80.25	16.47	3.28
P5-3	III	1.01	86.39	10.36	3.25
P5-3B	IV	1.06	89.01	8.18	2.82
P5-4	IV	1.10	91.82	6.25	1.94
P5-4B	IV	1.09	88.70	8.95	2.35
P5-5	IV	1.13	84.43	12.02	3.55
Dust samples					
S12 (dust)		X	3.17	80.17	16.66
S14 (dust)		X	12.74	72.94	14.32
S22 (dust)		X	3.68	82.54	13.78
S23 (dust)		X	12.51	71.73	15.76

Appendix C-II – Luminescence dating

The luminescence samples were prepared in the Cologne Luminescence Laboratory (University of Cologne; CLL) under subdued red-light conditions. In a first step the samples were sieved to obtain the 100 – 350 µm fraction. They were then treated with HCl (10 %) and H_2O_2 (10 %) to remove carbonates and organic matter. Following Zinelabedin et al. (2025), calcium sulphates were removed using NaCl (10 %). Subsequently a $Na_2C_2O_4$ solution (0.01 N) was used to disperse the particles. To enrich the K-rich feldspar fraction a heavy liquid density separation (ρ <2.58 g/cm^3) was used. The feldspar separates were sieved again to obtain the 200 – 250 µm fraction and a magnet was used to remove contaminants from the separates.

To determine the measurement protocol, dose recovery, residuals and fading preheat plateau, tests were carried out for one sample (**P4-2**) on 2 mm multi grain three aliquots of the isolated K-feldspar fraction for each test and temperature, mounted on stainless-steel discs using silicone oil. After selecting a protocol (cf. Table C3) further dose recovery, residuals and fading tests were carried out on six samples using 2 mm multi-grain aliquots (Fig. C3). On five further samples residuals were determined using single-grain discs and for one of those samples a single-grain dose recovery test was carried out (Fig. C4).

Three automated Risø TL/OSL-DA-20 reader (Bøtter-Jensen et al., 2010) equipped with $^{90}Sr/^{90}Y$ beta sources for irradiation were used for all single-grain measurements. They deliver dose rates between ~0.07 Gy/s and ~0.12 Gy/s. The CLL determines the dose rate of the instruments by applying a regression fit to multiple calibration measurements. These calibrations are conducted every six months using Risø calibration quartz. For grains measured in two out of three luminescence readers, administered dose-rates were corrected using dose-rate maps (Lapp et al., 2012), created by using radiosensitive film (GAFCHROMIC EBT2), and the correction software (CorrSGbin). The dose uniformity across the sample area of the third reader (~4.5 %) is not expected to contribute significantly to the received doses of each grain. Thus, measurements obtained on this reader were not corrected. A centred IR laser (150 mW; 830 nm) operating at 90 % power stimulated the grains, and the blue emission (~410 nm) was detected through a combination of a 2 mm Schott BG-39 filter and a 3 mm Corning 7-59 glass filter (blue filter package) by a photomultiplier tube.

A single-aliquot regenerative-dose (SAR) pIRIR protocol (Thomsen et al., 2008), adapted for single-grains, with a preheat of 250 °C for 60 s, an IR stimulation of 50 °C for 2 s, and a pIRIR stimulation of 225 °C for 3 s ($pIRIR_{225}$; Buylaert et al., 2009) was used. For further details on the measurement protocol see Table C3. Individual grains were brushed into single-grain discs with 100 holes of 300 µm each.

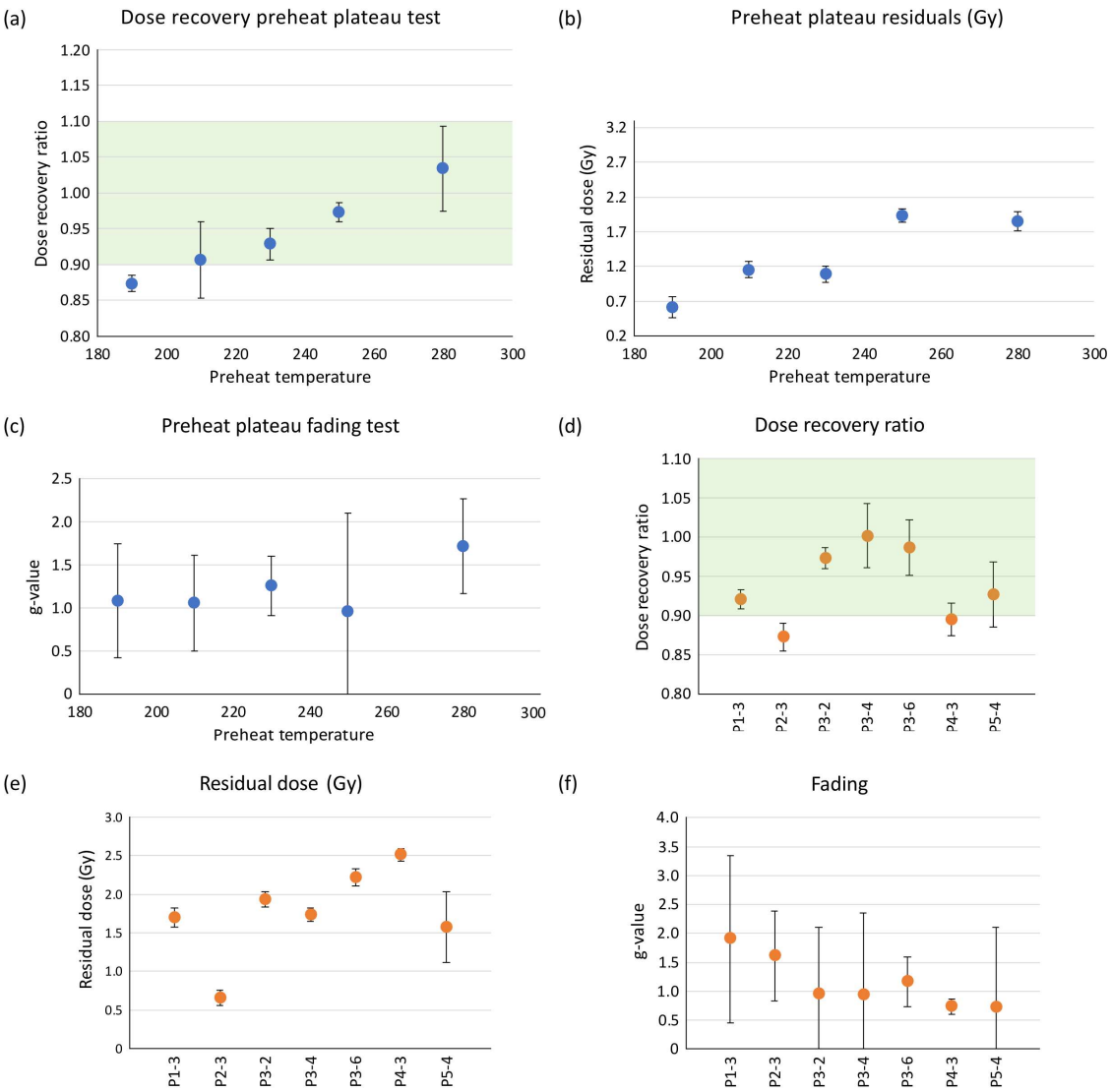

Fig. C3: *Protocol testing. Results of the multi-grain preheat plateau test on sample P3-2 (a-c) and further test on multi-grain level on seven additional samples using a preheat temperature of 250 °C and a pIRIR temperature of 225 °C.* ***a)*** *Dose recovery ratios,* ***b)*** *residuals, and* ***c)*** *g-values of the fading measurements.* ***d)*** *Dose recovery ratios,* ***e)*** *residuals, and* ***f)*** *g-values of the fading measurements.*

Table C4: *Single-grain SAR pIRIR$_{225}$ measurement protocol. Heating rate for steps 2–4 and 6–8 2 °C/s.*

Step	Treatment[a]	Observation
1	Given dose D_i	
2	Preheat, 60s at 250 °C	
3	IRSL, 2s at 50 °C	
4	IRSL, 3s at 225 °C	L_x
5	Given test dose D_t	
6	Preheat, 60s at 250 °C	
7	IRSL, 2s at 50 °C	
8	IRSL, 3s at 225 °C	T_x
9	Return to step 1	

[a]given dose D_i [Gy]: 0 (L_n/T_n cycle), 0, 50, 150, 300, 500, 800, 0, 50, 150; test dose D_t [Gy]: 50.

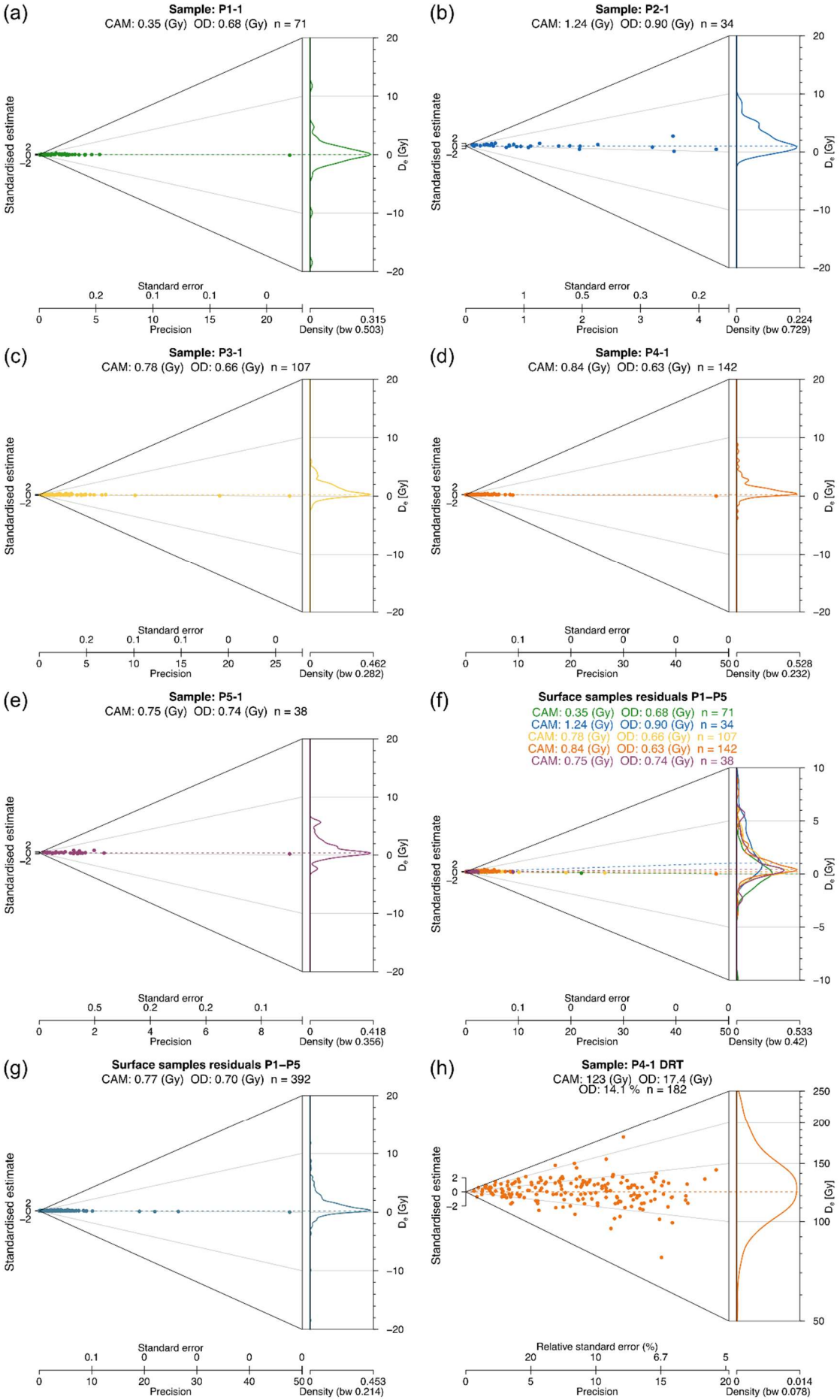
(a)
Sample: P1-1
CAM: 0.35 (Gy) OD: 0.68 (Gy) n = 71
(b)
Sample: P2-1
CAM: 1.24 (Gy) OD: 0.90 (Gy) n = 34
(c)
Sample: P3-1
CAM: 0.78 (Gy) OD: 0.66 (Gy) n = 107
(d)
Sample: P4-1
CAM: 0.84 (Gy) OD: 0.63 (Gy) n = 142
(e)
Sample: P5-1
CAM: 0.75 (Gy) OD: 0.74 (Gy) n = 38
(f)
Surface samples residuals P1–P5
CAM: 0.35 (Gy) OD: 0.68 (Gy) n = 71
CAM: 1.24 (Gy) OD: 0.90 (Gy) n = 34
CAM: 0.78 (Gy) OD: 0.66 (Gy) n = 107
CAM: 0.84 (Gy) OD: 0.63 (Gy) n = 142
CAM: 0.75 (Gy) OD: 0.74 (Gy) n = 38
(g)
Surface samples residuals P1–P5
CAM: 0.77 (Gy) OD: 0.70 (Gy) n = 392
(h)
Sample: P4-1 DRT
CAM: 123 (Gy) OD: 17.4 (Gy)
OD: 14.1 % n = 182
Standardised estimate
Standard error
Precision
Density (bw 0.503)
Density (bw 0.729)
Density (bw 0.282)
Density (bw 0.232)
Density (bw 0.356)
Density (bw 0.42)
Density (bw 0.214)
Density (bw 0.078)
Relative standard error (%)
D_e [Gy]

Fig. C4: *Abanico plots of the single-grain residual measurements (a-g) and the single-grain dose recovery test (DRT) (h).* ***a-e)*** *Abanico plots of the individual samples;* ***f)*** *zoomed Abanico plot of all samples, with different colours representing different samples according to (a)-(d);* ***g)*** *all single-grain residuals combined. As a result of the dose uniformity of the used luminescence reader, each grain received a different dose for its DRT. The given dose ranged between 106 to 177 Gy. Dotted lines in all Abanico plots represent the weighted mean.*

The first 0.2 s minus a background of the last 0.4 s of stimulations were used for signal integration. All D_e estimates were calculated using the numOSL R package version 2.8 (Peng et al., 2018). A 2 % measurement error was used for the regenerative dose signals (L_x) and the corresponding test dose signals (T_x). Parameters used for growth curve fitting were: "exponential model", "forced through origin" and "using a weighted procedure". The following rejection criteria were used: test dose signal following natural dose measurement (T_n) >3σ above background, relative standard error (RSE) of T_n ≤25 %, recycling ratio = unity ± 20 % for all available recycling points, recuperation ≤20 % of the natural signal, recuperation ≤20 % of the maximum regenerative-dose signal, figure-of-merits (FOM) ≤15 %.

The $pIRIR_{225}$ signal exhibits generally low fading rates, ranging from −0.7 ± 0.1 % to 1.9 ± 1.4 % per decade, with a mean fading rate of 1.1 ± 0.1 % per decade (± standard error, n = 21; Fig. C3f). Following Roberts (2012), no fading correction was applied to the $pIRIR_{225}$ ages.

Uran (U), thorium (Th), and potassium (K) concentrations were determined using an Ortec Profile MSeries GEM Coaxial P-type high-precision Germanium Gamma-Ray detector. Approximately 200 g of each sample was homogenised, dried, and stored for at least four weeks in an airtight container filled to maximum capacity, to compensate for radon loss induced by sample preparation. Energy and efficiency calibration of the gamma spectrometers at the CLL are performed at least every three months. ^{60}Co and ^{152}Eu standards are used for the energy calibration, while efficiency calibration employs a Nussi sediment standard (Preusser and Kasper, 2001); the resulting measurements are compared to the updated concentrations reported by Murray et al. (2018). In this study, gamma samples were measured over an integration time of 200,000 s. For activity calculations, peaks were selected from the ^{232}Th decay series (338, 911, 969, 239, and 583 keV), the ^{238}U decay series (295, 352, 609, and 1765 keV), and the ^{40}K peak (1461 keV).

The internal K-concentration was determined using a Risø GM-25-5A beta multicounter system (Bøtter-Jensen and Mejdahl, 1985) and a Bruker M Tornado µ-XRF following the approach proposed by Maßon et al. (in press).

Dose rates were calculated using Dose Rate and Age Calculator (DRAC, Durcan et al., 2015). User-defined gamma dose rates were calculated for each sample using the

scale_GammaDose() function of the R Luminescence package version 0.9.25 (Kreutzer et al., 2012; Riedesel et al., 2023). The user-defined gamma dose rates account for gamma dose rate variations between the units of a profile and the influence from other units on a sample. The dose rate conversion factors of Guérin et al. (2011) were used to convert U-, Th-, and K-concentrations into dose rates. The factors for alpha and beta grain size attenuation following Bell (1980) and Guérin et al. (2012) were used. An alpha efficiency of 0.11 ± 0.03 was assumed (Balescu and Lamothe, 1994). The cosmic dose rates were calculated based on their geographical location and depth below surface (Prescott and Hutton, 1994). Water contents were determined by comparing the weight of the sample prior and after drying at 45 °C for two days, resulting in water contents of zero within uncertainties. Yet, field measurements in similar locations showed slightly greater water contents. Therefore, water contents of 3 ± 3 % were applied. For further details on dose rate calculation see Table C2.

Table C5: *Applied model for sample-wise D_e calculation, sample-wise D_e, elemental concentrations used for dose rate ($\dot{D}$) determination, corresponding $\dot{D}$s and ages.*

Sample	Dose model	D_e (Gy)	External U (ppm)	External Th (ppm)	External K (%)	Internal K (%)	$\dot{D}$	Age (ka)
P1-1	MAM-4	1.6 ± 0.17	2.45 ± 0.17	9.28 ± 0.64	1.87 ± 0.05	7.45 ± 3.01	3.85 ± 0.50	0.42 ± 0.07
P1-2	MAM-4	10.87 ± 1.45	2.25 ± 0.15	8.58 ± 0.60	1.89 ± 0.05	5.72 ± 3.01	3.91 ± 0.62	2.78 ± 0.57
P1-3	CAM	105.86 ± 5.02	2.38 ± 0.16	9.49 ± 0.66	1.88 ± 0.05	5.72 ± 3.01	3.77 ± 0.59	28.07 ± 4.55
P1-4	CAM	106.64 ± 2.77	2.40 ± 0.16	10.05 ± 0.70	1.88 ± 0.05	5.72 ± 3.01	3.71 ± 0.69	28.71 ± 5.37
P2-1	MAM-4	1.52 ± 0.55	1.49 ± 0.10	7.88 ± 0.55	1.54 ± 0.04	1.88 ± 3.01	2.35 ± 0.25	0.65 ± 0.24
P2-2	MAM-4	1.05 ± 0.57	1.43 ± 0.10	7.07 ± 0.49	1.64 ± 0.04	1.75 ± 3.01	2.50 ± 0.28	0.42 ± 0.23
P2-3	MAM-4	2.73 ± 0.46	1.43 ± 0.10	7.07 ± 0.49	1.64 ± 0.04	1.61 ± 3.01	2.54 ± 0.29	1.08 ± 0.22
P2-4	MAM-4	1.83 ± 1.02	1.31 ± 0.09	6.64 ± 0.46	1.6. ± 0.04	2.14 ± 3.01	2.52 ± 0.35	0.73 ± 0.42
P3-1	CAM	4.93 ± 0.63	2.29 ± 0.15	9.87 ± 0.68	1.83 ± 0.05	3.74 ± 3.01	3.16 ± 0.35	1.56 ± 0.26
P3-2	MAM-4	2.94 ± 0.74	2.32 ± 0.16	10.06 ± 0.70	1.82 ± 0.05	3.37 ± 3.01	3.36 ± 0.51	0.87 ± 0.26
P3-3	MAM-4	3.96 ± 1.11	2.32 ± 0.16	10.06 ± 0.70	1.82 ± 0.05	2.99 ± 3.01	3.43 ± 0.54	1.16 ± 0.37
P3-4	CAM	6.31 ± 5.68	2.40 ± 0.16	9.73 ± 0.67	1.74 ± 0.04	3.07 ± 3.01	3.43 ± 0.54	1.84 ± 1.68
P3-5	CAM	184.23 ± 12.22	2.40 ± 0.16	9.73 ± 0.67	1.74 ± 0.04	3.22 ± 3.01	3.48 ± 0.59	53.02 ± 9.59
P3-6	CAM	208.47 ± 12.75	2.40 ± 0.16	9.73 ± 0.67	1.74 ± 0.04	3.3 ± 3.01	3.60 ± 0.59	57.94 ± 10.07
P4-1	MAM-4	4.72 ± 0.26	3.45 ± 0.23	19.00 ± 1.31	2.23 ± 0.06	4.71 ± 3.01	4.28 ± 0.49	1.10 ± 0.14
P4-2	CAM	29.52 ± 2.69	3.45 ± 0.23	19.00 ± 1.31	2.23 ± 0.06	4.77 ± 3.01	4.51 ± 0.56	6.55 ± 1.01
P4-3	CAM	205.25 ± 13.01	3.21 ± 0.22	16.25 ± 1.12	2.7. ± 0.07	4.83 ± 3.01	4.92 ± 0.72	41.71 ± 6.65
P4-4	CAM	224.42 ± 10.58	3.46 ± 0.23	16.52 ± 1.14	2.5. ± 0.06	5.62 ± 3.01	5.00 ± 0.70	44.92 ± 6.65
P4-5	CAM	227.23 ± 11.89	2.80 ± 0.19	13.93 ± 0.96	2.29 ± 0.06	6.40 ± 3.01	4.53 ± 0.89	50.14 ± 10.17
P5-1	MAM-3	2.92 ± 0.34	1.21 ± 0.09	3.24 ± 0.24	1.5. ± 0.04	2.41 ± 3.01	2.26 ± 0.25	1.29 ± 0.21
P5-2	MAM-4	3.42 ± 0.44	1.48 ± 0.10	4.99 ± 0.36	1.42 ± 0.04	2.48 ± 3.01	2.41 ± 0.28	1.42 ± 0.25
P5-3	MAM-3	4.39 ± 0.59	1.54 ± 0.11	5.25 ± 0.38	1.41 ± 0.04	2.54 ± 3.01	2.48 ± 0.29	1.77 ± 0.31
P5-4	MAM-4	9.65 ± 1.07	1.39 ± 0.10	4.53 ± 0.33	1.39 ± 0.04	2.54 ± 3.01	2.44 ± 0.35	3.95 ± 0.71
P5-5	MAM-3	10.83 ± 1.49	1.39 ± 0.10	4.53 ± 0.33	1.39 ± 0.04	2.54 ± 3.01	2.46 ± 0.35	4.41 ± 0.87
P5-6	MAM-4	44.98 ± 3.42	1.36 ± 0.10	5.04 ± 0.36	1.52 ± 0.04	1.85 ± 3.01	2.52 ± 0.39	17.86 ± 3.06

Appendix C-III – Detailed description of the sampling sites

Sampling site P1 – 103 m a.s.l.

Sampling site **P1** is situated on top of a large coastal alluvial fan, which has been thoroughly described by Walk et al. (2023) at 103 m a.s.l. (Fig. 6.1a, Fig. 6.2a). The mean annual temperature estimated according to Quade et al. (2007) is around 17.8 °C and the annual precipitation around 11.9 mm. According to Walk et al. (2023) the alluvial fan consists of four generations, with each younger generation incising the older ones (Fig. 6.2a). Profile **P1** was dug on top of the oldest alluvial fan generation, in direct adjacency to the erosional edge of the central alluvial channel related to the incision by the youngest fan generation (Fig. 6.2a). While cosmogenic nuclide-based ages suggest deposition of the oldest generation at approximately 111 ± 20 ka ago, incision and deposition of the youngest generation seems to have occurred later than 59.2 ± 8.7 ka ago (Walk et al., 2023).

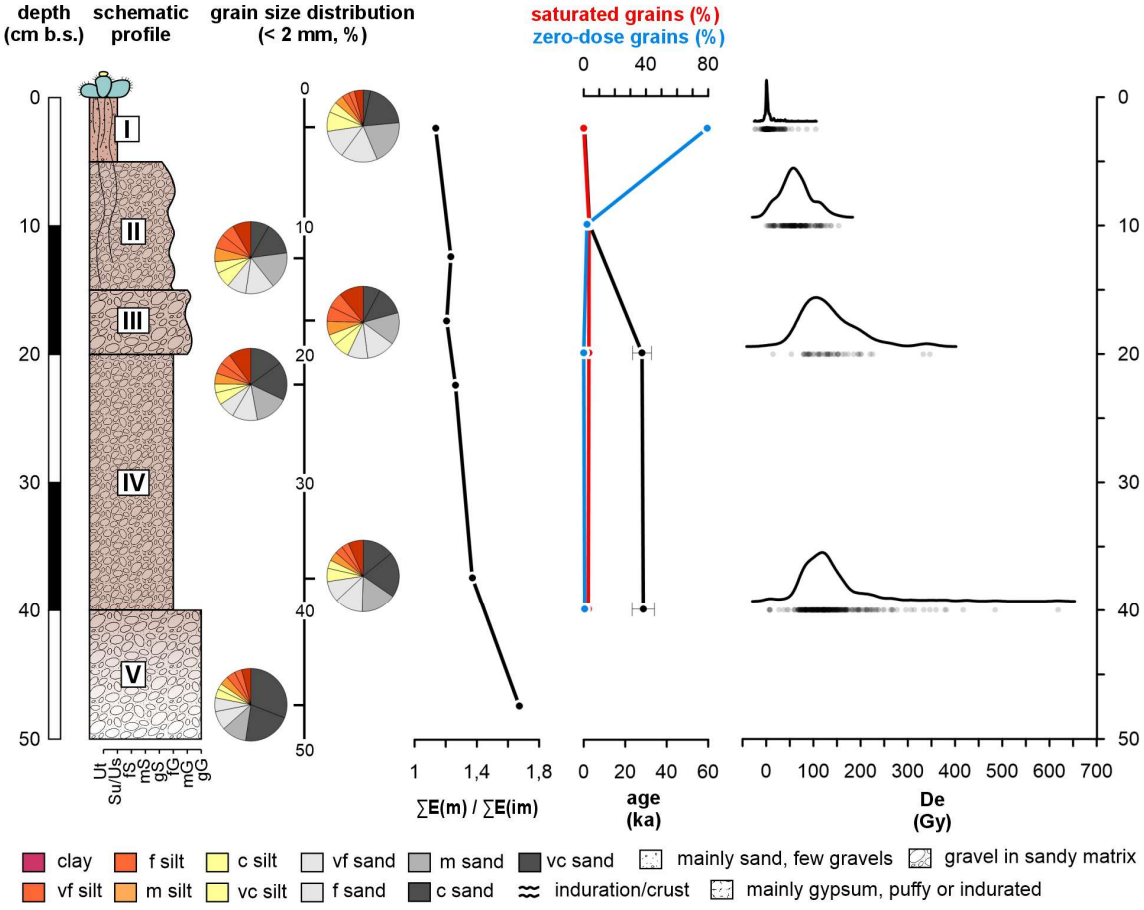

Fig. C5: *Stratigraphic, granulometric, geochemical, and luminescence characteristics of profile* ***P1****. From left to right: schematic lithology; grain size distribution; mobile to immobile elemental ratio ($\sum E_m/\sum E_{im}$); ages (black), saturated grains (red), zero dose grains (blue); D_e distributions.*

On the surface at **P1**, clasts ranging from 1 cm to 50 cm in size overlie a reddish-weathered, heterogeneous unit dominated by a sandy matrix. Various cacti – some already desiccated – are present, along with other sparse vegetation such as small

shrubs. Clasts exhibit heterogeneous lithologies and colours, with some displaying sub-rounded edges and others showing significant fracturing (Fig. C5).

Overall, no distinct horizontal layers are apparent in the profile. In the uppermost sedimentary unit I, the proportion of matrix relative to clasts is higher than in the deeper units. This unit is also the only one extensively penetrated by roots, with diameters reaching up to 5 mm. The underlying units II through IV show little variation, as illustrated by the grain size and the geochemical analysis of the reddish matrix. All units display roughly the same ratio of reddish, weathered matrix to multi-coloured clasts with varying sizes and roundness. In unit II, only a few fine roots are present, and their abundance decreases with depth. Starting from unit III, no roots are observed. On average, the clasts in units II and IV are somewhat smaller than those in units III and V. In unit V, there is no longer enough matrix available for sampling, and clast size increases markedly.

Sampling site P2 – 577 m a.s.l.

Sampling site **P2** is situated 1.2 km east of **P1** in the lower part of the Coastal Cordillera around 577 m a.s.l. and at the bottom edge of an alluvial fan (Fig. 6.1a, Fig. 6.2b). The fan is located within the fog occurrence zone in a tributary valley of the main Quebrada, that directly follows the Paposo fault (Fig. 6.1c). The mean annual temperature is around 18.1 °C and the annual precipitation approximately 6.7 mm (Quade et al., 2007). However, additional moisture input occurs in the form of fog precipitation (cf. Fig. C1). The Paposo fault directly crosses the alluvial fan in its flow direction. The surface slope of the fan is approximately 6°. Satellite images suggests different generations and recent to subrecent activity particularly in the eastern fan section (cf. Fig 6.2b). The profile was taken at a natural outcrop exposed by fluvial erosion, within the centre of the supposedly older part of the alluvial fan system. Shrub vegetation was present on the entire fan surface and about 20 cm behind the profile outcrop (i.e., west of the exposure). The surrounding area appeared noticeably more vegetated than surfaces at **P1**, with typical loma vegetation and cacti reaching up to 4 m in height, some of which were covered with lichens. The adjacent slopes exhibit distinct sediment colour changes (cf. Fig. 6.2b). The surface is covered with grey and reddish gravel composed of angular clasts, interspersed with a slightly reddish, weathered matrix (Fig. C6).

In unit I of the profile, a silty to fine-sandy sediment matrix fills the clast interspaces that is mainly built by fine gravel. This unit is penetrated by both fine and thick (~2 cm in diameter) roots. Some of the larger clasts from unit I extend into unit II but no deeper than 10 cm. The remainder of unit II primarily consists of fine gravel to coarse sand within the same silty to fine-sandy sediment matrix, although the

matrix colour appears reddish-brown. A thicker root (~2 cm in diameter) and several fine roots also traverse unit II. Unit III differs noticeably from the overlying layers. It is mainly dominated by medium-sized gravel that range in colour from grey to red and are embedded in a reddish-brown, sand-dominated matrix. No fine roots are observed in unit III. Underlying unit IV is clearly distinguishable from unit III. In unit IV, gravel and fine roots occur only in the lower part. The matrix remains reddish-brown and sand-dominated. The upper part exhibits lamination, and some layers appear distinctly indurated; however, there is no variation in colour or grain size between these layers. The lowermost unit V is dominated by fine to coarse gravel within a consistently reddish-brown, sandy matrix. Due to the reduced matrix content and the gravel-supported texture, no samples could be collected from this unit.

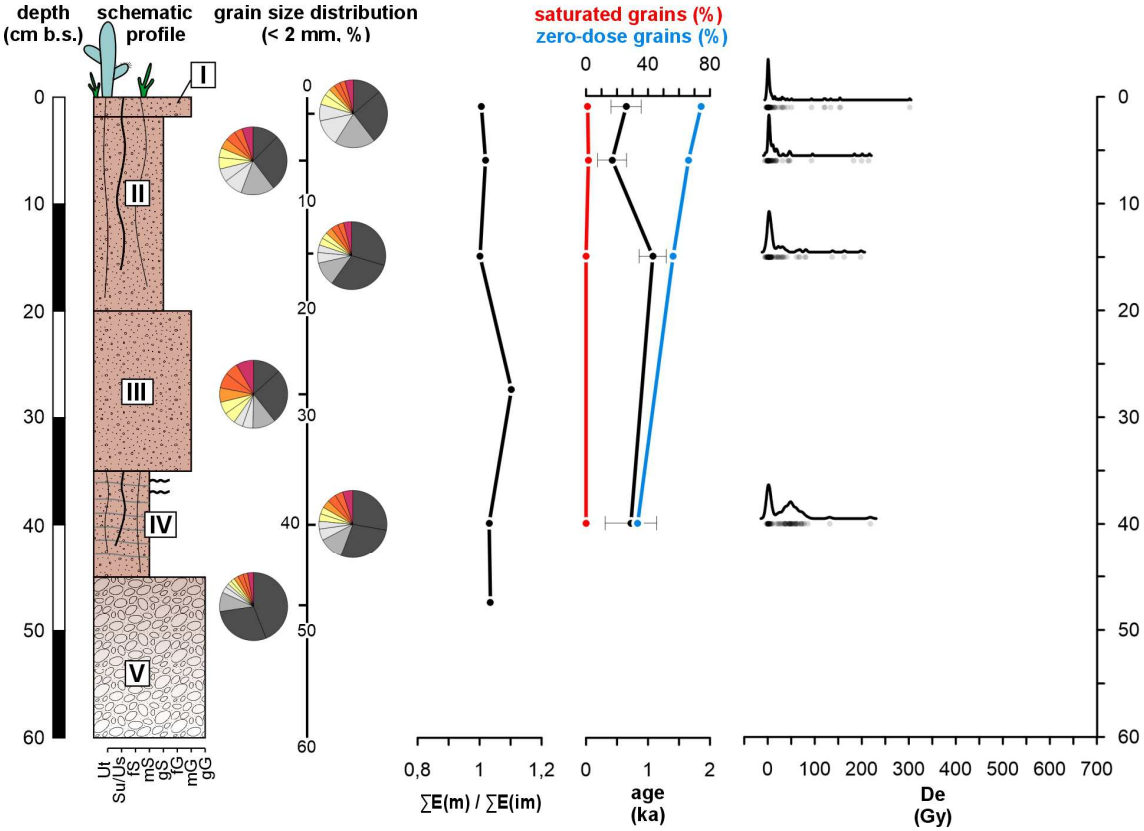

Fig. C6: *Stratigraphic, granulometric, geochemical, and luminescence characteristics of profile* ***P2****. From left to right: schematic lithology; grain size distribution; mobile to immobile elemental ratio ($\sum E_m/\sum E_{im}$); ages (black), saturated grains (red), zero dose grains (blue); D_e distributions. For legend see Fig. C5.*

Sampling site P3 – 1310 m a.s.l.

Profile **P3** is located within an alluvial channel at 1310 m a.s.l. (Fig. 6.1a, Fig 6.2c), i.e., slightly above the marine boundary layer. The channel is part of a larger alluvial channel system and located ~20 m upstream of the confluence of two channels. The channel system terminates in a small alluvial fan approximately 200 m downstream of the sampling location **P3**. The alluvial fan is affected by lateral erosion from the

main Quebrada and a road cut. Field observations and satellite images suggest the presence of multiple channel generations, with younger channels incising into older ones (cf. Fig. 6.2c). **P3** is oriented perpendicular to the flow direction of the main channel. The surface slope in the flow direction is approximately 8°, while the slope along the profile edge is about 2° from north to south. The profile was dug a few meters away from a gravel-covered slope, yet far enough to rule out any gravitational sediment input from the slope onto the channel surface at present. The area between the profile and the slope appeared slightly incised, with the surface lying 5-10 cm lower than at **P3**. Except for the incised area, the entire channel was covered with a layer of fine to medium sized gravel (Fig. C7). Vegetation on the entire channel was scarce, and remaining shrubs appeared largely desiccated. The MAT is approximately around 17.4 °C with MAP of 0.0 mm (Quade et al., 2007).

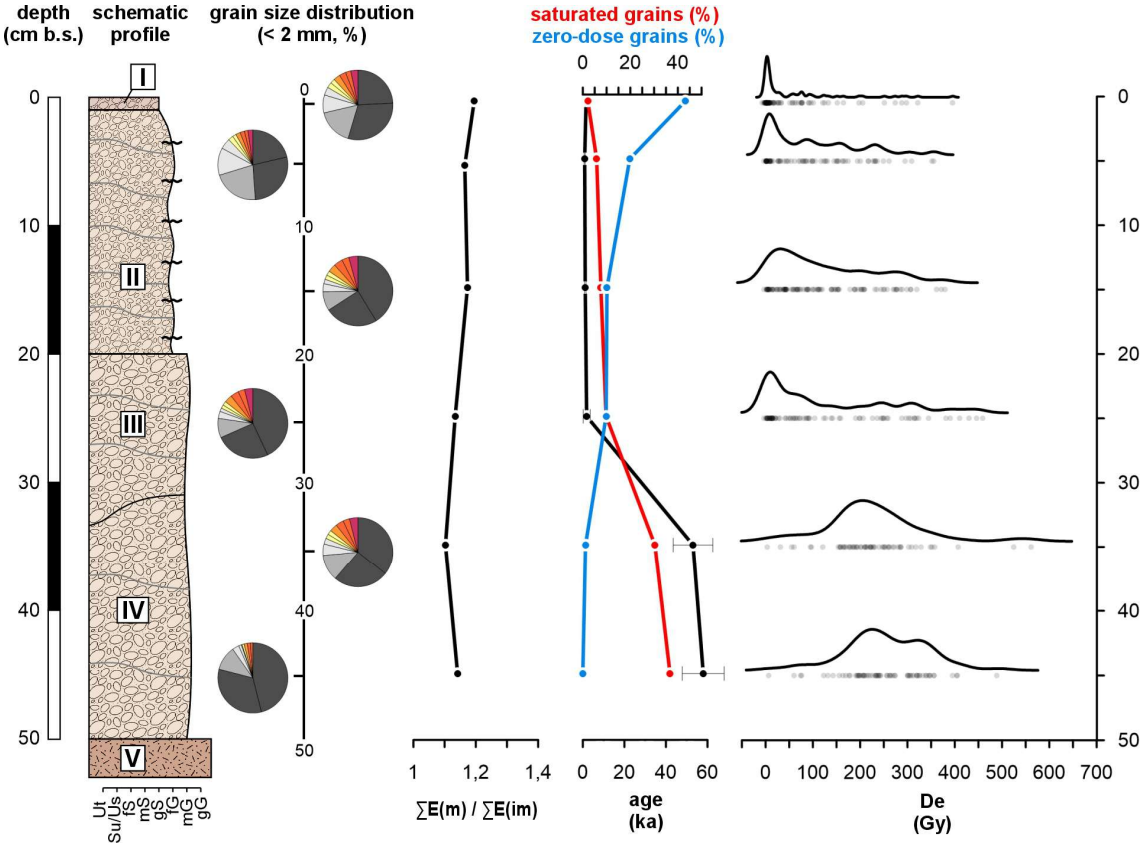

Fig. C7: *Stratigraphic, granulometric, geochemical, and luminescence characteristics of profile* ***P3****. From left to right: schematic lithology; grain size distribution; mobile to immobile elemental ratio ($\sum E_m/\sum E_{im}$); ages (black), saturated grains (red), zero dose grains (blue); D_e distributions. For legend see Fig. C5.*

Unit I is primarily composed of virtually matrix-free red and grey fine to medium gravel, which is noticeably finer compared to profiles **P1** and **P2**. The boundary to unit II is very distinct. Unit II consists predominantly of grey, partly reddish fine gravel within a brown–yellowish sandy matrix. Lamination due to individual layers of varying thickness is present. Some layers are slightly cemented, and some are not continuous across the entire profile unit. In the underlying unit III a few layers are

also visible but they are more discontinuous than in unit II and not cemented. Unit III is generally more heterogeneous, containing gravel of various sizes (from fine to coarse). The colour of both the gravel and the matrix, however, remains the same as in unit II. Below, unit IV appears to be composed of the same coarse material as the adjacent slope surface, i.e., large red to reddish-brown angular gravel lacking a sand- or silt-sized matrix; no samples were taken from this layer.

Sampling site P4 – 1480 m a.s.l.

Profile **P4** is situated in the older generation of the alluvial fan studied by Moradi et al. (2020) and Sun et al. (2023) (Fig. 6.1a, Fig. 6.2d). The alluvial fan is at ~1480 m a.s.l. and therefore considerably above the marine boundary layer. Moradi et al. (2020) described two distinct alluvial fan generations where the presumably older fan generation was called “crust” and the presumably younger fan generation “fan”. In our study, we used the same profile pit in the older fan generation previously described as P9 in Sun et al. (2023), now termed profile **P4**. Within the pit, the profile is oriented along the flow direction of the alluvial fan. The surface slope in flow direction and hence along the profile edge is ~7°. The surface is covered by gravel ranging from fine to coarse clasts (up to 20 cm), which are angular, heterogeneous, and not rounded. The surface appears red which is in contrast to the presumably younger fan surface at the centre of the alluvial system. This younger generation is incised by a modern channel, along which vegetation (i.e., dry shrubs) are abundant. In contrast, no vegetation was observed at and in the surroundings of profile **P4**, and the older fan generation as a whole exhibited no vegetation. The large gravels covering the surface lie within a matrix of fine gravel (Fig. C8). The MAT is approximately 17.2 °C with a MAP of 0.0 mm (Quade et al., 2007).

Below the overlying gravel, unit I predominantly comprises an unconsolidated layer of reddish-brown sandy silt. Unit II consists of partially consolidated yet porous fine sediment dominated by silt and clay, and it appears to display some layering. From this point down to the base of the profile, the sediment colour is pale beige. Unit III is a gravel layer composed of medium gravel in a consolidated, sandy matrix, with occasional larger clasts. The average gravel size increases in unit IV, although the matrix remains unchanged. Due to insufficient matrix material, unit IV could not be sampled. Units V and VII are likewise gravel layers, similar to unit III, featuring medium gravel in a sandy matrix. Unit VI, akin to unit IV, is a gravel layer dominated by coarse gravel in a sandy matrix and was also not suitable for sampling.

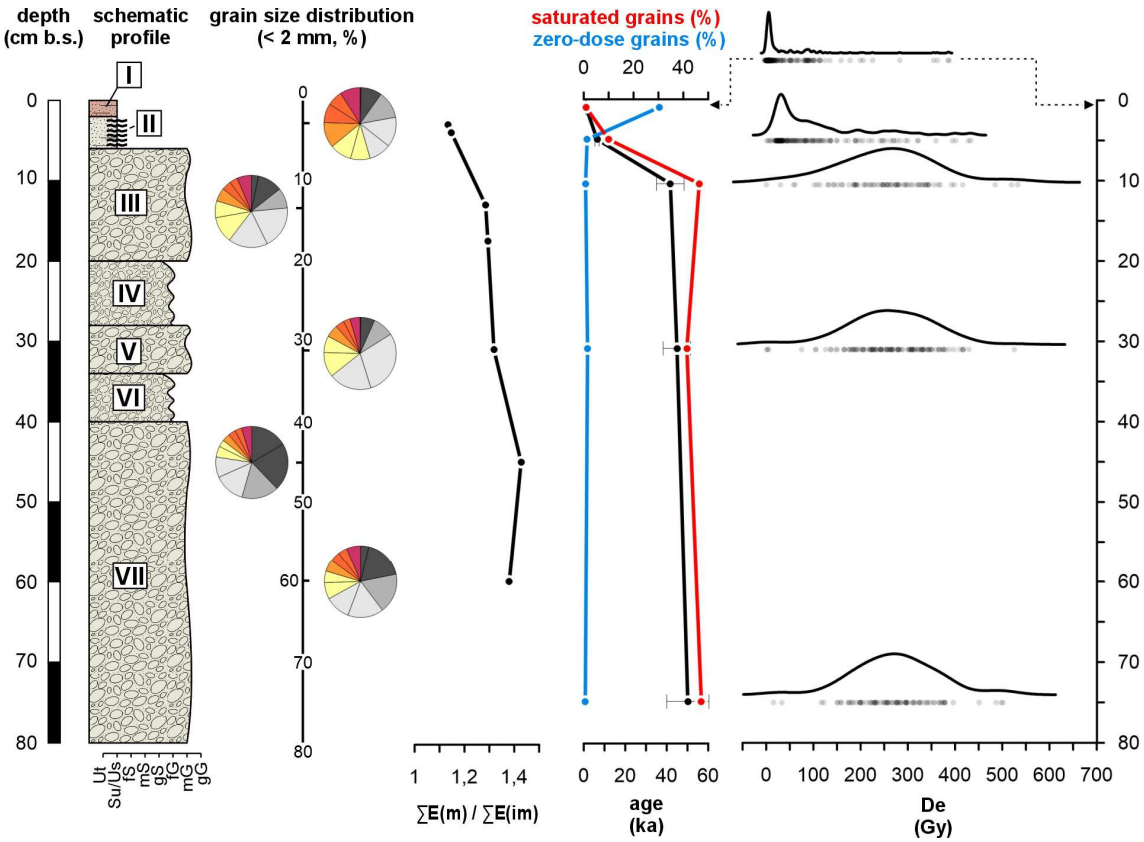

Fig. C8: *Stratigraphic, granulometric, geochemical, and luminescence characteristics of profile* ***P4****. From left to right: schematic lithology; grain size distribution; mobile to immobile elemental ratio ($\sum E_m/\sum E_{im}$); ages (black), saturated grains (red), zero dose grains (blue); D_e distributions. For legend see Fig. C5.*

<u>Sampling site P5 – 1930 m a.s.l.</u>

Sampling site **P5** is situated within an alluvial deposit, oriented perpendicular to the flow direction, at an elevation of roughly 1930 m a.s.l. (Fig. 6.1a, Fig. 6.2e). Thus, **P5** is located in the extremely hyperarid part of the central Atacama Desert, only affected by rare rainfall events. The surface slope in the flow direction is approximately 5°, while the edge of the profile had no visible slope. The alluvial deposits did not exhibit a characteristic fan shape but rather resembled the distal part of a large alluvial plain. The alluvial plain is intersected by the Quebrada Grande fault and two undescribed faults, located approximately 0.5 km, 1.5 km and 2.5 km upstream, respectively. The surface is predominantly covered by grey, though occasionally reddish, angular gravels of varying size (Fig. C9). The dominant gravel size fraction is fine gravel. Nevertheless, larger gravels and scattered larger stones, up to 40 cm in diameter, are also present on the surface. There is no vegetation in the surrounding area. The MAT is approximately below 17 °C with a MAP of 0.0 mm (Quade et al., 2007).

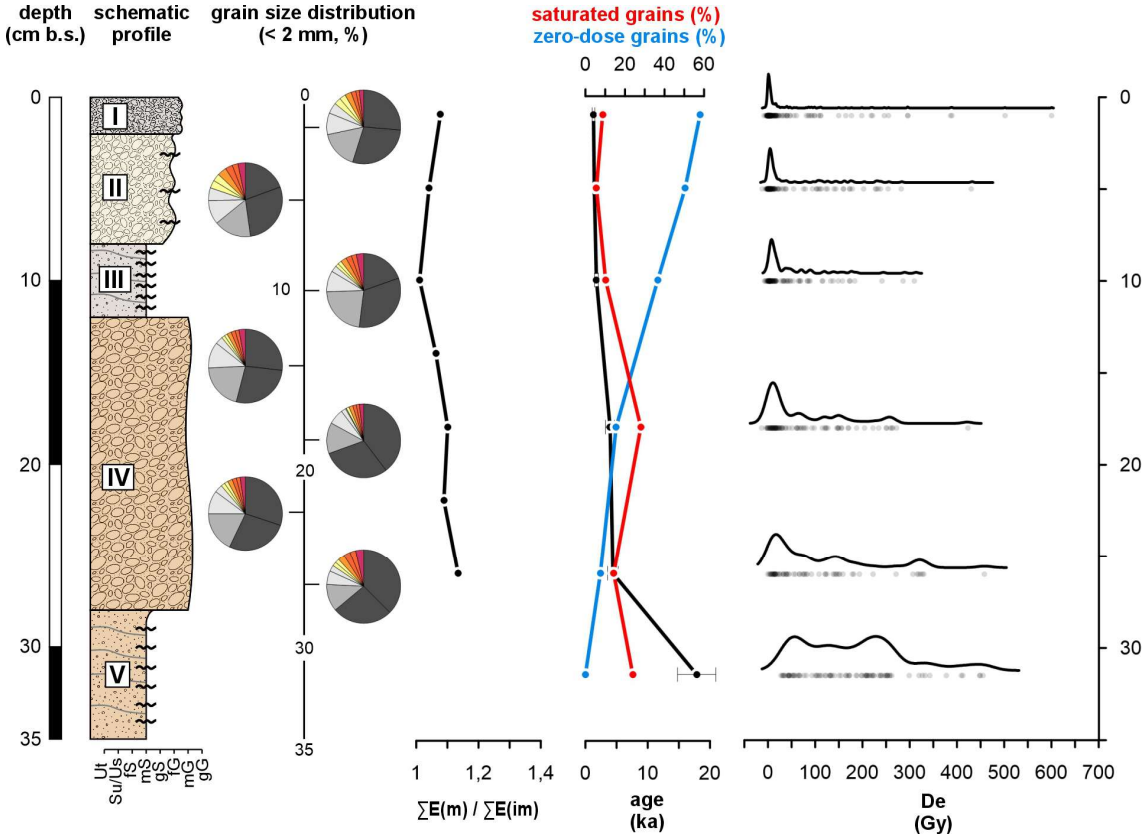

Fig. C9: *Stratigraphic, granulometric, geochemical, and luminescence characteristics of profile* ***P5****. From left to right: schematic lithology; grain size distribution; mobile to immobile elemental ratio ($\sum E_m/\sum E_{im}$); ages (black), saturated grains (red), zero dose grains (blue); D_e distributions. For legend see Fig. C5.*

Below the gravel cover, unit I is primarily composed of a greyish and loose sandy matrix. A clear boundary separates it from unit II, which is noticeably more consolidated and consists of fine gravel within a sandy matrix that contains more silt and clay compared to unit I. The matrix has a pale yellowish to beige colour, and the entire unit is consolidated but displays no visible layering; it crumbles easily under applied pressure. A distinct transition marks the boundary to unit III, which is even more consolidated, free of gravel, and composed exclusively of grey sand-dominated fine material. Laminations are visible throughout this unit. Underlying unit IV consists of fine to medium-sized clasts within a sandy, light brown to reddish matrix. It shows neither layering nor consolidation. Below, laminated and consolidated unit V again lacks gravel components. The clastic material in unit V exhibits the same light brown to red colour and sand-dominated grain size as the material in unit IV. Since below unit V the substrate was too consolidated, it was not possible to collect deeper samples.

Bibliography

The greatest part of knowledge is knowing where to find it.
(unknown)

Adamiec, G., Aitken, M., 1998. Dose-rate conversion factors: update. Ancient TL 16, 37–50.

Aguilar, G., Cabré, A., Fredes, V., Villela, B., 2020. Erosion after an extreme storm event in an arid fluvial system of the southern Atacama Desert: an assessment of the magnitude, return time, and conditioning factors of erosion and debris flow generation. Natural Hazards and Earth System Sciences 20, 1247–1265. https://doi.org/10.5194/nhess-20-1247-2020

Aitken, M.J., 1998. An Introduction to Optical Dating: The Dating of Quaternary Sediments by the Use of Photon-stimulated Luminescence. Oxford University Press, Oxford. https://doi.org/10.1093/oso/9780198540922.001.0001

Aitken, M.J., 1985a. Thermoluminescence Dating. Academic Press, London, United Kingdom.

Aitken, M.J., 1985b. Alpha particle effectiveness: numerical relationship between systems. Ancient TL 3, 22–25. https://doi.org/10.26034/la.atl.1985.095

Aitken, M.J., Bowman, S.G.E., 1975. Thermoluminescent dating: assessment of alpha particle contribution. Archaeometry 17, 132–138. https://doi.org/10.1111/j.1475-4754.1975.tb00127.x

Aitken, M.J., Clark, P.A., Gaffney, C.F., Løvborg, L., 1985. Beta and gamma gradients. Nuclear Tracks and Radiation Measurements (1982) 10, 647–653. https://doi.org/10.1016/0735-245X(85)90071-7

Aitken, M.J., Fleming, S.J., 1972. Thermoluminescent dosimetry in archaeological dating, in: Attix, F.H. (Ed.), Topics in Radiation Dosimetry. Academic Press, London, United Kingdom, pp. 1–78. https://doi.org/10.1016/B978-0-12-066501-3.50006-3

Aitken, M.J., Xie, J., 1990. Moisture correction for annual gamma dose. Ancient TL 8, 6–9. https://doi.org/10.26034/la.atl.1990.157

Aitken, M.J., Zimmerman, D.W., Fleming, S.J., 1968. Thermoluminescent Dating of Ancient Pottery. Nature 219, 442–445. https://doi.org/10.1038/219442a0

Al-Mishwat, A.T., 2016. OXDPPM: A Software to Convert Chemical Elements Between Oxides and Native Elements. Journal of Software Engineering and Applications 9, 561–576. https://doi.org/10.4236/jsea.2016.911038

Alvarez J.A., Jorquera R.B., Miralles C.G., Padel, M., Martínez P.E., 2016. Cartas Punta Posallaves y Sierra Vicuña Mackenna, Región de Antofagasta, Serie Geología Básica 183–184, mapa escala 1:100.000. Servicio Nacional de Geología y Minería, Santiago.

Amundson, R., Richter, D.D., Humphreys, G.S., Jobbágy, E.G., Gaillardet, J., 2007. Coupling between Biota and Earth Materials in the Critical Zone. Elements 3, 327–332. https://doi.org/10.2113/gselements.3.5.327

Anderson, R.S., Repka, J.L., Dick, G.S., 1996. Explicit treatment of inheritance in dating depositional surfaces using in situ ^{10}Be and ^{26}Al. Geology 24, 47–51. https://doi.org/10.1130/0091-7613(1996)024<0047:ETOIID>2.3.CO;2

Arnold, L.J., Roberts, R.G., 2009. Stochastic modelling of multi-grain equivalent dose (D_e) distributions: Implications for OSL dating of sediment mixtures. Quaternary Geochronology 4, 204–230. https://doi.org/10.1016/j.quageo.2008.12.001

Arnold, L.J., Roberts, R.G., Galbraith, R.F., DeLong, S.B., 2009. A revised burial dose estimation procedure for optical dating of young and modern-age sediments. Quaternary Geochronology 4, 306–325. https://doi.org/10.1016/j.quageo.2009.02.017

Bailey, R.M., Arnold, L.J., 2006. Statistical modelling of single grain quartz D_e distributions and an assessment of procedures for estimating burial dose. Quaternary Science Reviews 25, 2475–2502. https://doi.org/10.1016/j.quascirev.2005.09.012

Bailiff, I.K., 2000. Characteristics of time-resolved luminescence in quartz. Radiation Measurements 32, 401–405. https://doi.org/10.1016/S1350-4487(00)00126-8

Bailiff, I.K., Aitken, M.J., 1980. Use of thermoluminescence dosimetry for evaluation of internal beta dose-rate in archaeological dating. Nuclear Instruments and Methods 173, 423–429. https://doi.org/10.1016/0029-554X(80)90802-2

Balescu, S., Lamothe, M., 1994. Comparison of TL and IRSL age estimates of feldspar coarse grains from waterlain sediments. Quaternary Science Reviews 13, 437–444. https://doi.org/10.1016/0277-3791(94)90056-6

Balescu, S., Lamothe, M., 1993. Thermoluminescence dating of the holsteinian marine formation of Herzeele, northern France. Journal of Quaternary Science 8, 117–124. https://doi.org/10.1002/jqs.3390080204

Balian, H.G., Eddy, N.W., 1977. Figure-of-merit (FOM), an improved criterion over the normalized chi-squared test for assessing goodness-of-fit of gamma-ray spectral peaks. Nuclear Instruments and Methods 145, 389–395. https://doi.org/10.1016/0029-554X(77)90437-2

Barbouti, A.I., Rastin, B.C., 1983. A study of the absolute intensity of muons at sea level and under various thicknesses of absorber. Journal of Physics G: Nuclear Physics 9, 1577. https://doi.org/10.1088/0305-4616/9/12/018

Baril, M.R., Huntley, D.J., 2003. Optical excitation spectra of trapped electrons in irradiated feldspars Journal of Physics: Condensed Matter 15, 8011–8027. https://doi.org/10.1088/0953-8984/15/46/017

Barré, M., Lamothe, M., 2010. Luminescence dating of archaeosediments: A comparison of K-feldspar and plagioclase IRSL ages. Quaternary Geochronology 5, 324–328. https://doi.org/10.1016/j.quageo.2009.03.004

Bartz, M., Duval, M., Brill, D., Zander, A., King, G.E., Rhein, A., Walk, J., Stauch, G., Lehmkuhl, F., Brückner, H., 2020a. Testing the potential of K-feldspar pIR-IRSL and quartz ESR for dating coastal alluvial fan complexes in arid environments. Quaternary International 556, 124–143. https://doi.org/10.1016/j.quaint.2020.03.037

Bartz, M., Walk, J., Binnie, S.A., Brill, D., Stauch, G., Lehmkuhl, F., Hoffmeister, D., Brückner, H., 2020b. Late Pleistocene alluvial fan evolution along the coastal Atacama Desert (N Chile). Global and Planetary Change 190, 103091. https://doi.org/10.1016/j.gloplacha.2019.103091

Bateman, M.D., Boulter, C.H., Carr, A.S., Frederick, C.D., Peter, D., Wilder, M., 2007. Detecting post-depositional sediment disturbance in sandy deposits using optical luminescence. Quaternary Geochronology 2, 57–64. https://doi.org/10.1016/j.quageo.2006.05.004

Bateman, M.D., Frederick, C.D., Jaiswal, M.K., Singhvi, A.K., 2003. Investigations into the potential effects of pedoturbation on luminescence dating. Quaternary Science Reviews 22, 1169–1176. https://doi.org/10.1016/S0277-3791(03)00019-2

Bell, W.T., 1980. Alpha dose attenuation in quartz grains for thermoluminescence dating. Ancient TL 4, 4–8. https://doi.org/10.26034/la.atl.1980.039

Berger, G.W., 1990. Effectiveness of natural zeroing of the thermoluminescence in sediments. Journal of Geophysical Research: Solid Earth 95, 12375–12397. https://doi.org/10.1029/JB095iB08p12375

Berger, G.W., Leuternauer, J.L., 1987. Preliminary field work for thermoluminescence dating studies at the Fraser River delta, British Columbia. Current Research, Part A, Geological Survey of Canada Paper 87-1A, 901–904.

Bierman, P.R., Nichols, K.K., 2004. Rock to sediment—Slope to sea with ^{10}Be—Rates of landscape change. Annual Review of Earth and Planetary Sciences 32, 215–255. https://doi.org/10.1146/annurev.earth.32.101802.120539

Blair, T.C., McPherson, J.G., 2009. Processes and Forms of Alluvial Fans, in: Parsons, A.J., Abrahams, A.D. (Eds.), Geomorphology of Desert Environments. Springer Netherlands, Dordrecht, pp. 413–467. https://doi.org/10.1007/978-1-4020-5719-9_14

Blott, S.J., Pye, K., 2001. GRADISTAT: a grain size distribution and statistics package for the analysis of unconsolidated sediments. Earth Surface Processes and Landforms 26, 1237–1248. https://doi.org/10.1002/esp.261

Bonnet, S., Reimann, T., Wallinga, J., Lague, D., Davy, P., Lacoste, A., 2019. Landscape dynamics revealed by luminescence signals of feldspars from fluvial terraces. Scientific reports 9, 8569. https://doi.org/10.1038/s41598-019-44533-4

Bøtter-Jensen, L., Bulur, E., Duller, G.A.T., Murray, A.S., 2000. Advances in luminescence instrument systems. Radiation Measurements 32, 523–528. https://doi.org/10.1016/S1350-4487(00)00039-1

Bøtter-Jensen, L., Duller, G.A.T., Poolton, N.R.J., 1994. Excitation and emission spectrometry of stimulated luminescence from quartz and feldspars. Radiation Measurements 23, 613–616. https://doi.org/10.1016/1350-4487(94)90108-2

Bøtter-Jensen, L., Mejdahl, V., 1988. Assessment of beta dose-rate using a GM multicounter system. International Journal of Radiation Applications and Instrumentation. Part D. Nuclear Tracks and Radiation Measurements 14, 187–191. https://doi.org/10.1016/1359-0189(88)90062-3

Bøtter-Jensen, L., Mejdahl, V., 1985. Determination of potassium in feldspars by beta counting using a GM multicounter system. Nuclear Tracks Radiation Measurements (1982) 10, 663–666. https://doi.org/10.1016/0735-245X(85)90073-0

Bøtter-Jensen, L., Mejdahl, V., Murray, A.S., 1999. New light on OSL. Quaternary Science Reviews 18, 303–309. https://doi.org/10.1016/S0277-3791(98)00063-8

Bøtter-Jensen, L., Thomsen, K.J., Jain, M., 2010. Review of optically stimulated luminescence (OSL) instrumental developments for retrospective dosimetry. Radiation Measurements 45, 253–257. http://dx.doi.org/10.1016/j.radmeas.2009.11.030

Bovis, M.J., Jakob, M., 1999. The role of debris supply conditions in predicting debris flow activity. Earth Surface Processes and Landforms 24, 1039–1054. https://doi.org/10.1002/(SICI)1096-9837(199910)24:11<1039::AID-ESP29>3.0.CO;2-U

Brennan, B.J., 2003. Beta doses to spherical grains. Radiation Measurements 37, 299–303. http://dx.doi.org/10.1016/S1350-4487(03)00011-8

Brennan, B.J., Lyons, R.G., Phillips, S.W., 1991. Attenuation of alpha particle track dose for spherical grains. International Journal of Radiation Applications and Instrumentation. Part D. Nuclear Tracks and Radiation Measurements 18, 249–253. https://doi.org/10.1016/1359-0189(91)90119-3

Brill, D., Reimann, T., Wallinga, J., May, S.M., Engel, M., Riedesel, S., Brückner, H., 2018. Testing the accuracy of feldspar single grains to date late Holocene cyclone and tsunami deposits. Quaternary Geochronology 48, 91–103. https://doi.org/10.1016/j.quageo.2018.09.001

Bulur, E., 1996. An alternative technique for optically stimulated luminescence (OSL) experiment. Radiation Measurements 26, 701–709. https://doi.org/10.1016/S1350-4487(97)82884-3

Bulur, E., Duller, G.A.T., Solongo, S., Bøtter-Jensen, L., Murray, A.S., 2002. LM-OSL from single grains of quartz: a preliminary study. Radiation Measurements 35, 79–85. https://doi.org/10.1016/S1350-4487(01)00256-6

Bureau International des Poids et Mesures, 2024. Le Système international d'unités/The International System of Units, 9th edition. https://doi.org/10.59161/AUEZ1291

Burow, C., 2024a. calc_CentralDose(): Apply the central age model (CAM) after Galbraith et al. (1999) to a given D_e distribution., in: Kreutzer, S., Burow, C., Dietze, M., Fuchs, M.C., Schmidt, C., Fischer, M., Friedrich, J., Mercier, N., Philippe, A., Riedesel, S., Autzen, M., Mittelstrass, D., Gray, H.J., Galharret, J., 2024. Luminescence: Comprehensive Luminescence Dating Data Analysis. R package version 0.9.25.

Burow, C., 2024b. calc_MinDose(): Apply the (un-)logged minimum age model (MAM) after Galbraith et al. (1999) to a given D_e distribution, in: Kreutzer, S., Burow, C., Dietze, M., Fuchs, M.C., Schmidt, C., Fischer, M., Friedrich, J., Mercier, N., Philippe, A., Riedesel, S., Autzen, M., Mittelstrass, D., Gray, H.J., Galharret, J., 2024. Luminescence: Comprehensive Luminescence Dating Data Analysis. R package version 0.9.25.

Burrows, M.T., Schoeman, D.S., Richardson, A.J., Molinos, J.G., Hoffmann, A., Buckley, L.B., Moore, P.J., Brown, C.J., Bruno, J.F., Duarte, C.M., Halpern, B.S., Hoegh-Guldberg, O., Kappel, C.V., Kiessling, W., O'Connor, M.I., Pandolfi, J.M., Parmesan, C., Sydeman, W.J., Ferrier, S., Williams, K.J., Poloczanska, E.S., 2014. Geographical limits to species-range shifts are suggested by climate velocity. Nature 507, 492–495. https://doi.org/10.1038/nature12976

Buylaert, J.-P., Jain, M., Murray, A.S., Thomsen, K.J., Thiel, C., Sohbati, R., 2012. A robust feldspar luminescence dating method for Middle and Late Pleistocene sediments. Boreas 41, 435–451. https://doi.org/10.1111/j.1502-3885.2012.00248.x

Buylaert, J.-P., Murray, A.S., Thomsen, K.J., Jain, M., 2009. Testing the potential of an elevated temperature IRSL signal from K-feldspar. Radiation Measurements 44, 560–565. https://doi.org/10.1016/j.radmeas.2009.02.007

Buylaert, J.-P., Újvári, G., Murray, A.S., Smedley, R.K., Kook, M., 2018. On the relationship between K concentration, grain size and dose in feldspar. Radiation Measurements 120, 181–187. https://doi.org/10.1016/j.radmeas.2018.06.003

Buylaert, J.P., Vandenberghe, D., Murray, A.S., Huot, S., De Corte, F., Van den Haute, P., 2007. Luminescence dating of old (>70 ka) Chinese loess: A comparison of single-aliquot OSL and IRSL techniques. Quaternary Geochronology 2, 9–14. https://doi.org/10.1016/j.quageo.2006.05.028

Cabré, A., Aguilar, G., Mather, A.E., Fredes, V., Riquelme, R., 2020. Tributary-junction alluvial fan response to an ENSO rainfall event in the El Huasco watershed, northern Chile. Progress in Physical Geography: Earth and Environment 44, 679–699. https://doi.org/10.1177/0309133319898994

Canuckguy, 2006. BlankMap-wold.svg. (downloaded on 13. June 2023) https://commons.wikimedia.org/wiki/File:BlankMap-World.svg

Carson, M.A., Kirkby, M.J., 1972. Hillslope Form and Process. Cambridge University Press, Cambridge.

Cereceda, P., Larrain, H., Osses, P., Farías, M., Egaña, I., 2008a. The spatial and temporal variability of fog and its relation to fog oases in the Atacama Desert, Chile. Atmospheric Research 87, 312–323. https://doi.org/10.1016/j.atmosres.2007.11.012

Cereceda, P., Larrain, H., Osses, P., Farías, M., Egaña, I., 2008b. The climate of the coast and fog zone in the Tarapacá Region, Atacama Desert, Chile. Atmospheric Research 87, 301–311. https://doi.org/10.1016/j.atmosres.2007.11.011

Cereceda, P., Osses, P., Larrain, H., Farías, M., Lagos, M., Pinto, R., Schemenauer, R.S., 2002. Advective, orographic and radiation fog in the Tarapacá region, Chile. Atmospheric Research 64, 261–271. https://doi.org/10.1016/S0169-8095(02)00097-2

Chen, Q., Li, Z., Dong, S., Yu, Q., Zhang, C., Yu, X., 2021. Applicability of chemical weathering indices of eolian sands from the deserts in northern China. CATENA 198, 105032. https://doi.org/10.1016/j.catena.2020.105032

Clark, R.J., Bailiff, I.K., Tooley, M.J., 1997. A preliminary study of time-resolved luminescence in some feldspars. Radiation Measurements 27, 211–220. https://doi.org/10.1016/S1350-4487(96)00123-0

Clark, R.J., Sanderson, D.C.W., 1994. Photostimulated luminescence excitation spectroscopy of feldspars and micas. Radiation Measurements 23, 641–646. https://doi.org/10.1016/1350-4487(94)90113-9

Colarossi, D., Duller, G.A.T., Roberts, H.M., 2018. Exploring the behaviour of luminescence signals from feldspars: Implications for the single aliquot regenerative dose protocol. Radiation Measurements 109, 35–44. https://doi.org/10.1016/j.radmeas.2017.07.005

Cordier, S., Frechen, M., Tsukamoto, S., 2010. Methodological Aspects on Luminescence Dating of Fluvial Sands from the Moselle Basin, Luxembourg. Geochronometria 35, 67–74. https://doi.org/10.2478/v10003-010-0006-4

Corenblit, D., Baas, A.C.W., Bornette, G., Darrozes, J., Delmotte, S., Francis, R.A., Gurnell, A.M., Julien, F., Naiman, R.J., Steiger, J., 2011. Feedbacks between geomorphology and biota controlling Earth surface processes and landforms: A review of foundation concepts and current understandings. Earth-Science Reviews 106, 307–331. https://doi.org/10.1016/j.earscirev.2011.03.002

Cunningham, A.C., Wallinga, J., Hobo, N., Versendaal, A.J., Makaske, B., Middelkoop, H., 2015. Re-evaluating luminescence burial doses and bleaching of fluvial deposits using Bayesian computational statistics. Earth Surface Dynamics 3, 55–65. https://doi.org/10.5194/esurf-3-55-2015

Daniels, F., Boyd, C.A., Saunders, D.F., 1953. Thermoluminescence as a Research Tool. Science 117, 343–349. https://doi.org/10.1126/science.117.3040.343

Davis, W.M., 1938. Sheetfloods and streamfloods. GSA Bulletin 49, 1337–1416. https://doi.org/10.1130/GSAB-49-1337

De Corte, F., Vandenberghe, D., Hossain, S.M., De Wispelaere, A., Buylaert, J.-P., Van den Haute, P., 2007. Preparation and characterization of loess sediment for use as a reference material in the annual radiation dose determination for

luminescence dating. Journal of Radioanalytical and Nuclear Chemistry 272, 311–319. https://doi.org/10.1007/s10967-007-0522-5

de Haas, T., Ventra, D., Carbonneau, P.E., Kleinhans, M.G., 2014. Debris-flow dominance of alluvial fans masked by runoff reworking and weathering. Geomorphology 217, 165–181. https://doi.org/10.1016/j.geomorph.2014.04.028

de Porras, M.E., Maldonado, A., De Pol-Holz, R., Latorre, C., Betancourt, J.L., 2017. Late Quaternary environmental dynamics in the Atacama Desert reconstructed from rodent midden pollen records. Journal of Quaternary Science 32, 665–684. https://doi.org/10.1002/jqs.2980

Deer, W.A., Howie, R.A., Zussman, J., 2013. An Introduction to the Rock-Forming Minerals (3rd Edition). Mineralogical Society of Great Britain and Ireland, London, United Kingdom. https://doi.org/10.1180/DHZ

del Río, C., Garcia, J.-L., Osses, P., Zanetta, N., Lambert, F., Rivera, D., Siegmund, A., Wolf, N., Cereceda, P., Larraín, H., Lobos, F., 2018. ENSO Influence on Coastal Fog-Water Yield in the Atacama Desert, Chile. Aerosol and Air Quality Research 18, 127–144. https://doi.org/10.4209/aaqr.2017.01.0022

Del Río, I., Sawakuchi, A.O., González, G., 2019. Luminescence dating of sediments from central Atacama Desert, northern Chile. Quaternary Geochronology 53, 101002. https://doi.org/10.1016/j.quageo.2019.05.001

Díaz, F.P., Latorre, C., Maldonado, A., Quade, J., Betancourt, J.L., 2012. Rodent middens reveal episodic, long-distance plant colonizations across the hyperarid Atacama Desert over the last 34,000 years. Journal of Biogeography 39, 510–525. https://doi.org/10.1111/j.1365-2699.2011.02617.x

Diederich, J.L., Wennrich, V., Bao, R., Büttner, C., Bolten, A., Brill, D., Buske, S., Campos, E., Fernández-Galego, E., Gödickmeier, P., Ninnemann, L., Reyers, M., Ritter, B., Ritterbach, L., Rolf, C., Scheidt, S., Dunai, T.J., Melles, M., 2020. A 68 ka precipitation record from the hyperarid core of the Atacama Desert in northern Chile. Global and Planetary Change 184, 103054. https://doi.org/10.1016/j.gloplacha.2019.103054

Dietrich, W.E., Perron, J.T., 2006. The search for a topographic signature of life. Nature 439, 411–418. https://doi.org/10.1038/nature04452

Dietze, M., Dietze, E., Lomax, J., Fuchs, M., Kleber, A., Wells, S.G., 2016. Environmental history recorded in aeolian deposits under stone pavements, Mojave Desert, USA. Quaternary Research 85, 4–16. https://doi.org/10.1016/j.yqres.2015.11.007

Ditlefsen, C., 1992. Bleaching of K-feldspars in turbid water suspensions: A comparison of photo- and thermoluminescence signals. Quaternary Science Reviews 11, 33–38. https://doi.org/10.1016/0277-3791(92)90039-B

DTU Physics, 2021. Risø Manual “Guide to the Risø TL/OSL Reader.”. Technical University of Denmark, Roskilde, Denmark.

Duller, G., 2008a. Luminescence Dating. Guidelines on using luminescence dating in archaeology. English Heritage.

Duller, G., 2008b. Single-grain optical dating of Quaternary sediments: why aliquot size matters in luminescence dating. Boreas 37, 589–612. https://doi.org/10.1111/j.1502-3885.2008.00051.x

Duller, G.A.T., 1994. Luminescence dating of poorly bleached sediments from Scotland. Quaternary Science Reviews 13, 521–524. https://doi.org/10.1016/0277-3791(94)90070-1

Duller, G.A.T., 1992. Luminescence chronology of raised marine terraces, south-west north island, New Zealand. Dissertation. University of Wales, Aberystwyth, Wales.

Dunai, T.J., López, G.A.G., Juez-Larré, J., 2005. Oligocene–Miocene age of aridity in the Atacama Desert revealed by exposure dating of erosion-sensitive landforms. Geology 33, 321–324. https://doi.org/10.1130/G21184.1

Dunai, T.J., Melles, M., Quandt, D., Knief, C., Amelung, W., 2020. Whitepaper: Earth – Evolution at the dry limit. Global and Planetary Change 193, 103275. https://doi.org/10.1016/j.gloplacha.2020.103275

Durcan, J.A., 2021. Luminescence Dating, in: Alderton, D., Scott, A.E. (Eds.), Encyclopedia of Geology (2nd Edition). Academic Press, London, pp. 164–174. https://doi.org/10.1016/B978-0-12-409548-9.12105-0

Durcan, J.A., King, G.E., Duller, G.A.T., 2015. DRAC: Dose Rate and Age Calculator for trapped charge dating. Quaternary Geochronology 28, 54–61. https://doi.org/10.1016/j.quageo.2015.03.012

Duval, M., Guilarte, V., Campaña, I., Arnold, L.J., Miguens, L., Iglesias, J., González-Sierra, S., 2018. Quantifying hydrofluoric acid etching of quartz and feldspar coarse grains based on weight loss estimates: implication for ESR and luminescence dating studies. Ancient TL 36, 1–14. https://doi.org/10.26034/la.atl.2018.522

Ericksen, G.E., 1981. Geology and origin of the Chilean nitrate deposits (Professional Paper No. 1188), Geological Survey professional paper. United States Geological Survey, Washington (D.C.).

Escribano, J.A., Martínez, P.E., Domagala, J.P., Padel, M., Espinoza, M.V., Jorquera, R.B., Contreras, J.P.F., De La Cruz, R.S., Calderón, M.N., 2013. Cartas Bahía Isla Blanca y Taltal, Región de Antofagasta, Serie Geología Básica 164–165, mapa escala 1:100.000. Servicio Nacional de Geología y Minería, Santiago.

Evenstar, L.A., Mather, A.E., Hartley, A.J., Stuart, F.M., Sparks, R.S.J., Cooper, F.J., 2017. Geomorphology on geologic timescales: Evolution of the late Cenozoic Pacific paleosurface in Northern Chile and Southern Peru. Earth-Science Reviews 171, 1–27. https://doi.org/10.1016/j.earscirev.2017.04.004

Ewing, S.A., Sutter, B., Owen, J., Nishiizumi, K., Sharp, W., Cliff, S.S., Perry, K., Dietrich, W., McKay, C.P., Amundson, R., 2006. A threshold in soil formation at Earth's arid–hyperarid transition. Geochimica et Cosmochimica Acta 70, 5293–5322. https://doi.org/10.1016/j.gca.2006.08.020

Fano, U., 1954. Note on the Bragg-Gray Cavity Principle for Measuring Energy Dissipation. Radiation Research 1, 237. https://doi.org/10.2307/3570368

Finch, A.A., Klein, J., 1999. The causes and petrological significance of cathodo-luminescence emissions from alkali feldspars. Contributions to Mineralogy and Petrology 135, 234–243. https://doi.org/10.1007/s004100050509

Fitzsimmons, K.E., Rhodes, E.J., Barrows, T.T., 2010. OSL dating of southeast Australian quartz: A preliminary assessment of luminescence characteristics and behaviour. Quaternary Geochronology 5, 91–95. https://doi.org/10.1016/j.quageo.2009.02.009

Fleming, S., 1969. Unpublished D. Phil. thesis, Oxford University, Oxford, United Kingdom.

Fleming, S.J., 1966. Study of Thermoluminescence of Crystalline Extracts from Pottery. Archaeometry 9, 170–173. https://doi.org/10.1111/j.1475-4754.1966.tb00916.x

Folk, R.L., Ward, W.C., 1957. Brazos River bar [Texas]; a study in the significance of grain size parameters. Journal of Sedimentary Research 27, 3–26. https://doi.org/10.1306/74D70646-2B21-11D7-8648000102C1865D

Fuchs, M., Owen, L.A., 2008. Luminescence dating of glacial and associated sediments: review, recommendations and future directions. Boreas 37, 636–659. https://doi.org/10.1111/j.1502-3885.2008.00052.x

Galbraith, R.F., Green, P.F., 1990. Estimating the component ages in a finite mixture. International Journal of Radiation Applications and Instrumentation. Part D. Nuclear Tracks and Radiation Measurements 17, 197–206. https://doi.org/10.1016/1359-0189(90)90035-V

Galbraith, R.F., Roberts, R.G., 2012. Statistical aspects of equivalent dose and error calculation and display in OSL dating: An overview and some recommendations. Quaternary Geochronology 11, 1–27. https://doi.org/10.1016/j.quageo.2012.04.020

Galbraith, R.F., Roberts, R.G., Laslett, G.M., Yoshida, H., Olley, J.M., 1999. Optical dating of single and multiple grains of quartz from Jinmium rock shelter, northern Australia: Part I, Experimental Design and Statisctical Models. Archaeometry 41, 339–364. https://doi.org/10.1111/j.1475-4754.1999.tb00987.x

Garcia-Guinea, J., Townsend, P.D., Sanchez-Muñoz, L., Rojo, J.M., 1999. Ultraviolet-blue ionic luminescence of alkali feldspars from bulk and interfaces. Physics and Chemistry of Minerals 26, 658–667. https://doi.org/10.1007/s002690050231

Garreaud, R., 1999. Multiscale Analysis of the Summertime Precipitation over the Central Andes. Monthly Weather Review 127, 901–921. https://doi.org/10.1175/1520-0493(1999)127<0901:MAOTSP>2.0.CO;2

Garreaud, R., Barichivich, J., Christie, D.A., Maldonado, A., 2008. Interannual variability of the coastal fog at Fray Jorge relict forests in semiarid Chile. Journal of Geophysical Research: Biogeosciences 113, G04011. https://doi.org/10.1029/2008JG000709

Garreaud, R.D., Molina, A., Farias, M., 2010. Andean uplift, ocean cooling and Atacama hyperaridity: A climate modeling perspective. Earth and Planetary Science Letters 292, 39–50. https://doi.org/10.1016/j.epsl.2010.01.017

Gayo, E.M., Latorre, C., Jordan, T.E., Nester, P.L., Estay, S.A., Ojeda, K.F., Santoro, C.M., 2012. Late Quaternary hydrological and ecological changes in the hyperarid core of the northern Atacama Desert (~21°S). Earth-Science Reviews 113, 120–140. https://doi.org/10.1016/j.earscirev.2012.04.003

Gayo, E.M., Lima, M., Gurruchaga, A., Estay, S.A., Santoro, C.M., Latorre, C., McRostie, V., 2023. Towards understanding human–environment feedback loops: the Atacama Desert case. Philosophical Transactions of the Royal Society, B: Biological Sciences 379, 20220253. https://doi.org/10.1098/rstb.2022.0253

Geake, J.E., Walker, G., Mills, A.A., Garlick, G.F.J., 1972. Luminescence of lunar material excited by electrons. Proceedings of the Third Lunar Science Conference 3, 2971–2977.

Giardino, J.R., Houser, C., 2015. Principles and dynamics of the critical zone, Developments in earth surface processes (Vol. 19). Elsevier, Amsterdam, Netherlands.

Gillespie, R.G., Roderick, G.K., 2014. Geology and climate drive diversification. Nature 509, 297–298. https://doi.org/10.1038/509297a

Gliganic, L.A., Cohen, T.J., Slack, M., Feathers, J.K., 2016. Sediment mixing in aeolian sandsheets identified and quantified using single-grain

optically stimulated luminescence. Quaternary Geochronology 32, 53–66. https://doi.org/10.1016/j.quageo.2015.12.006

Gliganic, L.A., May, J.-H., Cohen, T.J., 2015. All mixed up: Using single-grain equivalent dose distributions to identify phases of pedogenic mixing on a dryland alluvial fan. Quaternary International 362, 23–33. https://doi.org/10.1016/j.quaint.2014.07.040

Godfrey-Smith, D.I., Huntley, D.J., Chen, W.-H., 1988. Optical dating studies of quartz and feldspar sediment extracts. Quaternary Science Reviews 7, 373–380. https://doi.org/10.1016/0277-3791(88)90032-7

Gonzales, F.N., Craven, D., Armesto, J.J., 2023. Islands in the mist: A systematic review of the coastal lomas of South America. Journal of Arid Environments 211, 104942. https://doi.org/10.1016/j.jaridenv.2023.104942

González, A.L., Fariña, J.M., Pinto, R., Pérez, C., Weathers, K.C., Armesto, J.J., Marquet, P.A., 2011. Bromeliad growth and stoichiometry: responses to atmospheric nutrient supply in fog-dependent ecosystems of the hyper-arid Atacama Desert, Chile. Oecologia 167, 835–845. https://doi.org/10.1007/s00442-011-2032-y

González-Pinilla, F.J., Latorre, C., Rojas, M., Houston, J., Rocuant, M.I., Maldonado, A., Santoro, C.M., Quade, J., Betancourt, J.L., 2021. High- and low-latitude forcings drive Atacama Desert rainfall variations over the past 16,000 years. Science Advances 7, eabg1333. https://doi.org/10.1126/sciadv.abg1333

Gray, H.J., Jain, M., Sawakuchi, A.O., Mahan, S.A., Tucker, G.E., 2019. Luminescence as a Sediment Tracer and Provenance Tool. Reviews of Geophysics 57, 987–1017. https://doi.org/10.1029/2019RG000646

Grögler, N., Houtermans, F.G., Stauffer, H., 1960. Über die Datierung von Keramik und Ziegel durch Thermolumineszenz. Helvetica Physica Acta 33, 595–596.

Grosjean, M., van Leeuwen, J.F.N., van der Knaap, W.O., Geyh, M.A., Ammann, B., Tanner, W., Messerli, B., Núñez, L.A., Valero-Garcés, B.L., Veit, H., 2001. A 22,000 14C year BP sediment and pollen record of climate change from Laguna Miscanti (23°S), northern Chile. Global and Planetary Change 28, 35–51. https://doi.org/10.1016/S0921-8181(00)00063-1

Guérin, G., Mercier, N., Adamiec, G., 2011. Dose-rate conversion factors: update. Ancient TL 29, 5–8.

Guérin, G., Mercier, N., Nathan, R., Adamiec, G., Lefrais, Y., 2012. On the use of the infinite matrix assumption and associated concepts: A critical review. Radiation Measurements 47, 778–785. https://doi.org/10.1016/j.radmeas.2012.04.004

Guerrero, P.C., Rosas, M., Arroyo, M.T.K., Wiens, J.J., 2013. Evolutionary lag times and recent origin of the biota of an ancient desert (Atacama–Sechura). Proceedings of the National Academy of Sciences 110, 11469–11474. https://doi.org/10.1073/pnas.1308721110

Guibert, P., Christophe, C., Urbanová, P., Guérin, G., Blain, S., 2017. Modeling incomplete and heterogeneous bleaching of mobile grains partially exposed to the light: Towards a new tool for single grain OSL dating of poorly bleached mortars. Radiation Measurements 107, 48–57. https://doi.org/10.1016/j.radmeas.2017.10.003

Guralnik, B., Jain, M., Herman, F., Ankjærgaard, C., Murray, A.S., Valla, P.G., Preusser, F., King, G.E., Chen, R., Lowick, S.E., Kook, M., Rhodes, E.J., 2015. OSL-

thermochronometry of feldspar from the KTB borehole, Germany. Earth and Planetary Science Letters 423, 232–243. https://doi.org/10.1016/j.epsl.2015.04.032

Hartley, A.J., Chong, G., 2002. Late Pliocene age for the Atacama Desert: Implications for the desertification of western South America. Geology 30, 43–46. https://doi.org/10.1130/0091-7613(2002)030<0043:LPAFTA>2.0.CO;2

Hartley, A.J., Mather, A.E., Jolley, E., Turner, P., 2005. Climatic controls on alluvial-fan activity, Coastal Cordillera, northern Chile, in: Harvey, A.M., Mather, A.E., Stokes, M. (Eds.), Alluvial Fans: Geomorphology, Sedimentology, Dynamics. The Geological Society of London, London, Special Publications, 251, pp. 95–115.

Harvey, A., 2011. Dryland Alluvial Fans, in: Thomas, D.S.G. (Ed.), Arid Zone Geomorphology: Process, Form and Change in Drylands (3rd Edition). Wiley, Chichester, pp. 333–371. https://doi.org/10.1002/9780470710777.ch14

Harvey, Adrian M., Mather, Anne E., Stokes, Martin, 2005. Alluvial fans: geomorphology, sedimentology, dynamics – introduction. A review of alluvial-fan research, in: Harvey, A. M., Mather, A. E., Stokes, M. (Eds.), Alluvial Fans: Geomorphology, Sedimentology, Dynamics. Geological Society of London, London, Special Publications, 251, pp. 1-7. https://doi.org/10.1144/GSL.SP.2005.251.01.01

Harvey, A.M., 1984. Debris Flows and Fluvial Deposits in Spanish Quaternary Alluvial Fans: Implications for Fan Morphology, in: Koster, E.H., Steel, R.J. (Eds.), Sedimentology of Gravels and Conglomerates. Geological Association of Canada, Special Publication 10, pp.123–132.

Haug, E.W., Kraal, E.R., Sewall, J.O., Van Dijk, M., Diaz, G.C., 2010. Climatic and geomorphic interactions on alluvial fans in the Atacama Desert, Chile. Geomorphology 121, 184–196. https://doi.org/10.1016/j.geomorph.2010.04.005

Heimsath, A.M., Chappell, J., Spooner, N.A., Questiaux, D.G., 2002. Creeping soil. Geology 30, 111–114. https://doi.org/10.1130/0091-7613(2002)030<0111:CS>2.0.CO;2

Hervé, M., 1987. Movimiento sinistral en el Cretácico Inferior de la Zona de Falla de Atacama al norte de Paposo (24°S), Chile. Revista Geológica de Chile 14, 37–42.

Hoffmeister, D., 2018a. Meteorological and soil measurements of the permanent basic weather station 31 - Caleta Sur de Punta Grande, Chile. CRC1211 Database. https://doi.org/10.5880/CRC1211DB.13

Hoffmeister, D., 2018b. Meteorological and soil measurements of the permanent basic weather station 32 - Quebrada Matancilla, Chile. CRC1211 Database. https://doi.org/10.5880/CRC1211DB.14

Hoffmeister, D., 2018c. Meteorological and soil measurements of the permanent master weather station 33 - Quebrada Grande, Chile. CRC1211 Database. https://doi.org/10.5880/CRC1211DB.15

Hoffmeister, D., 2018d. Meteorological and soil measurements of the permanent basic weather station 24 - Quebrada de Aroma, Chile. CRC1211 Database. https://doi.org/10.5880/CRC1211DB.11

Hoffmeister, D., 2018e. Meteorological and soil measurements of the permanent basic weather station 25 - Quebrada de Soga, Chile. CRC1211 Database. https://doi.org/10.5880/CRC1211DB.12

Hogg, S.E., 1982. Sheetfloods, sheetwash, sheetflow, or ...?. Earth-Science Reviews 18, 59–76. https://doi.org/10.1016/0012-8252(82)90003-4

Houston, J., 2006a. Variability of precipitation in the Atacama Desert: its causes and hydrological impact. International Journal of Climatology 26, 2181–2198. https://doi.org/10.1002/joc.1359

Houston, J., 2006b. Evaporation in the Atacama Desert: An empirical study of spatio-temporal variations and their causes. Journal of Hydrology 330, 402–412. https://doi.org/10.1016/j.jhydrol.2006.03.036

Houston, J., Hartley, A.J., 2003. The central Andean west-slope rainshadow and its potential contribution to the origin of hyper-aridity in the Atacama Desert. International Journal of Climatology 23, 1453–1464. https://doi.org/10.1002/joc.938

Houtermans, F.G., Jäger, E., Schön, M., Stauffer, H., 1957. Messungen der Thermolumineszenz als Mittel zur Untersuchung der thermischen und der Strahlungsgeschichte von natürlichen Mineralien und Gesteinen. Annalen der Physik 455, 283–292. https://doi.org/10.1002/andp.19574550129

Hülle, D., Hilgers, A., Kühn, P., Radtke, U., 2009. The potential of optically stimulated luminescence for dating periglacial slope deposits — A case study from the Taunus area, Germany. Geomorphology 109, 66–78. http://dx.doi.org/10.1016/j.geomorph.2008.08.021

Huntley, D.J., Baril, M.R., 1997. The K content of the K-feldspars being measured in optical dating or in thermoluminescence dating. Ancient TL 15, 11-13.

Huntley, D.J., Godfrey-Smith, D.I., Haskell, E.H., 1991. Light-induced emission spectra from some quartz and feldspars. International Journal of Radiation Applications and Instrumentation. Part D. Nuclear Tracks and Radiation Measurements 18, 127–131. https://doi.org/10.1016/1359-0189(91)90104-P

Huntley, D.J., Godfrey-Smith, D.I., Thewalt, M.L.W., 1985. Optical dating of sediments. Nature 313, 105–107. https://doi.org/10.1038/313105a0

Huntley, D.J., Hancock, R.G.V., 2001. The Rb contents of the K-feldspar grains being measured in optical dating. Ancient TL 19, 43–46.

Huntley, D.J., Lamothe, M., 2001. Ubiquity of anomalous fading in K-feldspars and the measurement and correction for it in optical dating. Canadian Journal of Earth Sciences 38, 1093–1106. https://doi.org/10.1139/e01-013

Huntley, D.J., Lian, O.B., 2006. Some observations on tunnelling of trapped electrons in feldspars and their implications for optical dating. Quaternary Science Reviews 25, 2503–2512. https://doi.org/10.1016/j.quascirev.2005.05.011

Hütt, G., Jaek, I., Tchonka, J., 1988. Optical dating: K-feldspars optical response stimulation spectra. Quaternary Science Reviews 7, 381–385. https://doi.org/10.1016/0277-3791(88)90033-9

Jaeschke, A., Böhm, C., Schween, J.H., Schefuß, E., Koch, M.A., Latorre, C., Contreras, S., Rethemeyer, J., Wissel, H., Lücke, A., 2024. Evaluating the isotopic composition of leaf organic compounds in fog-dependent Tillandsia landbeckii across the coastal Atacama Desert: Implications for hydroclimate reconstructions at the dry limit. Global and Planetary Change 235, 104393. https://doi.org/10.1016/j.gloplacha.2024.104393

Jain, M., 2009. Extending the dose range: Probing deep traps in quartz with 3.06 eV photons. Radiation Measurements 44, 445–452.

Jain, M., Ankjærgaard, C., 2011. Towards a non-fading signal in feldspar: Insight into charge transport and tunnelling from time-resolved

optically stimulated luminescence. Radiation Measurements 46, 292–309. https://doi.org/10.1016/j.radmeas.2010.12.004

Jara, I.A., Maldonado, A., Eugenia de Porras, M., 2020. Late Holocene dynamics of the south American summer monsoon: New insights from the Andes of northern Chile (21°S). Quaternary Science Reviews 246, 106533. https://doi.org/10.1016/j.quascirev.2020.106533

Jenny, H., 1994. Factors of Soil Formation: A System of Quantitative Pedology. Courier Corporation, New York, USA.

Jungers, M.C., Heimsath, A.M., Amundson, R., Balco, G., Shuster, D., Chong, G., 2013. Active erosion–deposition cycles in the hyperarid Atacama Desert of Northern Chile. Earth and Planetary Science Letters 371–372, 125–133. https://doi.org/10.1016/j.epsl.2013.04.005

Kanaya, K., Okayama, S., 1972. Penetration and energy-loss theory of electrons in solid targets. Journal of Physics D: Applied Physics 5, 43–58. https://doi.org/10.1088/0022-3727/5/1/308

Kars, R.H., Poolton, N.R.J., Jain, M., Ankjærgaard, C., Dorenbos, P., Wallinga, J., 2013. On the trap depth of the IR-sensitive trap in Na- and K-feldspar. Radiation Measurements 59, 103–113. https://doi.org/10.1016/j.radmeas.2013.05.002

Kars, R.H., Reimann, T., Wallinga, J., 2014. Are feldspar SAR protocols appropriate for post-IR IRSL dating? Quaternary Geochronology 22, 126–136. https://doi.org/10.1016/j.quageo.2014.04.001

Kendall, M.G., Kendall, S.F.H., Smith, B.B., 1939. The Distribution of Spearman's Coefficient of Rank Correlation in a Universe in which all Rankings Occur an Equal Number of Times. Biometrika 30, 251–273. https://doi.org/10.2307/2332649

Kennedy, G.C., Knopff, L., 1960. Dating by thermoluminescence. Archaeology 13, 147–148.

Knoll, G.F., 2000. Radiation detection and measurement (3rd Edition). Wiley, New York.

Kook, M.H., Murray, A.S., Lapp, T., Denby, P.H., Ankjærgaard, C., Thomsen, K., Jain, M., Choi, J.H., Kim, G.H., 2011. A portable luminescence dating instrument. Nuclear Instruments and Methods in Physics Research Section B: Beam Interactions with Materials and Atoms 269, 1370–1378. https://doi.org/10.1016/j.nimb.2011.03.014

Krbetschek, M.R., Götze, J., Dietrich, A., Trautmann, T., 1997. Spectral information from minerals relevant for luminescence dating. Radiation Measurements 27, 695–748. https://doi.org/10.1016/S1350-4487(97)00223-0

Krbetschek, M.R., Rieser, U., Stolz, W., 1996. Optical Dating: Some Luminescence Properties of Natural Feldspars. Radiation Protection Dosimetry 66, 407–412. https://doi.org/10.1093/oxfordjournals.rpd.a031765

Kreutzer, S., Burow, C., Dietze, M., Fuchs, M.C., Schmidt, C., Fischer, M., Friedrich, J., Mercier, N., Philippe, A., Riedesel, S., Autzen, M., Mittelstrass, D., Gray, H.J., Galharret, J.-M., Colombo, M., Steinbuch, L., De Boer, A.-M., 2012. Luminescence: Comprehensive Luminescence Dating Data Analysis. https://doi.org/10.32614/CRAN.package.Luminescence

Laity, J.E., 2011. Pavements and Stone Mantles, in: Thomas, D.S.G. (Ed.), Arid Zone Geomorphology: Process, Form and Change in Drylands (3rd Edition). Wiley, Chichester, pp. 181–207. https://doi.org/10.1002/9780470710777.ch9

Lambert, R., 2018. Investigating thermal decay in K-feldspar for the application of IRSL thermochronometry on the Mont Blanc massif. Dissertation. University of Lausanne, Lausanne.

Lapp, T., Jain, M., Thomsen, K.J., Murray, A.S., Buylaert, J.-P., 2012. New luminescence measurement facilities in retrospective dosimetry. Radiation Measurements 47, 803–808. https://doi.org/10.1016/j.radmeas.2012.02.006

Latorre, C., Betancourt, J.L., Rylander, K.A., Quade, J., 2002. Vegetation invasions into absolute desert: A 45 000 yr rodent midden record from the Calama–Salar de Atacama basins, northern Chile (lat 22°–24°S). GSA Bulletin 114, 349–366. https://doi.org/10.1130/0016-7606(2002)114<0349:VIIADA>2.0.CO;2

Latorre, C., González, A.L., Quade, J., Fariña, J.M., Pinto, R., Marquet, P.A., 2011. Establishment and formation of fog-dependent Tillandsia landbeckii dunes in the Atacama Desert: Evidence from radiocarbon and stable isotopes. Journal of Geophysical Research: Biogeosciences 116. https://doi.org/10.1029/2010JG001521

Latorre, C., Santoro, C.M., Ugalde, P.C., Gayo, E.M., Osorio, D., Salas-Egaña, C., De Pol-Holz, R., Joly, D., Rech, J.A., 2013. Late Pleistocene human occupation of the hyperarid core in the Atacama Desert, northern Chile. Quaternary Science Reviews 77, 19–30. https://doi.org/10.1016/j.quascirev.2013.06.008

Lauer, T., Krbetschek, M., Mauz, B., Frechen, M., 2012. Yellow stimulated luminescence from potassium feldspar: Observations on its suitability for dating. Radiation Measurements 47, 974–980. https://doi.org/10.1016/j.radmeas.2012.08.002

Lehmkuhl, F., Owen, L.A., 2024. Alluvial fan types, distribution, and formation: a global perspective. Zeitschrift für Geomorphologie 64, 95–142. https://doi.org/10.1127/zfg/2024/0826

Li, B., Jacobs, Z., Roberts, R.G., 2016. Investigation of the applicability of standardised growth curves for OSL dating of quartz from Haua Fteah cave, Libya. Quaternary Geochronology 35, 1–15. https://doi.org/10.1016/j.quageo.2016.05.001

Li, B., Jacobs, Z., Roberts, R.G., Galbraith, R., Peng, J., 2017. Variability in quartz OSL signals caused by measurement uncertainties: Problems and solutions. Quaternary Geochronology 41, 11–25. https://doi.org/10.1016/j.quageo.2017.05.006

Li, B., Jacobs, Z., Roberts, R.G., Li, S.-H., 2018. Single-grain dating of potassium-rich feldspar grains: Towards a global standardised growth curve for the post-IR IRSL signal. Quaternary Geochronology 45, 23–36. https://doi.org/10.1016/j.quageo.2018.02.001

Li, B., Li, S.-H., 2011. Luminescence dating of K-feldspar from sediments: A protocol without anomalous fading correction. Quaternary Geochronology 6, 468–479. https://doi.org/10.1016/j.quageo.2011.05.001

Li, B., Li, S.-H., Wintle, A.G., Zhao, H., 2008. Isochron dating of sediments using luminescence of K-feldspar grains. Journal of Geophysical Research: Earth Surface 113. https://doi.org/10.1029/2007JF000900

Li, B., Roberts, R.G., Jacobs, Z., Li, S.-H., 2015a. Potential of establishing a 'global standardised growth curve' (gSGC) for optical dating of quartz from sediments. Quaternary Geochronology 27, 94–104. https://doi.org/10.1016/j.quageo.2015.02.011

Li, B., Roberts, R.G., Jacobs, Z., Li, S.-H., Guo, Y.-J., 2015b. Construction of a 'global standardised growth curve' (gSGC) for infrared stimulated

luminescence dating of K-feldspar. Quaternary Geochronology 27, 119–130. https://doi.org/10.1016/j.quageo.2015.02.010

Li, S.-H., Wintle, A.G., 1992. Luminescence sensitivity change due to bleaching of sediments. International Journal of Radiation Applications and Instrumentation. Part D. Nuclear Tracks and Radiation Measurements 20, 567–573. https://doi.org/10.1016/1359-0189(92)90006-H

Lian, O.B., Roberts, R.G., 2006. Dating the Quaternary: progress in luminescence dating of sediments. Quaternary Science Reviews 25, 2449–2468. https://doi.org/10.1016/j.quascirev.2005.11.013

Liritzis, I., Singhvi, A.K., Feathers, J.K., Wagner, G.A., Kadereit, A., Zacharias, N., Li, S.-H., 2013. Dose Rate, in: Liritzis, I., Singhvi, A.K., Feathers, J.K., Wagner, G.A., Kadereit, A., Zacharias, N., Li, S.-H. (Eds.), Luminescence Dating in Archaeology, Anthropology, and Geoarchaeology: An Overview. Springer International Publishing, Heidelberg, pp. 21–24. https://doi.org/10.1007/978-3-319-00170-8_3

Lo, J., Turk, H., 1982. Defect inspection on rare-earth garnet surfaces. IEEE Transactions on Magnetics 18, 1304–1306. https://doi.org/10.1109/TMAG.1982.1062158

Madsen, A.T., Buylaert, J.-P., Murray, A.S., 2011. Luminescence dating of young coastal deposits from New Zealand using feldspar. Geochronometria 38, 379–390. https://doi.org/10.2478/s13386-011-0042-5

Mahan, S.A., Rittenour, T.M., Nelson, M.S., Ataee, N., Brown, N., DeWitt, R., Durcan, J., Evans, M., Feathers, J., Frouin, M., Guérin, G., Heydari, M., Huot, S., Jain, M., Keen-Zebert, A., Li, B., López, G.I., Neudorf, C., Porat, N., Rodrigues, K., Sawakuchi, A.O., Spencer, J.Q.G., Thomsen, K., 2022. Guide for interpreting and reporting luminescence dating results. GSA Bulletin https://doi.org/10.1130/B36404.1

Maldonado, A., Betancourt, J.L., Latorre, C., Villagran, C., 2005. Pollen analyses from a 50 000-yr rodent midden series in the southern Atacama Desert (25° 30′ S). Journal of Quaternary Science 20, 493–507. https://doi.org/10.1002/jqs.936

Malins, A.E.R., Poolton, N.R.J., Quinn, F.M., Johnsen, O., Denby, P.M., 2004. Luminescence excitation characteristics of Ca, Na and K-aluminosilicates (feldspars) in the stimulation range 5–40 eV: determination of the band-gap energies. Journal of Physics D: Applied Physics 37, 1439. https://doi.org/10.1088/0022-3727/37/10/005

Marfunin, A.S., 1979. Spectroscopy, Luminescence and Radiation Centers in Minerals. Springer, Berlin, Heidelberg. https://doi.org/10.1007/978-3-642-67112-8

Maßon, L.A.E., Riedesel, S., Opitz, S., Zander, A., Bell, A., Cieszynski, H., Reimann, T., in press. How much K is OK? – Evaluating different methods for K-concentration determination and the effect of the internal K-concentration on feldspar luminescence dating. EGUsphere [preprint] 2025. https://doi.org/10.5194/egusphere-2025-806

Maßon, L.A.E., Riedesel, S., Zander, A., Sontag-González, M., Reimann, T., 2024. Testing the applicability of standardised growth curves for chemically heterogeneous single-grain feldspars from the Atacama Desert, Chile. Quaternary Geochronology 83, 101585. https://doi.org/10.1016/j.quageo.2024.101585

Mather, A., 2006. Arid Environments, in: Perry, C., Taylor, K. (Eds.), Environmental Sedimentology. John Wiley and Sons, Chichester, pp. 536–536.

Mather, A.E., Hartley, A., 2005. Flow events on a hyper-arid alluvial fan: Quebrada Tambores, Salar de Atacama, northern Chile. in: Harvey, A.M., Mather, A.E.,

Stokes, M. (Eds.), Alluvial Fans: Geomorphology, Sedimentology, Dynamics. The Geological Society of London, London, Special Publications, 251, pp. 9–24. https://doi.org/10.1144/GSL.SP.2005.251.01.02

May, S.M., Meine, L., Hoffmeister, D., Brill, D., Medialdea, A., Wennrich, V., Gröbner, M., Schulte, P., Steininger, F., Deprez, M., de Kock, T., Bubenzer, O., 2020. Origin and timing of past hillslope activity in the hyper-arid core of the Atacama Desert – The formation of fine sediment lobes along the Chuculay Fault System, Northern Chile. Global and Planetary Change 184, 103057. https://doi.org/10.1016/j.gloplacha.2019.103057

May, S.M., Zander, A., Francois, J.P., Kelletat, D., Pötsch, S., Rixhon, G., Brückner, H., 2015. Chronological and geoarchaeological investigations on an anthropogenic shell accumulation layer in the Longotoma dune field (Central Chile). Quaternary International 367, 32–41. https://doi.org/10.1016/j.quaint.2014.06.005

McFadden, L.D., McDonald, E.V., Wells, S.G., Anderson, K., Quade, J., Forman, S.L., 1998. The vesicular layer and carbonate collars of desert soils and pavements: formation, age and relation to climate change. Geomorphology 24, 101–145. https://doi.org/10.1016/S0169-555X(97)00095-0

McFadden, L.D., Wells, S.G., Jercinovich, M.J., 1987. Influences of eolian and pedogenic processes on the origin and evolution of desert pavements. Geology 15, 504–508. https://doi.org/10.1130/0091-7613(1987)15<504:IOEAPP>2.0.CO;2

Medialdea, A., May, S.M., Brill, D., King, G., Ritter, B., Wennrich, V., Bartz, M., Zander, A., Kuiper, K., Hurtado, S., Hoffmeister, D., Schulte, P., Gröbner, M., Opitz, S., Brückner, H., Bubenzer, O., 2020. Identification of humid periods in the Atacama Desert through hillslope activity established by infrared stimulated luminescence (IRSL) dating. Global and Planetary Change 185, 103086. https://doi.org/10.1016/j.gloplacha.2019.103086

Mejdahl, V., 1987. Internal radioactivity in quartz and feldspar grains. Ancient TL 5, 10–17.

Mejdahl, V., 1985. Thermoluminescence dating based on feldspars. Nuclear Tracks and Radiation Measurements 10, 133–136. https://doi.org/10.1016/0735-245X(85)90019-5

Mejdahl, V., 1979. Thermoluminescence dating: beta-dose attenuation in quartz grains. Archaeometry 21, 61–72.

Mejdahl, V., 1970. Measurement of Environmental Radiation at Archaeological Excavation Sites. Archaeometry 12, 147–159. https://doi.org/10.1111/j.1475-4754.1970.tb00017.x

Merklinger, F.F., Zheng, Y., Luebert, F., Harpke, D., Böhnert, T., Stoll, A., Koch, M.A., Blattner, F.R., Wiehe, T., Quandt, D., 2020. Population genomics of Tillandsia landbeckii reveals unbalanced genetic diversity and founder effects in the Atacama Desert. Global and Planetary Change 184, 103076. https://doi.org/10.1016/j.gloplacha.2019.103076

Morad, S., 1978. Feldspars in sedimentary rocks, in: Sedimentology. Encyclopedia of Earth Science. Springer, Heidelberg, pp. 452–457. https://doi.org/10.1007/3-540-31079-7_84

Moradi, G., Bol, R., Trbojevic, L., Missong, A., Mörchen, R., Fuentes, B., May, S.M., Lehndorff, E., Klumpp, E., 2020. Contrasting depth distribution of colloid-associated phosphorus in the active and abandoned sections of an alluvial fan in a hyper-arid region of the Atacama Desert. Global and Planetary Change 185, 103090. https://doi.org/10.1016/j.gloplacha.2019.103090

Mueller, D., Preusser, F., 2022. Investigating the applicability of a standardised growth curve approach on Middle Pleistocene sediments from northern Switzerland. Quaternary Geochronology 67, 101238. https://doi.org/10.1016/j.quageo.2021.101238

Murray, A.S., Helsted, L.M., Autzen, M., Jain, M., Buylaert, J.P., 2018. Measurement of natural radioactivity: Calibration and performance of a high-resolution gamma spectrometry facility. Radiation Measurements 120, 215–220. https://doi.org/10.1016/j.radmeas.2018.04.006

Murray, A.S., Roberts, R.G., 1997. Determining the burial time of single grains of quartz using optically stimulated luminescence. Earth and Planetary Science Letters 152, 163–180. https://doi.org/10.1016/S0012-821X(97)00150-7

Murray, A.S., Wintle, A.G., 2003. The single aliquot regenerative dose protocol: potential for improvements in reliability. Radiation Measurements 37, 377–381. https://doi.org/10.1016/S1350-4487(03)00053-2

Murray, A.S., Wintle, A.G., 2000. Luminescence dating of quartz using an improved single-aliquot regenerative-dose protocol. Radiation Measurements 32, 57–73. https://doi.org/10.1016/S1350-4487(99)00253-X

Murray, A.S., Wintle, A.G., Wallinga (INVITED), J., 2002. Dose Estimation Using Quartz OSL in the Non-linear Region of the Growth Curve. Radiation Protection Dosimetry 101, 371–374. https://doi.org/10.1093/oxfordjournals.rpd.a006004

NASA Shuttle Radar Topography Mission (SRTM), 2013. Shuttle Radar Topography Mission (SRTM) Global. https://doi.org/10.5069/G9445JDF

Nash, D.J., 2011. Desert Crusts and Rock Coatings, in: Thomas, D.S.G. (Ed.), Arid Zone Geomorphology: Process, Form and Change in Drylands (3rd Edition). Wiley, Chichester, pp. 131–180. https://doi.org/10.1002/9780470710777.ch8

Nash, D.J., Bateman, M.D., Bullard, J.E., Latorre, C., 2018. Late Quaternary coastal evolution and aeolian sedimentation in the tectonically-active southern Atacama Desert, Chile. Palaeogeography, Palaeoclimatology, Palaeoecology 490, 546–562. https://doi.org/10.1016/j.palaeo.2017.11.040

Nathan, R.P., Thomas, P.J., Jain, M., Murray, A.S., Rhodes, E.J., 2003. Environmental dose rate heterogeneity of beta radiation and its implications for luminescence dating: Monte Carlo modelling and experimental validation. Radiation Measurements 37, 305–313. https://doi.org/10.1016/S1350-4487(03)00008-8

Navarro-González, R., Rainey, F.A., Molina, P., Bagaley, D.R., Hollen, B.J., De La Rosa, J., Small, A.M., Quinn, R.C., Grunthaner, F.J., Cáceres, L., Gomez-Silva, B., McKay, C.P., 2003. Mars-Like Soils in the Atacama Desert, Chile, and the Dry Limit of Microbial Life. Science 302, 1018–1021. https://doi.org/10.1126/science.1089143

Nester, P.L., Gayó, E., Latorre, C., Jordan, T.E., Blanco, N., 2007. Perennial stream discharge in the hyperarid Atacama Desert of northern Chile during the latest Pleistocene. Proceedings of the National Academy of Sciences 104, 19724–19729. https://doi.org/10.1073/pnas.0705373104

Nishiizumi, K., Caffee, M.W., Finkel, R.C., Brimhall, G., Mote, T., 2005. Remnants of a fossil alluvial fan landscape of Miocene age in the Atacama Desert of northern Chile using cosmogenic nuclide exposure age dating. Earth and Planetary Science Letters 237, 499–507. https://doi.org/10.1016/j.epsl.2005.05.032

Nordheim, L.W., 1938. A New Analysis of Cosmic Radiation Including the Hard Component. Physical Review 53, 694–706. https://doi.org/10.1103/PhysRev.53.694

Oeser, R.A., Stroncik, N., Moskwa, L.-M., Bernhard, N., Schaller, M., Canessa, R., van den Brink, L., Köster, M., Brucker, E., Stock, S., Fuentes, J.P., Godoy, R., Matus, F.J., Oses

Pedraza, R., Osses McIntyre, P., Paulino, L., Seguel, O., Bader, M.Y., Boy, J., Dippold, M.A., Ehlers, T.A., Kühn, P., Kuzyakov, Y., Leinweber, P., Scholten, T., Spielvogel, S., Spohn, M., Übernickel, K., Tielbörger, K., Wagner, D., von Blanckenburg, F., 2018. Chemistry and microbiology of the Critical Zone along a steep climate and vegetation gradient in the Chilean Coastal Cordillera. CATENA 170, 183–203. https://doi.org/10.1016/j.catena.2018.06.002

O'Gorman, K., Brink, F., Tanner, D., Li, B., Jacobs, Z., 2021a. Calibration of a QEM-EDS system for rapid determination of potassium concentrations of feldspar grains used in optical dating. Quaternary Geochronology 61, 101123. https://doi.org/10.1016/j.quageo.2020.101123

O'Gorman, K., Tanner, D., Sontag-González, M., Li, B., Brink, F., Jones, B.G., Dosseto, A., Jatmiko, Roberts, R.G., Jacobs, Z., 2021b. Composite grains from volcanic terranes: Internal dose rates of supposed 'potassium-rich' feldspar grains used for optical dating at Liang Bua, Indonesia. Quaternary Geochronology 64, 101182. https://doi.org/10.1016/j.quageo.2021.101182

Ollerhead, J., Huntley, D.J., Berger, G.W., 1994. Luminescence dating of sediments from Buctouche Spit, New Brunswick. Canadian Journal of Earth Sciences 31, 523–531. https://doi.org/10.1139/e94-046

Olley, J.M., Caitcheon, G.G., Roberts, R.G., 1999. The origin of dose distributions in fluvial sediments, and the prospect of dating single grains from fluvial deposits using optically stimulated luminescence. Radiation Measurements 30, 207–217. https://doi.org/10.1016/S1350-4487(99)00040-2

Olley, J.M., Murray, A., Roberts, R.G., 1996. The effects of disequilibria in the uranium and thorium decay chains on burial dose rates in fluvial sediments. Quaternary Science Reviews 15, 751–760. https://doi.org/10.1016/0277-3791(96)00026-1

Olley, J.M., Roberts, R.G., Murray, A.S., 1997. Disequilibria in the uranium decay series in sedimentary deposits at Allen's cave, nullarbor plain, Australia: Implications for dose rate determinations. Radiation Measurements 27, 433–443. https://doi.org/10.1016/S1350-4487(96)00114-X

Ortega, C., Vargas, G., Rojas, M., Rutllant, J.A., Muñoz, P., Lange, C.B., Pantoja, S., Dezileau, L., Ortlieb, L., 2019. Extreme ENSO-driven torrential rainfalls at the southern edge of the Atacama Desert during the Late Holocene and their projection into the 21th century. Global and Planetary Change 175, 226–237. https://doi.org/10.1016/j.gloplacha.2019.02.011

Ortega, C., Vargas, G., Rutllant, J.A., 2013. Major hydrological regime change along the semiarid western coast of South America — Response to comments by Maldonado and Moreiras [page number in this issue]. Quaternary Research 80, 140–142. https://doi.org/10.1016/j.yqres.2013.03.008

Ortega, C., Vargas, G., Rutllant, J.A., Jackson, D., Méndez, C., 2012. Major hydrological regime change along the semiarid western coast of South America during the early Holocene. Quaternary Research 78, 513–527. https://doi.org/10.1016/j.yqres.2012.08.002

Ortlieb, L., Vargas, G., Saliège, J.-F., 2011. Marine radiocarbon reservoir effect along the northern Chile–southern Peru coast (14–24°S) throughout the Holocene. Quaternary Research 75, 91–103. https://doi.org/10.1016/j.yqres.2010.07.018

Page, K., Frazier, P., Pietsch, T., Dehaan, R., 2007. Channel change following European settlement: Gilmore Creek, southeastern Australia. Earth Surface Processes and Landforms 32, 1398–1411. https://doi.org/10.1002/esp.1481

Parish, R., 1994. The influence of feldspar weathering on luminescence signals and the implications for luminescence dating of sediments, in: Allison, R.J. (Ed.), Rock weathering and landform evolution, John Wiley, Chichester, pp. 243–258.

Peng, J., Li, B., 2017. Single-aliquot Regenerative-Dose (SAR) and Standardised Growth Curve (SGC) Equivalent Dose Determination in a Batch Model Using the R Package 'numOSL' 35.

Peng, J., Li, B., More, J., Garbow, B., Hillstrom, K., Burkardt, J., Gilbert, P., Varadhan, R., 2018. numOSL: Numeric Routines for Optically Stimulated Luminescence Dating.

Pfeiffer, M., Latorre, C., Santoro, C.M., Gayo, E.M., Rojas, R., Carrevedo, M.L., McRostie, V.B., Finstad, K.M., Heimsath, A., Jungers, M.C., De Pol-Holz, R., Amundson, R., 2018. Chronology, stratigraphy and hydrological modelling of extensive wetlands and paleolakes in the hyperarid core of the Atacama Desert during the late quaternary. Quaternary Science Reviews 197, 224–245. https://doi.org/10.1016/j.quascirev.2018.08.001

Pfeiffer, M., Morgan, A., Heimsath, A., Jordan, T., Howard, A., Amundson, R., 2021. Century scale rainfall in the absolute Atacama Desert: Landscape response and implications for past and future rainfall. Quaternary Science Reviews 254, 106797. https://doi.org/10.1016/j.quascirev.2021.106797

Philippe, A., Guérin, G., Kreutzer, S., 2019. BayLum - An R package for Bayesian analysis of OSL ages: An introduction. Quaternary Geochronology 49, 16–24. https://doi.org/10.1016/j.quageo.2018.05.009

Pierson, T.C., 1980. Erosion and deposition by debris flows at Mt Thomas, North Canterbury, New Zealand. Earth Surface Processes 5, 227–247. https://doi.org/10.1002/esp.3760050302

Pierson, T.C., Scott, K.M., 1985. Downstream Dilution of a Lahar: Transition From Debris Flow to Hyperconcentrated Streamflow. Water Resources Research 21, 1511–1524. https://doi.org/10.1029/WR021i010p01511

Pinto, R., Barría, I., Marquet, P.A., 2006. Geographical distribution of Tillandsia lomas in the Atacama Desert, northern Chile. Journal of Arid Environments 65, 543–552. https://doi.org/10.1016/j.jaridenv.2005.08.015

Placzek, C.J., Matmon, A., Granger, D.E., Quade, J., Niedermann, S., 2010. Evidence for active landscape evolution in the hyperarid Atacama from multiple terrestrial cosmogenic nuclides. Earth and Planetary Science Letters 295, 12–20. https://doi.org/10.1016/j.epsl.2010.03.006

Poolton, N.R.J., Kars, R.H., Wallinga, J., Bos, A.J.J., 2009. Direct evidence for the participation of band-tails and excited-state tunnelling in the luminescence of irradiated feldspars. Journal of Physics: Condensed Matter 21, 485505. https://doi.org/10.1088/0953-8984/21/48/485505

Porat, N., 2006. Use of magnetic separation for purifying quartz for luminescence dating. Ancient TL 24. https://doi.org/10.26034/la.atl.2006.394

Porat, N., Faerstein, G., Medialdea, A., Murray, A.S., 2015. Re-examination of common extraction and purification methods of quartz and feldspar for luminescence dating. Ancient TL 33, 22-30.

Prasad, A.K., Jain, M., 2018. Breakdown of Kasha's Rule in a Ubiquitous, Naturally Occurring, Wide Bandgap Aluminosilicate (Feldspar). Scientific reports 8, 810. https://doi.org/10.1038/s41598-017-17466-z

Prasad, A.K., Poolton, N.R.J., Kook, M., Jain, M., 2017. Optical dating in a new light: A direct, non-destructive probe of trapped electrons. Scientific reports 7, 12097. https://doi.org/10.1038/s41598-017-10174-8

Prescott, J.R., Fox, P.J., 1993. Three-dimensional thermoluminescence spectra of feldspars. Journal of Physics D: Applied Physics 26, 2245–2254. https://doi.org/10.1088/0022-3727/26/12/024

Prescott, J.R., Hutton, J.T., 1994. Cosmic ray contributions to dose rates for luminescence and ESR dating: Large depths and long-term time variations. Radiation Measurements 23, 497–500. https://doi.org/10.1016/1350-4487(94)90086-8

Prescott, J.R., Hutton, J.T., 1988. Cosmic ray and gamma ray dosimetry for TL and ESR. International Journal of Radiation Applications and Instrumentation. Part D. Nuclear Tracks and Radiation Measurements 14, 223–227. https://doi.org/10.1016/1359-0189(88)90069-6

Prescott, J.R., Stephan, L.G., 1982. The contribution of cosmic radiation to the environmental dose for thermoluminescent dating. Latitude, altitude and depth dependences. PACT 6, 17–25.

Preusser, F., Degering, D., Fuchs, M., Hilgers, A., Kadereit, A., Klasen, N., Krbetschek, M., Richter, D., Spencer, J.Q.G., 2008. Luminescence dating: basics, methods and applications. E&G Quaternary Science Journal 57, 95–149. https://doi.org/10.3285/eg.57.1-2.5

Preusser, F., Kasper, H.U., 2001. Comparison of dose rate determination using high-resolution gamma spectrometry and inductively coupled plasma-mass spectrometry. Ancient TL 19.

Prohaska, T., Irrgeher, J., Benefield, J., Böhlke, J.K., Chesson, L.A., Coplen, T.B., Ding, T., Dunn, P.J.H., Gröning, M., Holden, N.E., Meijer, H.A.J., Moossen, H., Possolo, A., Takahashi, Y., Vogl, J., Walczyk, T., Wang, J., Wieser, M.E., Yoneda, S., Zhu, X.-K., Meija, J., 2022. Standard atomic weights of the elements 2021 (IUPAC Technical Report). Pure Applied Chemistry 94, 573–600. https://doi.org/10.1515/pac-2019-0603

Quade, J., Rech, J.A., Betancourt, J.L., Latorre, C., Quade, B., Rylander, K.A., Fisher, T., 2008. Paleowetlands and regional climate change in the central Atacama Desert, northern chile. Quaternary Research 69, 343–360. https://doi.org/10.1016/j.yqres.2008.01.003

Quade, J., Rech, J.A., Latorre, C., Betancourt, J.L., Gleeson, E., Kalin, M.T.K., 2007. Soils at the hyperarid margin: The isotopic composition of soil carbonate from the Atacama Desert, Northern Chile. Geochimica et Cosmochimica Acta 71, 3772–3795. https://doi.org/10.1016/j.gca.2007.02.016

Rech, J.A., Currie, B.S., Jordan, T.E., Riquelme, R., Lehmann, S.B., Kirk-Lawlor, N.E., Li, S., Gooley, J.T., 2019. Massive middle Miocene gypsic paleosols in the Atacama Desert and

the formation of the Central Andean rain-shadow. Earth and Planetary Science Letters 506, 184–194. https://doi.org/10.1016/j.epsl.2018.10.040

Rech, J.A., Currie, B.S., Michalski, G., Cowan, A.M., 2006. Neogene climate change and uplift in the Atacama Desert, Chile. Geology 34, 761–764. https://doi.org/10.1130/G22444.1

Rech, J.A., Quade, J., Betancourt, J.L., 2002. Late Quaternary paleohydrology of the central Atacama Desert (lat 22°–24°S), Chile. GSA Bulletin 114, 334–348. https://doi.org/10.1130/0016-7606(2002)114<0334:LQPOTC>2.0.CO;2

Reimann, T., Román-Sánchez, A., Vanwalleghem, T., Wallinga, J., 2017. Getting a grip on soil reworking – Single-grain feldspar luminescence as a novel tool to quantify soil reworking rates. Quaternary Geochronology 42, 1–14. https://doi.org/10.1016/j.quageo.2017.07.002

Reimann, T., Thomsen, K., Jain, M., Murray, A., Frechen, M., 2012. Single-grain dating of young sediments using the pIRIR signal from feldspar. Quaternary Geochronology 11, 28–41. https://doi.org/10.1016/j.quageo.2012.04.016

Reimann, T., Tsukamoto, S., 2012. Dating the recent past (<500 years) by post-IR IRSL feldspar – Examples from the North Sea and Baltic Sea coast. Quaternary Geochronology 10, 180–187. https://doi.org/10.1016/j.quageo.2012.04.011

Reimann, T., Tsukamoto, S., Naumann, M., Frechen, M., 2011. The potential of using K-rich feldspars for optical dating of young coastal sediments – A test case from Darss-Zingst peninsula (southern Baltic Sea coast). Quaternary Geochronology 6, 207–222. https://doi.org/10.1016/j.quageo.2010.10.001

Rein, B., Lückge, A., Reinhardt, L., Sirocko, F., Wolf, A., Dullo, W.-C., 2005. El Niño variability off Peru during the last 20,000 years. Paleoceanography 20, PA4003. https://doi.org/10.1029/2004PA001099

Rein, B., Lückge, A., Sirocko, F., 2004. A major Holocene ENSO anomaly during the Medieval period. Geophysical Research Letters 31. https://doi.org/10.1029/2004GL020161

Rhodes, E.J., 2011. Optically Stimulated Luminescence Dating of Sediments over the Past 200,000 Years. Annual Review of Earth and Planetary Sciences 39, 461–488. https://doi.org/10.1146/annurev-earth-040610-133425

Ribbe, P.H., 1983. Feldspar mineralogy, 2nd Edition, Reviews in mineralogy 2. Mineralogical society of America, Washington (D.C.).

Riedesel, S., Autzen, M., 2020. Beta and gamma dose rate attenuation in rocks and sediment. Radiation Measurements 133, 106295. https://doi.org/10.1016/j.radmeas.2020.106295

Riedesel, S., Autzen, M., Burow, C., 2023. scale_GammaDose(): Calculate the gamma dose deposited within a sample taking layer-to-layer variations in radioactivity into account (according to Aitken, 1985). Function version 0.1.2, in: Kreutzer, S., Burow, C., Dietze, M., Fuchs, M.C., Schmidt, C., Fischer, M., Friedrich, J., Mercier, N., Philippe, A., Riedesel, S., Autzen, M., Mittelstrass, D., Gray, H.J., Galharret, J., Colombo, M., Steinbuch, L., Boer, A.d. (eds.), 2024. Luminescence: Comprehensive Luminescence Dating Data Analysis. R package version 0.9.25. https://r-lum.github.io/Luminescence/

Riedesel, S., Bell, A.M.T., Duller, G.A.T., Finch, A.A., Jain, M., King, G.E., Pearce, N.J., Roberts, H.M., 2021. Exploring sources of variation in thermoluminescence emissions

and anomalous fading in alkali feldspars. Radiation Measurements 141, 106541. https://doi.org/10.1016/j.radmeas.2021.106541

Riedesel, S., King, G.E., Prasad, A.K., Kumar, R., Finch, A.A., Jain, M., 2019. Optical determination of the width of the band-tail states, and the excited and ground state energies of the principal dosimetric trap in feldspar. Radiation Measurements 125, 40–51. https://doi.org/10.1016/j.radmeas.2018.08.019

Rittenour, T.M., 2008. Luminescence dating of fluvial deposits: applications to geomorphic, palaeoseismic and archaeological research. Boreas 37, 613–635. https://doi.org/10.1111/j.1502-3885.2008.00056.x

Ritter, B., Wennrich, V., Medialdea, A., Brill, D., King, G., Schneiderwind, S., Niemann, K., Fernández-Galego, E., Diederich, J., Rolf, C., Bao, R., Melles, M., Dunai, T.J., 2019. "Climatic fluctuations in the hyperarid core of the Atacama Desert during the past 215 ka." Scientific reports 9, 5270. https://doi.org/10.1038/s41598-019-41743-8

Roberts, H.M., 2012. Testing Post-IR IRSL protocols for minimising fading in feldspars, using Alaskan loess with independent chronological control. Radiation Measurements 47, 716–724. https://doi.org/10.1016/j.radmeas.2012.03.022

Roberts, R.G., Galbraith, R.F., Yoshida, H., Laslett, G.M., Olley, J.M., 2000. Distinguishing dose populations in sediment mixtures: a test of single-grain optical dating procedures using mixtures of laboratory-dosed quartz. Radiation Measurements 32, 459–465. https://doi.org/10.1016/S1350-4487(00)00104-9

Román-Sánchez, A., Laguna, A., Reimann, T., Giráldez, J.V., Peña, A., Vanwalleghem, T., 2019a. Bioturbation and erosion rates along the soil-hillslope conveyor belt, part 2: Quantification using an analytical solution of the diffusion–advection equation. Earth Surface Processes and Landforms 44, 2066–2080. https://doi.org/10.1002/esp.4626

Román-Sánchez, A., Reimann, T., Wallinga, J., Vanwalleghem, T., 2019b. Bioturbation and erosion rates along the soil-hillslope conveyor belt, part 1: Insights from single-grain feldspar luminescence. Earth Surface Processes and Landforms 44, 2051–2065. https://doi.org/10.1002/esp.4628

Rundel, P.W., Dillon, M.O., Palma, B., Mooney, H.A., Gulmon, S.L., Ehleringer, J.R., 1991. The Phytogeography and Ecology of the Coastal Atacama and Peruvian Deserts. Aliso 13, 1–49. https://doi.org/10.5642/aliso.19911301.02

Rust, B.R., 1977. Depositional Models for Braided Alluvium, in: Mial, A.D. (Ed.), Fluvial Sedimentology – Memoir 5, Canadian Society of Petroleum Geologists, Calgary, pp. 605–625.

Sáez, A., Godfrey, L.V., Herrera, C., Chong, G., Pueyo, J.J., 2016. Timing of wet episodes in Atacama Desert over the last 15 ka. The Groundwater Discharge Deposits (GWD) from Domeyko Range at 25°S. Quaternary Science Reviews 145, 82–93. https://doi.org/10.1016/j.quascirev.2016.05.036

Samsonov, G.V., 2013. The Oxide Handbook. Springer US, New York, USA.

Sawakuchi, A.O., Blair, M.W., DeWitt, R., Faleiros, F.M., Hyppolito, T., Guedes, C.C.F., 2011. Thermal history versus sedimentary history: OSL sensitivity of quartz grains extracted from rocks and sediments. Quaternary Geochronology 6, 261–272. https://doi.org/10.1016/j.quageo.2010.11.002

Scheuber, E., Andriessen, P.A.M., 1990. The kinematic and geodynamic significance of the Atacama fault zone, northern Chile. Journal of Structural Geology 12, 243–257. https://doi.org/10.1016/0191-8141(90)90008-M

Schween, J.H., Hoffmeister, D., Löhnert, U., 2020. Filling the observational gap in the Atacama Desert with a new network of climate stations. Global and Planetary Change 184, 103034. https://doi.org/10.1016/j.gloplacha.2019.103034

Seeger, K., May, S.M., Brill, D., Herbrecht, M., Hoffmeister, D., Quandt, D., Stoll, A., Rhein, A., Keiser, M., Wolf, D., Bubenzer, O., 2024. Geomorphological and sedimentary traces of historical and modern exceptional flooding events in a dry valley of the Andean Precordillera (Tarapacá Region, N Chile). Geomorphology 466, 109417. https://doi.org/10.1016/j.geomorph.2024.109417

Singhvi, A.K., Porat, N., 2008. Impact of luminescence dating on geomorphological and palaeoclimate research in drylands. Boreas 37, 536–558. https://doi.org/10.1111/j.1502-3885.2008.00058.x

Smedley, R.K., Duller, G.A.T., Pearce, N.J.G., Roberts, H.M., 2012. Determining the K-content of single-grains of feldspar for luminescence dating. Radiation Measurements 47, 790–796. https://doi.org/10.1016/j.radmeas.2012.01.014

Smedley, R.K., Pearce, N.J.G., 2016. Internal U, Th and Rb concentrations of alkali-feldspar grains: Implications for luminescence dating. Quaternary Geochronology 35, 16–25. https://doi.org/10.1016/j.quageo.2016.05.002

Sohbati, R., Murray, A., Jain, M., Thomsen, K., Hong, S.-C., Yi, K., Choi, J.-H., 2013. Na-rich feldspar as a luminescence dosimeter in infrared stimulated luminescence (IRSL) dating. Radiation Measurement 51–52, 67–82. https://doi.org/10.1016/j.radmeas.2012.12.011

Sontag-González, M., Li, B., O'Gorman, K., Sutikna, T., Jatmiko, Jacobs, Z., Roberts, R.G., 2021. Establishing a pIRIR procedure for De determination of composite mineral grains from volcanic terranes: A case study of sediments from Liang Bua, Indonesia. Quaternary Geochronology 65, 101181. https://doi.org/10.1016/j.quageo.2021.101181

Spearman, C., 1904. The proof and measurement of association between two things. The American Journal of Psychology 15, 72–101. https://doi.org/10.2307/1412159

Spooner, N.A., 1994. The anomalous fading of infrared-stimulated luminescence from feldspars. Radiation Measurements 23, 625–632. https://doi.org/10.1016/1350-4487(94)90111-2

Spooner, N.A., 1992. Optical dating: Preliminary results on the anomalous fading of luminescence from feldspars. Quaternary Science Reviews 11, 139–145. https://doi.org/10.1016/0277-3791(92)90055-D

Starke, J., Ehlers, T.A., Schaller, M., 2020. Latitudinal effect of vegetation on erosion rates identified along western South America. Science 367, 1358–1361. https://doi.org/10.1126/science.aaz0840

Steffen, D., Preusser, F., Schlunegger, F., 2009. OSL quartz age underestimation due to unstable signal components. Quaternary Geochronology 4, 353–362. https://doi.org/10.1016/j.quageo.2009.05.015

Stuut, J.-B.W., Lamy, F., 2004. Climate variability at the southern boundaries of the Namib (southwestern Africa) and Atacama (northern Chile) coastal deserts during the last 120,000 yr. Quaternary Research 62, 301–309. https://doi.org/10.1016/j.yqres.2004.08.001

Sun, X., Amelung, W., Klumpp, E., Walk, J., Mörchen, R., Böhm, C., Moradi, G., May, S.M., Tamburini, F., Wang, Y., Bol, R., 2024. Fog controls biological cycling of soil phosphorus in the Coastal Cordillera of the Atacama Desert. Global Change Biology 30, e17068. https://doi.org/10.1111/gcb.17068

Sun, X., Matthias May, S., Amelung, W., Tang, N., Brill, D., Arenas-Díaz, F., Contreras, D., Fuentes, B., Bol, R., Klumpp, E., 2023. Water-dispersible colloids distribution along an alluvial fan transect in hyper-arid Atacama Desert. Geoderma 438, 116650. https://doi.org/10.1016/j.geoderma.2023.116650

Szymak, A., Moska, P., Poręba, G., Tudyka, K., Adamiec, G., 2022. Sciendo. Geochronometria 49, 9–17. https://doi.org/10.2478/geochr-2022-0002

Takahashi, K., Battisti, D.S., 2007a. Processes Controlling the Mean Tropical Pacific Precipitation Pattern. Part I: The Andes and the Eastern Pacific ITCZ. Journal of Climate 20, 3434–3451. https://doi.org/10.1175/JCLI4198.1

Takahashi, K., Battisti, D.S., 2007b. Processes Controlling the Mean Tropical Pacific Precipitation Pattern. Part II: The SPCZ and the Southeast Pacific Dry Zone. Journal of Climate 20, 5696–5706. https://doi.org/10.1175/2007JCLI1656.1

Tchakerian, V., Pease, P., 2015. Chapter 14 - The Critical Zone in Desert Environments, in: Giardino, J.R., Houser, C. (Eds.), Developments in Earth Surface Processes. Elsevier, pp. 449–472. https://doi.org/10.1016/B978-0-444-63369-9.00014-8

Thomsen, K.J., Murray, A.S., Jain, M., Bøtter-Jensen, L., 2008. Laboratory fading rates of various luminescence signals from feldspar-rich sediment extracts. Radiation Measurements 43, 1474–1486. https://doi.org/10.1016/j.radmeas.2008.06.002

Tite, M.S., Waine, J., 1962. Thermoluminescent dating: a re-appraisal. Archaeometry 5, 53–79. https://doi.org/10.1111/j.1475-4754.1962.tb00554.x

Tokuyasu, K., Tanaka, K., Tsukamoto, S., Murray, A., 2010. The Characteristics of OSL Signal from Quartz Grains Extracted from Modern Sediments in Japan. Geochronometria 37, 13-19.

Trabucco, A., Zomer, R., 2019. Global Aridity Index and Potential Evapotranspiration (ET0) Climate Database v2. https://doi.org/10.6084/M9.FIGSHARE.7504448.V3

Truscott, A.J., Duller, G.A.T., Bøtter-Jensen, L., Murray, A.S., Wintle, A.G., 2000. Reproducibility of optically stimulated luminescence measurements from single grains of Al_2O_3:C and annealed quartz. Radiation Measurements 32, 447–451. https://doi.org/10.1016/S1350-4487(00)00080-9

Tsukamoto, S., Jain, M., Murray, A., Thiel, C., Schmidt, E., Wacha, L., Dohrmann, R., Frechen, M., 2012. A comparative study of the luminescence characteristics of polymineral fine grains and coarse-grained K- and Na-rich feldspars. Radiation Measurements 47, 903–908. https://doi.org/10.1016/j.radmeas.2012.02.017

Tudyka, K., Koruszowic, M., Osadnik, R., Adamiec, G., Moska, P., Szymak, A., Bluszcz, A., Zhang, J., Kolb, T., Poreba, G., 2022. μRate: An online dose rate calculator for trapped charge dating. Archaeometry 65, 423–443. https://doi.org/10.1111/arcm.12828

Ugalde, P.C., Quade, J., Santoro, C.M., Holliday, V.T., 2020. Processes of Paleoindian site and desert pavement formation in the Atacama Desert, Chile. Quaternary Research 98, 58–80. https://doi.org/10.1017/qua.2020.39

van der Meij, W.M., Riedesel, S., Reimann, T., 2025. Mixed Signals: interpreting mixing patterns of different soil bioturbation processes through luminescence and numerical modelling. SOIL 11, 51–66. https://doi.org/10.5194/soil-11-51-2025

Vargas, G., Rutllant, J., Ortlieb, L., 2006. ENSO tropical–extratropical climate teleconnections and mechanisms for Holocene debris flows along the hyperarid coast of western South America (17°–24°S). Earth and Planetary Science Letters 249, 467–483. https://doi.org/10.1016/j.epsl.2006.07.022

Vásquez, P.I., Sepúlveda, F.V., Quezada, A.J., Aguilef, S.C., Franco, C.M., Blanco, N.P., 2018. Cartas Guanillos del Norte y Salar de Llamara, Regiones de Tarapacá y Antofagasta, Serie Geología Básica 195–196, mapa escala 1:100.000. Servicio Nacional de Geología y Minería, Santiago.

Veit, H., Preusser, F., Trauerstein, M., 2015. The Southern Westerlies in Central Chile during the two last glacial cycles as documented by coastal aeolian sand deposits and intercalating palaeosols. CATENA 134, 30–40. https://doi.org/10.1016/j.catena.2014.11.002

Veit, H., 1996. Southern Westerlies during the Holocene deduced from geomorphological and pedological studies in the Norte Chico, Northern Chile (27–33°S). Palaeogeography, Palaeoclimatology, Palaeoecology 123, 107–119. https://doi.org/10.1016/0031-0182(95)00118-2

Ventra, D., Clarke, L.E., 2018. Geology and geomorphology of alluvial and fluvial fans: current progress and research perspectives, in: Ventra, D., Clarke, L.E. (Eds.), Geology and Geomorphology of Alluvial and Fluvial Fans: Terrestrial and Planetary Perspectives. Geological Society, London, Special Publications 440, pp. 1–21. https://doi.org/10.1144/SP440.16

Vicencio Veloso, J., Böhm, C., Schween, J.H., Löhnert, U., Crewell, S., 2024. The Overlooked Role of Moist Northerlies as a Source of Summer Rainfall in the Hyperarid Atacama Desert. Journal of Geophysical Research: Atmospheres 129, e2024JD041021. https://doi.org/10.1029/2024JD041021

Visocekas, R., 1985. Tunnelling radiative recombination in labradorite: Its association with anomalous fading of thermoluminescence. Nuclear Tracks and Radiation Measurements (1982) 10, 521–529. https://doi.org/10.1016/0735-245X(85)90053-5

Vuille, M., 1999. Atmospheric circulation over the Bolivian Altiplano during dry and wet periods and extreme phases of the Southern Oscillation. International Journal of Climatology 19, 1579–1600. https://doi.org/10.1002/(SICI)1097-0088(19991130)19:14<1579::AID-JOC441>3.0.CO;2-N

Wainwright, J., Bracken, L.J., 2011. Runoff Generation, Overland Flow and Erosion on Hillslopes, in: Thomas, D.S.G. (Ed.), Arid Zone Geomorphology: Process, Form and Change in Drylands (3rd Edition). Wiley, Chichester pp. 235–267. https://doi.org/10.1002/9780470710777.ch11

Walk, J., 2020. Alluvial fans along the coastal Atacama Desert - landforms, processes, and evolution. Dissertation. RWTH Aachen University, Aachen, Germany. https://doi.org/10.18154/RWTH-2020-06003

Walk, J., Bartz, M., Stauch, G., Binnie, A., Brückner, H., Lehmkuhl, F., 2022. Weathering under coastal hyperaridity – Late Quaternary development of spectral, textural, and

gravelometric alluvial fan surface characteristics. Quaternary Science Reviews 277, 107339. https://doi.org/10.1016/j.quascirev.2021.107339

Walk, J., Schulte, P., Bartz, M., Binnie, A., Kehl, M., Mörchen, R., Sun, X., Stauch, G., Tittmann, C., Bol, R., Brückner, H., Lehmkuhl, F., 2023. Pedogenesis at the coastal arid-hyperarid transition deduced from a Late Quaternary chronosequence at Paposo, Atacama Desert. CATENA 228, 107171. https://doi.org/10.1016/j.catena.2023.107171

Walk, J., Stauch, G., Reyers, M., Vásquez, P., Sepúlveda, F.A., Bartz, M., Hoffmeister, D., Brückner, H., Lehmkuhl, F., 2020. Gradients in climate, geology, and topography affecting coastal alluvial fan morphodynamics in hyperarid regions – The Atacama perspective. Global and Planetary Change 185, 102994. https://doi.org/10.1016/j.gloplacha.2019.102994

Wallinga, J., 2002. Optically stimulated luminescence dating of fluvial deposits: a review. Boreas 31, 303–322. https://doi.org/10.1111/j.1502-3885.2002.tb01076.x

Wallinga, J., Bos, A.J.J., Dorenbos, P., Murray, A.S., Schokker, J., 2007. A test case for anomalous fading correction in IRSL dating. Quaternary Geochronology 2, 216–221. https://doi.org/10.1016/j.quageo.2006.05.014

Wallinga, J., Murray, A., Wintle, A., 2000. The single-aliquot regenerative-dose (SAR) protocol applied to coarse-grain feldspar. Radiation Measurements 32, 529–533. https://doi.org/10.1016/S1350-4487(00)00091-3

Warren, S.E., 1978. Thermoluminescence dating of pottery: an assessment of the dose-rate from rubidium. Archaeometry 20, 71–72. https://doi.org/10.1111/j.1475-4754.1978.tb00215.x

Wei, T., Simko, V., 2023. R package “corrplot”: Visualization of a Correlation Matrix. (Version 0.92).

Wells, S.G., Dohrenwend, J.C., McFadden, L.D., Turrin, B.D., Mahrer, K.D., 1985. Late Cenozoic landscape evolution on lava flow surfaces of the Cima volcanic field, Mojave Desert, California. GSA Bulletin 96, 1518. https://doi.org/10.1130/0016-7606(1985)96<1518:LCLEOL>2.0.CO;2

Wells, S.G., Harvey, A.M., 1987. Sedimentologic and geomorphic variations in storm-generated alluvial fans, Howgill Fells, northwest England. GSA Bulletin 98, 182–198. https://doi.org/10.1130/0016-7606(1987)98<182:SAGVIS>2.0.CO;2

Wennrich, V., Böhm, C., Brill, D., Carballeira, R., Hoffmeister, D., Jaeschke, A., Kerber, F., Maldonado, A., May, S.M., Olivares, L., Opitz, S., Rethemeyer, J., Reyers, M., Ritter, B., Schween, J.H., Sevinç, F., Steiner, J., Walber-Hellmann, K., Melles, M., 2024. Late Pleistocene to modern precipitation changes at the Paranal clay pan, central Atacama Desert. Global and Planetary Change 233, 104349. https://doi.org/10.1016/j.gloplacha.2023.104349

Williams, S.H., Zimbelman, J.R., 1994. Desert Pavement Evolution: An Example of the Role of Sheetflood. Journal of Geology 102, 243–248. https://doi.org/10.1086/629666

Wintle, A.G., 2008. Luminescence dating: where it has been and where it is going. Boreas 37, 471–482. https://doi.org/10.1111/j.1502-3885.2008.00059.x

Wintle, A.G., 1973. Anomalous Fading of Thermo-luminescence in Mineral Samples. Nature 245, 143–144. https://doi.org/10.1038/245143a0

Wintle, A.G., Huntley, D.J., 1980. Thermoluminescence dating of ocean sediments. Canadian Journal of Earth Sciences 17, 348–360. https://doi.org/10.1139/e80-034

Wintle, A.G., Huntley, D.J., 1979. Thermoluminescence dating of a deep-sea sediment core. Nature 279, 710–712. https://doi.org/10.1038/279710a0

Wintle, A.G., Murray, A.S., 2006. A review of quartz optically stimulated luminescence characteristics and their relevance in single-aliquot regeneration dating protocols. Radiation Measurements 41, 369–391. https://doi.org/10.1016/j.radmeas.2005.11.001

Woor, S., Durcan, J.A., Burrough, S.L., Parton, A., Thomas, D.S.G., 2022. Evaluating the effectiveness of heavy liquid density separation in isolating K-feldspar grains using alluvial sediments from the Hajar Mountains, Oman. Quaternary Geochronology 72, 101368. https://doi.org/10.1016/j.quageo.2022.101368

Zar, J.H., 2005. Spearman Rank Correlation, in: Armitage, P., Colton, T. (Eds.), Encyclopedia of Biostatistics (Online). John Wiley & Sons, Ltd., Bognor. https://doi.org/10.1002/0470011815.b2a15150

Zhao, H., Li, S.-H., 2005. Internal dose rate to K-feldspar grains from radioactive elements other than potassium. Radiation Measurements 40, 84–93. https://doi.org/10.1016/j.radmeas.2004.11.004

Zimmerman, D.W., 1971. Thermoluminescent Dating Using Fine Grains from Pottery. Archaeometry 13, 29–52. https://doi.org/10.1111/j.1475-4754.1971.tb00028.x

Zinelabedin, A., Mohren, J., Wierzbicka-Wieczorek, M., Dunai, T.J., Heinze, S., Ritter, B., 2025. Haloturbation in the northern Atacama Desert revealed by a hidden subsurface network of calcium sulfate wedges. Earth Surface Dynamics 13, 257–276. https://doi.org/10.5194/esurf-13-257-2025

Zinelabedin, A., Riedesel, S., Reimann, T., Ritter, B., Dunai, T.J., 2022. Testing the potential of using coarse-grain feldspars for post-IR IRSL dating of calcium sulphate-wedge growth in the Atacama Desert. Quaternary Geochronology 71, 101341. https://doi.org/10.1016/j.quageo.2022.101341

List of resources

Any sufficiently advanced technology is indistinguishable from magic.
(Arthur C. Clarke)

© Andreas Peffeköver

List of resources

All resources are grouped based on their primary purpose.

Software: Data Processing and Analysis

- R (version 4.4.1)
- R Studio (version 2024.04.2+764)
- R packages:
    - corrplot (version 0.92)
    - data.table (version 1.15.4)
    - dplry (version 2.5.0)
    - justapackage (version 0.9.0)
    - Luminescence (version 0.9.25)
    - numOSL (version 2.8)
    - stringr (version 1.5.1)
    - spatstat.utils (version 3.0-5)
    - tidyr (version 1.3.1)
    - tidyverse (version 2.0.0)
    - psych (version 2.4.12)
- Microsoft Excel (version professional plus 2019 16.0.10827.20181)
- Risø TL/OSL Software Package 2021-A (version 4.65)
- GradiStat (version 8.0)

Software: Data presentation and visualisation

- R packages:
    - factorextra (version 1.0.7)
    - ggplot2 (version 3.5.1)
    - ggrepel (version 0.9.6)
    - gridExtra (version 2.3)
- Affinity Designer 2 (version 2.6.3.3322)
- draw.io (version 20.2.3)
- Gimp 2.10.30 (version 2.10.30)

Software: spelling and grammar checking and reference manager

- Microsoft Word (version professional plus 2019 16.0.10827.20181)
- DeepL (version 25.7.2)
- ChatGpt (version GPT-4o)
- Zotero (version 6.0.4)

Analytical Instruments and Associated Software

- Luminescence reader: TL/OSL-DA-20 (Risø)
- SEM-EDX: Sigma 300-VP (Zeiss)
- M-XRF: Tornado M4 Mikro (Bruker)
- Low-level beta multicounter system: GM-25-5A (Risø)
- Laser diffractometer: LS 13320 (Beckman Coulter)

- High resolution Gamma-Spectrometer: PROFILE M-Series GEM Coaxial P-type HPGe Gamma-Ray Detecto (Ortec)
- High resolution Gamma-Spectrometer: PROFILE S-Series GEM Coaxial P-type HPGe Low-Background Gamma-Ray Detector (Ortec)
- EDXRF: Spectro Xepos (Spectro)
- WDXRF: ZSX Primus IV (Rigaku)
- Solar simulator SOL2 (Hönle)

Auxiliary equipment and consumables

In addition to the software and analytical instruments listed above, standard laboratory equipment (e.g. sieves, ultrasonic bath, drying oven) and laboratory consumables (e.g. HCl, H_2O_2) were used. Fieldwork further required general field equipment (e.g. hammer, shovel, tarp) and field consumables (e.g. plastic bags, tape).